Online ISSN:2322-5904

Print ISSN:2322-3049

# Nanomedicine Journal

Spring 2026 / Volume 13 / Issue 2

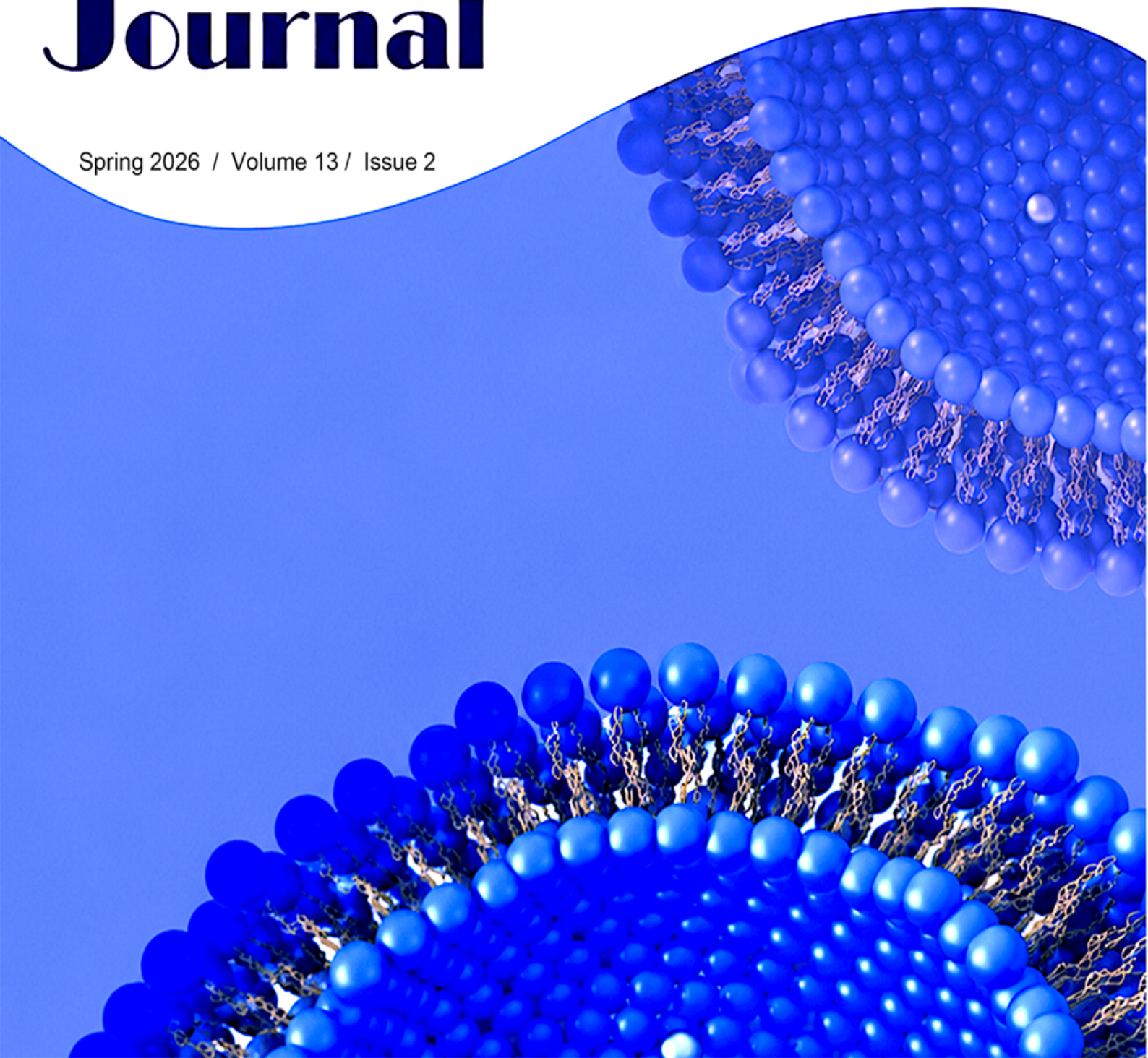

REVIEW PAPER

# Transfersomes-based nanocarriers for anticancer drug delivery: a promising approach

***Farnoush Mohamadpour[1], Zahra Chakeri[2], Mojgan Sheikhi[3], Saghi Naderpour [4,5], Milad Rahimzadegan[5], Alireza Sharafshah[6], Farshid Sefat[7,8*], Rahim Nosrati[6,9*]***

*[1] Department of Pharmaceutics, Faculty of Pharmacy, Tehran University of Medical Sciences, Tehran, Iran*
*[2] Cardiothoracic Imaging Section, Department of Radiology, University of Washington, Seattle, WA, USA*
*[3] Department of Drug and Food Control, Faculty of Pharmacy, Tehran University of Medical Sciences, Tehran, Iran*
*[4] Faculty of Pharmacy, Eastern Mediterranean University Famagusta, North Cyprus via Mersin 10, Turkey*
*[5] Functional Neurosurgery Research Center, Shohada Tajrish Comprehensive Neurosurgical Center of Excellence, Shahid Beheshti University of Medical Sciences, Tehran, Iran*
*[6] Cellular and Molecular Research Center, School of Medicine, Guilan University of Medical Sciences, Rasht, Iran*
*[7] Department of Bio-medical Engineering, School of Engineering, University of Bradford, Bradford, UK*
*[8] Interdisciplinary Research Center in Polymer Science & Technology (Polymer IRC), University of Bradford, Bradford, UK*
*[9] Student Research Committee, School of Medicine, Guilan University of Medical Sciences, Rasht, Iran*

## ABSTRACT

Chemotherapy is typically used to treat cancer, but it can have a number of negative side effects. Nanocarrier-based drug delivery systems have gained much interest cancer treatment in recent years due to their advantages compared to conventional delivery systems. Recently, transfersomes (TFs) have been known to be the most outstanding innovative drug delivery systems that make them an attractive carriers for drug administration and cancer therapy. TFs have a bilayered structure that facilitates the encapsulation of lipophilic and hydrophilic drugs/agents with higher permeation efficiencies, offering a promising alternative to conventional liposomes as an anti-cancer drug delivery method. They are highly interesting for applications that involve controlled release. TFs are being explored as a complex system for drug delivery, with a focus on enhancing local drug penetration. This paper overview the current advancements in transfersomes-encapsulated with anti-cancer drugs for intelligent medication delivery to various cancers. In conclusion, this paper briefly discusses the prospects and problems of transfersomes-based anti-cancer drug delivery.

***Keywords:*** *Nanocarriers; Transfersomes; Drug delivery; Cancer; Liposomes*

**How to cite this article**
*Mohamadpour F, Chakeri Z, Sheikhi M, Naderpour S, Rahimzadegan M, Sharafshah A, Sefat F, Nosrati R. Transfersomes-based nanocarriers for anticancer drug delivery: a promising approach. Nanomed J. 2026; 13(2): 238-255. DOI: 10.22038/NMJ.2025.86948.2203*

## INTRODUCTION

### *Cancer treatment*

The term "cancer" describes a wide range of malignant conditions in which abnormal cells reproduce uncontrolled and have the potential to invade other organs. Masses of cancerous cells that grow out of control and eliminate neighboring healthy tissues are known as tumors [1, 2]. Tumor cells that have spread throughout the blood or lymphatic system are responsible for metastasis, or the growth of secondary cancers in other organs or tissues [3, 4].

The World Health Organization's (WHO) most recent statistics indicate that cancer has a remarkable frequency and mortality frequency that is on the rise [5]. Chemotherapy is typically used to treat cancer, but because the medications are not very precise, it can have a number of negative side effects [6, 7]. The majority of anticancer medications on the market today do not distinguish between malignant and healthy cells very well, which might restrict the maximal dosage of the medication and cause systemic toxicities and side effects [8]. Furthermore, a medicine must be administered in large doses in order to have quick clearance and extensive distribution into the targeted tissues and organs. This increases the cost of therapy and elevates the risk of adverse outcomes [9, 10].

* *Corresponding authors:* Farshid Sefat, Ph.D; Department of Bio-medical Engineering, School of Engineering, University of Bradford, Bradford, UK. E-Mail address: *F.Sefat1@bradford.ac.uk.* Rahim Nosrati, Ph.D; Cellular and Molecular Research Center, School of Medicine, Guilan University of Medical Sciences, Rasht 41996-13769, Iran. Tel (Fax): +98 13 33690036. E-Mail address: *nosratirahim@gmail.com; Rahim_nosrati@gums.ac.ir.*

Note. This manuscript was submitted on March 31, 2025; approved on July 13, 2025.

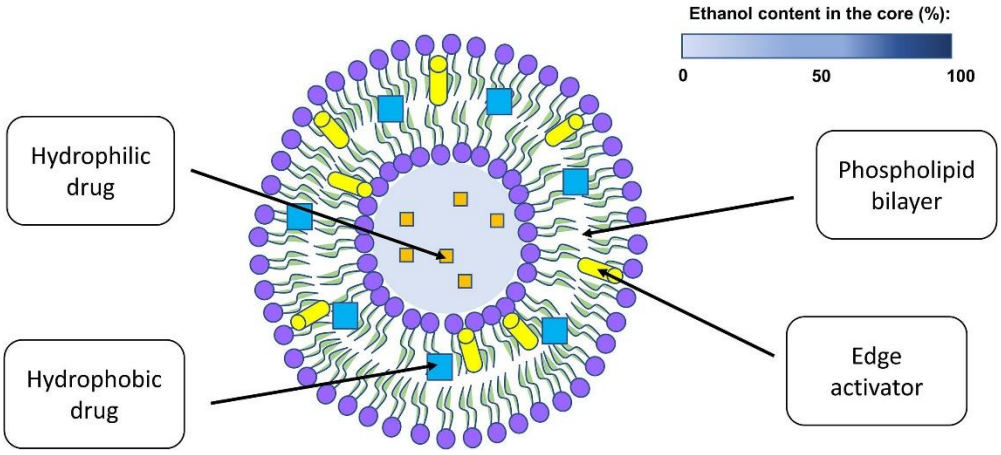


Fig. 1. Schematic showing the essential ingredients of a TFs: phospholipids, hydrophilic and hydrophobic medications, edge activator, and an interior core made of a combination of ethanol and water. Reprinted with permission from [18].

In fact, one of the most significant avenues for technological advances of the most advanced countries in the twenty-first century is nanotechnology, a vital field of study in technology and science that has been thoroughly investigated in the past 10 years [11]. Over the past ten years, pharmaceutical studies as well as clinical trials have shown the effectiveness of several drugs when administered *in vivo* through the application of pharmaceutical nanocarriers [12]. These carriers consist of vesicular and particulate systems, including micelles, liposomes, ethosomes, transfersomes (TFs), niosomes, dendrimers, and nanoparticles made of polymers, proteins, and lipids [13, 14]. Additionally, researched is on polymer–drug conjugates and antibody–drug conjugates [15].

***Transfersomes: adaptable and flexible nano-vesicular carriers***

Transfersomes/TFs (also known as transferosomes) are known as lipid-based vesicular carriers [16, 17] derived from the Greek term "soma," which means "body," and the Latin term "transferre," which means "to carry." [18, 19]. While the name transfersomes has been employed for over thirty years, it continues to be regarded as a new drug delivery mechanism due to the limited number of clinically available teransferosomal formulations [18, 20]. As a result, additional TFs would likely be marketed in the near future. TFs are made of four main components: phospholipids, an edge activator (EA), ethanol, and water (Fig. 1) [21, 22].

In this regard, phospholipids are typically including dipalmitylphosphatidylcholine, phosphatidylcholine, and distearylphosphatidylcholine. Surfactants or bile salts with a concentration of 10–25%, such as Tween 80 (T80), sodium deoxycholate, sodium cholate, Span® 80, and dipotassium glycyrrhizinate, are examples of EA. This component plays an essential role because it provides a wide radius of curvature that has the ability to weaken the lipid bilayer and enhance the flexibility of the lipid bilayer membrane of TFs. As a result, as the TFs move through the different layers of skin, they can compress naturally, which prevents the vesicles from rupturing. Water acts as a transport medium for ethanol, which is required in the TFs in smaller amount-typically below 10 percent [18, 22]. In the aqueous central cavity of TFs, hydrophilic drugs are encapsulated, while more hydrophobic drugs/active ingredients are incorporated into the phospholipid bilayer.

TFs have elasticity, flexibility, highly-deformability, and stress-responsivity [23] in contrast to liposomes with low lipid bilayer fluidity [24] or niosomes composed of non-ionic surfactants [25]. TFs can pass *via* the stratum corneum (SC) and enter the skin as intact vesicles smaller than 300 nm and in non-occlusive conditions. This preserves the gradient of trans-epidermal osmosis, allowing for elastic transport. Liposomes are among the most popular drug delivery devices. Their size and the lipid composition play a noteworthy role in permeation and treatment effects. In the case of niosomes, their ability to penetrate has been linked to decreased fluxes through the SC when compared to traditional liposomes, despite their higher stability and resistance to changes in osmolarity [26]. In comparison with niosomes and liposomes in liquid media, TFs appear to have demonstrated the

highest colloidal stability in terms of zeta-potential at 4 °C and 25 °C [27], TFs have demonstrated noticeable colloidal constancy (with no aggregation sign) for approximately some months, whereas liposomes and niosomes have demonstrated increased propensity for aggregation at the same temperatures and lower physical stability [28]. To ensure colloidal stability, TFs should have a zeta-potential that is either more than +30 mV or less than -30 mV; if not, there is a significant increase in the risk of aggregation [29].

The current review attempts to consider the researched TFs-based nanocarriers in the realm of anticancer drug delivery, their benefits and drawbacks, and future prospects.

This review article presents the current state of research concerning TFs-based nanocarriers for therapeutic agent's delivery to treat various cancers. The first section describes the properties of the general aspects of TFs, including their structure, synthesis methods, and properties, as well as the drug release mechanism. Then, a detailed discussion on the potential of TFs in the field of drug delivery for cancer treatment are presented. Finally, we summarize the challenges and future directions of drug delivery based on TFs as an emerging area of research.

## *Transfersomes for cancer drug delivery*

### *Skin cancer*

Today, one of the most widespread diseases in the world is skin cancer. Prolonged exposure to sunlight/ UV radiation and environmental pollution are the contributing factors. Today's world has seen a sharp rise in the incidence of skin cancer as a result of people's changing lifestyles. Skin cancer, specifically cutaneous malignant melanoma, is becoming more common than almost all other cancers. Melanoma continues to be a significant global issue, with current treatment options facing significant restrictions that emphasize the pressing need for innovative approaches [30, 31]. One promising strategy involves the targeted TFs of drugs through the skin to specifically attack cancer cells. Drugs with a higher molecular weight (above 500 Da) and ionized compounds should not be passed through the skin *via* the transdermal route, which is a non-invasive method suitable for systemic delivery. Numerous methods, including iontophoresis, microneedles, vesicular systems, penetration enhancers, and more, have been applied to increase the efficacy of the transdermal route [17]. However, they typically only penetrate the outer layers of the skin when applied topically. In transdermal drug delivery, vesicular delivery is becoming more and more important among the various methods [32]. Among them, TFs is most useful for transdermal delivery of substances with larger molecular weights due to its elastic and deformable nature, they can penetrate deeper skin layers through narrow pores that are significantly smaller than its size, come into contact with the systemic circulation, and then return to their original structure [33]. Some research were used TFs nanocarriers for transdermal delivery of anti-cancer natural active compounds for skin cancer therapy. This section, along with Table 1, provides a summary of various TFs that have been reported for use in skin cancer drug delivery.

Table 1. Transfersomes-based nanocarriers for skin cancer drug delivery

| Transfersome components | Delivery agents | Target | Effect | Ref. |
|---|---|---|---|---|
| Apigenin /TFs | Apigenin | Skin cancer/ Mice | Improved skin permeation | [30] |
| Apigenin/ TFs gel /Con A | | Melanoma (A375) cells | Enhanced skin targeting efficacy<br>Cytotoxic effects on melanoma | [34] |
| Embelin/TFs Carbopol 934/H3/ TFs-based gel | Embelin | B16F10 melanoma cell/ Rat | Enhanced skin cancer therapy | [35] |
| RSV/TFs/ PC/ non-ionic EA | Resveratrol | B16F10 melanoma cell | Increase in accumulation<br>Enhanced the stability, permeability, and uptake of drug | [36] |
| EGCG/TFs/HA | EGCG | HaCaT cells | Reduced lipid peroxidation, MMP expression, and intracellular ROS | [37] |
| Tea catechins (GTC)/TFs gel | Catechins | | Improved skin penetration<br>A remarkable decrease in IL-1β, IL-6, and TNF-α levels in mice | [38] |
| HK-loaded TFs | Honokiol (HK) | B16F10 melanoma cell | A prolonged release pattern<br>Inhibiting TGF-β signaling, and decreasing CD47 and CD133 expression | [39] |
| RB/TFs microneedle array (TDMNs) | Rose Bengal (RB) | | Superior intradermal transfer efficiency | [40] |
| Rtn-loaded TFs transdermal patches | Rutin (Rtn) | | Significant drug release<br>Increased inhibiting rate of cancer<br>A high skin deposition | [41] |

| Transfersome components | Delivery agents | Target | Effect | Ref. |
|---|---|---|---|---|
| 5-FU-loaded TFs | 5-fluorouracil (5-FU) | HaCaT cell line | The greatest cytotoxicity on the HaCaT cell | [42] |
| Celecoxib/T20/TFs | Celecoxib | Human skin fragments | An optimal vesicle characteristics and uniformity<br>Facilitated the drug permeation through the skin | [43] |
| CAR-loaded TFs | Carvedilol (CAR) | JB6 P+ and HaCaT cells | Induce cytotoxic effects Slowly drug penetration rates | [44] |
| CAR/TFs gel | | Porcine ear skin model | Reduced tumor incidence and intensity<br>Suppressed Ki-67 and COX-2 expression levels<br>Not affected heart rate | [45] |
| CAR/TFs | | | Exhibited the maximum retention of the drug in the skin<br>Reduced both acute and chronic skin inflammation of UV induction | [46] |
| PTX-CPP/TFs hydrogel | | Xenograft B10F16 melanoma mouse model | Effectively pass through the SC<br>Promoted effective delivery to tumor site<br>Suppressed tumor development | [47] |
| SFN/TFs<br>SFN/ethosomes | Sulforaphane (SFN) | SK-MEL 28 cells | Anticancer effects Enhanced percutaneous delivery | [48] |
| Cis-encapsulated TFs | Cisplatin (Cis) | | Increased drug efficacy with reduced systemic toxicity | [49] |
| LR@TFs-CPP Gel | lycorine (LR) | Cutaneous squamous cell carcinoma (cSCC) | Anti-cSCC properties<br>The skin and tumor permeability | [50] |
| Tamoxifen citrate/TFs gel | Tamoxifen citrate | | Promising outcomes with a high drug release | [51] |

Apigenin, a prevalent bioactive flavone detected in an extensive array of plants, fruits, and vegetables, has been recognized for its various pharmacological characteristics and anti-carcinogenic impacts. Apigenin serves as a chemotherapeutic agent for skin cancer therapy, both *in-vitro* and *in-vivo*. Jangdey et al's study aimed to utilize the Box-Behnken design in optimizing TFs that were developed using an altered rotary evaporation sonication system with the surfactant T80. The results showed an initial burst release followed by a controlled release, the optimized TFs (TW80-16) demonstrated a vesicle size 35.41 nm, the drug loading 8.042%, and an encapsulation efficiency (EE%) rate 84.24%. The permeation ability of apigenin was shown to be enhanced by this approach for prolonged periods of time, which may help cure skin cancer [30]. In another study, Jangdey *et al.* produced epigenin-loaded nano-TFs gel conjugated with Concanavalin-A (Con A) to specifically target melanocytes in the gel layer and treat UVB-induced skin carcinoma. The prepared formulation exhibited nano-sized vesicles (~179.0) with an EE% about 90%. The Con-A/TFs-based gel demonstrated cytotoxic effects on melanoma (A375) within a concentration ranging from of 0.4 to 2.0 mg/mL, while showing reduced toxicity towards HaCaT cells. The conjugated formulation exhibited an enhanced skin targeting efficacy both *in vitro* and *in vivo*, indicating a well-organized and cost-effective method for addressing skin cancer [34].

TFs-based vesicles carrying embelin, a naturally occurring benzoquinone derivative, was produced for transdermal medication delivery. Embelin, which comes from the dried fruit of *Embelia ribes*, is widely used because of its powerful anti-bacterial, anti-viral, anti-cancer, and anti-fungal properties. Employing the thin film hydration approach, embelin incorporated into several transferosomal formulations with varying ratios of Span-80 and Tween 80. A TFs-based gel with 2% embelin, carbopol 934 (at concentrations of 1%, 2%, 3%, and 4%), and propylene glycol (H3) was obtained as optimal formulation. The results showed that successful encapsulation of embelin in all formulations, with a maximum EE% 89.86%, suggesting the useful transdermal drugs delivery system for the skin cancer therapy [35]. Resveratrol (trans-3,5,4′-trihydroxystilbene, RSV), which is classified as a type of polyphenol, exhibits properties including antioxidant, anti-inflammatory, and anti-cancer effects, in addition to serving as a free-radical scavenger and a protector against cardiovascular ailments. Consequently, a RSV-encapsulated TFs was produced by phosphatidyl choline (PC) derived from a liposomal platform and non-ionic EA. The most favorable TFs production conditions involved using 5% PC/EA (3:1) and 5% ethanol in purified water, along with ultrasonic bath and rotating at 500 rpm, followed by high-pressure homogenization. The prepared TFs showed an EE% about 60%. Analysis of antioxidant functionality indicated that TFs exhibited a similar performance to free RSV. *In vitro* transdermal delivery analysis revealed a 27.59% increase in accumulation after 6 h with D1-20(W) formulation. Furthermore, cell

viability tests demonstrated a 34.45% reduction in cytotoxicity for D3-80(W) formulation compared to an equivalent concentration of RSV. As a result, the developed RSV-loaded TFs enhanced the stability, permeability, and entrance of drugs *via* the skin, even across the SC, owing to TFs deformability [36].

Epigallocatechin-3-gallate (EGCG) is known an effective antioxidant compound, most abundantly available in green tea. Avadhani *et al.* created TFs loaded with EGCG and hyaluronic acid (HA) to enhance the UV radiation-protective properties of both substances, while also providing anti-aging and antioxidant benefits. The nanosized TFs were produced using a thin-film-hydration method, utilizing sodium cholate and soy phosphatidylcholine, in conjunction with high-pressure homogenization. In HaCaT cells, it was shown that the improved TFs increased cell survival, reduced lipid peroxidation, MMP expression, and intracellular ROS. When compared to pure EGCG, the optimized EGCG/HA TFs showed considerably improved skin penetration and deposition of EGCG, demonstrating the potential use of the created TFs in sunscreen lotions and creams for improving UV protection [37]. Deka *et al.* developed a TFs herbal gel containing green tea catechins (GTC/TFs) to serve as an alternative to traditional invasive treatments of skin cancer and their associated side effects. The GTC/TFs was produced by the thin-film hydration technique, resulting in an EE% of 68.25%, and a drug loading of 10.41%. *In vitro* testing on B16F10 melanoma cell lines demonstrated favorable anticancer properties of the GTC/TFs. The treatment of skin cancer in mice as an animal model also showed a remarkable decrease in IL-1β, IL-6, and TNF-α levels, indicating both inhibiting and treating mice skin cancer of the formulation [38].

A naturally occurring bioactive substance called honokiol (HK) has been shown to have antineoplastic actions against melanoma. However, when taken orally, its bioavailability is very poor. The topical administration of HK presents a viable therapeutic option as an alternative. A modified scalable heating method was used to manufacture the HK-loaded TFs (HK-TFs). The cytotoxicity and cell uptake of HK-TFs were examined in B16F10 melanoma cells to scrutinize the influence of the complicated tumor microenvironment on the efficacy of HK. The improved formulation revealed an average size of 190 nm, a high EE% (89.9%), and a prolonged release pattern. HK-TFs demonstrated the immunosuppressive characteristics of B16F10 melanoma *in vitro* by inhibiting TGF-β signaling, and decreasing CD47 and CD133 expression (a hallmark of stem-like cells) [39].

Rose Bengal (RB) is a dye that is known for its selective toxicity towards melanoma cells. However, its therapeutic perspective is limited by its high water solubility and low permeability. In a research, RB-encapsulated TFs (RBTFs) were loaded into a trilayer dissolving microneedle array (RBTFs-TDMNs) to enhance intradermal delivery of RB for the treatment of melanoma. The RBTFs-TDMNs demonstrated sufficient strength to penetrate excised porcine skin, dissolve rapidly, and deliver RBTFs intradermally while preserving their physical and chemical properties. A dermatokinetic investigation revealed that RBTFs-TDMNs offer superior transfer efficiency in comparison with RBTFs dispersion and microneedles loaded with free drug, proposing its valuable potential for the topical treatment of melanoma [40]. Waldher *et al.* performed a study to improve the skin permeation of rutin (Rtn) by using TFs that integrated into transdermal patches (TPs) (Fig. 2).

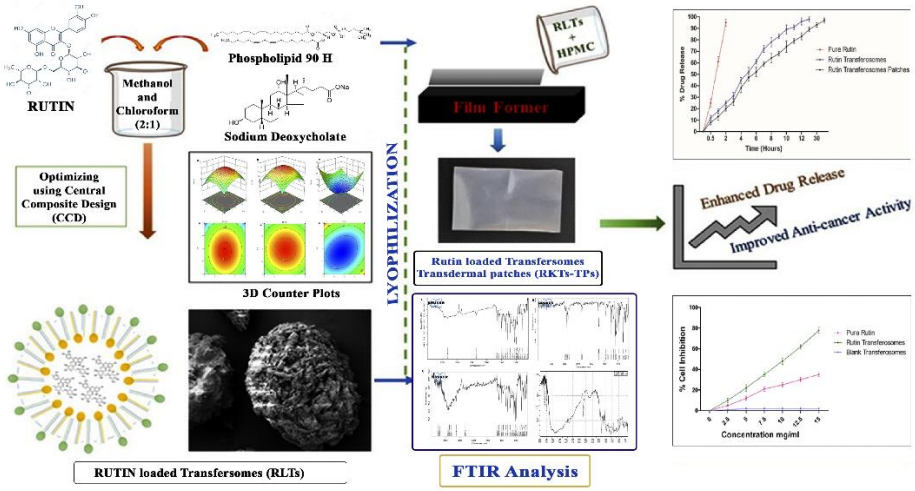


Fig.2. Development of rutin-loaded TFs to improve ex vivo membrane permeability and in vitro efficacy. Reprinted with permission from [41].

Rutin-loaded TFs (RtnTFs) were created using a central composite design (CCD) method and included different ratios of sodium deoxycholate and phospholipid 90H as variables. A greater Rtn encapsulation, enhanced formulation stability, and significant drug release were observed. Moreover, the RtnTFs exhibited an increased inhibiting rate B16–F10 melanoma cell line, and RtnTFs-loaded TPs cause a high skin deposition of approximately 0.921 ± 0.23 mg/cm$^3$ of Rtn. *Ex-vivo* skin diffusion tests showed a continues drug release of about 98% at 36 h. Skin irritancy assessments confirmed the compatibility of RtnTFs-TPs for dermal delivery, indicating high stability [41].

Based on the abovementioned research, the delay of drug release by topical delivery approach can enhance solubility and can be a hopeful approach for effective delivery of anti-tumor agents.

Topical 5-fluorouracil (5-FU) is used to treat non-melanoma skin cancer and actinic keratosis. Unfortunately, 5-FU does not penetrate the skin well, which reduces its effectiveness as an anticancer agent when applied topically. To that end, Alvi *et al.* synthesized 5-FU-loaded TFs, niosomes, and liposomes for topical application with EE% as high as 82.4%, 45.4%, and 43.4%, respectively. TFs were created using the solvent evaporation approach, whereas a reverse-phase evaporation was applied for liposomes and niosomes producing. , The skin permeability and retention revealed better permeability and retention when compared to the nonvesiculized dose form. After 72 hours, the $IC_{50}$ values of free 5-FU (15.89 µmol/l) were significantly higher than those of niosomes (9.91 µmol/l), TFs (1.02 µmol/l), and liposomes (6.83 µmol/l). Comparing to liposomes and niosomes, 5-FU-loaded TFs showed the greatest cytotoxicity on the HaCaT cell line, concluding that vesiculization of 5-FU increases both its cytotoxic effect and topical distribution [42].

The topical application of celecoxib has proven to be a successful method of preventing the development of skin cancer and improving the efficacy of anticancer drugs in the management of skin cancer. An effective topical construction of celecoxib that could simplify skin delivery of the drug was designed by three types of vesicular carriers, such as liposomes with a surfactant, ethosomes, and TFs, with proper EA. It was observed that TFs significantly enhanced (2.0 fold) the drug dosage that entered the skin compared to a celecoxib suspension. Among ethosomes incorporating ethanol and Tween 20 (T20) as an EA those exhibiting optimal vesicle characteristics and uniformity with a 54.4% of EE, which could facilitate the drug permeation through the skin, confirming the role of ethanol and T20 as permeation enhancers [43].

Carvedilol (CAR) is a β-blocker has been found to inhibit UV-induced skin cancer. However, the systemic administration of CAR can lead to undesired cardiovascular effects. To address this issue, topical TFs-based CAR delivery system was evaluated in several researches. A CAR-loaded TFs was created utilizing different ratios of surfactants and phospholipids. The optimized TFs (F18), consisted of CAR, T80, and soy phosphatidylcholine, at a ratio of 1:0.5:3, exhibited an EE% of 93.7%. F18 effectively restricted the EGF-mediated JB6 P+ cells neoplastic transformation at non-toxic amounts of EGF, although higher amounts did induce cytotoxic effects in JB6 P+ and HaCaT (human keratinocytes). Rather than a free drug, CAR was released more slowly from F18 and penetrated into the skin of porcine ear. Moreover, once selected to reconstruct the human skin in its full-thickness, F18 exhibited reduced drug penetration rates whereas effectively mitigating UV-induced DNA damage, gene expression in inflammatory events, and apoptosis [44]. In another study, a topical CAR-encapsulated TFs (CARTFs) that were loaded into carbopol gel or into suspension, exhibited comparable drug penetration and deposition in porcine ear skin model. CARTFs gel (10 µM) notably decreased skin edema and also formation of cyclobutane pyrimidine dimerization in singular dose UV-exposed mice, while this gel delayed tumor onset, reduced tumor incidence and intensity, and suppressed Ki-67 and COX-2 expression levels, in prolonged UV exposure. The treatment of mice with repeated doses of CARTFs gel (100 µM) could not affected heart rate, while significantly enhanced the skin deposition of CAR, suggesting its potentials for skin cancer prevention with minimal systemic impact [45]. In a same study, TFs containing CAR with a ratio of 1:3:0.5 for drug:lipid:surfactant exhibited the maximum retention of the drug in the skin. When applied topically at a concentration of 100 µM, CARTFs did not cause skin sensitivity in laboratory and animal tests and 10 µM CARTFs effectively reduced both acute and chronic skin inflammation of UV induction [46].

Topical application of anti-cancer drugs is a viable therapy strategy for cutaneous melanoma. However, natural barriers between the skin and the tumor impair the effectiveness of drug administration. In a study to increase the

transdermal administration of paclitaxel (PTX) for the treatment of melanoma, Jiang *et al.* used a paintable oligopeptide hydrogel incorporating PTX-encapsulated cell-penetrating-peptide (CPPs)-modified TFs (PTX-CTs/Gel). The PTX-CTs/Gel functioned as a patch to successfully extend the duration of PTX-CTs on the skin when applied to the skin above the melanoma lesion. The PTX-CTs were able to effectively pass through the SC due to the EA-induced fluidity and penetration of TFs in the SC. Furthermore, the CPP alteration promoted effective transportation among the tumor cells and increased penetration of PTX-CTs in the skin and tumor stroma. In a xenograft B10F16 melanoma mouse model, PTX-CTs successfully suppressed tumor development when paired with systemically administered chemotherapy (Fig.3) [47].

Sulforaphane (SFN) is a versatile medication with multiple effects, and its ability to combat cancer is driving increased interest in its potential. SFN has demonstrated antiproliferative properties against melanoma and other forms of skin cancer in laboratory settings. Unfortunately, due to its specific physical and chemical properties, this natural compound cannot be effectively applied directly to the skin. Cristiano and coworkers applied ethosomes- and TFs-based nanocarriers for delivering SFN *via* the skin for the treatment of skin cancer. Ethosomes revealed better anticancer effects on SK-MEL 28 cells and an enhanced percutaneous delivery of SFN, indicating that ethosomes were the most suitable vesicles for delivering SFN topically in comparison with TFs [48].

Despite promising treatment of topical anticancer medications for managing cutaneous squamous cell carcinoma (cSCC), the limited skin absorption capacity is a main challenge. Gupta *et al.* assayed topical delivery of Cisplatin (Cis)-encapsulated TFs for cSCC therapy. The EE% of Cis was determined to be 98%, with skin penetration of 560.20 ± 7.89 μg/cm$^2$ confirmed by a fluorescent marker. *In vivo* evaluation of the system revealed increased drug efficacy with reduced systemic toxicity, suggesting an enhanced, targeted, and localized drug delivery for cSCC treatment [49]. Li *et al.* confirmed the effect of lycorine (LR) in the topical treatment of cSCC by incorporating it into a cell-penetrating peptide (CPP)-modified cationic TFs gel (LR@TFs-CPP Gel). They revealed the anti-cSCC properties of LR and the skin and tumor permeability of LR-loaded TFs [50]. Gayathri and Sangeetha assessed the transdermal delivery of Tamoxifen citrate using TFs gel which was composed of different ratios of drug concentrations and Carbopol. The optimized TFs formulation MG2, containing 0.1 g Tamoxifen citrate, demonstrated promising outcomes with a high drug release of 94.32% [51].

***Breast cancer***

Breast cancer (BC) is diagnosed as the most frequent cancer in women and ranks the second origin of cancer-related deaths in women [52, 53]. Therefore, prompt and effective treatment is important. This section and Table 2 provide an overview of various TFs that have been reported for drug delivery in BC.

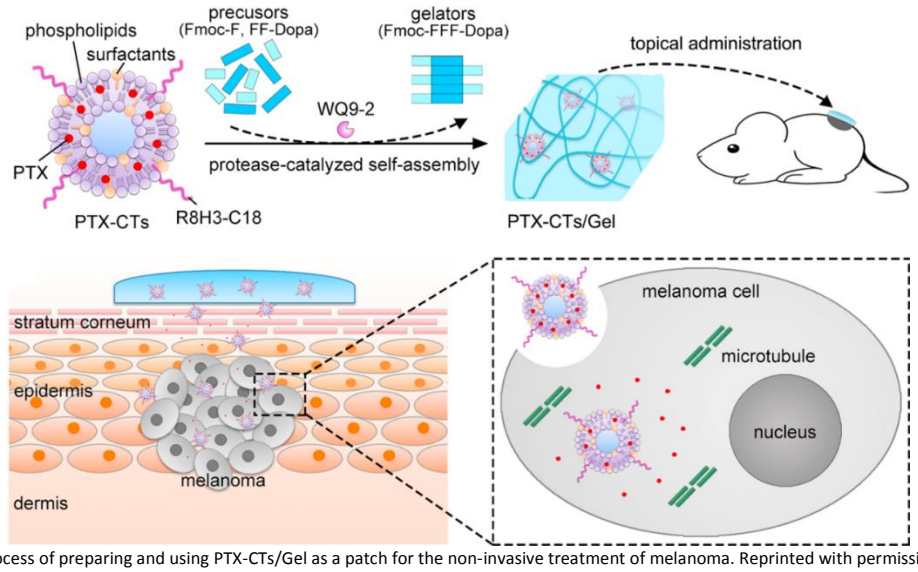


Fig. 3. The process of preparing and using PTX-CTs/Gel as a patch for the non-invasive treatment of melanoma. Reprinted with permission from [47].

Table 2. Transfersomes-based nanocarriers for breast cancer drug delivery

| Transfersome components | Delivery agents | Target | Effect | Ref. |
|---|---|---|---|---|
| RLX-loaded TFs | Raloxifene hydrochloride (RLX) | | Significant alterations in Rat skin | [54] |
| DOX/HA- GMS-TFs | doxorubicin (DOX) | MCF-7 cells | Increased in cellular uptake<br>Enhanced transdermal penetration<br>compatibility with mouse embryo fibroblast cells<br>a low hemolysis rate | [56] |
| DOX/HA/TFs/microneedles complex (TFs/MNs) | | Rat model of skin cancer | Develop lymphatic drug transport<br>Successfully penetrate rat skin<br>Increased the accumulation of DOX in lymph nodes | [57] |
| CUR-loaded oleic acid TFs | Curcumin (CUR) | MCF-7 cells | The *ex-vivo* permeation<br>Effective cytotoxicity | [58] |
| 4-OHT-loaded TFs/ emu oil | 4-hydroxytamoxifen (4-OHT) | Mice model of BC | Similar effectiveness to orally administered TAM without skin irritation | [59] |
| 4-OHT-loaded TFs/ratite oil | | *Ex vivo* porcine skin/breast cancer | Anti-inflammatory qualities of ratite oils<br>Enhanced penetration | [60] |
| DTX-CTs/Gel | Docetaxel (DTX) | Mice model of BC | Strong tumor and skin permeation<br>Enhancing DTX accumulation in cancer cells | [61] |
| Mannosylated naringenin-loaded TFs (MA-NgTFs) | Naringenin | | Enhanced of cellular uptake via mannose receptor-mediated TFs | [62] |
| HA/PVA/PVP- microneedle (MN) containing HA–GMS conjugated RB-TFs | Ribociclib (RB) | MDA-MB-231 | Maintained the drug concentrations within the effective range<br>Targeted delivery to tumor cells *via* CD44 as specific receptor of HA | [63] |
| iontophoresis-enhanced RSV-enclosed in TFs | RSV | BC rat model | A notable decrease in tumor volume and serum biomarker CA 15-3<br>High efficacy of transpapillary route delivery of RSV | [64] |
| iontophoresis-enhanced LPT and 5-FU encapsulated in TFs | Lapatinib (LPT) | MCF-7, MDA-MB-231 cells/ Rat skin | High efficacy of transpapillary route delivery of LPT | [65] |
| ERL-loaded TFs gel | Erlotinib (ERL) | Ductal carcinoma in situ | Superior effectiveness against MCF-7<br>Significantly lower $IC_{50}$ values | [66] |

Raloxifene hydrochloride (RLX) is approved to treat BC and decrease the invasive BC in high-risk women. RLX has extremely limited oral bioavailability. To overcome this problem, transdermal administration of RLX has been proposed. In this line, Mahmood *et al.* created RLX-loaded TFs for transdermal administration. The optimized TFs displayed spherical, unilamellar forms with an EE% of 91%, and transdermal flux of 6.5±1.1 μg/cm$^2$/hour. RLX-loaded TFs showed 6.25±1.50 drug permeability and 9.25±2.40 skin deposition that was better than traditional liposomes. Significant alterations in Rat skin structure were detected during the *ex vivo* drug diffusion research, indicating the higher potency of RLX-loaded TFs for oral medication administration [54].

Tumor-draining lymph nodes (TDLN) play a crucial role as primary metastatic foci in the progression and spread of various solid tumors. The use of the lymphatic system for drug delivery is considered beneficial for stimulating immune responses through vaccination or for the effective administration of chemotherapy to combat tumor metastasis. A novel TFs modified with HA was developed for the targeted delivery of doxorubicin (DOX) to the lymphatic system *via* the transdermal pathway for the management of tumor metastasis. DOX is a potent chemotherapeutic drug that is widely used in the treatment of various cancers [55]. The inclusion of DOX in HA-glycerol-a-monostearate(GMS)-TFs enabled efficient penetration into the deep layers of the skin, resulting in increased absorption by the lymphatics (Fig.4a). The optimized estimated values for EE% and loading capacity (LC) of HA-GMS-TFs were 60.86% and 4.63%, respectively. *In vitro* experiments showed that the transdermal penetration of DOX-loaded HA-GMS-TFs was 3 folds greater than the solution form. The modification with HA did not include the transdermal penetration efficiency of the TFs. Additionally, DOX-encapsulated HA-GMS-TFs resulted in a remarkable accumulation in lymph nodes *in vivo*, demonstrating good biocompatibility without cytotoxic effects. Moreover, HA-GMS-TFs significantly enhanced the endocytosis of breast tumor cells (MCF-7), leading to a 9-fold increase in

cellular uptake compared to unmodified TFs. HA-GMS-TFs also exhibited compatibility with mouse embryo fibroblast (MEF) cells and a low hemolysis rate of 4.65% compared to rabbit blood [56]. Another same research developed a new dissolving microneedle composed of HA, combined with TFs transdermal DOX delivery (Fig.4b). By leveraging the addition capabilities of microneedles and the lymphatic delivery potential of TFs, the TFs/microneedles complex (TFs/MNs) was anticipated to develop lymphatic drug transport. The findings demonstrated that the MNs could successfully penetrate rat skin and release DOX-loaded TFs into the dermis through self-dissolution. The DOX-TFs maintained their multilayer construction upon release from the dissolved MNs. The DOX-TFs/MNs formulation remarkably increased the accumulation of DOX in lymph nodes in comparison with diffusion through the epidermis, consequently elevating its bioavailability in the bloodstream. These results hold promise for enhancing chemotherapy of tumors *via* lymphatic drug delivery that can eradicate metastasized tumor cells present in draining lymph nodes [57].

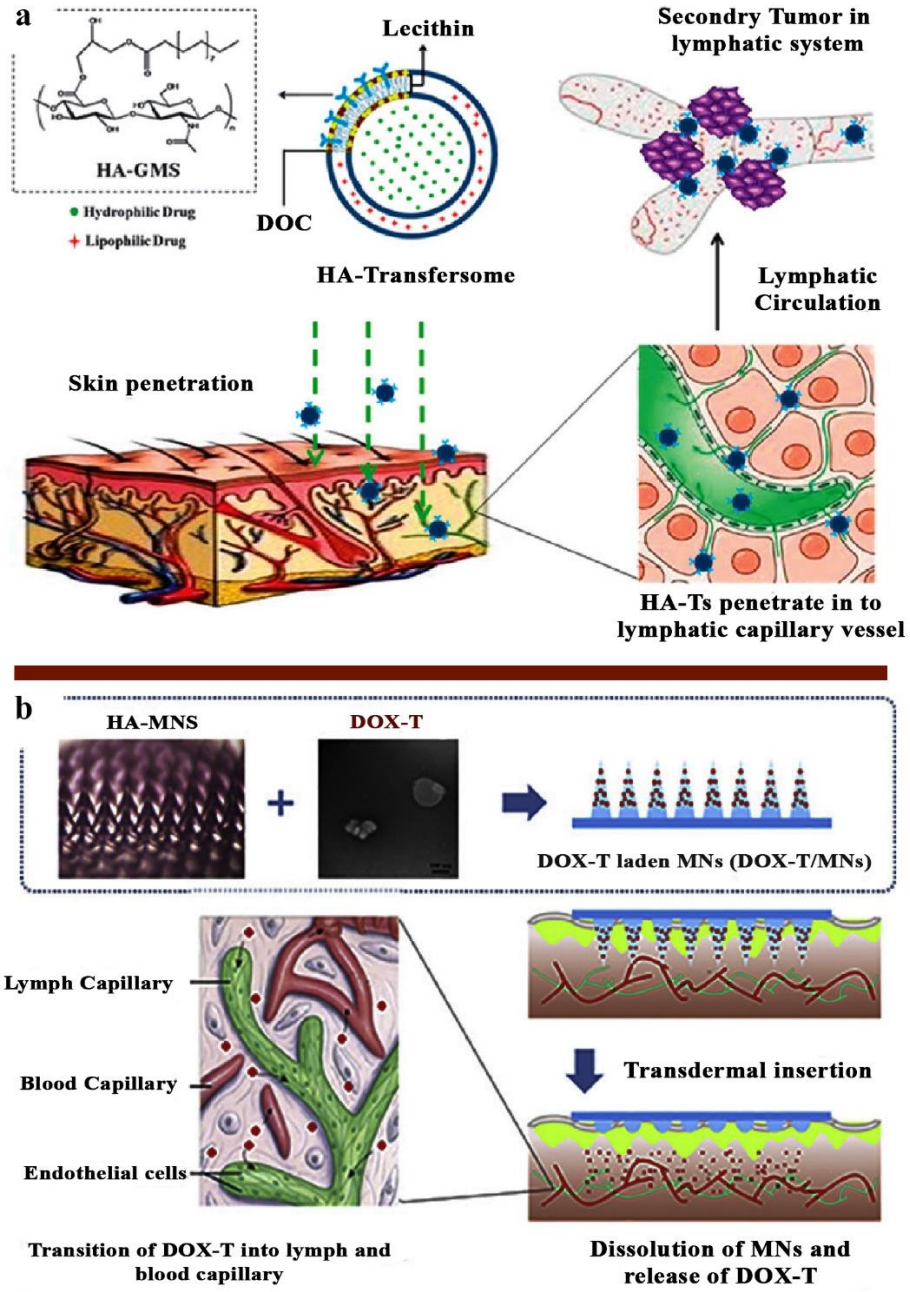


Fig.4. a) Schema of transdermal delivery of HA-modified TFs for tumor metastasis therapy; b) the mechanism of delivery of DOX *via* HA-based TFs/microneedle complex for the treatment of tumor metastasis. Reprinted with permission from [56] and [57].

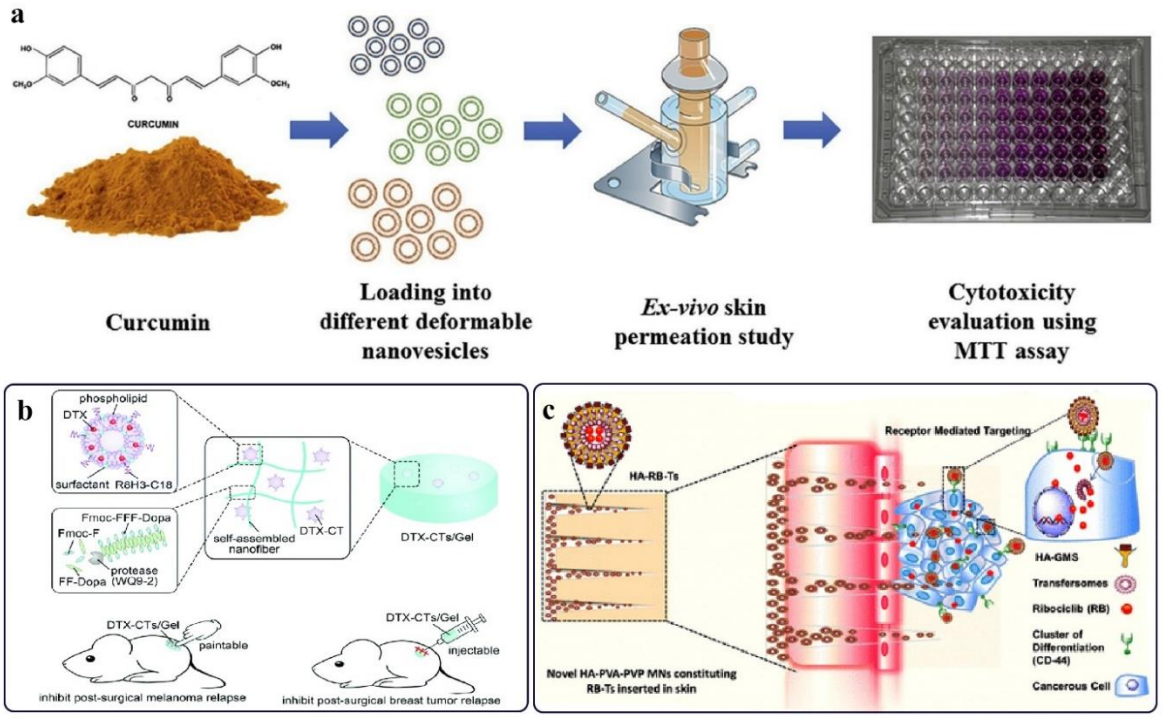


Fig. 5. a) Curcumin-loaded TFs as an impending delivery system for breast cancer treatment. b) A topical delivery manner of DTX utilizing DTX-CTs/Gel for the prevention the post-surgical melanoma and BC reappearance. c) The targeted delivery of Ribociclib-loaded TFs by a microneedle array and HA/CD44 interaction for breast cancer therapy. Reprinted with permission from [58] ,[61] and [63].

In order to target both surface and subcutaneous malignancies, such as BC, Abdel-Hafez *et al.* applied the transdermal method to give the poorly absorbable curcumin (CUR) into the circulation (Fig.5a). Thin film hydration and extrusion were used to manufacture CUR-loaded TFs by using EA included T80 and sodium cholate. The penetration-enhancing substances such oleic acid, Labrasol, Transcutol, and limonene were investigated for skin penetration efficacy. CUR, being hydrophobic, was efficiently encapsulated inside the lipid bilayers of the vesicles with high EE% of 93.91% and DL% of 7.04%. The *ex-vivo* permeation of CUR-TFs was confirmed on male albino mice's skin model. Cytotoxicity tests using MTT assay on MCF-7 cells showed that oleic acid TFs had an $IC_{50}$ of 20 µg/ml, indicating the potential of these nanovesicles as an effect delivery system for BC treatment [58].

Oral tamoxifen (TAM), a selective antiestrogen, is used for the prevention and treatment of non-invasive BC. TAM, is not widely accepted owing to some severe side effects. The main metabolite of TAM, 4-hydroxytamoxifen (4-OHT), is responsible for the anticancer effect of TAM. The local application of 4-OHT in the breast through transdermal therapy can help to avoid the harmful effects of oral tamoxifen and still be effective. Sundralingam *et al.* assessed skin irritation and the effectiveness of 4-OHT-loaded TFs formulations developed with or without emu oil. A lower plasma concentration of 4-OHT and similar effectiveness to orally administered TAM without skin irritation was observed in mice model of BC that was administered with prepared TF, with or without emu oil, through local transdermal manner [59]. In another study, an efficient TFs system was prepared for delivering 4-OHT utilizing ratite oil as a carrier for treating BC. The anti-inflammatory qualities of ratite oils, along with their ability to function as penetration enhancers, introduce them as excellent candidates for incorporation into transdermal formulations. The optimized TFs containing 4-OHT were formulated, with and without ratite oils, by various molar ratios of soy phosphatidylcholine and sodium taurocholate as EA through the rotary evaporation/ultrasonication approach. The ratite oil TFs formulation exhibited the highest EE% (95.1 ± 2.70%) with a constancy for 4 weeks at 4 °C, while TFs lacking ratite oils were stable for 8 weeks. *Ex vivo* penetrability investigations using porcine skin confirmed the transdermal delivery of 4-OHT TFs formulations without emu oil, offering promise in BC treatment [60].

Residual microtumors remaining after surgery can lead to tumor recurrence, posing a significant challenge in cancer treatment. Liu *et al.* prepared a nano-hybrid oligopeptide hydrogel to topically deliver the chemotherapeutic agent docetaxel (DTX), with the aim of preventing tumor recurrence after surgery (Fig.5b). The hydrogel, named DTX-CTs/Gel, was prepared by entrapping DTX in CCPs-modified TFs and embedding them in an oligopeptide gel. This formulation had the properties of being paintable and injectable, with the ability to stay longer at the application sites post-administration. The DTX-CTs released from the hydrogel displayed strong tumor and skin permeation ability, enhancing DTX accumulation in cancer cells and promoting cell death. The researchers demonstrated that the use of DTX-CTs/Gel for DTX delivery was effective in delaying tumor recurrence in mouse models of postoperative melanoma and BC [61].

Naringenin, a potent antioxidant abundant in citrus fruits, demonstrates significant potential in targeting skin carcinoma by scavenging reactive oxygen species (ROS). The created mannosylated naringenin-loaded TFs (MA-NgTFs) displayed vesicle sizes ranging from 102to 263, with an EE% from 72 to 82%. *In vitro* drug release analysis indicated percentages of 69.31%, 62.03%, 58.71%, and 65.02% for MA-NgTFs and marketed formulation dispersion, respectively. *Ex vivo* skin penetration and deposition investigations revealed that flux through the skin of mice was 6.5±3.07, with a drug retention percentage of 0.76±1.26, providing compelling evidence of cellular uptake *via* mannose receptor-mediated TFs [62].

HR+/HER2-metastatic BC (MBC) is a prevalent and serious ailment seen in women. The utilization of ribociclib (RB), an orally active CDK4/6 inhibitor, in endocrine therapy is a promising method for addressing HR+/HER2-MBC. Nevertheless, the current approach involving repetitive dosing over 3 to 6 cycles and non-targeted distribution of RB has resulted in severe side effects such as hepatobiliary, neutropenia, renal toxicities, and gastrointestinal, as well as QT interval prolongation. To tackle this issue, a HA/PVA/PVP-based microneedle (MN) array containing HA–GMS conjugated RB-TFs has been developed to deliver RB (Fig. 5c). The in the skin efficiently, enabling In this platform, HA-RB-TFs can penetrate to skin through MN-induced microchannels and targeted deliver to tumor cells *via* CD44 as specific receptor of HA, extending the drug release time by up to 6 times. Studies on pharmacokinetics and tissue distribution demonstrated that drug concentrations are maintained within the effective range for up to 48 h, reducing the dose administered thrice weekly, and reducing the risk of severe toxicities [63].

The local administration of drugs into the breast tissue is an interesting topic for the targeted administration of drugs. The administration of drugs through the mammary papilla offers advantages, as breast tumors often occur in the mammary ducts. A research study investigated the feasibility of using iontophoresis-enhanced transpapillary delivery of the RSV for treating BC. RSV was enclosed in TFs (RSV-TFs) to facilitate a gradual release of the drug by the biomaterial soya phosphatidylcholine (SPC). *In vitro* transpapillary iontophoresis experiments on porcine mammary papilla demonstrated increased permeation of RSV-TFs in comparison with passive diffusion. The optimized RSV-TFs administered *via* transpapillary delivery exhibited higher bioavailability values than pure RSV administered orally. In a chemically induced BC rat model, a notable decrease in tumor volume and serum biomarker CA 15-3 was observed, indicating the high efficacy of transpapillary route delivery of RSV in comparison to the oral route [64].

Combination chemotherapy, in which two or more anti-cancer drugs are used, has been a fundamental aspect of BC therapy due to its advantages over single-drug treatment. Fernandes *et al.* demonstrated the synergistic effects of Lapatinib (LPT) and 5-FU encapsulated in TFs on treating BC through the iontophoresis-induced transpapillary route. The $IC_{50}$ values for 5-FU and LPT were determined to be 5.7 µg/ml and 19.38 µg/ml, respectively. The *ex vivo* rat skin permeation studies showed that drug-loaded TFs had high stability and superior penetrability compared to the solution of LPT and 5-FU, suggesting an efficient alternative therapy of BC [65]. Mangla *et al.* developed erlotinib (ERL)-loaded TFs gel (ERL@TFs gel) for the management of ductal carcinoma in situ. The process involved using a thin-film hydration method to create ERL-loaded TFs, which were then combined with a carbopol gel matrix to produce ERL@TFs gel. When compared to plain ERL, the optimized ERL@TFs gel demonstrated superior effectiveness against MCF-7 cell lines, showing significantly lower $IC_{50}$ values, an improved safety profile with the ability to address ductal carcinoma in situ BC [66].

***Lung cancer***

Lung cancer is the second most common cancer and the leading cause of cancer-related mortality worldwide. A comprehensive overview of TFs

nanocarriers for lung cancer is provided in this section, as well as in Table 3.

Table 3. Transfersomes-based nanocarriers for anti-cancer drug delivery

| Cancer type | Transfersome components | Delivery agents | Target | Effect | Ref. |
|---|---|---|---|---|---|
| **Lung cancer** | Vinblastine-encapsulated TFs | Vinblastine | Human leukemia cell lines (HL-60, K562) | effective cytotoxic effects | [67] |
| | Uf-SUV/TFs | Vaccine | ErbB2-expressing cancer cells | effective antitumor effects against lung tumors | [68] |
| | PTX-loaded TFs Soya phosphatidylcholine | Paclitaxel (PTX) | MRC-5 SV2 cell line | a localized impact within the lungs toxicity towards lung cancer | [69] |
| | PDT + MPa-loaded nano-TFs | Methyl pheophorbide (MPa) | A549 and HeLa cells | a promising strategy for combating cancer through PDT | [70] |
| | ICG/TFs/gel + PDT | Indocyanine green (ICG) | Basal cell carcinoma (BCC) | the normal skin histology in mice following irradiation<br>minimum pain during the management | [71] |
| | Purpurin-18 sodium salt (P18Na) and DOX-loaded nano-TFs + PDT | P18Na and DOX | HeLa and A549 cell lines | effectively transported DOX and P18Na<br>pH-sensitive release | [72] |
| **Sarcomas** | MTM-loaded TFs | Mithramycin (MTM) | Chondrosarcoma and myxoid liposarcoma models | Strong anti-tumor effects<br>Inhibited the signaling pathway facilitated by the pro-oncogenic factor SP1 | [73] |
| **Head and neck squamous cell carcinoma** | Emodin-loaded TFs (NETFs)-ultrasound | Emodin | FaDu and CAL-27 cells | A remarkable dose-dependent ROS production<br>Enhanced apoptosis<br>Increased expression levels of caspase-3/9 genes | [60] |
| **Oral cancer** | 5-FU and Etodolac co-loaded TFs Hydrogel | 5-FU and Etodolac | FaDu cells | representing a synergistic impact of Et and 5-FU<br>Exhibited lag time, similar flux, and penetration coefficient | [74] |
| **Brain tumor** | FA-modified TPGS TFs containing DTX | Docetaxel (DTX) | U-87 MG cells | A superior internalization<br>FA-targeted GBM treatment | [75] |

In first study, vinblastine was encapsulated in cholesterol-based liposomes, sodium cholate-prepared TFs using the thin film hydration procedure, and the lipids dimiristoylphosphatidylcholine (DMPC) and dipalmitoylphosphatidylcholine (DPPC). The findings demonstrated that the percentage of vinblastine encapsulated into TFs varied between 50% and 80% at a ratio between 0.05 and 0.09. It was found that the drug retention in TFs and liposomes depended on time. The preservation of medication in TFs was shown to be lower than in liposomes due to the presence of sodium cholate. The cytotoxic and cytostatic capabilities of vinblastine-encapsulated TFs and liposomes was confirmed on nine human cell lines [67].

Mucosal surfaces offer pioneering opportunities for vaccination, particularly the mucosa of the respiratory tract, which enables the development of non-invasive methods for vaccine delivery. This research project focused on using the nasal route to evaluate the efficacy of various di-epitopic liposomal constructs in inducing antitumor responses by prophylactic vaccination in mice. Intranasal delivery of liposomal vesicles containing specific epitopes and adjuvants with different sizes, structures, and compositions including multilamellar vesicles (MLV), small unilamellar vesicles (SUV), ultraflexible small unilamellar vesicles (Uf-SUV/TFs), and reverse-phase evaporation (REV) were assessed. The vaccines were delivered nasally to BALB/c mice, prior to the introduction of ErbB2-expressing cancer cells either intravenously or subcutaneously. Nasal management of the SUV vaccine demonstrated effective antitumor effects against lung tumors, with limited protection against subcutaneous tumors. Interestingly, unlike the total vaccine dose or adjuvant concentration, the structure, size, and flexibility of the liposomes and TFs did not significantly influence vaccine-induced immunity or antitumor responses against lung tumors [68]. A straightforward method was utilized in the development of innovative proTFs tablets

containing paclitaxel (PTX) for pulmonary drug delivery. The extensive surface region of the pulmonary system serves as an advantageous location for the deposition of anti-cancer medication, resulting in a localized impact within the lungs. A PTX-loaded TFs Soya phosphatidylcholine was designed for lung cancer treatment. The hydrated TFs formulations (F3, F6, and F9) showed PTX entrapment levels of 93–96% with a toxicity towards lung cancer MRC-5 SV2 cell line (about 60, 68, and 67% cell viability) while being non-toxic to normal lung fibroblast cells (MRC-5) [69].

Photodynamic therapy (PDT) is a targeted therapy that does not require invasion. Photosensitizers (PSs), crucial components in PDT, tend to aggregate directly due to their lipophilic nature. Methyl pheophorbide (MPa)-loaded nano-TFs were produced using sonication, which displayed a gradual release of the drug over 48 h in a natural environment, making it suitable for controlled drug release in PDT, and leading to enhanced photodynamic effects and decreased adverse effects. The formulations exhibited minimal toxicity in the absence of light but demonstrated anti-cancer effects upon light exposure. Notably, nano-TFs with the smallest size revealed a higher level of photodynamic activity, indicating that the MPa-loaded nano-TFs system presents a promising strategy for combating cancer through PDT [70]. Indocyanine green (ICG) is a fluorescent dye that emits near-infrared light and shows promise for use as a photosensitizer in PDT for skin conditions. Of note, its effectiveness has been limited due to its rapid degradation. To address this issue, a study encapsulated ICG in colloidal TFs. A preliminary clinical trial was carried out to evaluate the efficacy of ICG/TFs in PDT for basal cell carcinoma (BCC). The ICG/TFs exhibited a particle size of approximately 125 nm and a sustained release of ICG for over 2 h. When ICG/TFs was incorporated into a gel formulation, it preserved the normal skin histology in mice following irradiation with an 820 nm diode laser. Additionally, PDT using ICG/TFs achieved an 80% clearance rate for BCC patients, with minimum pain described during the management [71]. In another study, purpurin-18 sodium salt (P18Na) and DOX-loaded nano-TFs were produced for a dual approach combining PDT and chemotherapy against cancer. The release of P18Na and DOX from the nano-TFs showed a consistent pH-responsive pattern, releasing gradually in normal conditions and rapidly in acidic pH. Consequently, the nano-TFs effectively transported DOX and P18Na to cancer cells with minimal leakage, demonstrating pH-sensitive release within the cancer cells. The finding confirmed a photo-cytotoxicity in HeLa and A549 cell lines [72].

***Other cancers***

***Sarcomas***

Sarcomas represent a diverse collection of cancerous growths that develop from mesenchymal stem/progenitor cells (MSCs), impacting mesodermal tissues like bones, cartilage, fat, or muscles. While these malignancies account for a mere 1% of total cancer diagnoses worldwide, the percentage increases to 12%–15% when considering pediatric cases. This underscores the necessity for more effective treatment strategies as a promising therapeutic option, our focus was on mithramycin (MTM), a natural antibiotic known for its potential anti-tumor properties but also for causing significant systemic toxicity. Hence, the utilization of nano-delivery systems to encapsulate MTM could potentially widen its therapeutic gateways. The comprehensive data on the use of TFs for the delivery of anti-cancer drug is presented in the following report and can also be found in Table 3. Estupiñán *et al.* developed innovative PLGA polymeric TFs (MTM-loaded TFs) through ethanol injection and thin film hydration techniques. The optimized MTM-loaded TFs displayed an EE 87% with a strong anti-tumor effects against adherent and cancer stem cell-enriched tumorsphere cultures of chondrosarcoma and myxoid liposarcoma models. Moreover, MTM delivered *via* nanocarriers effectively hinders the signaling pathway facilitated by the pro-oncogenic factor SP1 [73].

***Head and neck squamous cell carcinoma***

Non-invasive sonodynamic therapy (SDT) employs low-intensity ultrasound to induce chemical agent sensitizers for cancer treatment in a targeted manner. Pourhajibagher *et al*. explored the impact of ultrasound in combination with emodin-loaded TFs (NETFs) on head and neck squamous cell carcinoma (HNSCC) cell lines (Table 3). The final formulation exhibited a high drug-loading capacity and EE% with a significant hemolytic activity. The cytotoxicity test showed 97.3% and 98.2% cytotoxicity with $10 \times 10^{-4}$ g/L of NETFs combined with ultrasound irradiation for about 5 minutes (frequency: 1 MHz and intensity: 2 W/cm$^2$) on CAL-27 and FaDu cell lines, respectively. Moreover, a remarkable dose-dependent ROS

production, an enhanced apoptosis, and increased expression levels of caspase-3/9 genes were observed in NETFs group [60].

***Oral cancer***

Oral cancer (or mouth cancer) is among the most prevalent malignancies with a rising incidence rate. An amalgam of 5-FU and Etodolac (Et) is an efficient chemotherapy approach for treating oral cancer. Et is a cyclooxygenase-2 inhibitor and enhances the sensitivity of cancer cells to chemotherapeutic agents. In a study, TFs co-loaded 5-FU and Et formulations were created through the thin-film hydration system. The maximum EE% was ~37% for 5-FU and ~80% for Et (1:1). In a cell viability assay on FaDu cells with varying concentrations of Et and 5-FU, a combination index of 0.36 was observed, representing a synergistic impact. The uptake of Et/5-FU-loaded TFs by FaDu cells was meaningfully higher than that of free form. The TFs hydrogel containing HPMC (2% w/w) exhibited lag time, similar flux, and penetration coefficient to that of drug-loaded TFs when tested on excised porcine buccal tissue, suggesting a targeted delivery in the management of oral cancer (Table 3) [74].

***Brain tumor***

Glioblastoma multiforme (GBM) is acknowledged as an initial central nervous system (CNS) tumor that is highly prevalent and deadly. The treatment of this tumor is hindered by the challenges associated with breaching the blood-brain barrier (BBB) and by the nonspecificity of chemotherapeutic agents towards tumor cells. Luiz *et al.* developed folate (FA)-modified TPGS TFs containing docetaxel (DTX/TFs/FA) to enhance the treatment of GBM (Table 3). The optimized formulation examined a small particle size (below 200 nm) and high EE% (about 79% for DTX/TFs and 75.6% for FA-modified DTX/TFs). Additionally, DTX/TFs/FA revealed the significant capability to decrease the viability of U-87 MG cells compared to the DTX commercial formulation and TF-DTX. The *in vitro* cellular uptake demonstrated a superior internalization of DTX/TFs/FA into U-87 MG cells compared to DTXTFs (72% and 63%, respectively, after 24 h), proposing the potential of folate modification for targeted GBM treatment [75].

***Challenges of TFs-based anticancer drug delivery***

Various factors could affect the anticancer drug delivery by TFs. The ratio of phospholipid/EA can affect the entrapment efficiency, vesicle size, and permeation ability. A higher surfactant concentration can decrease TFs size and reduce the EE% via the generation of pores within the TFs membrane and the leakage of the encapsulated drug. In addition, increasing EA content may lead to pore formation in the bilayer and a reduced permeation ability of the TFs. The selection of a suitable solvent is another critical factor. A proper solvent can enhance the penetration of the drug into the SC by different mechanisms, such as increasing the drug solubility in TFs, altering the solubility properties of the target tissue, and improving the drug partitioning into the membrane. Despite this, a high concentration of ethanol in the TFs may lead to a decrease in the %EE. The suitable pH of the hydration medium can also influence the entrapment of the drug into TFs and the permeation of the drug into the cell membrane. Another main drawback of TFs is related to the loading of hydrophobic drugs into the TFs, which can interfere with their elastic and deformability properties.

Transdermal delivery systems are a promising approach for anticancer drug delivery as they are minimally invasive methods without first-pass effects. However, the main challenge with transdermal delivery systems is the barrier function of the skin, which prevents the transdermal delivery of therapeutic agents and needs to be overcome. Molecules with a molecular weight of more than 500 Da and ionized compounds generally cannot pass through the skin. Therefore, only a limited number of drugs can be administered this way. Encapsulation of drugs in TFs is one of the possible approaches to overcome the above-mentioned challenge. Compared to liposomes, TFs are known to be the most outstanding innovative transdermal drug carrier to date.

When TFs reach the skin pores, they can change their membrane flexibility and spontaneously pass through the skin pores. In addition, TFs are elastic and extremely deformable. Therefore, they can deform and compress as an intact vesicle to easily pass through even very narrow pores that are significantly smaller than their size. The high deformability of the vesicles facilitates the transport of drugs through the skin without measurable losses and can be used for both topical and systemic treatments. They are also able to enhance transdermal flow and improve the site specificity of therapeutic agents.

Phospholipids as a component of TFs can facilitate their formability. In this context, the use of natural phospholipids is preferable due to their biocompatibility and biodegradability. However, the difficulty in achieving the purity of natural

phospholipids may be a further obstacle in the use of TFs as a transdermal drug delivery system.

According to current evidence, most studies utilizing TFs-based anticancer drug delivery systems have been conducted in vitro, with only a limited number progressing to preclinical in vivo models. These early-stage studies, while promising, indicate that TFs are still far from entering clinical evaluation for oncology. Several key factors contribute to the current absence of clinical trials for TFs-based cancer therapies. First, TFs are primarily optimized for transdermal or localized delivery, which suits conditions such as osteoarthritis but poses challenges in treating cancers, particularly systemic or metastatic types, that require precise tumor targeting, deep tissue penetration, and prolonged systemic circulation. Second, regulatory and safety considerations are more demanding in oncology. Clinical translation of TFs is limited by the need for comprehensive data on biodistribution, immunogenicity, and long-term toxicity. Compared to more established nanocarriers like PEGylated liposomes, TFs lack the extensive clinical data required to meet these regulatory standards. Third, pharmacokinetic limitations restrict the applicability of TFs in cancer therapy. Their short systemic circulation time and limited passive or active tumor-targeting capabilities reduce their effectiveness in treating internal or deep-seated tumors. Lastly, formulation-related challenges such as scale-up, reproducibility, and variability across patients in skin permeability and tumor physiology further hinder their clinical development in oncology. Nonetheless, future advances including ligand-functionalized TFs, hybrid delivery systems (e.g., microneedle- or iontophoresis-assisted delivery), and application in localized cancers (such as melanoma and oral squamous cell carcinoma) may overcome current limitations and facilitate the translation of TFs into clinical oncology trials.

## CONCLUSIONS AND FUTURE PERSPECTIVES

In the arena of drug delivery, TFs have attracted significant attention in recent years. They are being explored as a complex system for drug delivery, with a focus on enhancing local drug penetration.

As previously mentioned, TFs are highly interesting for applications that involve controlled release. They act as carriers for various substances such as medications, chemicals, peptides, and proteins, protecting them from degradation. Researchers have developed numerous formulations of TFs for the treatment of infections, cancer, bone-related issues, and tissues.

The penetration through skin can be a challenge of TFs-based anti-cancer drug delivery. Two key factors influence the passage of TFs through the skin and delivery to tumor site, including the level of flexibility and the partition coefficient of the active substance. The primary mechanism involved is the passive movement of TFs through the SC, driven by the gradient of water content between SC (15%) and the epidermis (75%) [76].

This report discussed the use of TFs for delivering drugs and bioactive materials to various cancers. These techniques are currently in the initial phases of development. Altering the surface properties of TFs can be a key factor in improving their performance, enhancing biocompatibility, and bio-functionality.

Future advancements in TFs could involve optimizing the concentration of therapeutic agents and achieving specific and reversible binding to target sites using targeting molecules like aptamers or peptides. Moreover, enhancing uptake can be achieved by modifying TFs with positively charged nanoparticles or peptides that can interact with negatively charged receptors on cells or tissues. The increasing number of documents related to TFs indicates their potential to serve as innovative and efficient smart drug delivery systems in the future.

## ACKNOWLEDGMENTS

The authors acknowledge the financial support from Guilan University of Medical Sciences (GUMS), Rasht, Iran (grant no. IR.GUMS.REC.1402.198).

## CONFLICTS OF INTERESTS

All authors declare no financial/commercial conflicts of interest.

## DECLARATION OF GENERATIVE AI TOOLS

During the preparation of this work, the authors were not used any AI-assisted technologies.

## AUTHORSHIP CONTRIBUTIONS

The specific contributions made by each author:
**F.M, Z.Ch:** Original draft, Writing & editing
**M.Sh, S.N:** Graphical abstract, figures and tables
**M.R, A.Sh:** Writing & Critical revision
**F.S, R.N:** Conception and design of study, Writing & Critical revision
All authors read and approved the final manuscript.

## REFERENCES

1. Wang J-J, Lei K-F, Han F. Tumor microenvironment: recent advances in various cancer treatments. Eur Rev Med Pharmacol Sci. 2018; 22(12).
2. Arneth B. Tumor microenvironment. Medicina. 2019; 56(1): 15.

3. Rahman M, Mohammed S. Breast cancer metastasis and the lymphatic system. Oncol Lett. 2015; 10(3): 1233-1239.
4. Majidpoor J, Mortezaee K. Steps in metastasis: an updated review. Med Oncol. 2021; 38(1): 3.
5. Mattiuzzi C, Lippi G. Current cancer epidemiology. J Epidemiol Glob Health. 2019; 9(4): 217-222.
6. A Baudino T. Targeted cancer therapy: the next generation of cancer treatment. Curr Drug Disc Technol. 2015; 12(1): 3-20.
7. Anand U, Dey A, Chandel AKS, Sanyal R, Mishra A, Pandey DK, et al. Cancer chemotherapy and beyond: Current status, drug candidates, associated risks and progress in targeted therapeutics. Genes & Diseases. 2022; 10(4): 1367-1401.
8. Liu Z, Delavan B, Roberts R, Tong W. Lessons learned from two decades of anticancer drugs. Trends Pharmacol Sci. 2017; 38(10): 852-872.
9. Wen H, Jung H, Li X. Drug delivery approaches in addressing clinical pharmacology-related issues: opportunities and challenges. The AAPS journal. 2015; 17: 1327-1340.
10. Dawidczyk CM, Kim C, Park JH, Russell LM, Lee KH, Pomper MG, et al. State-of-the-art in design rules for drug delivery platforms: lessons learned from FDA-approved nanomedicines. J Controlled Release. 2014; 187: 133-144.
11. Haleem A, Javaid M, Singh RP, Rab S, Suman R. Applications of nanotechnology in medical field: a brief review. Glob Health J. 2023; 7(2): 70-77.
12. Dutta B, Barick K, Hassan P. Recent advances in active targeting of nanomaterials for anticancer drug delivery. Adv Colloid Interface Sci. 2021; 296: 102509.
13. Bandopadhyay S, Manchanda S, Chandra A, Ali J, Deb PK. Overview of different carrier systems for advanced drug delivery. Drug Delivery Systems: Elsevier; 2020: 179-233.
14. Sudhakar K, Fuloria S, Subramaniyan V, Sathasivam KV, Azad AK, Swain SS, et al. Ultraflexible liposome nanocargo as a dermal and transdermal drug delivery system. Nanomaterials. 2021; 11(10): 2557.
15. Estanqueiro M, Amaral MH, Conceição J, Sousa Lobo JM. Nanotechnological carriers for cancer chemotherapy: The state of the art. Colloids Surf B Biointerfaces. 2015; 126: 631-648.
16. Simrah, Hafeez A, Usmani SA, Izhar MP. Transfersome, an ultra-deformable lipid-based drug nanocarrier: an updated review with therapeutic applications. Naunyn-Schmiedeberg's Arch Pharmacol. 2024; 397(2): 639-673.
17. Stefanov SR, Andonova VY. Lipid nanoparticulate drug delivery systems: Recent advances in the treatment of skin disorders. Pharmaceuticals. 2021; 14(11): 1083.
18. Fernández-García R, Lalatsa A, Statts L, Bolás-Fernández F, Ballesteros MP, Serrano DR. Transferosomes as nanocarriers for drugs across the skin: Quality by design from lab to industrial scale. Int J Pharm. 2020; 573: 118817.
19. Shahidulla S, Yameen SH. Transferosomes-a highly permeable nanocarriers of drugs for transdermal drug delivery. World J Pharm Pharm Sci. 2022; 11(9): 509-527.
20. Matharoo N, Mohd H, Michniak-Kohn B. Transferosomes as a transdermal drug delivery system: Dermal kinetics and recent developments. Wiley Interdiscip Rev Nanomed Nanobiotechnol. 2024; 16(1): e1918.
21. Modi C, Kanada K, Prajapati B, Vaghela S, Chadha H. Transfersomes as Transporters via Lipid-Based Drug Delivery System. Lipid-Based Drug Delivery Systems: Jenny Stanford Publishing; 2024: 185-212.
22. Das B, Nayak AK, Mallick S. Transferosomes: a novel nanovesicular approach for drug delivery. Systems of Nanovesicular Drug Delivery: Elsevier; 2022:103-114.
23. Dey S, Hasnain MS, Jha SK, Sahoo N, Nayak AK. Transferosomes: a novel nanotechnological approach for transdermal drug delivery. Advanced and Modern Approaches for Drug Delivery: Elsevier. 2023:199-221.
24. Zhao J, Mao S. Tuning the membrane fluidity of liposomes for desirable in vivo fate with enhanced drug delivery. Adv Biomembr Lipid Self-Assem: Elsevier. 2021 (34):67-106..
25. Li D, Martini N, Liu M, Falconer JR, Locke M, Wu Z, et al. Non-ionic surfactant vesicles as a carrier system for dermal delivery of (+)-Catechin and their antioxidant effects. J Drug Targeting. 2021; 29(3): 310-322.
26. Moammeri A, Chegeni MM, Sahrayi H, Ghafelehbashi R, Memarzadeh F, Mansouri A, et al. Current advances in niosomes applications for drug delivery and cancer treatment. Materials Today Bio. 2023; 23: 100837.
27. Chamel S, Mishra A, Gull A. Transferosomes as innovative drug delivery systems for enhanced antifungal therapy: A comprehensive review. J Drug Deliv Sci Technol. 2024: 105545.
28. Moqejwa T, Marimuthu T, Kondiah PP, Choonara YE. Development of stable nano-sized transfersomes as a rectal colloid for enhanced delivery of cannabidiol. Pharmaceutics. 2022; 14(4): 703.
29. Leonyza A, Surini S. Optimization of sodium deoxycholate-based transfersomes for percutaneous delivery of peptides and proteins. Int J Appl Pharm. 2019; 11(5): 329-332.
30. Jangdey MS, Gupta A, Saraf S, Saraf S. Development and optimization of apigenin-loaded transfersomal system for skin cancer delivery: in vitro evaluation. Artif Cells Nanomed Biotechnol. 2017; 45(7): 1452-1462.
31. Iqubal MK, Khan MA, Agarwal NB, Ali J, Baboota S. Nanoformulations-based advancement in the delivery of phytopharmaceuticals for skin cancer management. J Drug Deliv Sci Technol. 2021; 66: 102912.
32. El-Zaafarany GM, Nasr M. Insightful exploring of advanced nanocarriers for the topical/transdermal treatment of skin diseases. Pharm Dev Technol. 2021; 26(10): 1136-1157.
33. Priyanka K, Singh S. A review on skin targeted delivery of bioactives as ultradeformable vesicles:

Overcoming the penetration problem. Curr Drug Targets. 2014; 15(2): 184-198.
34. Jangdey MS, Kaur CD, Saraf S. Efficacy of Concanavalin-A conjugated nanotransfersomal gel of apigenin for enhanced targeted delivery of UV induced skin malignant melanoma. Artif Cells Nanomed Biotechnol. 2019; 47(1): 904-916.
35. Jain S, Jain N. PUB040 formulation and evaluation of embelin loaded transfersome for effective treatment of skin cancer. J Thorac Oncol. 2017; 12(11): S2378.
36. Wu PS, Li YS, Kuo YC, Tsai SJJ, Lin CC. Preparation and evaluation of novel transfersomes combined with the natural antioxidant resveratrol. Molecules. 2019; 24(3): 600.
37. Avadhani KS, Manikkath J, Tiwari M, Chandrasekhar M, Godavarthi A, Vidya SM, et al. Skin delivery of epigallocatechin-3-gallate (EGCG) and hyaluronic acid loaded nano-transfersomes for antioxidant and anti-aging effects in UV radiation induced skin damage. Drug Deliv. 2017; 24(1): 61-74.
38. Deka T, Das MK, Das S, Das P, Singha LR. Box-behnken design approach to develop nano-vesicular herbal gel for the management of skin cancer in experimental animal model. Int J Appl Pharm. 2022; 14(6): 148-166.
39. Ezzeldeen Y, Swidan S, ElMeshad A, Sebak A. Green synthesized honokiol transfersomes relieve the immunosuppressive and stem-like cell characteristics of the aggressive B16F10 melanoma. Int J Nanomedicine. 2021: 5693-5712.
40. Demartis S, Anjani QK, Volpe-Zanutto F, Paredes AJ, Jahan SA, Vora LK, et al. Trilayer dissolving polymeric microneedle array loading Rose Bengal transfersomes as a novel adjuvant in early-stage cutaneous melanoma management. Int J Pharm. 2022; 627: 122217.
41. Wadher K, Trivedi S, Rarokar N, Umekar M. Development and assessment of rutin loaded transfersomes to improve ex vivo membrane permeability and in vitro efficacy. Hybrid Adv. 2024; 5: 100144.
42. Alvi IA, Madan J, Kaushik D, Sardana S, Pandey RS, Ali A. Comparative study of transfersomes, liposomes, and niosomes for topical delivery of 5-fluorouracil to skin cancer cells: Preparation, characterization, in-vitro release, and cytotoxicity analysis. Anti-Cancer Drugs. 2011; 22(8): 774-782.
43. Bragagni M, Mennini N, Maestrelli F, Cirri M, Mura P. Comparative study of liposomes, transfersomes and ethosomes as carriers for improving topical delivery of celecoxib. Drug Deliv. 2012; 19(7): 354-361.
44. Chen M, Shamim MA, Shahid A, Yeung S, Andresen BT, Wang J, et al. Topical delivery of carvedilol loaded nano-transfersomes for skin cancer chemoprevention. Pharmaceutics. 2020; 12(12): 1-17.
45. Shamim MA, Yeung S, Shahid A, Chen M, Wang J, Desai P, et al. Topical carvedilol delivery prevents UV-induced skin cancer with negligible systemic absorption. Int J Pharm. 2022; 611: 121302.
46. Shamim MA, Shahid A, Sardar PK, Yeung S, Reyes J, Kim J, et al. Transfersome Encapsulated with the R-carvedilol Enantiomer for Skin Cancer Chemoprevention. Nanomaterials. 2023; 13(5): 929.
47. Jiang T, Wang T, Li T, Ma Y, Shen S, He B, et al. Enhanced transdermal drug delivery by transfersome-embedded oligopeptide hydrogel for topical chemotherapy of melanoma. ACS Nano. 2018; 12(10): 9693-9701.
48. Cristiano MC, Froiio F, Spaccapelo R, Mancuso A, Nisticò SP, Udongo BP, et al. Sulforaphane-loaded ultradeformable vesicles as a potential natural nanomedicine for the treatment of skin cancer diseases. Pharmaceutics. 2019; 12(1): 6.
49. Gupta V, Karthikeyan C, Trivedi P. Localized delivery of cisplatin for the effective management of squamous cell carcinoma from protransfersome formulation. Arch Pharmacal Res. 2012; 35(5): 851-859.
50. Li Y, Tai Z, Ma J, Miao F, Xin R, Shen C, et al. Lycorine transfersomes modified with cell-penetrating peptides for topical treatment of cutaneous squamous cell carcinoma. J Nanobiotechnology. 2023; 21(1): 139.
51. Gayathri H, Sangeetha S. Pharmaceutical development of tamoxifen citrate loaded transferosomal gel for skin cancer by doe approach. J Posit Sch Psychol. 2022: 1879–1890.
52. Yousefi M, Nosrati R, Salmaninejad A, Dehghani S, Shahryari A, Saberi A. Organ-specific metastasis of breast cancer: molecular and cellular mechanisms underlying lung metastasis. Cell Oncol. 2018; 41(2): 123-140.
53. Bray F, Ferlay J, Soerjomataram I, Siegel RL, Torre LA, Jemal A. Global cancer statistics 2018: GLOBOCAN estimates of incidence and mortality worldwide for 36 cancers in 185 countries. CA Cancer J Clin. 2018; 68(6): 394-424.
54. Mahmood S, Taher M, Mandal UK. Experimental design and optimization of raloxifene hydrochloride loaded nanotransfersomes for transdermal application. Int J Nanomedicine. 2014; 9: 4331-4346.
55. Catuogno S, Esposito CL, De Franciscis V. Aptamer-mediated targeted delivery of therapeutics: An update. Pharmaceuticals. 2016; 9(4): 69.
56. Kong M, Hou L, Wang J, Feng C, Liu Y, Cheng X, et al. Enhanced transdermal lymphatic drug delivery of hyaluronic acid modified transfersomes for tumor metastasis therapy. ChCom. 2015; 51(8): 1453-1456.
57. Yang H, Wu X, Zhou Z, Chen X, Kong M. Enhanced transdermal lymphatic delivery of doxorubicin via hyaluronic acid based transfersomes/microneedle complex for tumor metastasis therapy. Int J Biol Macromol. 2019; 125: 9-16.
58. Abdel-Hafez SM, Hathout RM, Sammour OA. Curcumin-loaded ultradeformable nanovesicles as a potential delivery system for breast cancer therapy. Colloids Surf B Biointerfaces. 2018; 167: 63-72.
59. Sundralingam U, Chakravarthi S, Radhakrishnan AK, Muniyandy S, Palanisamy UD. Efficacy of emu oil transfersomes for local transdermal delivery of 4-oh tamoxifen in the treatment of breast cancer. Pharmaceutics. 2020; 12(9): 1-19.

60. Pourhajibagher M, Etemad-Moghadam S, Alaeddini M, Bahador A. Modulation of the triggered apoptosis by nano emodin transfersome-mediated sonodynamic therapy on head and neck squamous cell carcinoma cell lines. Photodiagnosis Photodyn Ther. 2021; 34: 102253.
61. Liu C, Ma Y, Guo S, He B, Jiang T. Topical delivery of chemotherapeutic drugs using nano-hybrid hydrogels to inhibit post-surgical tumour recurrence. Biomater Sci. 2021; 9(12): 4356-4363.
62. Verma N, Saraf S. Development and optimization of mannosylated naringenin loaded transfersomes using response surface methodology for skin carcinoma. Int J Appl Pharm. 2021; 13(2): 235-241.
63. Sharma M, Mittapelly N, Banala VT, Urandur S, Gautam S, Marwaha D, et al. Amalgamated microneedle array bearing ribociclib-loaded transfersomes eradicates breast cancer via CD44 targeting. Biomacromolecules. 2022; 23(3): 661-675.
64. Gadag S, Narayan R, Sabhahit JN, Hari G, Nayak Y, Pai KSR, et al. Transpapillary iontophoretic delivery of resveratrol loaded transfersomes for localized delivery to breast cancer. Biomater Adv. 2022; 140: 213085.
65. Fernandes NB, Velagacherla V, Spandana KJ, N B, Mehta CH, Gadag S, et al. Co-delivery of lapatinib and 5-fluorouracil transfersomes using transpapillary iontophoresis for breast cancer therapy. Int J Pharm. 2024; 650.
66. Mangla B, Mittal P, Kumar P, Javed S, Ahsan W, Aggarwal G. Development of erlotinib-loaded nanotransferosomal gel for the topical treatment of ductal carcinoma in situ. Nanomedicine. 2024; 19(10): 855-874.
67. Maswadeh H, Demetzos C, Dimas K, Hatziantoniou S, Georgopoulos A, Rallis M, et al. Accumulation of vinblastine into transfersomes and liposomes in response to a transmembrane ammonium sulfate gradient and their cytotoxic / cytostatic activity in vitro. Anticancer Res. 2001; 21(4 A): 2577-2583.
68. Kakhi Z, Frisch B, Heurtault B, Pons F. Liposomal constructs for antitumoral vaccination by the nasal route. Biochimie. 2016; 130: 14-22.
69. Khan I, Apostolou M, Bnyan R, Houacine C, Elhissi A, Yousaf SS. Paclitaxel-loaded micro or nano transfersome formulation into novel tablets for pulmonary drug delivery via nebulization. Int J Pharm. 2020; 575: 118919.
70. Yeo S, Yoon I, Lee WK. Design and Characterisation of pH-Responsive Photosensitiser-Loaded Nano-Transfersomes for Enhanced Photodynamic Therapy. Pharmaceutics. 2022; 14(1): 210.
71. Fadel M, Samy N, Nasr M, Alyoussef AA. Topical colloidal indocyanine green-mediated photodynamic therapy for treatment of basal cell carcinoma. Pharm Dev Technol. 2017; 22(4): 545-550.
72. Yeo S, Kim MJ, Yoon I, Lee WK. pH-Responsive Nano-transferosomes of Purpurin-18 Sodium Salt and Doxorubicin for Enhanced Anticancer Efficiency by Photodynamic and Chemo Combination Therapy. ACS Omega. 2023; 8(18): 16479-16490.
73. Estupiñán Ó, Rendueles C, Suárez P, Rey V, Murillo D, Morís F, et al. Nano-encapsulation of mithramycin in transfersomes and polymeric micelles for the treatment of sarcomas. J Clin Med. 2021; 10(7): 1358.
74. Bollareddy SR, Krishna V, Roy G, Dasari D, Dhar A, Venuganti VVK. Transfersome Hydrogel Containing 5-Fluorouracil and Etodolac Combination for Synergistic Oral Cancer Treatment. AAPS PharmSciTech. 2022; 23(2): 70.
75. Luiz MT, Viegas JSR, Abriata JP, Tofani LB, Vaidergorn MdM, Emery FdS, et al. Docetaxel-loaded folate-modified TPGS-transfersomes for glioblastoma multiforme treatment. Mater Sci Eng C. 2021; 124: 112033.
76. Sala M, Diab R, Elaissari A, Fessi H. Lipid nanocarriers as skin drug delivery systems: Properties, mechanisms of skin interactions and medical applications. Int J Pharm. 2018; 535(1-2): 1-17.

*Nanomed J. 13(2): 256-267, 2026*

REVIEW PAPER

# Quantum dot-based sensors and nanotheranostics for early detection and targeted therapy for colorectal cancer

***Dilpreet Singh[1*], Raj Kamal[2]***

*[1] School of Pharmaceutical Sciences, CT University, Ferozepur Rd, Sidhwan Khurd, Punjab, India*
*[2]School of Pharmacy, Desh Bhagat University, Mandi Gobindgarh, Punjab, India*

## ABSTRACT

***Introduction:*** Colorectal cancer (CRC) remains one of the most prevalent and fatal cancers worldwide, highlighting the urgent need for the development of advanced diagnostic and therapeutic strategies.

***Objective(s)***: Quantum dots (QDs), semiconductor nanomaterials with distinctive optical properties, have emerged as promising tools in the fight against colorectal cancer (CRC).

***Materials and Methods***: The ability of QDs to emit tunable fluorescence, combined with their small size and potential for surface functionalization, enables high sensitivity and specificity in early detection and targeted treatment. In the context of CRC, QDs can be used to identify biomarkers such as carcinoembryonic antigen (CEA) and folate receptors, facilitating non-invasive imaging with high resolution.

***Results:*** Furthermore, QDs can be functionalized for targeted therapy, enhancing the selective delivery of chemotherapeutic agents to tumor sites, reducing systemic toxicity, and allowing real-time monitoring of treatment efficacy. Despite these advantages, the clinical application of QDs in CRC is limited by challenges, including toxicity, biocompatibility, long-term stability, and efficient targeting. This review examines the current state of quantum dot-based technologies in CRC diagnostics and therapy, emphasizing their potential as nanotheranostic platforms. We also address the key barriers to clinical translation and propose future research directions to improve quantum dots' safety, efficiency, and clinical utility in CRC management.

***Conclusion:*** Ultimately, quantum dots offer significant potential to revolutionize the diagnosis and treatment of colorectal cancer, paving the way for more personalized and effective patient care.

***Keywords:*** *Colorectal neoplasms, Quantum dots, Nanoparticles, Nanotheranostics, Targeted therapy, Early detection*

**How to cite this article**
*Singh D, Kamal R. Quantum dot-based sensors and nanotheranostics for early detection and targeted therapy for colorectal cancer. Nanomed J. 2026; 13(2): 257-268. DOI: 10.22038/NMJ.2025.86235.2168*

## INTRODUCTION

Colorectal cancer (CRC) remains one of the leading causes of cancer-related morbidity and mortality worldwide, placing an increasing burden on healthcare systems due to its high incidence and late-stage diagnosis [1]. Early detection of CRC is crucial for improving survival rates, as prognosis is heavily dependent on the stage at which the cancer is diagnosed [1, 2]. Unfortunately, current diagnostic methods, such as colonoscopy, computed tomography (CT) colonography, and fecal occult blood tests (FOBT), have significant limitations, including invasiveness, discomfort, and limited sensitivity, particularly in early-stage cancer or small lesions [2]. These shortcomings underscore the urgent need for novel, more effective diagnostic approaches that offer non-invasive, highly sensitive, and accurate detection of CRC at its earliest stages [2, 3].

Nanotechnology, particularly quantum dots (QDs), has emerged as a promising solution to address colorectal cancer (CRC) diagnostic challenges. Quantum dots are semiconductor nanocrystals with unique optical properties,

* *Corresponding authors:* Dilpreet Singh; Ph.D, Associate Professor, School of Pharmaceutical Sciences, CT University, Ferozepur Rd, Sidhwan Khurd, Punjab 142024, India. E-Mail address: *dilpreet.daman@gmail.com.*
Note. This manuscript was submitted on February 20, 2025; approved on March 10, 2025.

including size-tunable fluorescence, high quantum yield, and narrow emission spectra [4]. These properties make QDs highly suitable for biomedical applications, especially in molecular imaging, where their fluorescence enables the detection of cancer biomarkers with high sensitivity and specificity [5]. Unlike traditional dyes, QDs can generate multiplexed signals, allowing for the simultaneous detection of multiple biomarkers, which is essential for enhancing the accuracy of cancer diagnostics [6].

In addition to their diagnostic role, quantum dots (QDs) are increasingly being explored for their potential in targeted therapy, particularly colorectal cancer (CRC). Due to their small size and the ability to be functionalized with targeting ligands, such as antibodies or peptides, QDs can selectively deliver therapeutic agents to tumor sites, minimizing the side effects associated with conventional therapies [7]. Furthermore, QDs facilitate real-time monitoring of therapeutic progress through their optical properties, offering a non-invasive method to track treatment efficacy. The concept of "nanotheranostics," which integrates diagnostic and therapeutic functions into a single platform, holds significant promise for revolutionizing CRC treatment, enabling more personalized and effective patient care [7, 8]. Despite the exciting potential of QDs in CRC detection and therapy, several challenges remain. Issues such as toxicity, biocompatibility, long-term stability, and efficient targeting must be addressed before widespread clinical implementation can be realized [9]. Additionally, the regulatory and ethical considerations surrounding the use of nanoparticles in humans remain a critical concern, requiring careful attention.

This review aims to comprehensively explore the role of quantum dots in the early detection and targeted therapy of colorectal cancer (CRC). We will examine the fundamental properties of quantum dots, their applications in CRC diagnostics, and their potential in targeted treatment strategies [10]. Additionally, we will discuss the current challenges and future perspectives for the clinical translation of QD-based technologies in CRC management [10]. Through this discussion, we aim to highlight the transformative potential of quantum dots in colorectal cancer care, paving the way for more accurate, efficient, and personalized approaches to CRC diagnosis and treatment.

### *Fundamentals of quantum dots*

Quantum dots (QDs) are nanoscale semiconductor materials that exhibit unique optical and electronic properties, including size-dependent fluorescence, high quantum yield, and tunability across the electromagnetic spectrum by adjusting their size and composition [11]. These properties result from quantum confinement effects, where the motion of charge carriers is restricted in all three spatial dimensions, creating discrete energy levels. Quantum dot-based imaging offers several advantages over traditional diagnostic methods [11, 12], such as enhanced sensitivity and real-time monitoring, while addressing some of the limitations of colonoscopy and CT colonography, including invasiveness and radiation exposure (Table 1). A detailed depiction of the core-shell structure of quantum dots, including surface functionalization with targeting ligands (e.g., antibodies, peptides) for specific cancer cell recognition and drug delivery, is shown in Figure 1.

Quantum dots (QDs) are typically composed of elements from groups II-VI (e.g., CdSe, CdTe), III-V (e.g., InP), and IV-VI (e.g., PbS) of the periodic table. Their surface properties are engineered to enhance stability and prevent aggregation [13]. Various quantum dot materials, such as CdSe, CdTe, InP, and PbS, exhibit distinct optical properties and varying levels of toxicity, with carbon-based QDs emerging as a promising alternative due to their biocompatibility and tunable fluorescence for colorectal cancer (CRC) applications (Table 2).

Table 1. Comparison of Quantum Dots and Traditional Diagnostic Methods in Colorectal Cancer Detection

| Diagnostic Method | Sensitivity | Specificity | Invasiveness | REF |
|---|---|---|---|---|
| Quantum Dot-Based Imaging | 90-95% | 85-90% | Non-invasive | [16] |
| Colonoscopy | 85-90% | 95% | Invasive (requires sedation) | [17] |
| CT Colonography (Virtual Colonoscopy) | 80-90% | 90-95% | Non-invasive (with radiation) | [17] |
| Fecal Occult Blood Test (FOBT) | 60-75% | 90-95% | Non-invasive | [18] |
| CT Scan (Abdominal) | 70-80% | 85-90% | Non-invasive (with radiation) | [19] |
| MRI (Magnetic Resonance Imaging) | 80-85% | 85-90% | Non-invasive | [19] |

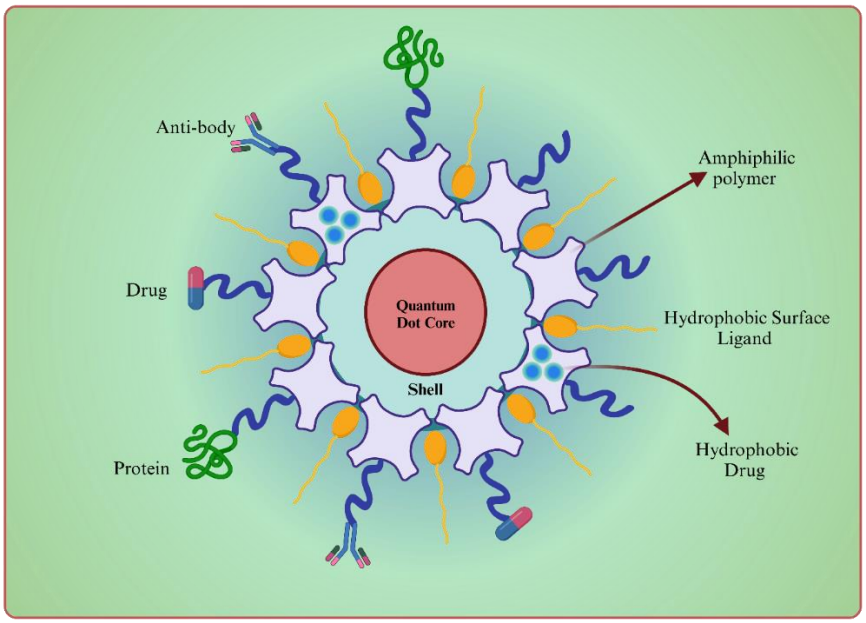


Fig. 1. Schematic Representation of Quantum Dot (QD) Structure and Functionalization

Table 2. Properties of Different Quantum Dot Materials for Colorectal Cancer Applications

| Quantum Dot Material | Composition | Optical Properties | Toxicity Concerns | Synthesis Method | Applications in CRC |
|---|---|---|---|---|---|
| CdSe | Cadmium selenide | Tunable fluorescence, high quantum yield | High toxicity (Cd2+) | Colloidal synthesis, chemical vapor deposition | Imaging, drug delivery |
| CdTe | Cadmium telluride | Strong fluorescence, high stability | High toxicity (Cd2+, Te2-) | Colloidal synthesis | Imaging, targeting CRC cells |
| InP | Indium phosphide | Narrow emission spectrum, low toxicity | Lower toxicity than Cd-based QDs | Colloidal synthesis | Imaging, potential theranostics |
| PbS | Lead sulfide | Infrared emission, stable in biological systems | Toxicity from lead (Pb) | Colloidal synthesis, laser ablation | In vivo imaging, drug delivery |
| Carbon-Based QDs | Carbon nanostructures | Broad emission spectrum, high biocompatibility | Non-toxic | Chemical vapor deposition, laser ablation | Imaging, sensing, drug delivery |

Functionalization of QDs is essential to improve their biocompatibility and enable targeting of specific cells or tissues. Surface coatings, such as polyethylene glycol (PEG), and conjugation with targeting ligands like antibodies, peptides, or aptamers make QDs ideal candidates for biomedical applications [14], particularly in molecular imaging and therapy. In vivo, QDs can be tracked using fluorescence microscopy, confocal microscopy, or other imaging modalities, providing high-resolution detection of disease markers, such as those associated with CRC [14, 15]. Quantum dots are primarily synthesized through colloidal synthesis and chemical vapor deposition (CVD). Colloidal synthesis involves the nucleation and growth of QDs in a solution containing precursor compounds, surfactants, and stabilizing agents, allowing for precise size control [14]. This method is widely used due to its scalability and tunable optical properties. Alternatively, CVD and molecular beam epitaxy (MBE) facilitate QD growth on substrates under controlled conditions, often employed in electronic and optoelectronic applications. Post-synthesis surface modification, such as ligand exchange or passivation, further enhances QD stability and functionality for biomedical and diagnostic applications [15]. A combination of optical properties, ease of functionalization, and tunability makes QDs a significant tool for cancer diagnosis and targeted therapy, especially in the early detection of CRC, where precise identification of tumor markers and tracking their progression are crucial for effective management.

### *Quantum dot-based sensors in early detection of colorectal cancer*

Quantum dot-based sensors have emerged as a promising tool for the early detection of colorectal cancer (CRC), utilizing the unique optical properties of quantum dots (QDs) to enhance sensitivity and

specificity in detecting cancer biomarkers [20]. The size-tunable fluorescence emission of QDs enables multiplexed imaging, where different QDs can be functionalized with antibodies or ligands specific to various CRC-related biomarkers [21], such as carcinoembryonic antigen (CEA), Kirsten rat sarcoma viral oncogene homolog (KRAS) mutations, or microsatellite instability. The detailed mechanism of quantum dots in the early detection of colon cancer is illustrated in Figure 2. Quantum dots can be functionalized with various targeting ligands, including anti-CEA antibodies, folate, and peptides like RGD, facilitating selective targeting of colorectal cancer biomarkers and enhancing their effectiveness in imaging and therapy (Table 3). These bio-functionalized QDs can selectively bind to their target biomarkers on cancer cells or body fluids, such as blood or stool, enabling early detection even in asymptomatic stages [21]. The bar chart illustrates the detection accuracy of different quantum dot (QD) types—CdSe, CdTe, InP, PbS, and carbon QDs—when targeting key colorectal cancer biomarkers, including CEA, epidermal growth factor receptor (EGFR), folate receptor, KRAS mutation, and mucin-1 (MUC1) [21, 22] (Figure 3).

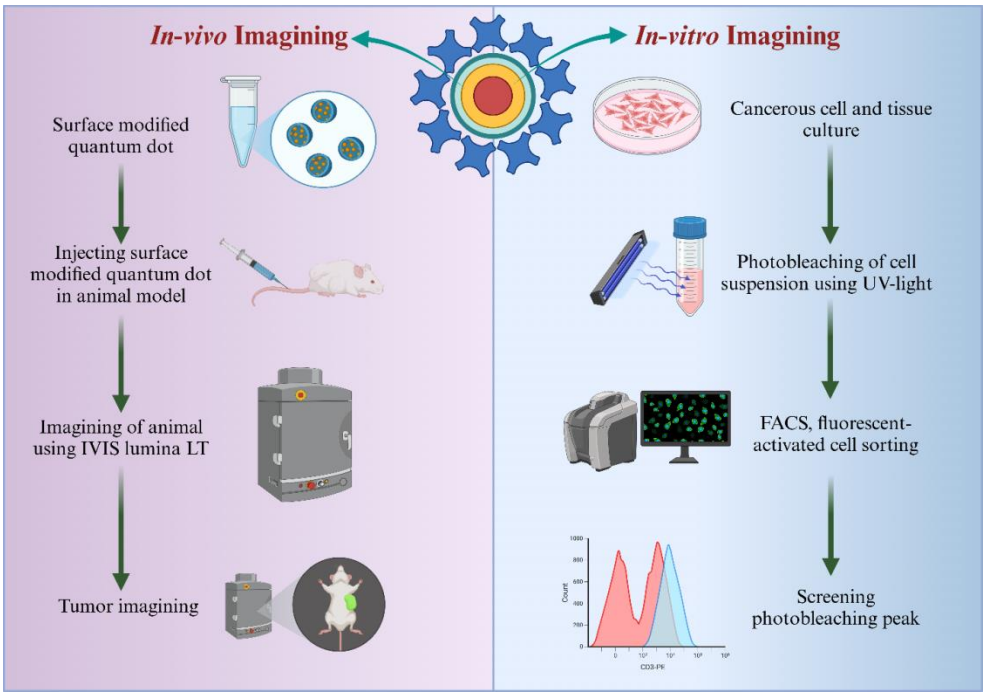


Fig. 2. Mechanism of quantum Dot-Based Imaging for Early Detection of Colorectal Cancer

Table 3. List of Targeting Ligands Used for Quantum Dot Functionalization in Colorectal Cancer

| Targeting Ligand | Type | Target Biomarker | Functionalization Method |
|---|---|---|---|
| Anti-CEA Antibody | Monoclonal antibody | Carcinoembryonic Antigen (CEA) | Conjugation via thiol groups |
| Folate | Small molecule (vitamin) | Folate receptor overexpressed in CRC cells | Covalent bonding via amine groups |
| Anti-EGFR Antibody | Monoclonal antibody | Epidermal Growth Factor Receptor (EGFR) | Bioconjugation using EDC/NHS |
| Peptide (RGD) | Peptide | Integrin αvβ3 (expressed in tumors) | Peptide conjugation to QDs |
| Anti-MUC1 Antibody | Monoclonal antibody | Mucin 1 (MUC1) | Conjugation via carboxyl groups |
| Aptamers | Nucleic acid-based ligand | CRC-related biomarkers (e.g., KRAS mutations) | Covalent linkage through thiol groups |

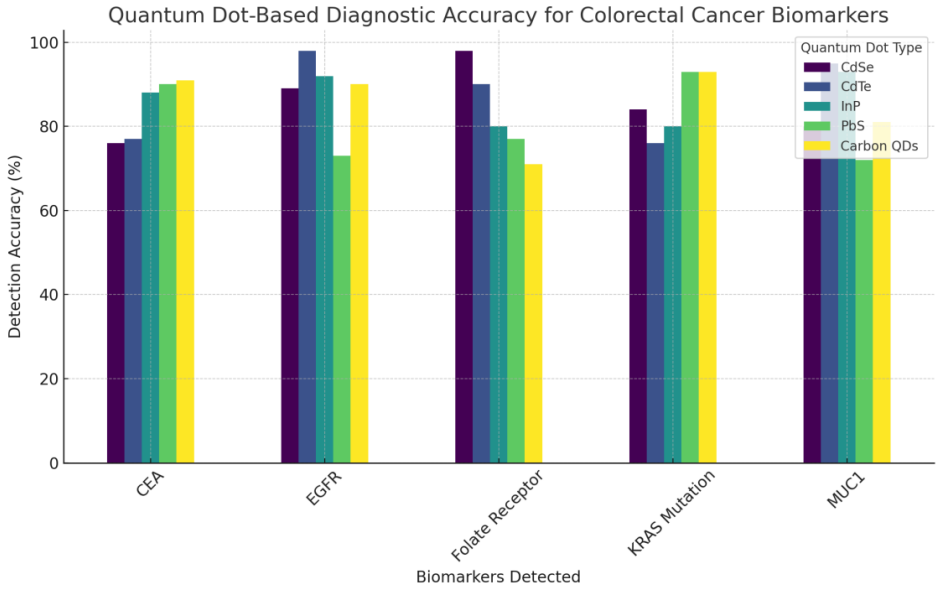


Fig. 3. Quantum Dot-Based Diagnostic Accuracy for Colorectal Cancer Biomarkers

The detection efficiency is represented as a percentage, highlighting variations in quantum dot (QD) performance across different biomarkers. Recent advancements in QD-based biosensors leverage surface plasmon resonance, fluorescence resonance energy transfer (FRET), and Förster resonance energy transfer (FRET) to achieve higher sensitivity in detecting minute quantities of biomarkers [22, 23]. Additionally, incorporating QDs into imaging modalities such as fluorescence tomography and magnetic resonance imaging (MRI) has enabled deeper tissue penetration, making them suitable for non-invasive in vivo detection of colorectal tumors [24]. QDs have also demonstrated the potential to enhance the accuracy of traditional diagnostic methods, such as colonoscopy and endoscopy, by providing real-time molecular imaging of lesions with sub-cellular resolution [24, 25]. Despite these advances, challenges remain in optimizing targeting efficiency and minimizing non-specific binding, affecting detection sensitivity. Furthermore, addressing the potential toxicity of quantum dots, particularly those containing heavy metals such as cadmium, continues to be an active area of research [26]. Nevertheless, integrating quantum dots into CRC detection represents a significant step toward more precise, early, and non-invasive diagnostic methods, offering a promising alternative to current screening techniques.

***Molecular targeting using quantum dots in colorectal cancer therapy***

Quantum dots (QDs) have emerged as highly effective tools for molecular targeting in colorectal cancer (CRC) therapy, leveraging their unique ability to conjugate with targeting moieties such as antibodies, peptides, or small molecules, which enhance their specificity for cancer cells [27]. These functionalized QDs can selectively deliver therapeutic agents directly to CRC cells, which minimizes off-target effects and improves the overall therapeutic index. QDs can serve as carriers for various therapeutic payloads, including chemotherapeutic drugs, small interfering RNA (siRNA) [28], or genetic material, enabling a targeted delivery approach that maximizes therapeutic efficacy while minimizing systemic toxicity [28, 29]. The surface modification of QDs with tumor-specific ligands, such as anti-CEA antibodies or folate [24, 25], facilitates their selective accumulation at the tumor site via receptor-mediated endocytosis, a critical step in molecular targeting [29].

In addition, the surface of quantum dots (QDs) can be further engineered to incorporate drugs released in response to environmental stimuli, such as pH or specific enzymes in the tumor microenvironment. This allows for the controlled release of therapeutic agents precisely where needed [30]. Moreover, QDs enable the tracking of therapeutic delivery and the monitoring of treatment progress in real-time using their fluorescence properties, providing clinicians with a non-invasive means to assess the treatment's effectiveness [30, 31]. The application of QDs in photodynamic therapy (PDT) has also been

evaluated, where QDs, upon exposure to specific light wavelengths, generate reactive oxygen species that induce localized tumor cell death [28]. However, challenges remain in optimizing the size, surface coating, and stability of QDs to ensure efficient drug delivery while minimizing potential toxicity [32]. Additionally, the long-term biocompatibility and clearance of QDs in vivo remain significant concerns that require further investigation [33]. Despite these challenges, the potential of QDs for targeted delivery and therapy in CRC is immense, offering the possibility of more effective and less toxic treatment strategies [34]. Table 4 lists clinical and preclinical studies showing quantum dot-based sensors, particularly those functionalized with CEA or folate, provide high sensitivity and specificity for early detection and imaging of colorectal cancer, often outperforming traditional diagnostic methods. A schematic illustrating the targeted drug delivery process using QDs—from functionalized QDs binding to CRC cell surface receptors to the release of therapeutic agents within cancerous cells—is shown in Figure 4.

Table 4. Clinical Applications and Preclinical Studies of Quantum Dot-Based Sensors in Colorectal Cancer Detection

| Study Type | Study Focus | Quantum Dot Material | Target Biomarker | Key Findings | Ref |
|---|---|---|---|---|---|
| Preclinical | Early detection of CRC in animal models | CdSe/ZnS QDs | Carcinoembryonic Antigen (CEA) | QDs successfully detected early-stage tumors in mice models, providing real-time tumor localization | [35] |
| Clinical Trial | Imaging of CRC biomarkers in patients | InP QDs | Folate receptor α, CEA | QDs demonstrated enhanced imaging compared to traditional methods like colonoscopy | [36] |
| Preclinical | Detection of CRC-related gene mutations | CdTe QDs | KRAS mutation biomarkers | QDs used for multiplexed detection of mutations, improving diagnostic precision in CRC | [37] |
| Preclinical | Fluorescence-guided CRC surgery | PbS QDs | MUC1 antigen, EGFR | Real-time fluorescence imaging assisted in the precise surgical removal of CRC tumors | [38] |
| Clinical Trial | Evaluation of QD-based endoscopic imaging | Carbon QDs | CRC-specific biomarkers | Carbon-based QDs offered a non-invasive, effective imaging tool for early CRC detection during colonoscopy | [39] |
| Preclinical | Tumor-targeted drug delivery in CRC | CdSe/ZnS QDs | CEA, EGFR | Quantum dots enabled targeted delivery of chemotherapeutics, reducing systemic toxicity and enhancing therapeutic efficacy | [40] |

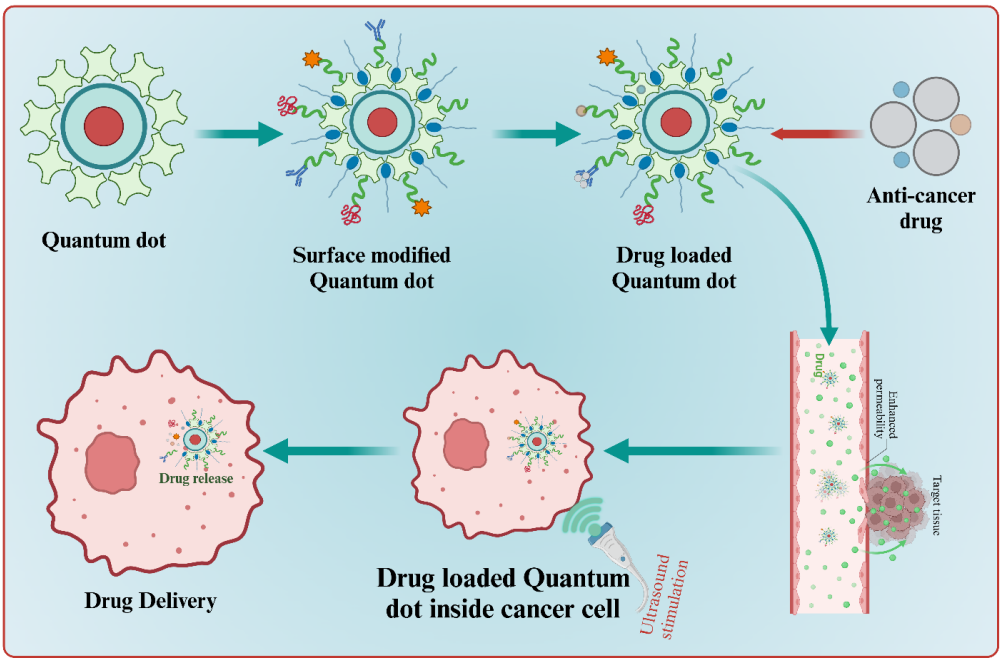


Fig. 4. Mechanism of Quantum Dot-Mediated Drug Delivery in Colorectal Cancer Therapy

***Quantum dots in nanotheranostics for colorectal cancer***

Nanotheranostics, which integrates diagnostic and therapeutic modalities into a single platform, represents a cutting-edge approach in colorectal cancer (CRC) treatment, with quantum dots (QDs) playing a central role in this emerging field [41]. QDs enable simultaneous tumor detection and therapy, leveraging their unique optical properties for real-time imaging while delivering therapeutic payloads directly to the cancer site [42, 43]. This dual functionality is particularly valuable in CRC, where early detection and localized treatment are crucial for improving patient outcomes [44]. QDs can be conjugated with targeting ligands, such as antibodies or peptides specific to CRC biomarkers (e.g., CEA or folate receptors), facilitating the selective targeting of malignant tissues [45].

Once bound to cancer cells, quantum dots (QDs) can be used in non-invasive imaging techniques such as fluorescence microscopy, positron emission tomography (PET), and fluorescence-guided surgery, providing detailed insights into the tumor's size, location, and molecular characteristics [46]. Simultaneously, QDs can be loaded with therapeutic agents—chemotherapeutic drugs, gene therapies, or RNA-based therapies—released in response to tumor-specific triggers, such as acidic pH or specific enzymes. This ensures the therapy is delivered precisely to the cancerous cells while sparing healthy tissue [47, 48]. Figure 5 illustrates the dual function of quantum dots in both the diagnosis (fluorescence imaging) and therapy (drug delivery and photodynamic therapy) of colorectal cancer (CRC) within a single system.

Additionally, the ability to modify quantum dots (QDs) with photosensitizers opens up the possibility for photodynamic therapy (PDT), where QDs, upon light activation, generate cytotoxic species that specifically target and kill cancer cells [48]. Figure 6 depicts a scatter plot comparing different quantum dot types based on their imaging sensitivity (%) and therapeutic effectiveness (%) in colorectal cancer applications as nanotheranostic agents [49, 50]. InP QDs demonstrate the highest therapeutic potential, while CdSe QDs excel in imaging. Figure 6 also highlights the trade-off between diagnostic efficiency and drug delivery capability among quantum dots [50]. The integration of QDs in nanotheranostics presents the advantage of personalized treatment, as the same nanocarrier can be tailored for both the detection and treatment of CRC based on the patient's specific tumor profile [50].

While early studies and clinical trials have shown promising results, challenges remain in optimizing the size, surface modification, and toxicity of quantum dots (QDs) to ensure their safe and effective use in clinical settings [51]. Additionally, the long-term clearance of QDs from the body, particularly those containing heavy metals like cadmium, requires further investigation. Nevertheless, the potential of QDs in nanotheranostics for colorectal cancer (CRC) holds immense promise, offering a powerful tool for accurate diagnosis and precision treatment, which could revolutionize the management of colorectal cancer in the future [51].

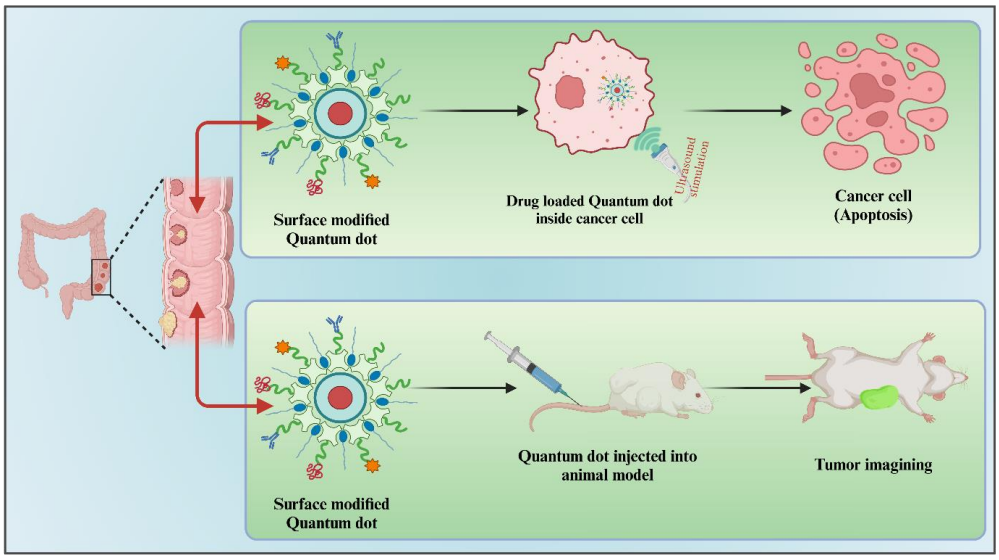


Fig. 5. Quantum Dot Conjugates in Nanotheranostic Applications for Colorectal Cancer

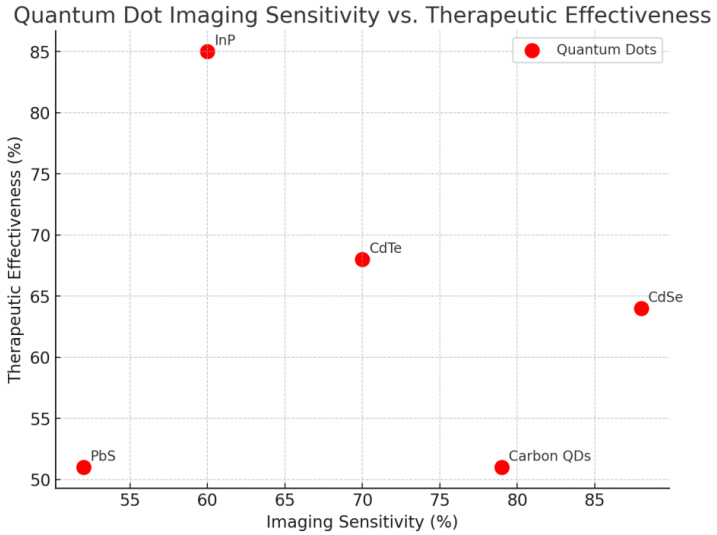


Fig. 6. scatter plot showing the relationship between Quantum Dot Imaging Sensitivity and Therapeutic Effectiveness

***Toxicity and biocompatibility of quantum dots in colorectal cancer applications***

The use of quantum dots (QDs) in colorectal cancer (CRC) applications raises critical concerns regarding their toxicity and biocompatibility, which should be thoroughly addressed to ensure their safe clinical use [52]. While QDs offer significant advantages in imaging and therapy, particularly for the early detection and targeted treatment of CRC, the potential for toxicity primarily arises from the heavy metals (such as cadmium, lead, and selenium) commonly used in their composition [52]. These metals can leach from the quantum dots, especially in the physiological environment, leading to cellular damage, oxidative stress, and inflammation [53], which can result in adverse effects on normal tissues and organs, such as liver or kidney damage, which are especially concerning in the context of systemic drug delivery [53].

Additionally, the small size and surface charge of quantum dots (QDs) enables them to accumulate in various organs, raising concerns about their long-term clearance from the body and the potential for chronic toxicity [54]. Significant efforts have been made to address these concerns and develop safer, more biocompatible QDs. Surface modifications with biocompatible polymers, such as polyethylene glycol (PEG) or inorganic materials like silica, have reduced toxicity by preventing QD aggregation, enhancing stability, and promoting renal clearance [55]. Moreover, QDs can be functionalized with ligands that enable selective targeting of colorectal cancer (CRC) cells, minimizing the exposure of healthy tissues to the potentially harmful effects of the QDs [56]. Researchers are also evaluating non-toxic alternatives, such as carbon-based or graphene quantum dots, which offer comparable optical properties without the associated risks of heavy metals. Furthermore, studies on the biodistribution and metabolic pathways of QDs in animal models have been essential for understanding their potential long-term effects [57]. While advances in QD design and functionalization have mitigated some of these concerns, further research is needed to ensure their safe use in clinical settings [58]. Regulatory bodies and ethical considerations also play a key role in establishing safety guidelines and standards for using QDs in biomedical applications. Ensuring the safe integration of quantum dots into CRC therapies and diagnostics will be essential for realizing their full potential in clinical practice.

***Recent advances and future perspectives***

Recent advances in quantum dot (QD) technology have significantly expanded their potential applications in colorectal cancer (CRC) detection and therapy, offering promising solutions to current clinical challenges [58]. The synthesis of QDs with improved biocompatibility and lower toxicity profiles is one of the most notable developments. Innovations in surface coating techniques, such as silica or lipid-based shells, have mitigated the harmful effects of traditional heavy-metal-containing QDs, enabling their safe use in vivo [59]. Furthermore, advancements in QD conjugation techniques have allowed for the incorporation of multiple functional groups on a

single particle, facilitating the simultaneous targeting of various CRC biomarkers and enhancing detection sensitivity and therapeutic efficacy [60]. Additionally, integrating QDs with other nanomaterials, such as gold nanoparticles or magnetic nanoparticles, has led to the creation of multifunctional nanocomposites that combine imaging, targeted therapy, and even gene editing into a single platform, providing a more holistic approach to CRC treatment [61].

The advent of quantum dot-based nanotheranostics represents another significant area of progress, where quantum dots (QDs) can simultaneously function in diagnostic imaging and as delivery vehicles for chemotherapeutic agents, RNA-based therapies, or photodynamic therapy [62]. These multifunctional systems offer unprecedented precision in targeting and treating colorectal cancer (CRC) while enabling real-time monitoring of therapeutic responses. Looking ahead, the future of QDs in CRC applications is likely to be driven by the incorporation of artificial intelligence (AI) and machine learning (ML) technologies, which could facilitate the development of more intelligent, adaptive systems capable of optimizing drug delivery and diagnosis based on real-time data [62]. Moreover, as personalized medicine advances, QDs may play a pivotal role in tailoring treatments to individual CRC patients by identifying unique molecular signatures and guiding the development of personalized therapeutic strategies [63].

Despite these exciting advancements, challenges such as improving the long-term stability, in vivo clearance, and standardization of quantum dot (QD)-based systems must be addressed before widespread clinical adoption [64]. In summary, the future of quantum dots in colorectal cancer (CRC) detection and treatment is promising, with ongoing innovations pushing the boundaries of precision medicine. Their integration into clinical practice could revolutionize diagnosing and treating CRC [65]. Figure 7 presents a stacked chart summarizing the cumulative contributions of quantum dots across various performance categories, highlighting their overall potential for CRC applications.

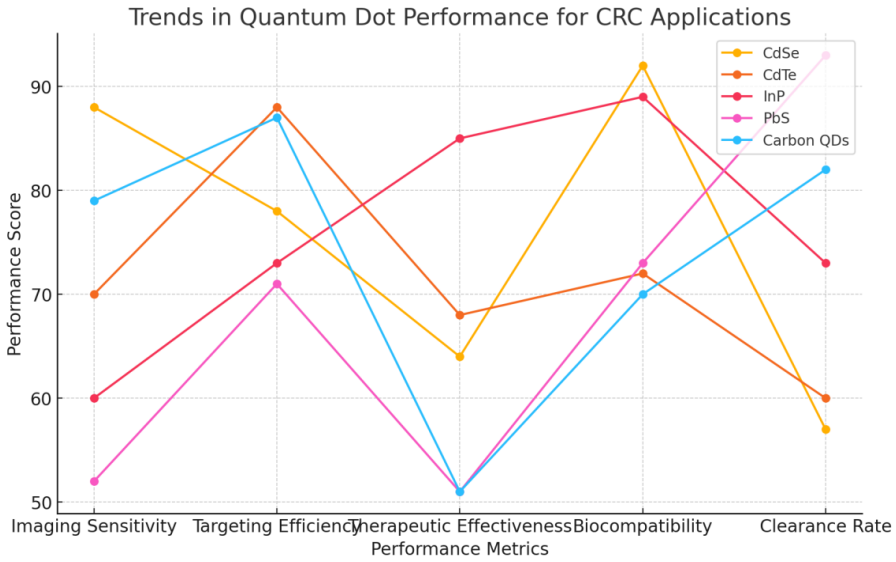


Fig. 7. Trends in quantum dots in CRC theranostics, as summarized in performance metrics

## CONCLUSION

Quantum dots represent a transformative approach to colorectal cancer (CRC) diagnosis and treatment, integrating imaging and therapeutic functions within a single nanoplatform. Although challenges remain regarding toxicity and targeting efficiency, quantum dot (QD) synthesis and functionalization advances provide promising solutions. As research progresses, quantum dots may become essential tools in the early detection and precise treatment of CRC, ultimately leading to improved patient outcomes and enhanced personalized care.

## ACKNOWLEDGEMENTS

Na

## CONFLICT OF INTEREST

The authors declare that there are no conflict of interest

**FUNDING**

NA

**REFERENCES**

1. Cañellas-Socias A, Sancho E, Batlle E. Mechanisms of metastatic colorectal cancer. Nat Rev Gastroenterol. Hepatol. 2024;21(9):609-625.
2. Li Q, Geng S, Luo H, Wang W, Mo YQ, Luo Q, Wang L, Song GB, Sheng JP, Xu B. Signaling pathways involved in colorectal cancer: Pathogenesis and targeted therapy. Signal Transduct Target Ther. 2024;9(1):266.
3. Ashique S, Bhowmick M, Pal R, Khatoon H, Kumar P, Sharma H, Garg A, Kumar S, Das U. Multi-drug resistance in colorectal cancer—approaches to overcome, advancements, and future success. Adv Cancer Biol Metastasis. 2024;10:100114.
4. Rengers C, Gaponik N, Eychmüller A. Quantum Dots and Quantum Rods. In Book: Biological Responses to Nanoscale Particles (Springer Cham Pvt Ltd, Neitherlands) 2019: 29-51
5. Guandalini A, Rozzi C, Rasanen E, Pittalis S. Fundamental gaps of quantum dots on the cheap. Phys Rev B. 2019;99:125140.
6. Langbein W. Quantum dots: all spins under control. Nat Mater. 2006;5:519-520.
7. Li C, Yan Z, Chen L, Jin J, Li D. Desmin detection by facile prepared carbon quantum dots for early screening of colorectal cancer. Medicine (Baltimore). 2017;96.
8. Gazouli M, Lyberopoulou A, Pericleous P, Rizos S, Aravantinos G, Nikiteas N, Anagnou N, Efstathopoulos E. Development of a quantum-dot-labelled magnetic immunoassay method for circulating colorectal cancer cell detection. World J Gastroenterol. 2012;18(32):4419-4426.
9. Carbary-Ganz JL, Barton J, Utzinger U. Quantum dots targeted to vascular endothelial growth factor receptor 2 as a contrast agent for the detection of colorectal cancer. J Biomed Opt. 2014;19:086003.
10. Bostick R, Kong K, Ahearn T, Chaudry Q, Cohen V, Wang MD. Detecting and quantifying biomarkers of risk for colorectal cancer using quantum dots and novel image analysis algorithms. Conf Proc IEEE Eng Med Biol Soc. 2006;3313-3316.
11. Chaudry Q, Kong K, Ahearn T, Cohen V, Bostick R, Wang MD. An integrated image quantification system for colorectal cancer risk assessment using quantum dots and molecular profiling. Proc IEEE Int Symp Biomed Imaging. 2007;1280-1283.
12. Zhang H, Fu X, Hu J, Zhu Z. Microfluidic bead-based multienzyme-nanoparticle amplification for detection of circulating tumor cells in the blood using quantum dots labels. Anal Chim Acta. 2013;779:64-71.
13. Wang Y, Li Y, Chen Z, Wang T, Gu J, Wu X, Yin Y, Wang M, Pan Z. The evaluation of colorectal cancer risk in serum by anti-DESMIN-conjugated CdTe/CdS quantum dots. Clin Lab. 2017;63(3):579-586.
14. Wang S, Li W, Yuan D, Song J, Fang J. Quantitative detection of the tumor-associated antigen large external antigen in colorectal cancer tissues and cells using quantum dot probe. Int J Nanomedicine. 2016;11:235-247.
15. Rohith V, Namboori PK. Design and development of an 'early prediction machine' for colorectal cancer from pathological images through quantum image processing technique – a theranostic approach. Proc Int Conf Adv Sci Innov Sci Eng Technol. ICASISET. 2021.
16. Yang C, Xu C, Wang X, Hu X. Quantum-dot-based biosensor for simultaneous detection of biomarker and therapeutic drug: first steps toward an assay for quantitative pharmacology. Analyst. 2012;137(5):1205-1209.
17. Li Z, Huang P, He R, Lin J, Yang S, Zhang X, Ren Q, Cui D. Aptamer-conjugated dendrimer-modified quantum dots for cancer cell targeting and imaging. Mater Lett. 2010;64:375-378.
18. Lian S, Zhang P, Gong P, Hu D, Shi B, Zeng C, Cai L. A universal quantum dots-aptamer probe for efficient cancer detection and targeted imaging. J Nanosci Nanotechnol. 2012;12(10):7703-7708.
19. Balakrishnan T, Ang WL, Mahmoudi E, Sambudi NS. Recent development of quantum dots@ metal-organic framework composites as potential chemical and biological luminescence nanosensors. Phys B Condens Matter. 2024;673:415485.
20. Li Z, Huang P, Lin J, He R, Liu B, Zhang X, Yang S, Xi P, Zhang X, Ren Q, Cui D. Arginine-glycine-aspartic acid-conjugated dendrimer-modified quantum dots for targeting and imaging melanoma. J Nanosci Nanotechnol. 2010;10(8):4859-4867.
21. Zhang Y, Zhang J. Confocal study of specific targeting of quantum dot nanocomposites to cancer cells. Key Eng Mater. 2005;288-289:155-158.
22. Yao C, Tu Y, Ding L, Li C, Wang J, Fang H, Huang Y, Zhang K, Lu Q, Wu M, Wang Y. Tumor cell-specific nuclear targeting of functionalized graphene quantum dots in vivo. Bioconjug Chem. 2017;28(10):2608-2619.
23. Wang X, Ding J, Li JY, Jiang H, Wang Z, Shi W. Applications of quantum dots in cancer research. Adv Mater Res. 2011;345:29-34.
24. Haikang H, Yan J, Liu P, Zhao B-Y, Cao Y, Zhang X. A novel cancer nanotheranostics system based on quantum dots encapsulated by a polymer-prodrug with controlled release behaviour. Aust J Chem. 2017;70:1302-1311.
25. Abdelhamid AS, Helmy M, Ebrahim S, Bahey-El-Din M, Zayed D, Zein El Dein EA, El-Gizawy S, Elzoghby AO. Layer-by-layer gelatin/chondroitin quantum dots-based nanotheranostics: combined rapamycin/celecoxib delivery and cancer imaging. Nanomedicine (Lond.) 2018; 13(14):1707-30.
26. Trantum JR, Jayagopal A. Imaging of cell populations in atherosclerosis using quantum dot nanocrystals. Methods Mol Biol. 2013;1026:35-44.
27. Parhi P, Sahoo S. Trastuzumab guided nanotheranostics: A lipid-based multifunctional

nanoformulation for targeted drug delivery and imaging in breast cancer therapy. J Colloid Interface Sci. 2015;451:198-211.
28. Panchal H, Panjwani D, Patel S, Ahlawat P, Patel LD, Dharamsi A, Patel A. Quantum dots functionalized polymeric nanoparticles as cancer theranostics: An advanced nanomedicine strategy. Curr Cancer Drug Targets. 2024: 1-13
29. Mohammadnejad P, Hosseini SM, Sohrabi B. The graphene quantum dots encased in the molecularly imprinted polymer as a new fluorescent nanosensor for the detection of biotin. Sens. Actuators Rep. 2024;7:100187.
30. Nguyen QK, Nguyen DT, Pham TM, Pham B, Nguyen TA, Pham TD, Sharma S, Pham DT, Gangavarapu RR, Pham TN. A highly sensitive fluorescence nanosensor for determination of amikacin antibiotics using composites of carbon quantum dots and gold nanoparticles. Spectrochim. Acta A Mol Biomol Spectrosc. 2024;305:123466.
31. Bao L, Luo W, Li Q, Zhang Y, Zhang Z, Li X, Wang L, Zhang J, Huang K, Yu X, Xu L. Chiral carbon dots based on ternary carbon sources: A multifunctional therapeutic agent for Cu2+-induced Alzheimer's disease. Carbon. 2024;228:119333.
32. Li J, Yang Y, Liu P. Hybrid micelles of carbon quantum dot-doxorubicin conjugates as nanotheranostics for tumor therapy and turn-on fluorescence imaging: Impact of conjugated structures and on-off-on mechanism. Mol Pharm. 2023.
33. Won SY, Singhmar R, Sahoo S, Kim H, Kim CM, Choi SM, Sood A, Han SS. Fabrication of albumin-Ti3C2 MXene quantum dots-based nanohybrids for breast cancer imaging and synergistic photo/chemotherapeutics. Colloids Surf B: Biointerfaces. 2025;245:114207.
34. Ree A, Bratland A, Dueland S. Molecular targeted therapy in colorectal cancer. Tidsskr Nor Laegeforen. 2008;128(2):190-193.
35. Borner M. Molecular targets in colon cancer. Ther Umsch. 2006;63(4):243-248.
36. Sablin M, Dreyer C, Colichi C, Bouattour M, Faivre S. Targeted therapies in colorectal cancer. Rev Prat. 2010;60(8):1094-1099.
37. Van Cutsem E, Dicato M, Arber N, Berlin J, Cervantes A, Ciardiello F, de Gramont A, et al. Molecular markers and biological targeted therapies in metastatic colorectal cancer: expert opinion and recommendations derived from the 11th ESMO/World Congress on Gastrointestinal Cancer, Barcelona, 2009. Ann Oncol. 2010;21 Suppl 6:vi1-10.
38. Patel MR, Park TJ, Kailasa SK. $Eu^{3+}$ ion-doped strontium vanadate perovskite quantum dots-based novel fluorescent nanosensor for selective detection of creatinine in biological samples. J Photochem Photobiol A Chem. 2024;449:115376.
39. Ebru N. Therapeutic targeting of molecular pathways in colorectal cancer. Exp Oncol. 2022;44(1):2-6.
40. El Hamd MA, El-Maghrabey M, Almawash S, Radwan AS, El-Shaheny R, Magdy G. Citrus/urea nitrogen-doped carbon quantum dots as nanosensors for vanillin determination in infant formula and food products via factorial experimental design fluorimetry and smartphone. Luminescence. 2024;39(2):e4643.
41. Bartos A, Bartos D, Szabo B, Breazu C, Opincariu I, Mironiuc A, Iancu C. Recent achievements in colorectal cancer diagnostic and therapy by the use of nanoparticles. Drug Metab Rev. 2016;48:27-46.
42. Wang N, Chen L, Huang W, Gao Z, Jin M. Current Advances of Nanomaterial-Based Oral Drug Delivery for Colorectal Cancer Treatment. Nanomaterials (Basel). 2024;14.
43. Kasi P, Mallela VR, Ambrożkiewicz F, Trailin A, Liska V, Hemminki K. Theranostics Nanomedicine Applications for Colorectal Cancer and Metastasis: Recent Advances. Int J Mol Sci. 2023;24.
44. Chauhan S, Sharma S. Recent Approaches on Molecular Markers, Treatment and Novel Drug Delivery System Used for the Management of Colorectal Cancer: A Comprehensive Review. Curr Pharm Biotechnol. 2024;25(15):1969-85.
45. Viswanath B, Kim S, Lee K. Recent insights into nanotechnology development for detection and treatment of colorectal cancer. Int J Nanomedicine. 2016;11:2491-2504.
46. Shrivastav J, Khansili N. Recent progress on multiplexed detection strategies of heavy metals with emphasis on Quantum dots. Trends Environ. Anal Chem. 2024;e00244.
47. Cabeza L, Perazzoli G, Mesas C, Jiménez-Luna C, Prados J, Rama A, Melguizo C. Nanoparticles in Colorectal Cancer Therapy: Latest In Vivo Assays, Clinical Trials, and Patents. AAPS Pharm Sci Tech. 2020;21.
48. Jain A, Bhattacharya S. Recent advances in nanomedicine preparative methods and their therapeutic potential for colorectal cancer: a critical review. Front Oncol. 2023;13:1211603.
49. Öztürk D, Durmuş M. N-Doped carbon quantum dot–based ratiometric fluorescent nanosensor platforms for detection of gastric cancer-associated Helicobacter pylori genes. Microchim Acta. 2025;192(3):147.
50. Yadav A, Kumar R, Jaiswal R, Singh AK, Kumar P, Singh K. Surface modification of CdS quantum dots: an effective approach for improving biocompatibility. Mater Res Express. 2019;6: 182-192
51. Jin G, Jiang L, Yi D, Sun H, Sun HC. The Influence of Surface Modification on the Photoluminescence of CdTe Quantum Dots: Realization of Bio-Imaging via Cost-Effective Polymer. Chem Phys Chem. 2015;16(17):3687-3694.
52. Liu X, Luo Y. Surface Modifications Technology of Quantum Dots Based Biosensors and Their Medical Applications. Chin J Anal Chem. 2014;42:1061-1069.

53. Lisichkin G, Olenin A. Synthesis of surface-modified quantum dots. Russ Chem Bull. 2020;69:1819-1828.
54. Wang J, Han S, Ke D, Wang R. Semiconductor quantum dots surface modification for potential cancer diagnostic and therapeutic applications. J Nanomater. 2012;2012:1-8.
55. Alaghmandfard A, Sedighi O, Tabatabaei Rezaei N, Abedini A, Malek Khachatourian A, Toprak M, Seifalian A. Recent advances in the modification of carbon-based quantum dots for biomedical applications. Mater Sci Eng C. 2021;120:111756.
56. Matsuno R, Goto Y, Konno T, Takai M, Ishihara K. Controllable nanostructured surface modification on quantum dot for biomedical application in aqueous medium. J Nanosci Nanotechnol. 2009;9(1):358-365.
57. Girma WM, Fahmi MZ, Permadi A, Abate M, Chang JY. Synthetic strategies and biomedical applications of I-III-VI ternary quantum dots. J Mater Chem. B. 2017;5(31):6193-6216.
58. Argudo PG, Carril M, Martín-Romero MT, Giner-Casares JJ, Carrillo-Carrión C. Surface-active fluorinated quantum dots for enhanced cellular uptake. Chemistry. 2018;25(1):195-199.
59. Dezfuli AA, Abu-Elghait M, Salem SS. Recent insights into nanotechnology in colorectal cancer. Appl Biochem Biotechnol. 2024;196(7):4457-4471.
60. Hajjafari A, Sadr S, Rahdar A, Bayat M, Lotfalizadeh N, Dianaty S, Rezaei A, Moghaddam SP, Hajjafari K, Simab PA, Kharaba Z. Exploring the integration of nanotechnology in the development and application of biosensors for enhanced detection and monitoring of colorectal cancer. Inorg Chem Commun. 2024;112409.
61. Mao X, Li X, Liu S, Dong H, Jia W, Xu W, Wu X, Zhang Y. Global research trends on nanotechnology and colorectal cancer: a two-decade analysis. Nanomedicine (Lond.) 2025; 1-2.
62. Astolfi M, Zonta G, Malagù C, Anania G, Rispoli G. MOX nanosensors to detect colorectal cancer relapses from patient's blood at three years follow-up, and gender correlation. Biosensors (Basel). 2025;15(1):56.
63. Yang G, Cao Y, Yang X, Cui T, Tan NZ, Lim YK, Fu Y, Cao X, Bhandari A, Enikeev M, Efetov S. Advancements in nanomedicine: Precision delivery strategies for male pelvic malignancies–Spotlight on prostate and colorectal cancer. Exp Mol Pathol. 2024;137:104904.
64. Lahouty M, Fadaee M, Shanehbandi D, Kazemi T. Exosome-driven nano-immunotherapy: Revolutionizing colorectal cancer treatment. Mol Biol Rep. 2025;52(1):1-8.
65. Dang Q, Zuo L, Hu X, Zhou Z, Chen S, Liu S, Ba Y, Zuo A, Xu H, Weng S, Zhang Y. Molecular subtypes of colorectal cancer in the era of precision oncotherapy: Current inspirations and future challenges. Cancer Med. 2024;13(14):e70041.

REVIEW PAPER

# The influence of cell penetrating peptides on efficiency of lipid nanoparticles containing chemotherapeutics

***Behrad Khoshbin[1], Zahra Khalili Azimi[2], Mahmoud Reza Jaafari[3], Bizhan Malaekeh-Nikouei[3*]***

*[1]Department of Pharmaceutical Nanotechnology, School of Pharmacy, Mashhad University of Medical Sciences, Mashhad, Iran*
*[2]Department of Chemical Engineering, School of Biotechnology, Malek Ashtar University, Tehran, Iran*
*[3]Nanotechnology Research Center, Pharmaceutical Technology Institute, Mashhad University of Medical Sciences, Mashhad, Iran*

**ABSTRACT**

Cell-penetrating peptides (CPPs) are a group of short peptides that easily pass through the cell membrane and are able to carry various types of cargoes, such as drugs, nucleic acids, and proteins, into cells. Therefore, CPPs are investigated with the aim of effective drug delivery to treat diseases such as cancer, diabetes and genetic disorders. CPPs have different applications in different fields.

CPPs have common functions and some structural features, such as a high content of positively charged amino acids, but their structural differences are in the high variety of elements in them. In this paper, the effect of cell penetrating peptides on the efficiency of lipid nanoparticles containing chemotherapeutics is reviewed. Various drug delivery systems such as liposomes, solid lipid nanoparticles and exosomes were considered. Both *in-vitro* and *in-vivo* delivery routes were discussed.

***Keywords:*** *Cell-penetrating peptides, Drug delivery, Lipid nanoparticles, Cancer*

**How to cite this article**

*Khoshbin B, Khalili Azimi Z, Jaafari MR, Malaekeh-Nikouei B. The influence of cell penetrating peptides on efficiency of lipid nanoparticles containing chemotherapeutics. Nanomed J. 2026; 13(2): 268-282. DOI: 10.22038/nmj.2025.87867.2230*

**Abbreviations**

***CPPs:*** Cell-penetrating peptides; ***PFV:*** Persistent fetal vasculature; ***siRNA:*** small interfering RNA; ***SLN:*** Solid Lipid Nanoparticles; ***TAT:*** transcribing protein; ***NLC:*** Nanostructured Lipid Carriers; ***HIV:*** Human immunodeficiency virus; ***MCAO:*** middle cerebral artery occlusion; ***PEG:*** polyethylene glycols; ***HA:*** hyaluronic acid; ***MCS:*** myocardium cells; ***BBB:*** blood-brain barrier.

## INTRODUCTION

Cell-penetrating peptides (CPP) are a group of peptides that have the ability to pass through the cell membrane and transfer molecules such as DNA, protein, siRNA (small interfering RNA) and plasmid (1). The ability of CPPs to pass through the molecules has described this group of peptides as a promising candidate for drug delivery. CPPs are hydrophobic short lengths of amino acids and are usually considered sequences containing 5 to 30 amino acids. CPPs also known as protein transduction domains (2). Various factors such as temperature, cell type, size of the carrier and peptide concentration have different effects on the entry of CPPs into the cell (3). Most of CPPs are cationic and contain 5 positive charges. Direct penetration and endocytosis are the two main mechanisms for the entry of CPP peptides into cells, and these two mechanisms differ in the way of energy usage (4). In the direct permeation model, CPPs pass through lipid bilayer independently of energy and without the involvement of receptors (5). While in the process of endocytosis, CPPs enter the endosome or lysosome along with their therapeutic molecules with energy consumption. In addition, CPPs are classified into three main categories: spherical, natural and synthetic (6). Also, based on structural features, CPPs are divided into two main categories, including arginine-rich and amphipathic CPPs (3).

**Corresponding author(s):* Bizhan Malaekeh-Nikouei, Professor, School of Pharmacy, Mashhad University of Medical Sciences, P.O. Box 91775-1365, Mashhad, Iran, Phone: 98 51 31801325, Fax: 98 51 38823251,. Email: *malaekehb@mums.ac.ir.*

Note. This manuscript was submitted on April 29, 2025; approved on July 20, 2025.

In 1988, Frankel and Pabo discovered that the transcribing protein (TAT) from the HIV (Human immunodeficiency virus) can penetrate the cell membrane (7). This discovery was an introduction to the identification and characterization of different CPP peptides (8). TAT peptide has the ability to carry molecules with different molecular weight, including siRNA, antisense oligonucleotides and therapeutic agents (9). Recent studies show that CPPs can be considered as an appropriate candidate for cancer treatment (6). For example, Lim *et al* (2013) introduced a new CPP peptide named BR2, which showed the ability to interact with tumor cell membrane gangliosides and had a cytotoxic effect on HeLa, HCT116, and B16-F10 cancer cells (10). One of the important applications of CPPs is their use as carriers for the transfer of anticancer drugs (11). Although chemotherapy is considered as a treatment method for most cancers, drug resistance is one of the main problems of this treatment method. One of the important mechanisms of drug resistance is the reduction of membrane permeability and drug metabolism (12). It has been established that adding anticancer drugs to CPPs reduces this drug resistance (13). In recent years, drug delivery using CPPs has been considered for many diseases, including cancer (14). Evidence shows that CPPs easily transport cytotoxic drugs into tumor cells and induce apoptosis (15). It was also shown that the use of CPPs in combination with silver nanoparticles has stronger effects in killing MCF-7 cancer cells by increasing the penetration of silver nanoparticles in cancer cells compared to silver nanoparticles alone (16).

CPPs can be classified into two main categories based on the interaction between drug and CPP, the first category requires chemical bonding with the drug and the second group includes the formation of stable, non-covalent complexes with the drug. In recent years, many studies have investigated CPPs conjugated to small molecules and macromolecules in order to treat cancer (17).

Today, cancer is one of the main causes of death in the world. The common method of cancer treatment, chemotherapy, in most patients has drug resistance and lack of specific action on tumors. Therefore, it is very important to develop new methods. CPPs with features such as small size, easy synthesis, high activity and specificity, and biodiversity have become the target of many researchers' studies (18). In recent years, anti-cancer cationic peptides and cell-permeable peptides have been used to treat cancer. In this research, a number of studies conducted in this field, especially in the field of anti-cancer peptides and permeable peptides, are given. The results of various studies indicate that antimicrobial peptides with anticancer properties act against cancer cells and tumors using membrane and non-membrane mechanisms (19). Also, cell permeable peptides conjugated with therapeutic agents are considered as an effective mechanism in cancer treatment by overcoming drug resistance. In addition, anticancer and cell-permeable peptides can be proposed as a successful method for cancer treatment due to factors such as low toxicity, mode of action, and the ability to penetrate the cell membrane. However, further studies are needed to understand the mechanism of action of these peptides with therapeutic potential (20, 21).

In a study, several cell-penetrating peptides were designed and made from the sequence related to RGD. These analogs were designed to interact with integrins to increase entry into the cell through these receptors, and due to their amphipathic and basic properties, they can facilitate endosomal escape (5). In another study conducted on four cell lines (A549, NCIH322, NCIH460, NIH3T3), cell penetrating peptides derived from RGD and its analogs were tested. These peptides including PL, PD1, PD2, PE1, PE2) were mounted on liposomes and each of them was tested on the cell groups mentioned above. A group of liposomes without peptides was considered as a control group; the result of penetration in cell lines was that the control group did not show any penetration into any of the cell lines. The cell penetration of PE1, PE2 was more than that of PD1, and the penetration of PD2 was much higher than that of PD1 (22).

In this study, we investigated the effect of cell penetrating peptides on the efficiency of lipid nanoparticles containing chemotherapeutics. In the present paper, the effect of cell penetrating peptides on the efficiency of lipid and polymeric nanoparticles will be reviewed. All data has been summarized in Table 1.

Table 1. Some studies have been conducted on the effect of cell penetrating peptides on efficiency of lipid nanoparticles in cancer treatment.

| Nanoparticles | CPP Type | Active Ingredient | Results | *in vitro / in vivo* | Ref. |
|---|---|---|---|---|---|
| Liposome | histidine amino acids | Paclitaxel | Better inhibition against tumor cell growth | *in vitro* and *in vivo* | (59) |
| Liposome | 17-amino acid peptide (BR2) | 2-aminoethyl dihydrogen phosphate (2-AEH$_2$P) | Better cytotoxicity in tumor lines | *in vivo* | (60) |
| Liposome | TAT and PCM | Coumarin-6 | Improvement of the myocardial targeting | *in vitro* and *in vivo* | (68) |
| Liposomes | H16 | alpha-galactosidase A (GLA) | Specific lysosomal delivery into the lysosome | | (69) |
| Liposomes | photolabile-caged cell-penetrating peptide and asparagine-glycine-arginine peptide | siRNA | Selective targeted delivery of siRNA | *in vivo* | (71) |
| Liposome | RLYMRYYSPTTRRYG | Gossypol | Better cytotoxic effects on the MCF-7 cells | *in vitro* | (74) |
| Liposome | C-terminal domain of the cationic antimicrobial peptide CAP18 | Actinomycin D | High cytotoxic activity against cancer cells | *in vivo* | (76) |
| Liposome | TAT and PEN | Paclitaxel and doxorubicin | Enhanced targeting efficiency and increased therapeutic efficacy | *in vitro* and *in vivo* | (79) |
| SLN | TAT | Paclitaxel and TOS-cisplatin | Synergistic effect in the suppression of cervical tumor cell growth and superior antitumor efficiency | *in vivo* | (87) |
| SLN | octaarginine | Paclitaxel | Enhanced cytotoxicity in A549 cells | *in vitro* | (107) |

***Characterization and classification of CPPs***

CPPs are usually cationic or amphipathic peptides with 5-30 amino acids and soluble in water, which can be extracted from natural sources or designed (23). Compared to traditional methods such as microinjection and electroporation, CPPs have the ability to enter living cells in a non-invasive manner and without destroying the integrity of the cell membrane, and therefore are safe and very efficient (24). Recent studies have shown that CPPs pass a wide range of active pharmaceutical molecules, nanoparticles, liposomes, micelles, nucleic acids, proteins and peptides with high efficiency through the cell membranes of plants, bacteria and mammals (25).

In 1988, CPP derived from TAT protein of HIV-1 virus with amino acid sequence RKKRRQRRR was discovered and introduced for the first time (26). Related studies showed that TAT effectively crosses the cell membrane of cultured mammalian cells and accumulates in the nucleus and followed by other CPPs of natural origin such as VP22 derived from herpes simplex virus (HSV) and antennapedia or penetratin derived from *Drosophila melanogaster* or of synthetic origin such as transportan, all of which were able to pass through the cell membrane either individually or attached to cargo molecules were identified (26). CPPs, even in concentrations less than micromolar, are able to bind to glycosaminoglycans on the cell surface and enter the cell through the endocytic pathway without destroying the membrane structure (27). Of course, the exact mechanism of the entry of CPPs from the membrane into the cell is still under discussion, however, during the last decade, much evidence has been presented for their entry through endocytic mechanisms, especially endocytosis by receptors and micropinocytosis (28). In Figure 1. The mechanism of CPP penetrating to cell membranes is shown.

Direct energy-independent permeation occurs at low temperatures and using endocytosis inhibitors. As shown in Figure 1, positively charged CPPs interact with negatively charged cell membranes, causing membrane instability. Researchers have proposed three proposed mechanisms for this phenomenon: pore formation, carpet-like model, and reverse micelle model. In these mechanisms, small, hydrophobic CPP cargoes can permeate via energy-dependent pathways, while large, hydrophilic cargoes preferentially act as direct permeation (Figure 1) (29). So far, the exact mechanism by which CPPs cross cell membranes has not been elucidated. CPPs can enter cells in different ways under different conditions. Studies by researchers indicate that at low concentrations, arginine-rich CPPs are predominantly endocytosed, while at higher concentrations, they rapidly enter the cytoplasm (29).

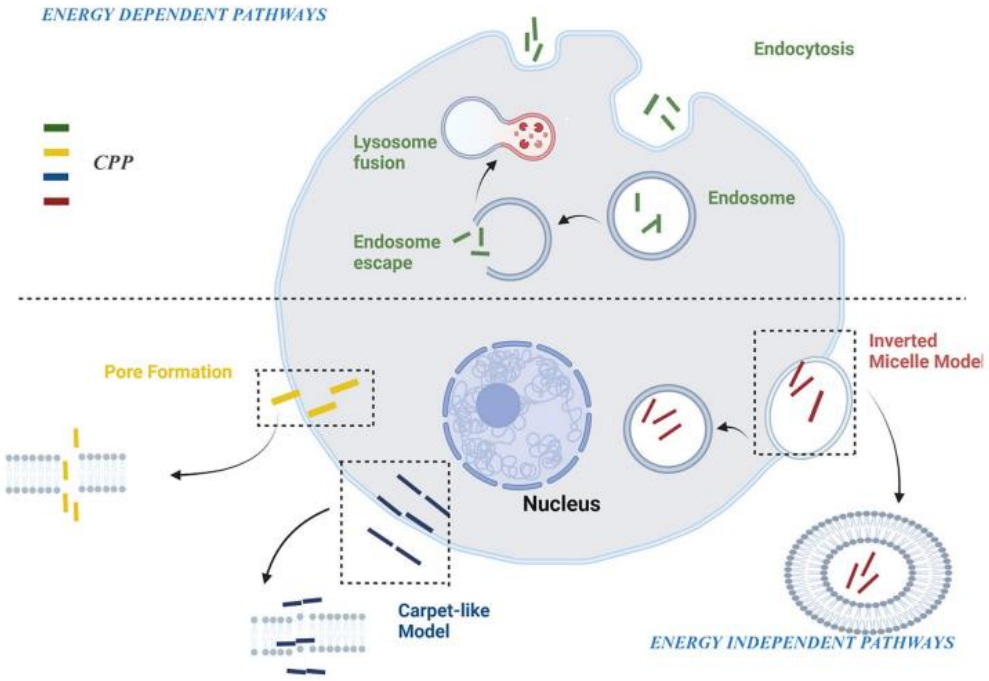


Fig. 1. Mechanism of CPP penetrating cell membranes (29).

***Classification of CPPs***

CPPs can be classified into different groups based on the physicochemical characteristics and based on the origin from the CPPs derived from proteins, natural peptides (28).

***Classification of CPPs based on physicochemical characteristics***

Based on the physicochemical characteristics of the overall net charge, CPPs can be classified into three hydrophobic, amphipathic and cationic groups (30). Anionic CPPs are not placed in a separate group and based on their characteristics they are placed in the group of amphipathic and hydrophobic CPPs. Cationic CPPs have a short amino acid sequence and are usually made of lysine, histidine and arginine amino acids and do not have any amphipathic helix in their three-dimensional structure (28). As mentioned above, the first discovered cationic CPP is the TAT peptide. Also, various studies on peptides based on the number of arginine amino acids from 3 to 12 have shown that the minimum sequence required for the cellular uptake of these peptides is octa-arginine (R8), so that the increase in the number of arginine increases the rate of cellular uptake. According to the studies, the presence of at least eight basic amino acids is necessary for efficient absorption of cationic CCPs (31). Although positively charged residues play an important role for the absorption of cationic CPPs, other residues are also important, for example, the W14F mutation in penetration with the amino acid sequence RQIKIWFQNRRMKWKK disrupts the absorption of this peptide into the cell (32).

Some cationic CPPs are Nuclear Localization Sequences (NLS) which are short peptides based on lysine-arginine or proline rich motifs. NLSs can enter the nucleus through the nuclear pore complex. NLSs are divided into two groups: monopartite signals (one cluster of four or more basic amino acids) and bipartite signals (two clusters of four or more basic amino acids) (33). For example, nucleoplasmin is a bipartite NLS with the amino acid sequence KRPAATKKAGQAKKKL, while the NLS derived from simian virus 40 (SV40) with the sequence PKKKRKV is a monopartite NLS (34). Among the NLSs, some peptides are not suitable for use as CPP, such as: NF-κB with the sequence TFIIE-beta VKQKLMP with the sequence SKKKKTKV and 6-Oct with the sequence GRKRKKRT because the number of charged amino acids in most NLSs is less than eight; However, they can be covalently attached to hydrophobic peptide sequences to produce hydrophobic CPPs with high cell absorption capability (35). Amphipathic CPPs are composed of both cationic and anionic peptide groups and four group of primary amphipathic peptides (primary amphipathic CPPS) and secondary amphipathic alpha-helix peptides (36).

β-Sheet amphipathic peptides are divided to β-Sheet amphipathic CPP and amphipathic peptides

amphipathic peptides rich in proline of amphipathic CPPs (37). Several types of primary amphipathic peptides are derived as chimeric peptides from the coupling of the covalent NLS to a hydrophobic domain, for example by fusing the NLS sequence of the SV40 virus (hydrophilic part PKKRKV) to the glycoprotein 1-HIV fusion sequence GALFGLGAAGSTMGA by the chimeric and amphipathic CPP WSQP linker (38).

Other primary amphipathic peptides are completely derived from natural proteins (39). Proteins are available from plants, animals and cells of microorganisms. Abundant economic proteins can be obtained from plant seeds. Natural proteins can be isolated by separation methods based on the physicochemical properties of the proteins. Worldwide, plant protein is of great importance because it contains essential amino acids to meet human physiological needs. However, many diverse plant proteins are used as pharmaceutical agents, which are produced using molecular tools of biotechnology. Examples such as pVEC, ARF, and BPrPp are derived from natural proteins. These peptides possess both hydrophilic and hydrophobic regions, enabling interaction with both aqueous environments and cell membranes (40).

In secondary amphipathic alpha-helix peptides, hydrophilic and hydrophobic amino acids are located on both sides of the helix, so that the hydrophilic side consists of anionic or polar cationic amino acids and interacts with the cell membrane; while the hydrophobic side is responsible for disruption and penetration across the membrane. Hydrophobic CPPs can be peptides based on natural amino acids and chemically modified peptides, which include pepducin peptides (41). Pepducins are produced by connecting palmitoyl or other fatty acids or steroid groups to the amine end of peptides. These types of peptides are able to pass through the plasma membrane and enter the cytosol part of a large number of transmembrane proteins such as GPRS (G) protein binding receptors and adrenergic receptors (24). Pepducins can be used to control various physiological processes, such as platelet-dependent homeostasis and thrombosis (42), tumor growth, invasion and angiogenesis, stabilization of the peptide in the alpha-helix conformation by covalent binding of adjacent two compounds with a hydrophobic chemical linker, and proteolytic stability (43). It should be noted that by being stapled, there is no guarantee that the peptide will become a CPP; however, most of the peptides have this ability. Not only the cationic stapled alpha-helix peptides, but also the uncharged and anionic types are converted into CPPs, and some impenetrable anionic peptides have the ability to enter the cell after replacing the charged amino acids. Negative effects are obtained by neutral and cationic types (44). Among these peptides, 8-AH and MTide (45), which are able to activate the tumor suppressor protein P53 by inhibiting Mdm2. Based on studies, prenylation of peptides by adding farnesyl (Cis) or geranylgeranyl (C20) gives them the ability to enter the cell in an ATP-independent and endocytic manner (46).

***Classification of CPPs based on origin***

CPPs can be classified into three groups based on their origin: CPPs derived from proteins, natural peptides, synthetically designed CPPs, and chimeric CPPs. CPPs derived from proteins, natural peptides with diverse motifs, are able to enter cells and are classified into several groups based on the protein from which they are derived (2). Cationic CPPs are endocytosed, for example, DPV3 and DPV3/10 from superoxide desmutase, DPV6 from platelet-derived growth factor, DPV7 from epidermal-like growth factors, DPV10 and DPV10/6 are derived from rhododend mucin (47). CPPs derived from proteins that bind to DNA, RNA contains highly cationic motifs so that they bind to nucleic acids after entering the nucleus. CPPs derived from DNA-binding proteins include human cJun and cFos, as well as GCN4 transcription factor in yeast (48). Homeoproteins are a special class of DNA-binding proteins that have a conserved homeodomain motif for DNA binding. In addition to human cJun and cFos, as well as GCN4 in yeast, this class includes penetratin and 1-PDX (49).

***Lipid-based delivery systems***

***Liposomes***

Liposomes can be used to deliver drugs, nutrients, and to prepare carriers such as lipid nanoparticles in mRNA vaccines and DNA vaccines (50). To prepare liposomes, the method of disrupting biological membranes using processes such as ultrasound is often used. If compatible with the lipid bilayer structure, fats such as egg phosphatidylethanolamine can also be used in the liposome structure. Sometimes surface ligands are also used for the construction and design of liposome to attach to unhealthy tissue (51).

Liposomes are one of the lipid-based drug delivery systems, the most common of which have a simple emulsion in which there is a simultaneous combination of oil and water. Despite the knowledge of basic emulsions for many years, with the introduction of synthetic surfactants such as polyethylene glycols (PEG), complex emulsions with

a high application scope in the field of drug delivery were developed (52). Incorporation of high-performance material processing methods for particle size distribution, such as sonication and homogenization, resulted in dispersed droplets with nanoscale sizes of 10-200 nm. As a result, micelles and nanoemulsions (particles with an oily core surrounded by a monolayer of surfactants) and subsequently species such as solid lipid nanoparticles (particles with a lipid core or solid wax and monolayer or surfactants) and nanostructures (lipid carriers) were created. The possibility of preparing particles with a core of a mixture of solid and liquid lipids with a size of less than 100 nm made it possible for the Brownian motion (intrinsic random vibration of the particles) to overcome the gravitational force that pushes oils and other heavy substances upwards. This results in a higher stability and longer shelf life of the prepared compositions and produces a characteristic transparency (particles smaller than visible light wavelengths), while suspensions of larger particles are opaque or milky (53).

In a study, liposomes treated with transferrin and TAT, which contained the drug doxorubicin, were tested on U87 cells, and the rate of crossing the blood-brain barrier was also evaluated in rats. This study showed the effective role of these peptides in crossing the blood-brain barrier and it also showed a significant inhibition of U87 cell line proliferation. This formulation was effective against glioma (54).

The use of CPPs in *in vivo* models is problematic due to their loss in non-target tissues and enzymatic degradation. This failure requires a strategy to camouflage these peptides and protect them before they reach the target tissue. For this purpose, heat-sensitive liposomes containing the NGR sequence were used. CPPs were hidden in the heat-sensitive liposomes and were made available in the target tissue by the application of heat and also the NGR sequence (55). Liposomes containing doxorubicin were used against HT-1080 fibrosarcoma cells and MCF-7 cell line which increased penetration into cell line compared to heat-sensitive liposomes containing NGR. This new formula was able to inhibit tumor growth in nude mice Xenograft HT-1080 tumors and did not damage other body tissues (56).

Cell-penetrating peptides were used to increase the penetration of lipopeptide vaccines. Lipopeptide vaccines were administered to Swiss mice by CPP-treated liposomes (57). Various CPPs were used, including Tat 47-57, an effective combination for stimulation of immune responses. The immunogenic potential of other types of CPPs was investigated after intranasal administration. Among them, Tat and KALA induced the highest antibody titer. Therefore, the use of cell-penetrating peptides in liposomes containing vaccines is a promising strategy for the development of liposome-based vaccines (57).

In one study, the TAT peptide was attached to the surface of the liposome by a UV-sensitive linker, and when exposed to UV light, breaking the link, the peptide TAT is exposed to cells and leads to increased cellular uptake and penetration (58). In another study, TH peptide was used. This peptide is sensitive to pH changes. Because of the neutral pH in blood and other healthy tissues, the ability of this peptide to penetrate into the cell is preserved, and consequently, due to the acidic pH of the target tissue, histidine amino acids are protonated and the surface charge of liposomes containing this peptide changes from negative to positive. Because of this, the amount of cellular absorption increases and when this formulation, along with paclitaxel, was used in an animal model, it inhibited tumor growth by 86.3% (59). In one study, BR2 peptide was used to modify the surface of the liposome, and the drug cantharidin was loaded inside the liposome to be used for the treatment of liver cancer. The results of cell uptake on MIHA cell line as a control group as well as HepG 2 cells, showed that liposomes modified with BR2 peptide containing cantharidin drug had better anti-cancer effects. *In vivo* studies show the accumulation of liposomes modified with BR2 at the tumor site and the reduction of tumor growth (60).

Liposomes are among the systems of interest to researchers for lipid delivery (61). In these drug delivery systems, phospholipids are placed in spherical fat layers like the cell membrane, and their hydrophilic heads face the aqueous environment and their fatty tails face each other. In the interior of these structures, water and water-soluble compounds are trapped, which have the potential to protect them from hostile digestive conditions and facilitate possible gastrointestinal absorption. Also, the bilayer hydrophobic fatty acid core hosts hydrophobic compounds and forms a small spherical package that can carry hydrophilic and hydrophobic compounds. The interactions between the liposome membrane and the cell membrane make this idea more attractive and increase cellular uptake through endosomal mechanisms (62). Liposomes have been a very attractive drug delivery technology since day one, but until the late 90s, there was no news of using this technology. From the late 1990s to today,

successful commercial products have been developed based on liposomal drug delivery technology. Examples of drugs are liposomal carriers of doxorubicin, amphotericin B, nystatin, and vincristine (63).

It was shown that the penetration of pH-sensitive liposomes containing doxorubicin modified by CPP into the cytosol was 1.6 times higher compared to pH-sensitive liposomes. But at pH below 7, no significant difference was observed between pH-sensitive liposomes modified with CPP and liposomes modified with CPP. In pharmacokinetic studies using Tc-99 and gamma counter, it was shown that pH-sensitive liposomes modified with CPP can circulate in the body as long as pegylated liposomes. In biodistribution studies, it was found that the highest accumulation rate of pH-sensitive liposomes modified with CPP was in the liver and to a lesser extent in the spleen, which was compared to pegylated liposomes. But in heart, brain, lung and kidney, they did not differ much (64).

In a study that was conducted in order to investigate the crossing of the blood-brain barrier and access to the central nervous system, three different types of CPP were used, and these peptides along with transferrin were placed on the surface of liposomes containing the active ingredient (65). This study, which was conducted on the End3 cell line, primary striatal cells and primary neurons, showed an increase in the transfer of modified liposomes. In an *in vitro* model in which the blood-brain barrier was simulated, it was observed that these modified liposomes have a greater ability to cross this barrier. Biodistribution studies showed that liposomes modified with KFGF peptide in intravenous injection had a greater ability to cross the blood-brain barrier and were more present in the brain of mice (66).

In another study, conventional liposome, liposome modified with TAT, liposome with Tat /PCM (Pericardial Mesothelium) and liposome with PCM were investigated in order to pass through the myocardium (67). The study conducted on myocardium cells (MCS) showed that liposomes modified by Tat and PCM have a great ability to drug transportation (68). In another study, a new CPP containing 16 histidine amino acids called H16 was used. Thus, when this CPP was placed on the desired liposomes, this peptide could increase the penetration of the liposome into the lysosome. This formulation can be used to target the intracellular lysosome and treat diseases related to lysosome dysfunction (69).

In another study, light-sensitive CPP was used in this way that ultraviolet light was previously used to release cell-penetrating peptides, but in this study, infrared radiation was used, because its power to penetrate tissues is greater and it does not cause the destruction of healthy tissues. In this study, NGR sequence was used along with CPP involved in the hydrophobic layer of liposome. The NGR sequence causes liposomes to actively bind to tumor cells. Then, with Non-ionizing radiation (NIR) radiation, the peptides in the liposome come into contact with the surface of the tumor cells, and in this way, the entry into the cell was increased (70). The proof of this claim is the entry of the active substance inside the liposome into the HT-1080 cell line and the silencing of the relevant gene and the reduction of tumor growth (71).

In an animal study, the researchers used liposomes modified with CPP containing doxorubicin with pH-sensitive pegylated groups on their surface in terms of pharmacokinetics, biocompatibility and pharmacodynamics. This comparison was made with conventional pegylated liposomes containing doxorubicin. It was found that pH-sensitive pegylated liposomes modified with cell-penetrating peptides had 1.9 times more selectivity and effectiveness than conventional pegylated liposomes. Also, histological studies showed that no necrosis and inflammation were observed in healthy tissues (72).

Artemisinin is a well-known drug in the treatment of malaria and its anti-tumor effects have been reported in in vitro studies. The disadvantage of artemisinin is its low solubility in water. In order to increase the solubility of artemisinin and its cytotoxic effect in the target tissue, this drug was loaded into nanocarriers. To increase the permeability of liposomes containing artemisinin, these liposomes were modified by HER6 CPPs. In this study, which was carried out both in vivo and ex vivo, it was shown that in different pH conditions, these liposomes have a slow release and in acidic pH conditions, liposomes modified with CPP have a higher rate of entering the cell than conventional liposomes, and as a result, they have more cytotoxic effects. It was also found that the residence time of CPP-modified liposomes in tumor tissue was longer than conventional liposomes, which increases efficiency and effectiveness (73).

In a study, two biological and physical factors were used together to increase the effectiveness of the drug doxorubicin. CPP was considered as the biological agent and the physical agent of the magnetic field was considered. The biological factor

increases the cell penetration and the physical factor increases the drug release by increasing the temperature. In the *in vitro* study, the cytotoxic property was effective on the MCF-7 cell line, and it has also been successful in the *in vivo* study, both in the stage of targeted drug delivery and antitumor effects on the MCF-7 xenograft mice (74).

A study was conducted in order to investigate the effectiveness of various CPPs in crossing the cell membrane and delivering the drug doxorubicin into the cell. In this study, liposomes containing transferrin and CPP were used to determine the efficiency of each of these CPPs. The passage barrier for these liposomes was considered the brain endothelial barrier, which was evaluated both *in vivo* and *in vitro*. In this evaluation, it was found that the release of doxorubicin using liposomes modified by transferrin and CPP was improved compared to single-ligand liposomes (75). Among the liposomes containing transferrin and CPP, the liposome containing penetratin was able to show the highest rate of passing through the endothelial barrier, approximately 15% of the *in vitro* model and only 4% of the *in vivo* model. Penetratin-containing liposomes as well as TAT-containing liposomes have excellent biocompatibility and did not show any hemolytic activity up to a concentration of 200 nanomolar. The three types of CPP studied include TAT, Penetratin, and mastoparan (24).

Also, liposomes modified by Persistent fetal vasculature (PFV) peptide were loaded with paclitaxel. It was shown that the presence of hydrophobic CPP can better interact with MCF-7 cell membrane. The better interaction of the surface of the nanoparticle with the surface of the cell membrane facilitates the entry of the nanoparticle into the cell. By increasing the entry of liposomes modified by PFV, more paclitaxel enters the cell, as a result, the effectiveness of the drug increases and its toxicity to other organs decreases. This study, which was carried out both *in vivo* and *in vitro*, tried to simulate the breast cancer model in mice and MCF-7 cell line was used (76).

Two CPP-type peptides named TAT and PEN were separately mounted on liposome. The kinetics of cellular uptake depend on the type of cell as well as the peptide. Intracellular accumulation of TAT-modified liposomes increases with time (77), but PEN-modified liposomes reach maximum intracellular accumulation in the first hour (78). TAT-modified liposomes containing doxorubicin could increase the absorption of the drug by 12 times by affecting the A431 cell line within two hours. Binding of CPP to the cell surface does not affect the rate of drug release inside the cell, and an additional approach is needed to release the drug inside the cell. In a study conducted on glioma tumor cells, a new peptide named CB5005 was loaded onto liposomes containing doxorubicin. The reason for choosing this peptide was due to its double effect, firstly, this peptide is a CPP. And secondly, it is a disruptor of NF-κB, since the level of NF-κB activity increases in cancer cells, this peptide inhibits the growth of cancer cells through disruption of NF-κB activity (79).

***Solid lipid nanoparticles***

Colloidal drug carrier have received a lot of attention from researchers in the fields of medicine and pharmacy in recent years. In addition to overcoming many problems due to the low solubility of hydrophobic drugs, the attention of many researchers was drawn to the transport of various drugs, especially lipophilic drugs, from these carriers (80). Lipid nanoparticles are very important as drug carriers. These nanoparticles have been successfully used to deliver lipophilic drugs and sometimes hydrophilic drugs (81). The use of two types of solid and liquid lipids during the preparation of these nanoparticles has created two different forms of these particles with the titles of solid lipid nanoparticles and nanostructured lipid carriers. Applications of Solid Lipid Nanoparticles (SLN) or Nanostructured Lipid Carriers (NLC) have been studied as carrier systems (82). SLNs contain pure solid fats, while NLCs are composed of a solid matrix in which nanoparticles are trapped in liquid fats. Many drugs with diverse applications have been placed in NLCs and SLNs successfully (83).

The initial studies in this field were conducted by three groups of researchers named Muller, Kasko and Westsen. SLN is a colloidal carrier characterized by the delivery of drugs with limited solubility. To prepare SLN, the oily phase of the w/o emulsion is replaced with a solid oil or a mixture of solid oils, i.e. a mixture of lipid matrix particles that are solid at room temperature and in the body (84). In the structure of SLN, 0.1 to 30% of solid fat is dispersed in the liquid phase and 0.5 to 5% of surfactant is formed (85). The average size of SLN particles ranges from 40 to 1000 nm. It has been reported in studies that the physicochemical properties and stability of drugs loaded in SLN depend on the properties of drugs and components used in it (86).

In a study to investigate the combined effect of paclitaxel and cisplatin in the treatment of ovarian cancer, these two drugs were loaded into solid lipid particles. In order to increase penetration into the

cell by the carrier system, the surface of SLN was modified by TAT peptide. Modified SLNs containing two combination drugs of cisplatin as prodrug and paclitaxel were evaluated in the treatment of mice infected with ovarian tumor by HeLa cells. The modified SLN system was able to increase intracellular accumulation by 80% within 4 hours after injection. This carrier system, together with two drugs, cisplatin and paclitaxel, was able to reduce the tumor growth rate by 72.2%. The combined treatment system is an effective method to treat ovarian cancer, it is also probably effective for the treatment of other cancers as well (87).

The size of SLN particles is a function of the proper selection of lipids, surfactants, compounds and their amounts, these parameters can affect the long-term stability during drug storage, load and release. Therefore, for each drug, a specific formulation for SLN is required (88). The use of SLN is limited due to problems such as drug loading limitation, irregular drug release, and drug excretion during storage in SLN preparation. In the late 1990s, NLCs were introduced due to their ability to load more drugs and their favorable stability compared to SLNs (89). Three methods have been proposed to produce NLCs:

In the first method, fats such as glycerides, which are composed of different fatty acids, are mixed together. The use of different lipids leads to a greater distance between the fatty acid chains of the crystallized glycerides and thus creates more space for the entry of guest molecules (90). A mixture of solid lipids and a small amount of liquid lipids increases the ability of the drug to enter the matrix, which is called the incomplete NLC model (91).

In the second method, to prepare different types of nanostructures, a large amount of oil is mixed with solid fat. Therefore, the solubility of oil molecules in solid fat increases and leads to phase separation and the formation of oily nanostructures inside the solid fat matrix (91). Research has shown that many drugs are more soluble in oils than in solid fats, which helps to dissolve them in the oil and prevent it from being excreted by the surrounding solid fats. This model is called multiple NLC and is very similar to w/o/w emulsions, as both oil in solid and fat in water are dispersed here (92). The addition of liquid lipids leads to the formation of colonies of small particles that contribute to the dynamics of the matrix.

In the third method, which is known as the amorphous type of SLN and in which solid particles are also used, by mixing certain fats (such as hydroxyoctacosanyl hydroxystearate and isopropyl myristate) crystals are created that are formed by cooling (93).

The solid fats that are used in the production of NLCs are: terpalmitin, glyceryl bihanate (Campritol), glyceryl distearate (Percyrol) and cetyl palmitate. In order to prepare the particle matrix, solid fats are mixed with liquid fats in the ratio of 70 to 30 or 1.99 to 0.1 (94). Due to the presence of oil in these matrices, the melting point of these compounds is lower than pure solid fats. Although the resulting mixture will be solid at room temperature and body temperature (95).

The solid content of NLC can increase up to 95%. Tri-palmetin is a triglyceride that is generally used as a solid fat in SLNs and NLCs to facilitate emulsification and the formation of solid nanoparticles. For its compatibility and stability, phospholipids that are naturally derived from it are used as the main emulsifiers in the preparation of injection emulsions (96). Gelucire is a multi-purpose fat additive consisting of mono, deuteryglycerides and mono, diesters of fatty acids of polyethylene glycol. Glucyric acid is a fat additive that is obtained by mixing polyethylene glycol fatty acid esters and glycerides (97). The existence of a special combination made with surfactants, surfactants and fatty phase for its production has been considered as an emulsifier, drug solubility enhancer and granule formation. Their entry into lipid nanostructures may be useful in increasing drug loading in hydrophilic components (98). Gelucire can be used as a surfactant, co-surfactant and lipid matrix in drug delivery systems. Vitamin E (tocopherol) has recently been suggested as a drug delivery agent (99).

***Exosomes***

Surface functionalization of exosomes (or exosome-like vesicles) with cell-penetrating peptides (CPPs) involves modifying the outer membrane of these vesicles to enhance their ability to deliver therapies into cells. Exosomes are small vesicles naturally released from cells, playing a crucial role in intercellular communication and transport of biomolecules. When exosomes are functionalized with CPPs, these peptides facilitate the uptake of the exosomes by target cells. CPPs are short sequences of amino acids that can penetrate cell membranes and promote the internalization of the attached exosomes, potentially delivering drugs, proteins, or genetic material more effectively. This process can improve the therapeutic efficacy of exosome-based treatments and is an area of significant interest in drug delivery and biomedical applications. By using CPPs,

researchers aim to enhance the targeting and delivery capabilities of exosomes, making them more effective carriers in various therapeutic contexts (100).

Extracellular vesicles (EVs), particularly exosomes, are gaining attention in biomedical applications due to their biocompatibility, suitable size, and low immunogenicity, which enhance their circulation time. Exosomes, formed from endosomal multivesicular bodies, range from 40 to 120 nm in size and can interact with their microenvironment after being released from cells. They serve as effective drug delivery systems capable of encapsulating proteins and genetic material, with advantages such as enhanced permeability and retention in vivo. Recent advancements include modifying exosome surfaces and creating hybrid nanovesicles to improve anticancer therapy and drug delivery (101).

The safe and effective delivery of drugs for ischemic stroke treatment is challenging. Exosomes are promising as an endogenous drug delivery system due to their low immunogenicity, stability, high delivery efficiency, and ability to cross the blood-brain barrier. However, their limited targeting capability restricts clinical use. This study demonstrates the conjugation of the c(RGDyK) peptide onto exosomes using a quick and bio-orthogonal chemistry approach. In a transient middle cerebral artery occlusion (MCAO) mouse model, the engineered c(RGDyK)-conjugated exosomes (cRGD-Exo) effectively targeted ischemic brain lesions after intravenous administration. Additionally, curcumin was loaded onto these exosomes, leading to significant suppression of inflammatory responses and cellular apoptosis in the affected areas. The findings indicate that cRGD-Exo can serve as targeted delivery vehicles for cerebral ischemia and highlight a strategy for the efficient production of functionalized exosomes (102).

Exosomes are cell-derived extracellular vesicles with significant potential for diagnostic and therapeutic applications. The surface characteristics of exosomes are crucial for their biological behavior; however, existing surface modification methods are often limited or complex. Wang et al. present a straightforward and rapid approach to modify exosome surfaces using polydopamine coating. This coating enables customizable functionalization through subsequent reactions, thereby facilitating new possibilities for the application of exosomes in various biomedical fields (103).

***In vivo delivery***

Cell-penetrating peptides (CPPs) are known for their ability to rapidly permeate cell membranes without causing cytotoxicity, with the HIV-1 TAT protein being a notable example that can enter cell nuclei. Modified TAT peptides, such as CG-TAT-GC, show improved penetration but lack specificity. As common lipid nanoparticles (NPs) often lack specific targeting capabilities, developing targeted NPs is crucial for effective molecular imaging and therapy. Targeting strategies include ligand-mediated active targeting and ultrasound or radiofrequency-mediated passive targeting. Specifically, the cluster of differentiation CD44, overexpressed in human hepatoma SMMC-7721 cells, serves as a potential target for liver cancer treatment since it binds hyaluronic acid (HA), a biocompatible and biodegradable polysaccharide. HA-enhanced delivery systems can improve drug targeting to tumor sites, minimize toxicity to normal cells, and boost therapeutic efficacy. Additionally, the presence of hyaluronidase in tumor microenvironments can expose CPPs in HA-coated NPs, enhancing their effectiveness as drug carriers for cancer chemotherapy (104).

Despite significant advancements in nanomedicine, challenges remain, including off-targeting, poor endosomal escape efficiency, and clearance by the liver and kidneys. Additionally, barriers like the blood-brain barrier (BBB), skin, and mucosal barriers hinder access to affected tissues and organs. Liposomes and lipid nanoparticles (LNPs) have emerged as effective and biocompatible delivery systems, with PEGylation enhancing their circulation times. While improvements in endosomal escape have facilitated pharmaceutical applications such as Doxil, Onpattro, and Comirnaty, the endosomal uptake pathway limits the full therapeutic potential of these formulations. To address these issues, researchers are exploring ways to bypass the endosomal pathway and enhance the targeting of lipid-based particles through functionalization with CPPs and cell-targeting peptides (CTPs). Various nanoparticle types, including liposomes, LNPs, polymeric nanoparticles, gold/metal nanoparticles, and silica quantum dots, are being modified to overcome physiological and cellular barriers for more effective drug delivery (105, 106).

Recent research has demonstrated the successful internalization of lipid nanoparticles (LNPs) through membrane fusion using coiled-coil-forming lipopeptides, CPE and CPK. In this study, LNPs encapsulating EGFP-mRNA were functionalized with either 1 mol % CPE3 or CPE4

and tested on HeLa cells pretreated with CPK. Consistent with previous findings regarding liposomes, the combination of CPK4 and CPE4 resulted in significantly enhanced cellular uptake compared to the CPK3/CPE3 pair. Additionally, the physicochemical analysis of LNP formulations revealed no major differences between those with CPE4 functionalization and those without, indicating that the lipopeptide modification effectively improved uptake without altering the LNP characteristics significantly. The schematic representation illustrates nonviral lipid nanoparticles (LNPs) that effectively deliver mRNA into cells when modified with fusogenic coiled-coil peptides. These peptides enhance the nanoparticles' ability to fuse with cell membranes, facilitating the release of mRNA into the cytoplasm for efficient intracellular delivery (Figure 2) (105).

***Future outlook and limitations***

Cell-penetrating peptides (CPPs) have shown significant promise in macromolecular drug delivery and cancer treatment, enhancing the efficacy of therapies like botulinum toxin and irinotecan while reducing gastrointestinal toxicity. Their ability to facilitate intracellular transport positions CPPs as valuable tools for delivering anticancer drugs, genes, and imaging agents. However, challenges such as lack of specificity for tumor cells, poor stability, and rapid elimination from the body hinder their effectiveness. Ongoing research focuses on modifying CPPs for targeted delivery, improving their pharmacological properties, and enhancing endosomal escape mechanisms. Despite advancements in tumor immunotherapy, the integration of CPPs with existing therapies presents a novel strategy to improve treatment outcomes, although overcoming their inherent limitations remains essential for future clinical applications (29).

CPPs offer several advantages in drug delivery, but they also face significant limitations, including low cell selectivity, penetrating efficacy, and in vivo stability. Many CPPs exhibit low selectivity due to their chemical properties, necessitating direct administration to target tumors to minimize adverse effects. Additionally, immunogenicity can restrict their clinical applications, emphasizing the need for thorough immunogenicity assessments for CPPs used as delivery carriers. Endosomal uptake and escape are critical for enhancing efficacy; strategies such as incorporating membrane-disrupting peptides and chemical modifications to stabilize CPPs against protease inactivation are being explored. Recent advancements in peptide chemistry aim to address these challenges and develop the next generation of CPPs (2).

**CONCLUSION**

The ability of CPPs to pass molecules has caused this group of peptides to be used as a promising candidate for drug delivery. Antimicrobial peptides with anticancer properties act against cancer cells and tumors through membrane and non-membrane mechanisms. Also, cell permeable peptides conjugated to therapeutic agents through overcoming drug resistance are considered as an effective mechanism in cancer treatment. In addition, anticancer and cell-permeable peptides can be suggested as a favorable candidate in cancer treatment due to factors such as low toxicity, mode of action, and the ability to penetrate the cell membrane. Evidence shows that CPPs can be used as a drug delivery method. The main problem of using these peptides is the lack of selectivity and specificity against cancer cells and tumors.

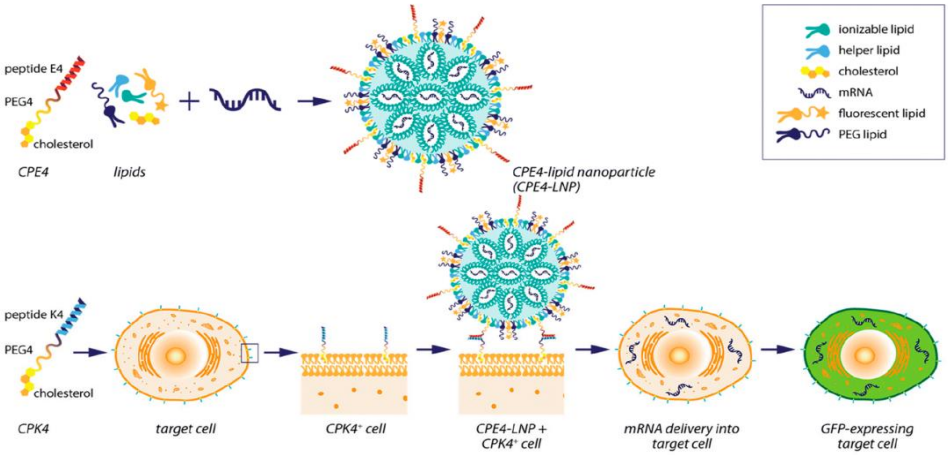


Fig. 2. Nonviral lipid nanoparticles (LNPs) that induce efficient mRNA delivery (105).

Therapeutic peptides are CPPs that are used in cancer treatment through covalent or non-covalent binding with small and macromolecules and entering cells. The use of lipid nanoparticles attached to CPPs has improved the performance of transferring substances into the membrane. Although CPPs have many advantages, limitations such as high cost and lack of specificity have been described for them. However, scientists have proposed various methods to overcome these problems. Therefore, the use of CPPs peptides along with lipid nanoparticles is suggested as a promising method in cancer treatment. However, more extensive studies are needed in order to use these therapeutic peptides in the clinical phase and to understand their mechanism.

## AUTHOR CONTRIBUTION

**Behrad Khoshbin**: Writing original draft; **Zahra Khalili Azimi**: Writing original draft; **Mahmoud Reza Jaafari**: Reviewing and editing; **Bizhan Malaekeh-Nikouei**: Reviewing and editing.

## FUNDING

This study was partially supported by Mashhad University of Medical Sciences, Mashhad, Iran (Grant number: 4000920).

## CONFLICTS OF INTERESTS

The authors declare no competing interests.

## ACKNOWLEDGEMENTS

None.

## REFERENCES

1. Ghosh A, Sharma M, Zhao Y. Cell-penetrating protein-recognizing polymeric nanoparticles through dynamic covalent chemistry and double imprinting. Nat Commun. 2024;15(1):3731.
2. Bottens RA, Yamada T. Cell-penetrating peptides (CPPs) as therapeutic and diagnostic agents for cancer. Cancers. 2022;14(22):5546.
3. Milletti F. Cell-penetrating peptides: classes, origin, and current landscape. Drug Discov. 012;17(15-16):850-860.
4. Lundberg P, Langel Ü. A brief introduction to cell-penetrating peptides. J Mol Recognit. 2003;16(5):227-233.
5. Copolovici DM, Langel K, Eriste E, Langel U. Cell-penetrating peptides: design, synthesis, and applications. ACS nano. 2014;8(3):1972-1994.
6. Langel Ü. Cell-penetrating peptides: Springer; 2011.
7. Frankel AD, Pabo CO. Cellular uptake of the tat protein from human immunodeficiency virus. Cell. 1988;55(6):1189-1193.
8. Gautam A, Sharma M, Vir P, Chaudhary K, Kapoor P, Kumar R, et al. Identification and characterization of novel protein-derived arginine-rich cell-penetrating peptides. Eur J Pharm Biopharm. 2015;89:93-106.
9. Torchilin VP. Tat peptide-mediated intracellular delivery of pharmaceutical nanocarriers. Adv Drug Deliv. 2008;60(4-5):548-558.
10. Lim KJ, Sung BH, Shin JR, Lee YW, Kim DJ, Yang KS, Kim SC. A cancer specific cell-penetrating peptide, BR2, for the efficient delivery of an scFv into cancer cells. PloS one. 2013;8(6):e66084.
11. Borrelli A, Tornesello AL, Tornesello ML, Buonaguro FM. Cell penetrating peptides as molecular carriers for anti-cancer agents. Molecules. 2018;23(2):295.
12. Duan Z, Chen C, Qin J, Liu Q, Wang Q, Xu X, Wang J. Cell-penetrating peptide conjugates to enhance the antitumor effect of paclitaxel on drug-resistant lung cancer. Drug Deliv. 2017;24(1):752-764.
13. Klimpel A, Luetzenburg T, Neundorf I. Recent advances of anti-cancer therapies including the use of cell-penetrating peptides. Curr Opin Pharmacol. 2019; 47:8-13.
14. Pescina S, Ostacolo C, Gomez-Monterrey I, Sala M, Bertamino A, Sonvico F, et al. Cell penetrating peptides in ocular drug delivery: State of the art. J Control Release. 2018;284:84-102.
15. Javadzadeh Y, Bahari LA. Chapter 8-Therapeutic nanostructures for dermal and transdermal drug delivery. Nano- and Microscale Drug Delivery Systems. Elsevier. 2017; 131-146.
16. Kovács D, Igaz N, Gopisetty MK, Kiricsi M. Cancer therapy by silver nanoparticles: fiction or reality? Int J Mol Sci. 2022; 23(2):839.
17. Gessner I, Neundorf I. Nanoparticles modified with cell-penetrating peptides: Conjugation mechanisms, physicochemical properties, and application in cancer diagnosis and therapy. Int J Mol Sci. 2020;21(7):2536.
18. Kroemer G, Chan TA, Eggermont AM, Galluzzi L. Immunosurveillance in clinical cancer management. CA Cancer J Clin. 2024;74(2):187-202.
19. Chen P, Ye T, Li C, Praveen P, Hu Z, Li W, Shang C. Embracing the era of antimicrobial peptides with marine organisms. Nat Prod Rep. 2024; 41(3):331-346.
20. Zhang L-j, Gallo RL. Antimicrobial peptides. Curr Biol. 2016; 26(1):R14-R19.
21. Lei J, Sun L, Huang S, Zhu C, Li P, He J, et al. The antimicrobial peptides and their potential clinical applications. Am J Transl Res. 2019;11(7):3919.
22. Patel SG, Sayers EJ, He L, Narayan R, Williams TL, Mills EM, et al. Cell-penetrating peptide sequence and modification dependent uptake and subcellular distribution of green florescent protein in different cell lines. Sci Rep. 2019;9(1):6298.
23. Heitz F, Morris MC, Divita G. Twenty years of cell-penetrating peptides: from molecular mechanisms to therapeutics. Br J Pharmacol. 2009;157(2):195-206.
24. Langel Ü. CPP, cell-penetrating peptides: Springer; 2019.
25. Nakase I, Akita H, Kogure K, Graslund A, Langel U, Harashima H, Futaki S. Efficient intracellular delivery of nucleic acid pharmaceuticals using cell-penetrating peptides. Acc Chem Res. 2012;45(7):1132-1139.

26. Rizzuti M, Nizzardo M, Zanetta C, Ramirez A, Corti S. Therapeutic applications of the cell-penetrating HIV-1 Tat peptide. Drug Discov Today. 2015;20(1):76-85.
27. Pae J, Liivamägi L, Lubenets D, Arukuusk P, Langel Ü, Pooga M. Glycosaminoglycans are required for translocation of amphipathic cell-penetrating peptides across membranes. Biochim Biophys Acta. 2016;1858(8):1860-1867.
28. Desale K, Kuche K, Jain S. Cell-penetrating peptides (CPPs): An overview of applications for improving the potential of nanotherapeutics. Biomater Sci. 2021;9(4):1153-1188.
29. Yang D, Liu B, Sha H. Advances and prospects of cell-penetrating peptides in tumor immunotherapy. Sci Rep. 2025;15(1):3392.
30. Madani F, Lindberg S, Langel Ü, Futaki S, Gräslund A. Mechanisms of cellular uptake of cell-penetrating peptides. Biophys J. 2011;2011.
31. Holm T, Johansson H, Lundberg P, Pooga M, Lindgren M, Langel Ü. Studying the uptake of cell-penetrating peptides. Nat Protoc. 2006;1(2):1001-1005.
32. Delgado EM. Chemical Approaches to Improve the Manufacturability of Disulfide-Rich Peptide Toxins: Engineering a Stable and Selective Peptide Blocker of the K Ca 1.1 Channel: University of Hawai'i at Manoa; 2022.
33. Li J, Li S, Du M, Song Z, Han H. Nuclear Delivery of Exogenous Gene in Mature Plants Using Nuclear Location Signal and Cell-Penetrating Peptide Nanocomplex. ACS Appl Nano Mater. 2022;6(1):160-170.
34. Ohshima K, Takeda S, Hirose M, Akiyama Y, Iguchi K, Hoshino M, et al. Structure-function relationship of the nuclear localization signal sequence of parathyroid hormone-related protein. Biomed Res. 2012;33(3):191-199.
35. Chen H-CG, Chiou S-T, Zheng J-Y, Yang S-H, Lai S-S, Kuo T-Y. The nuclear localization signal sequence of porcine circovirus type 2 ORF2 enhances intracellular delivery of plasmid DNA. Arch Virol. 2011;156:803-815.
36. Deshayes S, Morris MC, Divita G, Heitz F. Interactions of amphipathic CPPs with model membranes. BBA Biomembranes. 2006;1758(3):328-335.
37. Oba M. Chapter 5- Amphipathic peptide. Cell-penetrating peptides; Design, development and applications. Wiely. 2023:57-67.
38. Dariushnejad H, Karimitabar F, Hamidi M, Ahmadi NA. Cell-penetrating peptides (CPPs): A tool in modern biotechnology. J Paramed Sci. 2014; 5(3): 108-113.
39. Johansson HJ, El-Andaloussi S, Holm T, Mäe M, Jänes J, Maimets T, Langel Ü. Characterization of a novel cytotoxic cell-penetrating peptide derived from p14ARF protein. Mol Ther. 2008;16(1):115-123.
40. Nehete JY, Bhambar RS, Narkhede MR, Gawali SR. Natural proteins: Sources, isolation, characterization and applications. Phcog Rev. 2013;7(14):107.
41. Song J, Qian Z, Sahni A, Chen K, Pei D. Cyclic cell-penetrating peptides with single hydrophobic groups. Chembiochem. 2019;20(16):2085-2088.
42. Freedman JE. Molecular regulation of platelet-dependent thrombosis. Circulation. 2005;112(17):2725-2734.
43. Lai Z, Yuan X, Chen H, Zhu Y, Dong N, Shan A. Strategies employed in the design of antimicrobial peptides with enhanced proteolytic stability. Biotechnol Adv. 2022;59:107962.
44. Mello LR, Hamley IW, Castelletto V, Garcia BB, Lourenço TC, Vassiliades SV, et al. Self-assembly and intracellular delivery of DNA by a truncated fragment derived from the Trojan peptide Penetratin. Soft Matter. 2020;16(20):4746-4755.
45. Varnamkhasti BS, Jafari S, Taghavi F, Alaei L, Izadi Z, Lotfabadi A, et al. Cell-penetrating peptides: As a promising theranostics strategy to circumvent the blood-brain barrier for CNS diseases. Curr Drug Deliv. 2020;17(5):375-386.
46. Qian Y, Wang X, Liu Y, Li Y, Colvin RA, Tong L, et al. Extracellular ATP is internalized by macropinocytosis and induces intracellular ATP increase and drug resistance in cancer cells. Cancer Lett. 2014;351(2):242-251.
47. Tiwari MG. From inception of herbal medicine to an ideal perception of therapeutic agent: Rhododendron as a therapeutic agent–A review. IJMSCR. 2020;3(6):147-162.
48. Greene LA, Zhou Q, Siegelin MD, Angelastro JM. Targeting transcription factors ATF5, CEBPB and CEBPD with cell-penetrating peptides to treat brain and other cancers. Cells. 2023;12(4):581.
49. Zhang X, Liu E, Song Y, Yu P, Redkar S, Yu G-L. Dependence of EGFR-mutant NSCLC on MET as demonstrated by vebreltinib, a novel and selective brain-penetrating MET kinase inhibitor. Cancer Res. 2024;84(6_Supplement):6500.
50. Filipczak N, Pan J, Yalamarty SSK, Torchilin VP. Recent advancements in liposome technology. Adv. Drug Deliv Rev. 2020;156:4-22.
51. Nsairat H, Khater D, Sayed U, Odeh F, Al Bawab A, Alshaer W. Liposomes: Structure, composition, types, and clinical applications. Heliyon. 2022;8(5): e09394.
52. Bozzuto G, Molinari A. Liposomes as nanomedical devices. Int J Nanomedicine. 2015:975-999.
53. Allen TM, Cullis PR. Liposomal drug delivery systems: from concept to clinical applications. Adv. Drug Deliv Rev. 2013;65(1):36-48.
54. Mojarad-Jabali S, Mahdinloo S, Farshbaf M, Sarfraz M, Fatahi Y, Atyabi F, Valizadeh H. Transferrin receptor-mediated liposomal drug delivery: Recent trends in targeted therapy of cancer. Expert Opin Drug Deliv. 2022;19(6):685-705.
55. Sauer WH, Steiger NA, Tzou WS, Schuller JL, Zheng L, Nguyen DT. Facilitated myocardial ablation using heat-sensitive liposomes containing doxorubicin: A proof-of-concept preclinical study. JACC Clin Electrophysiol. 2023; 9(8 Pt 1):1404-1408.
56. Xu J, Khan AR, Fu M, Wang R, Ji J, Zhai G. Cell-penetrating peptide: a means of breaking through the physiological barriers of different tissues and organs. J Control Release. 2019;309:106-124.

57. Hamley IW. Lipopeptides for vaccine development. Bioconjug Chem. 2021;32(8):1472-1490.
58. de Jong H, Bonger KM, Löwik DW. Activatable cell-penetrating peptides: 15 years of research. RSC Chem Biol. 2020;1(4):192-203.
59. Zhang Q, Tang J, Fu L, Ran R, Liu Y, Yuan M, He Q. A pH-responsive α-helical cell penetrating peptide-mediated liposomal delivery system. Biomater. 2013;34(32):7980-7993.
60. de Sousa Cabral LG, Hesse H, Freire KA, de Oliveira CS, Pedron CN, Alves MG, et al. The BR2 peptide associated with 2-aminoethyl dihydrogen phosphate is a formulation with antiproliferative potential for a triple-negative breast cancer model. Biomed Pharmacother. 2022;153:113398.
61. Saraf S, Jain A, Tiwari A, Verma A, Panda PK, Jain SK. Advances in liposomal drug delivery to cancer: An overview. J Drug Deliv Sci Technol. 2020;56:101549.
62. Fan Y, Marioli M, Zhang K. Analytical characterization of liposomes and other lipid nanoparticles for drug delivery. J Pharm Biomed Anal. 2021;192:113642.
63. Nekkanti V, Kalepu S. Recent advances in liposomal drug delivery: a review. Pharm Nanotechnol. 2015;3(1):35-55.
64. Reveret L, Leclerc M, Morin F, Émond V, Calon F. Pharmacokinetics, biodistribution and toxicology of novel cell-penetrating peptides. Sci Rep.2023;13(1):11081.
65. Dymek M, Sikora E. Liposomes as biocompatible and smart delivery systems–the current state. Acta Odontol Scand. 2022;309:102757.
66. Yengopal V, Mickenautsch S. Caries preventive effect of casein phosphopeptide-amorphous calcium phosphate (CPP-ACP): a meta-analysis. Acta Odontologica Scandinavica. 2009;67(6):321-332.
67. Liu X, Zhang L, Jiang W, Yang Z, Gan Z, Yu C, et al. In vitro and in vivo evaluation of liposomes modified with polypeptides and red cell membrane as a novel drug delivery system for myocardium targeting. Drug Deliv. 2020;27(1):599-606.
68. Wang X, Huang H, Zhang L, Bai Y, Chen H. PCM and TAT co-modified liposome with improved myocardium delivery: in vitro and in vivo evaluations. Drug Deliv. 2017;24(1):339-345.
69. Hayashi T, Shinagawa M, Kawano T, Iwasaki T. Drug delivery using polyhistidine peptide-modified liposomes that target endogenous lysosome. Biochem Biophys Res Commun. 2018;501(3):648-653.
70. Mazhar A, El-Hansi N, Shafaa MW, Shalaby M. Radiation sterilization of liposomes: A literature review. Radiat Phys Chem. 2024:111592.
71. Yang Y, Yang Y, Xie X, Wang Z, Gong W, Zhang H, et al. Dual-modified liposomes with a two-photon-sensitive cell penetrating peptide and NGR ligand for siRNA targeting delivery. Biomater. 2015;48:84-96.
72. Cho HJ, Jung JI, Lim DY, Kwon GT, Her S, Park JH, Park JHY. Bone marrow-derived, alternatively activated macrophages enhance solid tumor growth and lung metastasis of mammary carcinoma cells in a Balb/C mouse orthotopic model. Breast Cancer Res. 2012;14:1-12.
73. Ding Y, Cui W, Sun D, Wang G-L, Hei Y, Meng S, et al. In vivo study of doxorubicin-loaded cell-penetrating peptide-modified pH-sensitive liposomes: biocompatibility, bio-distribution, and pharmacodynamics in BALB/c nude mice bearing human breast tumors. Drug Des Devel Ther. 2017:3105-3117.
74. Maity SK, Stahl P, Hensel A, Knauer S, Hirschhäuser C, Schmuck C. Cancer-cell-specific drug delivery by a tumor-homing CPP-gossypol conjugate employing a tracelessly cleavable linker. Chem Eur J. 2020;26(14):3010-3015.
75. dos Santos Rodrigues B, Kanekiyo T, Singh J. In vitro and in vivo characterization of CPP and transferrin modified liposomes encapsulating pDNA. Nanomedicine: NBM. 2020;28:102225.
76. Gronewold A, Horn M, Ranđelović I, Tóvári J, Muñoz Vázquez S, Schomäcker K, Neundorf I. Characterization of a cell-penetrating peptide with potential anticancer activity. Chem Med Chem. 2017;12(1):42-49.
77. Shi J, Guo S, Wu Y, Chen G, Lai J, Xu X. Behaviour of cell penetrating peptide TAT-modified liposomes loaded with salvianolic acid B on the migration, proliferation, and survival of human skin fibroblasts. J. Liposome Res. 2020;30(1):93-106.
78. Kawak P, Sawaftah NMA, Pitt WG, Husseini GA. Transferrin-targeted liposomes in glioblastoma therapy: a review. Int J Mol Sci. 2023;24(17):13262.
79. Yuan M, Qiu Y, Zhang L, Gao H, He Q. Targeted delivery of transferrin and TAT co-modified liposomes encapsulating both paclitaxel and doxorubicin for melanoma. Drug Deliv. 2016;23(4):1171-1183.
80. Paliwal R, Paliwal SR, Kenwat R, Kurmi BD, Sahu MK. Solid lipid nanoparticles: A review on recent perspectives and patents. Opin Ther Pat. 2020;30(3):179-194.
81. Mirchandani Y, Patravale VB, Brijesh S. Solid lipid nanoparticles for hydrophilic drugs. J Control Release. 2021;335:457-464.
82. Mendoza-Munoz N, Urbán-Morlán Z, Leyva-Gómez G, de la Luz Zambrano-Zaragoza M, Quintanar-Guerrero D. Solid lipid nanoparticles: an approach to improve oral drug delivery. J Pharm Pharm Sci. 2021;24:509-532.
83. Scioli Montoto S, Muraca G, Ruiz ME. Solid lipid nanoparticles for drug delivery: pharmacological and biopharmaceutical aspects. Front Mol Biosci. 2020;7:319.
84. Salah E, Abouelfetouh MM, Pan Y, Chen D, Xie S. Solid lipid nanoparticles for enhanced oral absorption: A review. Colloids Surf B Biointerfaces. 2020;196:111305.
85. Khairnar SV, Pagare P, Thakre A, Nambiar AR, Junnuthula V, Abraham MC, et al. Review on the scale-up methods for the preparation of solid lipid nanoparticles. Pharmaceutics. 2022;14(9):1886.

86. Satapathy MK, Yen T-L, Jan J-S, Tang R-D, Wang J-Y, Taliyan R, Yang C-H. Solid lipid nanoparticles (SLNs): an advanced drug delivery system targeting brain through BBB. Pharmaceutics. 2021;13(8):1183.
87. Liu B, Han L, Liu J, Han S, Chen Z, Jiang L. Co-delivery of paclitaxel and TOS-cisplatin via TAT-targeted solid lipid nanoparticles with synergistic antitumor activity against cervical cancer. Int J Nanomedicine. 2017:955-968.
88. Costa CP, Moreira JN, Lobo JMS, Silva AC. Intranasal delivery of nanostructured lipid carriers, solid lipid nanoparticles and nanoemulsions: A current overview of in vivo studies. Acta Pharm Sin B. 2021;11(4):925-940.
89. Ganesan P, Ramalingam P, Karthivashan G, Ko YT, Choi D-K. Recent developments in solid lipid nanoparticle and surface-modified solid lipid nanoparticle delivery systems for oral delivery of phyto-bioactive compounds in various chronic diseases. Int J Nanomedicine. 2018:1569-1583.
90. Garcês A, Amaral M, Lobo JS, Silva AC. Formulations based on solid lipid nanoparticles (SLN) and nanostructured lipid carriers (NLC) for cutaneous use: A review. Eur J Pharm Sci. 2018;112:159-167.
91. Weber S, Zimmer A, Pardeike J. Solid lipid nanoparticles (SLN) and nanostructured lipid carriers (NLC) for pulmonary application: a review of the state of the art. Eur J Pharm Sci. 2014;86(1):7-22.
92. Pimentel-Moral S, Teixeira M, Fernandes A, Borrás-Linares I, Arráez-Román D, Martínez-Férez A, et al. Polyphenols-enriched Hibiscus sabdariffa extract-loaded nanostructured lipid carriers (NLC): Optimization by multi-response surface methodology. J Drug Deliv Sci Technol. 2019;49:660-667.
93. Assefi M, Ataeinaeini M, Nazari A, Gholipour A, Vertiz-Osores JJ, Calla-Vásquez KM, et al. A state-of-the-art review on solid lipid nanoparticles as a nanovaccines delivery system. J Drug Deliv Sci Technol. 2023:104623.
94. Subroto E, Andoyo R, Indiarto R. Solid lipid nanoparticles: Review of the current research on encapsulation and delivery systems for active and antioxidant compounds. Antioxid. 2023;12(3):633.
95. Mohammed HA, Khan RA, Singh V, Yusuf M, Akhtar N, Sulaiman GM, et al. Solid lipid nanoparticles for targeted natural and synthetic drugs delivery in high-incidence cancers, and other diseases: Roles of preparation methods, lipid composition, transitional stability, and release profiles in nanocarriers' development. Nanotechnol Rev. 2023;12(1):20220517.
96. López KL, Ravasio A, González-Aramundiz JV, Zacconi FC. Solid lipid nanoparticles (SLN) and nanostructured lipid carriers (NLC) prepared by microwave and ultrasound-assisted synthesis: Promising green strategies for the nanoworld. Pharmaceutics. 2023;15(5):1333.
97. Harish V, Mohd S, Tewari D, Pandey NK, Vishwas S, Babu MR, et al. Unravelling the role of solid lipid nanoparticles in drug delivery: Journey from laboratory to clinical trial. J Drug Deliv Sci Technol. 2023:104616.
98. Salminen H, Kasapoğlu KN, Özçelik B, & Weiss J. Stabilization of solid lipid nanoparticles with glycyrrhizin. Eur Food Res Technol. 2023;249(3):787-798.
99. Chauhan I, Singh L. A comprehensive literature review of lipids used in the formulation of lipid nanoparticles. Curr Nanosci. 2023;8(2):126-152.
100. Salunkhe S, Basak M, Chitkara D, Mittal A. Surface functionalization of exosomes for target-specific delivery and in vivo imaging & tracking: Strategies and significance. J Control Release. 2020; 326:599-614.
101. Mondal J, Pillarisetti S, Junnuthula V, Saha M, Hwang SR, Park I-k, Lee Y-k. Hybrid exosomes, exosome-like nanovesicles and engineered exosomes for therapeutic applications. J Control Release. 2023; 353:1127-1149.
102. Tian T, Zhang H-X, He C-P, Fan S, Zhu Y-L, Qi C, et al. Surface functionalized exosomes as targeted drug delivery vehicles for cerebral ischemia therapy. Biomater. 2018;150:137-149.
103. Wang C, Kimura K, Li J, Richardson JJ, Naito M, Miyata K, et al. Polydopamine-Mediated Surface Functionalization of Exosomes. Chem Nano Mat. 2021;7(6):592-595.
104. Zhao H, Wu M, Zhu L, Tian Y, Wu M, Li Y, et al. Cell-penetrating peptide-modified targeted drug-loaded phase-transformation lipid nanoparticles combined with low-intensity focused ultrasound for precision theranostics against hepatocellular carcinoma. Theranostics. 2018;8(7):1892.
105. Aschmann D, Knol RA, Kros A. Lipid-based nanoparticle functionalization with coiled-coil peptides for in vitro and in vivo drug delivery. Acc Chem Res. 2024;57(8):1098-1110.
106. Qin J, Xue L, Gong N, Zhang H, Shepherd SJ, Haley RM, et al. RGD peptide-based lipids for targeted mRNA delivery and gene editing applications. RSC Advances. 2022;12(39):25397-25404.
107. Zhang Y-L, Zhang Z-H, Jiang T-Y, Lv H-X, Zhou J-P. Cell uptake of paclitaxel solid lipid nanoparticles modified by cell-penetrating peptides in A549 cells. Pharmazie. 2013;68(1):47-53.

REVIEW PAPER

# Harnessing liposome technology for precision medicine: design, delivery, and clinical impact

***Ganugapenta Nikhil Kumar[1], Edukulla Satheesh Kumar[1], Thirumalesh Naik Sugali Banoth[1], Archana Sugunarajan Latha[1], Bhargavi Melehalli Shivaraju[1], Hindustan Abdul Ahad[*1]***

*[1]Department of R R College of Pharmacy, Chikkabanavara, Bengaluru, Karnataka, India*

**ABSTRACT**

***Background:*** Liposomes are microspheres formed by phospholipids and have received attention as sophisticated drug carriers because they can retain both water-soluble and fat-soluble drugs. Their applications have made them very versatile and have resulted in their great exploration in many aspects of therapy.

***Objective(s):***The present review sets out to provide an exhaustive overview of the nature of liposomes, their preparation tactics, measures of their efficiency, and the trending applications of liposomes in contemporary medicine, with a focus on optimization measures and the future of this technology.

***Materials and Methods:*** The mini-review of the literature was done with an emphasis on the various methods of liposome preparation, which included the Bangham method, solvent injection methods, as well as the removal methods of detergents. Efficiency was analyzed based on optimization and evaluation parameters, including vesicle size, shape, zeta potential, and in vitro release profile of the drug to evaluate their contribution to formulation efficiency.

***Results:*** Recent innovations have resulted in the creation of new generation liposomal systems, such as active targeting liposomes, stimuli-reactive liposomes, and surface-modified liposomes. These advances bring substantive benefits to drug delivery effectiveness and outcomes in the therapeutic arena and decreased systemic toxicities. Liposomal formulations find increasing use in cancer treatment, in the treatment of infectious diseases, and in gene delivery. A number of novel systems are in the clinical trial stage, indicating their translational potential.

***Conclusion:*** Liposomes are a very flexible and evolving drug delivery mechanism. The development of improved surface modification, targeting approaches, and stimuli-responsive systems still augers well with the therapeutic potential. Continuing advances in the development and clinical assessment of new liposomal preparations demonstrate the future of these agent-carrying constructs to transform the field of disease management in the domains of cancer, infectious disease, and gene therapy.

***Keywords:*** *Antineoplastic agents, Drug delivery systems, Gene therapy, Liposomes, Nanomedicine*

**How to cite this article**

*Nikhil Kumar G, Satheesh Kumar E, Banoth Th NS, Sugunarajan Latha A, Melehalli Shivaraju Bh, Abdul Ahad H. Harnessing liposome technology for precision medicine: design, delivery, and clinical impact. Nanomed J. 2026; 13(2): 283-295. DOI: 10.22038/NMJ.2025.86734.2188*

## INTRODUCTION

In Liposomes, "lipo" means “fat," & "soma" means "body." Constructively, they have two-layered vesicles. The first publication on the subject was released in 1964, stating that phospholipids and other amphiphilic lipid molecules in solution self-assemble to create liposomes, which are colloidal spherical structures. The liposomal membrane contains one or multiple phospholipid bilayers (lamellas) surrounding an internal aqueous area where polar head groups face internal and external water phases (Fig.1). The layered structure of liposomes allows them to carry and move molecules that do not easily dissolve because they are uniformly structured [1]. The lipid bilayer contains hydrophobic molecules, the interior aqueous core contains hydrophilic molecules, and the water/lipid bilayer interface contains amphiphilic molecules. Because they are water-attracted, the heads group together to create a surface facing the water wherever there is any. The tails group creates an out-of-water surface because they are water-repellent. There is one layer of heads attracted to water in the environment and pointing towards the exterior of the cage [2].

Another layer of heads is turned inward, attracted by the water within the cell. Because of their diverse shapes, liposomes have been studied more than any other carrier system.

**Corresponding author(s):* Hindustan Abdul Ahad, Professor, Department of R R College of Pharmacy, Chikkabanavara, Bengaluru-560090, Karnataka, India. Email: *h.abdulahad@rrcollegeofpharmacy.com.*

Note. This manuscript was submitted on March 13, 2025; approved on October 20, 2025.

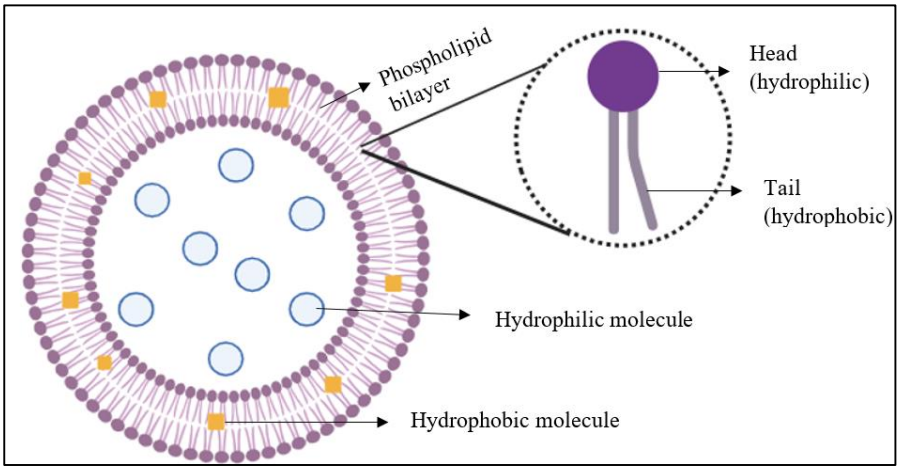


Fig.1. Structural organization of a liposome showing phospholipid bilayer, aqueous core, and drug encapsulation sites.

By adding phospholipids to a water solution, phospholipid bilayer membranes can form sphere-shaped structures known as liposomes that include internal hydrophilic compartments. Small, spherical vesicles called Phospholipids, cholesterol, and non-toxic detergents are all able to encapsulate liposomes [3]. Even for membrane proteins, the investigations led to the consideration of liposomes as delivery systems, which are distinguished by the presence of a diverse range of chemicals in the core region. Both hydrophilic and hydrophobic chemicals can be adversely delivered and encapsulated by these devices. Because they improve the bio-distribution and stabilize medicinal substances, Liposomes as drug delivery technology enhance therapy for many medical conditions and eliminate obstacles for cellular and tissue uptake of chemicals to target tissues *in vivo* [4]. This is because the liposome shields the drug from the physiological processes that include enzymatic degradation, chemical and immunological inactivation, and rapid clearance from plasma, enhancing and prolonging its efficacy. As the therapeutic agent is entrapped inside the liposome, its contact with normal tissue is reduced compared to the free drug, thus reducing the risk of adverse side effects [5].

### *Optimization in the process of liposome formulation and testing*

Optimization plays an important role in liposome studies in order to achieve high entrapment efficiency, as well as stability, controlled release, size reduction of the vesicles, and biocompatibility. Traditional methods of trial-and-error learning are ineffective; thus, Design of Experiments (DoE) and Response Surface Methodology (RSM) are used [6-10].

### *Factorials design (full & fractional factorial)*

Research design in which many factors (formulation variables) are studied at once at several levels. In a $2^2$ factorial design, there exist 2 factors which are run in two levels (low and high) hence resulting in 4 experimental runs.

***Digits meaning:*** A $3^2$ design is a two-factor statistical experimental design with three levels (low, medium, and high) of each factor, making a total of $3^2$ =9 experimental runs. The former digit (3), which is found in this notation, signifies the number of levels within each of the factors, and the superscript (2) shows the level of factors under investigation. It is the common design used in a full factorial experiment to systematically research the effects of several factors and their interaction with a response variable.

***Use in liposomes:*** Liposomes are used in an initial screening of variables such as the phospholipid-to-cholesterol ratio, hydration time, or sonication power. It aids in the discovery of important variables that may affect the size of the vesicles, zeta potential, as well as entrapment efficiency.

### *Central Composite Design (CCD)*

Response surface design (RSD) Expanding on a factorial design are the center points and axial (star) points added to assess reproducibility of a factor and explore the curvature of surfaces. A common CCD consists of three components: factorial points (a 2-level factorial design), center points, and axial points that enable one to explore extreme values. In a 2-factor CCD, each factor will have five levels ($-\alpha$, -1, 0, +1, $+\alpha$). In this case, the design can support quadratic modeling. This allows CCD to be a well-used tool in applications involving optimizing liposomes, where we can model linear and quadratic effects of parameters on dependent

responses such as bilayer rigidity, the rate of drug release, and stability.

***Box Behnken design***

A Box Behnken design (BBD) is a dataset of an RSM that is less costly as compared to a CCD, based on its ability to require fewer experimental runs and does not employ extreme axial points. It is designed by the midpoints of the design space edges and the center points, and factors were studied in three levels (−1, 0, and +1). The main benefit of BBD is that it does not cause severe conditions in an experiment, but this aspect may be highly beneficial in cases where such conditions may result in unstable products such as liposomes. With liposomes, a BBD would be suitable in investigating the collective effects of the concentration of the lipid, the drug-to-lipid ratio, and the rate of stirring on key properties such as the size of the vesicles and polydispersity index.

***Taguchi design***

A robust design. A Taguchi robust design is a method of design that uses the concept of orthogonal arrays to effectively screen the interactions of many factors on a process or product in a much smaller number of runs than would be needed to study a wide range of interactions in a full factorial design. The use of such an approach in the context of liposomes would be very beneficial to a preliminary screening of many of the process parameters, such as the pH, hydration medium, and sonication time, and can point out which variables are most influential by requiring the least effort.

***Plackett–Burman design***

Plackett-Burman design (PBD) is a screening design to be used to separate the most important variables out of many possible variables. The reason is that it considers in evaluations of the main effects of each factor and not the interactions, hence it is efficient. Within the context of liposomes, a PBD can be useful to reduce the key formulation variables, such as type of lipid or surfactant concentration, to consider first with the aid of a more complex optimization approach, e.g., a CCD or a BBD.

Table 1 provides a comprehensive summary of various optimization techniques utilized in the formulation and evaluation of liposomes, highlighting their principles, methodologies, and significance in enhancing liposomal stability, drug entrapment efficiency, and therapeutic efficacy.

Table 1. Summarize different optimization techniques used for the formulation and evaluation of liposomes.

| Drug | Design | Independent variables | Dependent variables | Ref. |
|---|---|---|---|---|
| Oridonin | BBD (Box Behnken design) | Ethanol ($X_1$), extraction time ($X_2$), and solid/lipid ($X_3$). | Entrapment efficiency ($Y_1$), particle size ($Y_2$), polydispersity index ($Y_3$), and zeta potential ($Y_4$) | [11] |
| 5- fluorouracil | $3^2$ factorial design (FFD) | Drug: lipid ($X_1$), Ascorbyl-6-palmitate ($X_2$). | Particle size ($Y_1$), entrapment efficiency ($Y_2$), and zeta potential ($Y_3$). | [12] |
| Rifampicin | $3^2$ FFD | Soya lecithin /cholesterol ($X_1$). | Particle size ($Y_1$) and entrapment efficiency ($Y_2$). | [13] |
| Lycopene | $3^3$ FFD | Soy lecithin ($X_1$), and cholesterol/ β-CD ($X_2$). | Particle size ($Y_1$), entrapment efficiency ($Y_2$), drug release ($Y_3$), and zeta potential ($Y_4$). | [14] |
| Amisulpride | $2^3$ FFD | Cyclodextrins (CDs) ($X_1$), drug/CDs ($X_2$), and liposomes ($X_3$). | Particle size ($Y_1$), entrapment efficiency ($Y_2$), polydispersity index ($Y_3$), and zeta potential ($Y_4$). | [15] |
| Glipizide | $3^2$ FFD | Paraffin wax ($X_1$) and the stearic acid in the wax($X_2$). | Particle size ($Y_1$), entrapment efficiency ($Y_2$), and drug release ($Y_3$) | [16] |
| Bufalin | $3^3$ FFD | Bufalin: lipid ($X_1$) and cholesterol: EPC ($X_2$). | Particle size ($Y_1$), zeta potential ($Y_2$), and entrapment efficiency ($Y_3$). | [17] |
| Pingyangmycin | BBD | PYM ($X_1$), CS ($X_2$), and GP ($X_3$). | Drug release ($Y_1$) and release rate constant ($Y_3$). | [18] |
| Acyclovir | $3^3$ FFD | The vol. of the organic phase ($X_1$), the vol. of the aqueous phase ($X_2$), and Drug/Phosphatidylcholine /Cholesterol ($X_3$). | Entrapment efficiency ($Y_1$). | [19] |
| Paeonol | BBD | Soybean phosphatidylcholine: Cholesterol ($X_1$), paeonol ($X_2$), pH of PBS($X_3$). | Entrapment efficiency ($Y_1$). | [20] |
| Ophiopogon polysaccharide | BBD | Soybean phosphatide/ OP ($X_1$), soybean phospholipid/ cholesterol ($X_2$), and chloroform to a phosphate-buffered saline ($X_3$). | Particle size ($Y_1$) and zeta potential ($Y_2$). | [21] |
| Epimedium | $3^4$ FFD | Drug to lipid ($X_1$), soybean phospholipid/ cholesterol ($X_2$). | Entrapment efficiency ($Y_1$) and Drug-loading ($Y_2$). | [17] |

| Drug | Design | Independent variables | Dependent variables | Ref. |
|---|---|---|---|---|
| Travoprost | $3^1 \times 2^1$ FFD | Type of permeation enhancer (PE) ($X_1$), PE ($X_2$), and lecithin/ cholesterol ($X_3$). | Entrapment efficiency ($Y_1$), particle size ($Y_2$), polydispersity index ($Y_3$), and zeta potential ($Y_4$). | [22] |
| Temozolomide | $3^2$ FFD | Lipid/ organic phase ($X_1$). | Particle size, entrapment efficiency ($Y_2$), and drug loading ($Y_3$). | [23] |
| Ginsenoside | BBD | Lipid to drug ($X_1$), ePC to cholesterol ($X_2$), Lipid ($X_3$). | Entrapment efficiency ($Y_1$). | [24] |
| Primaquine | BBD | Phospholipid type ($X_1$), cholesterol ($X_2$), charge ($X_3$), and citrate ($X_4$). | Entrapment efficiency ($Y_1$) and particle size ($Y_2$). | [25] |
| Methazolamide | $3^2$ FFD | Cholesterol ($X_1$) and drug ($X_2$). | Entrapment efficiency ($Y_1$) and particle size ($Y_2$). | [26] |
| Liposome polycation-DNA complexes (LPD) | CCD (central composite design) | Protamine/DNA ($X_1$), Chems/ DNA ($X_2$), and Chems/ Dioleoylphosphatidylethanolamine ($X_3$). | Particle size ($Y_1$) and entrapment efficiency ($Y_2$). | [27] |
| Piroxicam | CCD | HLB ($X_1$), Total Lipid amount ($X_2$), and Surfactant: cholesterol ($X_3$). | Entrapment efficiency ($Y_1$) and drug release ($Y_2$). | [28] |
| Besifloxacin hydrochloride | $3^2$ FFD | Soya lecithin: cholesterol($X_1$), and lipid: drug ($X_2$). | Entrapment efficiency ($Y_1$), drug loading ($Y_2$), and Particle size ($Y_3$). | [29] |
| Bovine Lactoferrin | $2^4$ FFD | Percentage of cholesterol in lipid content ($X_1$), drug ($X_2$), surfactant ($X_3$), and sonication time ($X_4$). | Particle size ($Y_1$) and Entrapment efficiency ($Y_2$). | [30] |
| Ganoderma lucidum polysaccharide | BBD | Soybean phosphatide/ cholesterol ($X_1$), soybean Phosphatide/ tween 80 ($X_2$), and ultrasonic time ($X_3$). | Entrapment efficiency ($Y_1$). | [31] |
| Doxorubicin and curcumin | BBD | Phospholipid ($X_1$), curcumin ($X_2$), Doxorubicin ($X_3$), Working temperature ($X_4$), Buffer pH ($X_5$), and Phospholipid: cholesterol molar ratio ($X_6$). | Entrapment efficiency of curcumin ($Y_1$), Entrapment efficiency of doxorubicin ($Y_2$), and zeta potential ($Y_3$). | [32] |
| Quercetin | D-optimal experimental design | dipalmitoyl phosphatidylcholine (DPPC) ($X_1$), DPPC: Cholesterol ($X_2$), and quercetin ($X_3$). | Drug loading ($Y_1$), polydispersity index ($Y_2$), and entrapment efficiency ($Y_3$). | [33] |

**Benefits of liposomes**

Liposome delivery presents several benefits to the drug delivery process, and it increases the efficacy, shelf life, and safety of several drugs. The liposomes can overcome these effects and reduce the accompanying side effects of toxicity to healthy tissue by encapsulating the chemotherapeutic compounds so that, at optimum doses, the accompanying toxicity to healthy tissue is reduced, as well as protecting against enzymatic axerophagy. This flexible system can encapsulate a broad chemical composition, including water-soluble, amphiphilic, lipid-soluble drugs, and even big fragments of DNA. Also, the construction of liposomes can reduce exposure of the cytotoxic drugs to sensitive tissue, and the shuttles can be used to carry either positively or negatively charged drugs. They may be specifically designed to target selected cells or tissue, and are themselves non-toxic, biocompatible, and biodegradable [34-36].

***Drawbacks of liposomes***

Although liposomes are very efficient in drug delivery, they still possess a number of disadvantages. Their reduced stability is a major concern, which will cause leakage of the encapsulated drug or molecule and subsequent fusion of the vesicles. Also, although the internal compartment (inside the liposome) is aqueous, the lipid bilayer itself is not water-soluble. The liposome is also composed of phospholipids that may experience degradation in the form of dephosphorylation, hydrolysis, and oxidation, further disrupting the stability. These aspects make liposomal formulations have a short half-life in the body. Lastly, they are extremely costly to produce, and as such, they may restrict their usage on a larger scale [37, 38].

***Types of liposomes***

***Grounded on structure***

Table 2 provides a detailed overview of the different types of vesicles, categorizing them based on their size ranges and lamellarity while explaining their structural characteristics, formation methods, and applications in drug delivery and biomedical research.

Table 2. Types of vesicles with their size ranges and lamellarity [39].

| Vesicle type | Size | Lamella |
|---|---|---|
| Unilamellar vesicle (ULV) | All sizes range | 1 |
| Small Unilamellar Vesicle (SUV) | 0.02-0.1µm | 1 |
| Medium Unilamellar Vesicle (MUV) | >0.1µm | 1 |
| Large Unilamellar Vesicle (LUV) | >0.1µm | 1 |
| Giant Unilamellar Vesicle (GUV) | >1µm | 1 |
| Oligolamellar vesicle (OLV) | 0.1-1µm | 5 |
| Multilamellar vesicle (MLV) | >0.5µm | 5-25 |
| Multi-vesicular vesicle (MVV) | >1µm | 1 |

**Grounded on the methods of preparation**

Liposomes are spherical vesicles with phospholipid bilayers, prepared using the Bangham method, sonication, extrusion, reverse-phase evaporation, and solvent injection (Fig.2). Each technique affects size, entrapment efficiency, and stability, optimizing them for drug delivery applications [40, 41].

**Different liposomes with their composition**

The composition of the liposomes is described [42, 43] (Fig.3).

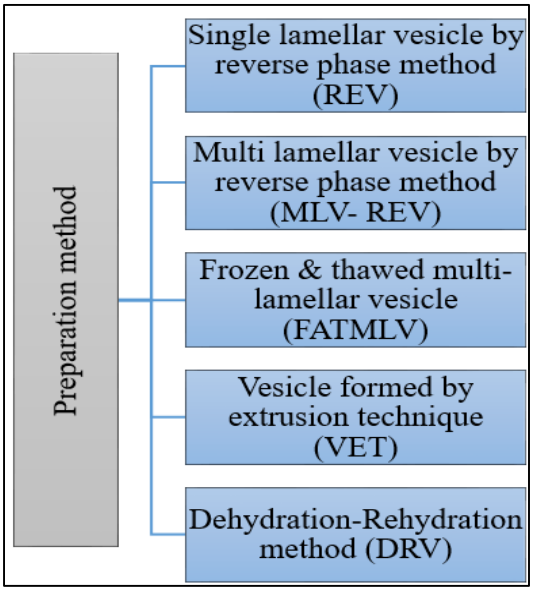


Fig.2. Types of Liposomes Based on Preparation Methods like Multilamellar Vesicles, Small Unilamellar Vesicles, Large Unilamellar Vesicles, and Giant Unilamellar Vesicles.

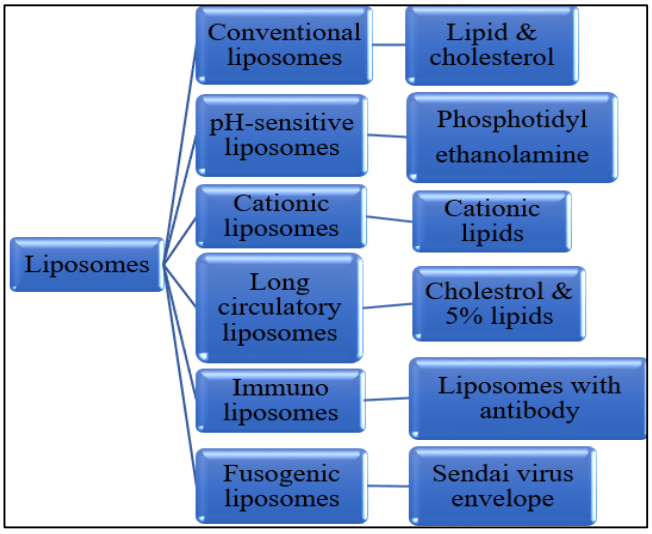


Fig.3. Different Types of Liposomes with Their Composition, like Conventional Liposomes, Stealth Liposomes, Cationic Liposomes, Immunoliposomes, and Stimuli-Sensitive Liposomes.

## MATERIALS AND METHODS

The successful incorporation of medication, along with the achievement of monodisperse patches with controlled size distribution and desired lamellar arrangement, forms a basis for stable colloids over time and is the primary claim of a system for liposome nano formulation conformation. The traditional methods involve dissolving liposomes in an unexpected organic detergent and combining them with a waterless phase. The stability of the produced nano-formulation may be impacted, or the chemical composition of the integrated active composites may be disturbed by the presence of an organic detergent. The following key steps are involved in the traditional liposome medication styles [44]:

- Lipids dissolve in an organic detergent.
- The organic detergent's accompanying lipidic outcome is dried down.
- Using a waterless medium to hydrate the lipid, then stirring or moving it
- Diminished size (and/or altered lamellarity)
- Processing after formation (sterilization, sanctification)
- The final nano formulation product's characteristics

### *Bangham method*

A round-bottom flask dissolves a hydrophobic drug and lipids in an organic solvent, forming a thin film that evaporates under reduced pressure. A heated aqueous buffer hydrates the film, incorporating hydrophilic drugs into the liposome's interior. Slower hydration improves entrapment efficiency. Liposome scaling, lamellarity, and size distribution are controlled via sonication or membrane extrusion, with extrusion preferred for stability and efficiency. While sonication aids SUV liposome production, it can degrade lipids or drugs and may cause metal contamination (Fig.4) [45].

### *Ethanol injection method*

Ethanol-solubilized phospholipids are rapidly injected into a heated buffer, causing self-assembly as ethanol dilutes. This leads to lipid precipitation, forming bilayer fragments that merge into unilamellar vesicles upon solvent depletion. Ethanol content is crucial, ≤7.5% ensuring homogenous SUVs, while rapid addition to excess buffer produces MLVs. Residual ethanol is removed via dialysis and filtration, with spontaneous SUV and LUV formation. Ethanol evaporates at room temperature (Fig.5) [46].

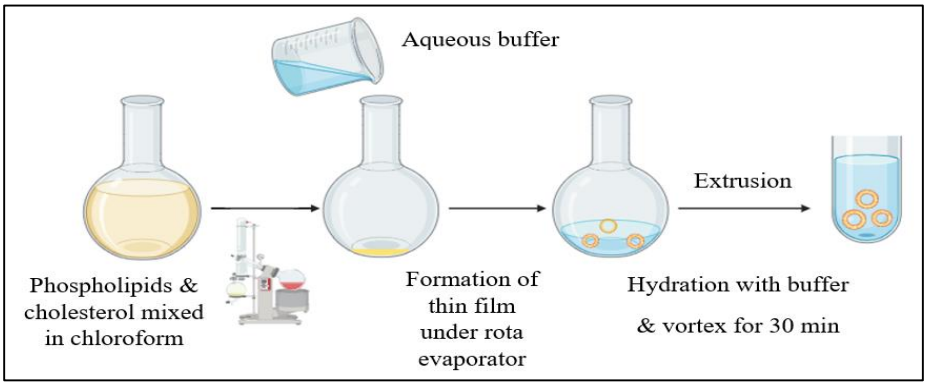


Fig.4. Liposome Preparation Using the Bangham Method by hydrating the thin lipid film formed by evaporating the solvent.

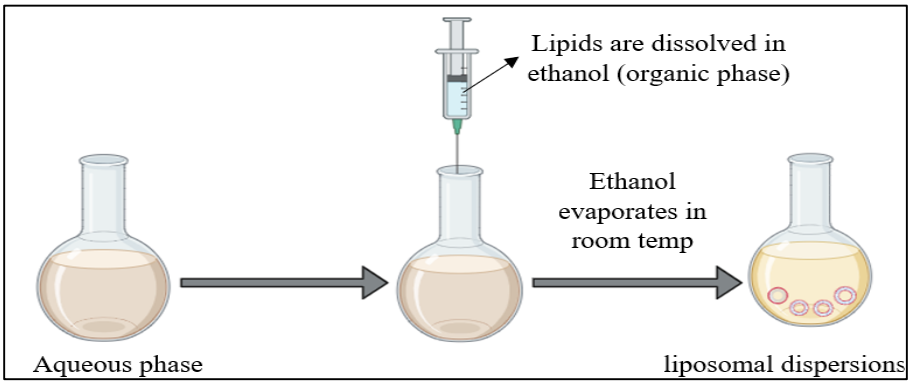


Fig.5. Preparation of Liposomes by Ethanol Injection Method, which involves a lipid solution in ethanol that is rapidly injected into an aqueous phase under stirring, leading to spontaneous formation of small unilamellar vesicles.

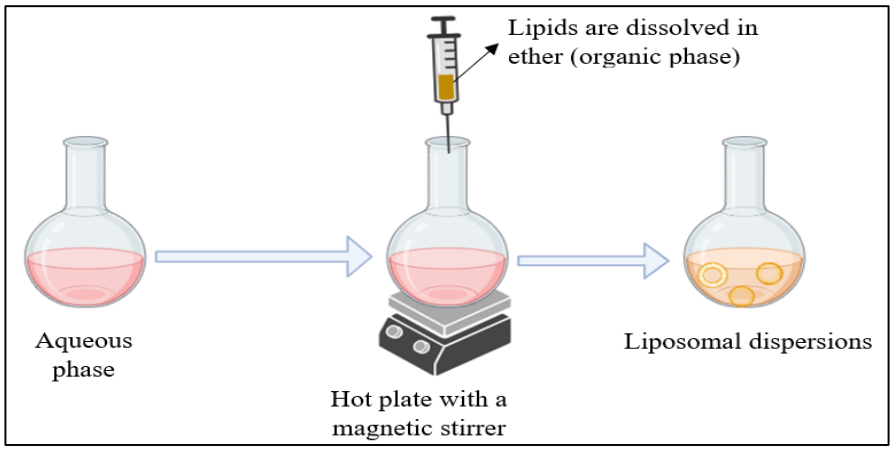


Fig.6. Preparation of Liposomes by Ether Injection Method that involves a lipid solution in volatile ether is slowly injected into an aqueous phase at 55–65 °C, causing ether evaporation and the gradual formation of liposomes.

***Ether injection method***

In the ether injection method, lipids in ether are slowly added to an aqueous phase containing encapsulated ingredients and then heated (55–65°C) to evaporate the solvent. Slow evaporation under reduced pressure favors LUV formation, while SUVs arise via ether vaporization. This method removes solvents more effectively than ethanol injection, improving liposome concentration and entrapment efficiency. However, it results in polydisperse liposomes and exposes active agents to solvents and heat, potentially affecting stability and safety (Fig.6) [47].

***Solvent- evaporation method***

Solvent- phase evaporation relies on inverted micelle formation, enabling high aqueous space-to-lipid ratios and efficient encapsulation. Hydrophilic substances are enclosed in a buffered aqueous phase, while amphiphilic molecules in an organic phase are sonicated to form micelles. Slow solvent removal increases viscosity until micelles disrupt, forming bilayers around the remaining micelles. This method produces liposomes with more aqueous content than MLVs. Sonication of a phospholipid suspension creates an oil-water emulsion, which, under reduced pressure, forms a gel that transitions into liposomes upon further solvent removal. It achieves high entrapment efficiency in low-ionic-strength media but risks denaturing proteins or shearing DNA due to sonication and solvent exposure [48].

***Detergent removal method***

In the detergent removal method, lipids are hydrated and solubilized in a detergent solution, forming mixed micelles. As the detergent is gradually removed, lipid-enriched micelles transition into unilamellar vesicles. The most convenient removal method is dilution (10–100 fold) with a buffer, causing micelles to grow, become polydisperse, and eventually form vesicles beyond the micellar phase boundary. In lecithin-bile salt systems, dilution reduces bile salt concentration, decreasing monolayer curvature and promoting liposome formation. Liposomes emerge when detergent levels fall below the critical micelle concentration (CMC), but low liposome concentration and inefficient entrapment of lipid-soluble contents limit the process [49].

***The dehydration-rehydration method***

This involves rehydrating said SUVs in the void volume with the material-containing aqueous fluid of interest to entrap and immediately dry. Consequently, the solid lipids are finely fractured and dispersed. There are various methods, but freeze-drying is the most common one. The vesicles are then rehydrated. The oligolamellar vesicles (OLV) were obtained with this method (Fig.7) [50].

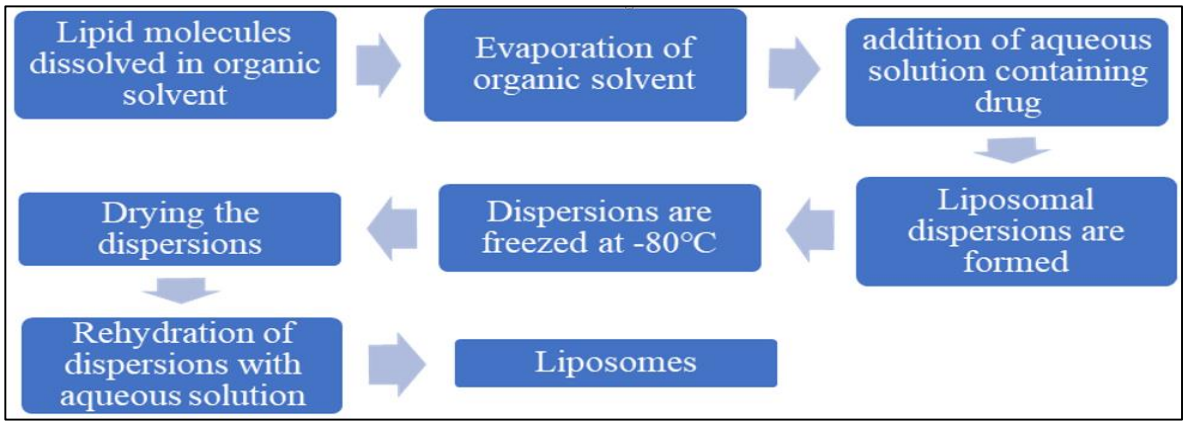


Fig.7. Scheme of Preparing Liposomes by the Dehydration–Rehydration Method

***Proliposome method***

The pro-liposomal approach is a simple method for liposome production with high entrapment efficiency but low repeatability. For small-scale preparation, lipids are dissolved in ethanol and water, stirred at 60°C for 10 minutes, cooled, then mixed with water or buffer to form MLVs, which hydrate for an hour. For large-scale production, a lipid-ethanol-buffer mixture (1:1:2) is stirred at 60°C, cooled, and hydrated dropwise. MLVs are further hydrated via sonication. Liposomes are stored under nitrogen gas at -80°C or 4°C. Lipophilic molecules are added in ethanol, while hydrophilic molecules are incorporated in the aqueous phase(Fig.8) [51].

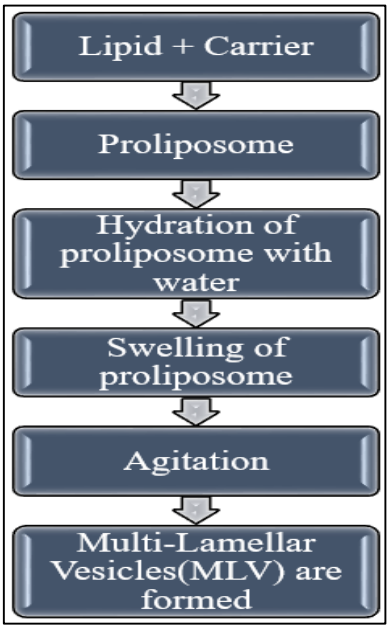


Fig.8. Detailed process of liposome preparation through the proliposome method for enhanced stability and encapsulation efficiency

***Heating method***

It is a non-organic solvent-based process. Lipid Hydration Direct hydration of lipids with an aqueous solution containing a 3-5 per cent hydration agent such as glycerin or propylene glycol, which is then heated to the melting point of the phospholipids used for at least an hour, is the method adopted for liposome production. If cholesterol is added to the composition, the suspension can be heated to 100 °C, and the hydrating agents will act as stabilizers and isochronizing additives to stop the lumping and settling of nanoparticles. Furthermore, the heat treatment is efficient in forming powder-inhalable liposomes due to the cryoprotective action of the hydrating agents (Fig.9) [52].

***Microfluidic channel method***

The microfluidic channel method is a recent technique of liposome preparation that has been introduced. Microfluidics provides a means of using liquids in thin channels. In this method, as per the technique, lipids are dissolved in a suitable organic solvent, and the solution is injected into the microchannels standing or against the flow of the aqueous medium. The aqueous and organic solutions are mixed axially continuously in the method to create liposomes. Surfactants are used to stabilize liposomes, preventing their separation and coagulation. The production of consistent liposomes with desired characteristics, such as average size, polydispersity, morphology, and lamellarity, is achieved through microfluidic channel techniques that regulate the blending of aqueous and organic phases [53].

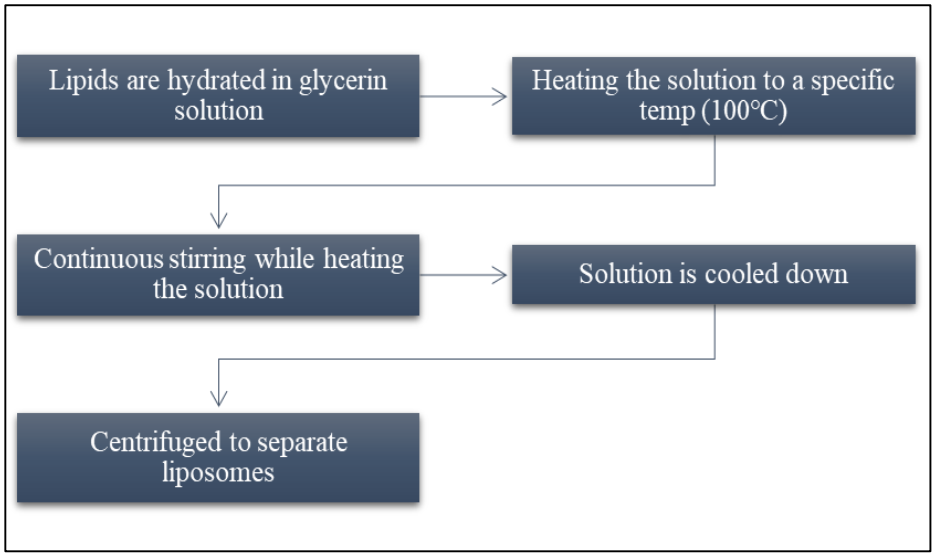


Fig.9. Stepwise process of liposome preparation using the heating method for improved vesicle formation and stability

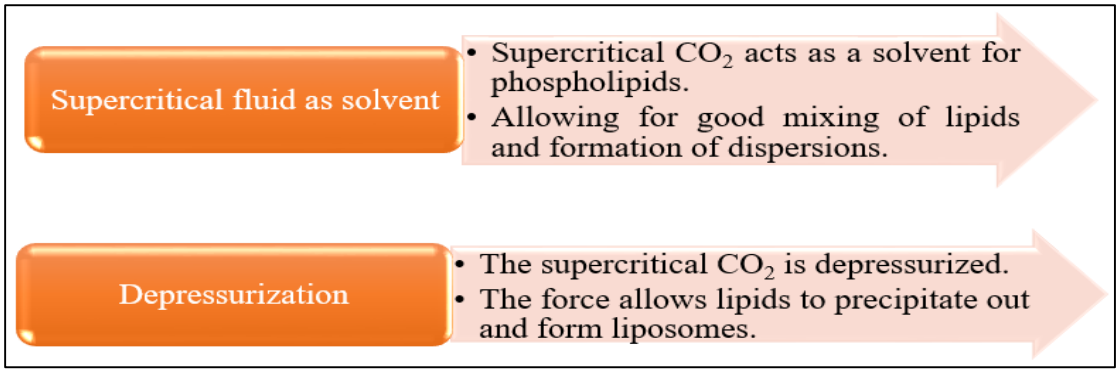


Fig.10. Stepwise process of liposome preparation using the supercritical fluid method for enhanced particle size control and stability

***Supercritical fluidic method***

Instead of employing organic detergents, this technique uses lipids that are solubilized using $CO_2$, which is a supercritical fluid. A high-pressure liquid pump continuously introduces the water-free phase into a cell where the supercritical lipid product can be delivered so that the phase transformation of solubilized phospholipids is facilitated. After all the $CO_2$ is removed, the liposomes would be created by an instantaneous drop in pressure. This system achieved a 5-fold improvement in encapsulation edge. This system uses inexpensive, environmentally safe carbon dioxide; however, it has unique designs, excessive costs, and low yields (Fig.10) [54].

***pH jumping method***

The pH jumping method is an additional solvent-free technique for liposome production. This approach breaks down MLVs into SUVs by subjecting the phosphatidic acid and phosphatidylcholine aqueous solution to a pH increase of four times in a short amount of time. SUV production rates differ from LUV rates because of the relative concentrations of phosphatidic acid and phosphatidylcholine (Fig.11) [55].

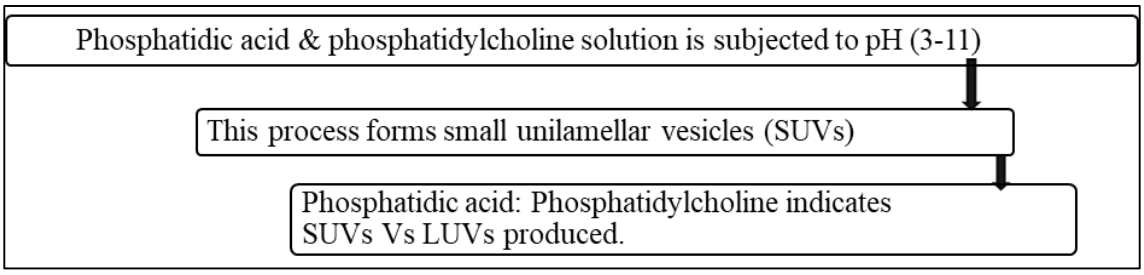


Fig.11. Stepwise process of liposome preparation using the pH jumping method for controlled vesicle formation and stability

***Evaluations of liposomes***

***Vesicle shape***

Liposome morphology is best examined using microscopy. Electron microscopy, particularly TEM, allows direct visualization but requires sample alteration, making it time-consuming and unsuitable for routine use. TEM may also distort liposome shape. Cryo-TEM, using liquid nitrogen flash-freezing, preserves liposomes' original form but is more effective for smaller nanoparticles. AFM enables non-destructive, high-resolution 3D imaging without sample manipulation, making it a faster and more effective alternative to electron microscopy [56].

***Vesicle size & polydispersity index***

Key characteristics for liposome characterization are size and polydispersity index (PDI). Size affects circulation time; smaller liposomes (50–200 nm) last longer, while larger ones are cleared faster. PDI (<0.3) indicates uniformity, with higher values suggesting heterogeneous populations. Dynamic light scattering (DLS) is the primary technique for measuring both, utilizing Brownian motion and light scattering to determine size, but struggles with particle separation and contamination sensitivity. Nanoparticle tracking analysis (NTA) tracks individual particle movement to calculate size and concentration, complementing DLS for verification [57].

***Zeta potential (ZP)***

Zeta potential measures the net charge on liposomes, influencing electrostatic interactions and stability. It depends on lipid composition, head groups, and environmental factors like ionic strength. Low zeta potential increases aggregation risk, while highly charged liposomes repel each other, enhancing stability. Measurement involves laser illumination of the sample, analyzing scattered light changes under an electric field to determine electrophoretic mobility. Using the Henry equation, the zeta potential is calculated. Capillary electrophoresis and laser Doppler electrophoresis (LDE) are the primary methods for measurement [58].

***Lamellarity***

Another property that may influence future liposomal applications is lamellarity because it affects the EE and drug release characterization. The most widely employed method, cryo-TEM, gives useful information on the lamellarity of liposomes, e.g., their bilayer thickness and bilayer-to-bilayer distance. Other techniques for determining lamellarity are based on differences in the visible or fluorescence response of lipid markers following the addition of specific reagents. The $^{31}$P NMR method has been employed to assess the value of lamellarity for liposomes, specifically the outer-to-inner phospholipid amount ratio. Paramagnetic ions in sample preparation for the NMR samples quench the $^{31}$P NMR signal of the lipids. As the contact of ions with the bilayer changes the NMR spectrum, the lamellarity of liposomes can be approximated by comparing the two spectra before and after the addition of paramagnetic ions. The other methods that can be employed to approximate the lamellarity of liposomes are SAXS and trapped volume determination [59].

***Phase behavior***

Phase behavior is essential in drug delivery as increased lipid membrane fluidity enhances hydrophilic drug permeability. It also affects liposome fusion, aggregation, stability, and protein interactions. The transition temperature is primarily studied using Differential Scanning Calorimetry (DSC), which measures heat flow differences between a sample and reference under controlled conditions. Other methods include Thermogravimetric Analysis (TGA), fluorescence probe polarization, electron paramagnetic resonance, nuclear magnetic resonance, FTIR spectroscopy, X-ray diffraction, and molecular dynamics simulations [60].

***Entrapment efficiency***

Entrapment efficiency (EE) is influenced by bilayer rigidity, liposome composition, and production methods. It measures the percentage of the drug encapsulated within liposomes compared to the total drug used. EE quantification involves separating free (unencapsulated) drugs via centrifugation or ultracentrifugation, followed by drug measurement in liposomes. Indirect methods subtract unencapsulated drugs from the total, while direct methods dissolve lipids in organic solvents for measurement. Drug quantification techniques include protein/enzyme assays, UV-Vis and fluorescence spectroscopy, and advanced methods like GC, UPLC, HPLC, $^{1}$H NMR, and ESR [61].

***In vitro drug release***

Dialysis conditions help determine the in vitro drug release profile. The dialysis membrane must allow free drug permeation without adsorption interference. A liposomal sample is sealed in a

dialysis bag and submerged in a pH 7.4 buffered saline medium at 37°C with agitation to simulate physiological conditions. At set intervals, aliquots are removed, analyzed, and replaced with fresh medium to maintain volume. The release profile is plotted as a cumulative release over time, aiding in designing liposomes for controlled drug delivery [62].

Table 3 provides a comprehensive overview of various analytical techniques employed for the assessment of liposomes, detailing their principles, methodologies, and significance in evaluating critical parameters such as size, surface charge, entrapment efficiency, stability, and drug release profiles.

Table 3. Different analytic techniques are used for the assessment of liposomes.

| Evaluation test | Analytic techniques |
|---|---|
| Particle Shape | TEM (Transmission electron microscopy), AFM, and cryo-TEM. |
| Particle Size | Atomic force microscopy (AFM), and transmission electron microscopy (TEM). |
| Zeta potential | Laser Doppler electrophoresis (LDE) and Capillary electrophoresis. |
| Lamellarity | Cryo-TEM |
| Phase behavior | DSC (differential scanning calorimetry) and thermogravimetric study (TGA), fluorescence probe polarization, NMR, Fourier transform infrared spectroscopy (FTIR), and X-ray diffraction (XRD). |
| Entrapment efficiency | HPLC, liquid chromatography with ultra (UPLC), liquid chromatography-mass spectrometry. |
| *In vivo* release | HPLC and UPLC. |

## FUTURE PERSPECTIVES

As an increasing number of drugs are safe to be transferred through the membranes of the liposomal outer layer, the liposomal vesicles have become one of the most popular methods to deliver drugs of various aspects, such as pain relievers and cancer treatments. There remain, however, several severe obstacles in their development and commercial production, such as the increased blood clearance of PEGylated liposomes, the inter-individual variability in the action of EPR (Enhanced Permeability and Retention) entities, and the reproducibility and control of excipients. These challenges notwithstanding, research is underway in developing many different new liposomal systems, including active targeting liposomes and stimuli-sensitive liposomes. One major multi-phase clinical failure was that of a thermosensitive liposome known as ThermoDox that failed during its Phase III trial in treating hepatocellular carcinoma in combination with radiofrequency ablation. Active targeting strategies are aimed at targeted targets not only in receptors on the cell surface of cancer cells or the tumor microenvironment but also in nonstandard stimuli, including pH, temperature, redox, enzymes, light, and ultrasound inducers of drug release. Coupling ligands such as proteins, peptides, carbohydrates, or monoclonal antibodies to the surface of liposomes and targeting tumor microenvironment components, such as integrins, matrix metalloproteinases, and vascular cell adhesion molecules, has also been studied. An important limitation is the nonhomogeneous population of tumor cells and expression of surface antigens, in which the applicability of ligand-based targeted therapies is restricted to a minority of tumors. The future Outlook Combinations of various ligands might be a promising solution to the detection and treatment of malignant lesions [63, 64].

## CONCLUSION

Liposomes are the exclusive novel drug delivery systems, which have the potential to be used in controlled and targeted medicine delivery. Liposomes can be administered orally, parenterally, and topically, and in prolonged-release formulations. Liposomes solubilize lipophilic drug candidates; otherwise, they would be. Intravenous administration is challenging. Because phospholipids are lipophilic, liposomes can pass through the blood-brain barrier, so even hydrophilic medications can pass through with ease. Although there are several ways to make liposomes, the thin film approach, dehydration, rehydration, and many more are the most often employed techniques. The pharmaceutical industry has already seen the successful discovery, registration, and introduction of some commercial liposomes. Liposomal drug formulations have a broad range of therapeutic applications, from pain control to cancer treatment, and provide a way to get around the drawbacks of traditional medicines. Although there are still numerous barriers to achieving their full potential, increasing interest in creating medication formulations based on liposomes may encourage the creation of the next generation of liposomes as drug carriers, which would enhance patients' quality of life. This review has also briefly summarized the classification, preparations, evaluations, and different applications of liposomes. Upcoming developments in vesicular systems, particularly in cancer therapy, will be revolutionized by liposomal drug delivery systems.

**ACKNOWLEDGEMENTS**

The authors are thankful to the college management for providing facilities for doing this work.

**FUNDING**

None.

**AUTHOR'S CONGRATULATIONS**

All authors are equally contributed for this work

**CONFLICT OF INTEREST**

Author's declares no conflict of interest.

**REFERENCES**

1. Nsairat H, Khater D, Sayed U, Odeh F, Al Bawab A, Alshaer W. Liposomes: Structure, composition, types, and clinical applications. Heliyon. 2022; 8:e08967.
2. Ricci A, Stefanuto L, Gasperi T, Bruni F, Tofani D. Lipid nanovesicles for antioxidant delivery in skin: Liposomes, ufasomes, ethosomes, and niosomes. Antioxidants (Basel). 2024; 13:1516.
3. Hamad I, Harb AA, Bustanji Y. Liposome-based drug delivery systems in cancer research: an analysis of global landscape efforts and achievements. Pharmaceutics. 2024; 16:400.
4. Huang Z, Meng H, Xu L, Pei X, Xiong J, Wang Y, et al. Liposomes in the cosmetics: present and outlook. J Liposome Res. 2024; 34:715-727.
5. Paramshetti S, Angolkar M, Talath S, Osmani RAM, Spandana A, Al Fatease A, et al. Unravelling the in vivo dynamics of liposomes: insights into biodistribution and cellular membrane interactions. Life Sci. 2024; 342:122616.
6. Pal R, Nandi V, Datta M, Pal S, Bhattacharjee J, Mazumder B. The Utilization of Response Surface Methodology (RSM) In the Optimization of Diclofenac Sodium (DS) Liposomes Formulate through the Thin Film Hydration (TFH) Technique with Involving Computational Method. J Adv Med Med Res. 2023;35(15):7–15.
7. Singh H, Verma P, Gupta B, Bhardwaj A, Chauhan S. Factors affecting response variables with emphasis on drug release and loading for optimization of liposomes. J Drug Deliv Sci Technol. 2024;94:105526.
8. Jain A, Gaba B, Jain SK, Jain SK. Development of liposomes using formulation by design: Basics to recent advances. Chem Phys Lipids. 2019;222:115–123.
9. Hadjou H, Vacher S, Poinard F, Benyahia B, De Brier L, N'Diaye S, et al. Microfluidic Manufacturing of Liposomes: Development and Optimization by Design of Experiment and Machine Learning. ACS Appl Mater Interfaces 2022;14(43):48530–48540.
10. Patel J, Rawat S, Kumar V, Patel D. Development of optimized formulation of liposome using 3-factor Box-Behnken Design. Int J Pharma Bio Sci 2021;12(1):1–8.
11. Wang Y, Wang M, Lin F, Zhang X, Zhao Y, Guo C, et al. Preparation, characterization, and evaluation of liposomes containing oridonin from Rabdosia rubescens. Molecules. 2022; 27:860.
12. Katharotiya K, Shinde G, Katharotiya D, Shelke S, Patel R, Kulkarni D, et al. Development, evaluation and biodistribution of stealth liposomes of 5-fluorouracil for effective treatment of breast cancer. J Liposome Res. 2022; 32:146-158.
13. Lankalapalli S, Tenneti SVK. Formulation and evaluation of rifampicin liposomes for buccal drug delivery. Curr Drug Deliv. 2016; 13:1084-1099.
14. Jhan S, Pethe AM. Double-loaded liposomes encapsulating lycopene β-cyclodextrin complexes: preparation, optimization, and evaluation. J Liposome Res. 2020; 30:80-92.
15. Shukr MH, Ahmed Farid OA. Amisulpride–CD-loaded liposomes: optimization and in vivo evaluation. AAPS Pharm Sci Tech. 2018; 19:2658-2671.
16. Shivakumar H, Patel P, Desai B, Ashok P, Arulmozhi S. Design and statistical optimization of glipizide loaded lipospheres using response surface methodology. Acta Pharm. 2007; 57:269-278.
17. Li Y, Zhao H, Duan LR, Li H, Yang Q, Tu HH, et al. Preparation, characterization and evaluation of bufalin liposomes coated with citrus pectin. Colloids Surf A Physicochem Eng Asp. 2014; 444:54-62.
18. Zhang L, Chen F, Zheng J, Wang H, Qin X, Pan W. Chitosan-based liposomal thermogels for the controlled delivery of pingyangmycin: design, optimization and in vitro and in vivo studies. Drug Deliv. 2018; 25:690-702.
19. Seth AK, Misra A. Mathematical modelling of preparation of acyclovir liposomes: reverse phase evaporation method. J Pharm Pharm Sci. 2002; 5:285-291.
20. Huang S, Zhai B, Fan Y, Sun J, Cheng J, Zou J, et al. Development of paeonol liposomes: design, optimization, in vitro and in vivo evaluation. Int J Nanomedicine. 2022; 17:5027-5041.
21. Fan Y, Song X, Gao Y, Chen Y, Ma L, Zhang W, et al. Preparation and optimization of ophiopogon polysaccharide liposome and its activity on Kupffer cells. Int J Pharm. 2014; 477:421-430.
22. Gao H, Fan Y, Wang D, Hu Y, Liu J, Zhao X, et al. Optimization on preparation condition of epimedium polysaccharide liposome and evaluation of its adjuvant activity. Int J Biol Macromol. 2012; 50:207-213.
23. Shukr MH, Ismail S, El-Hossary GG, El-Shazly AH. Design and evaluation of mucoadhesive in situ liposomal gel for sustained ocular delivery of travoprost using two steps factorial design. J Drug Deliv Sci Technol. 2021; 61:102333.
24. Vanza J, Jani P, Pandya N, Tandel H. Formulation and statistical optimization of intravenous temozolomide-loaded PEGylated liposomes to treat glioblastoma multiforme by three-level factorial design. Drug Dev Ind Pharm. 2018; 44:923-933.
25. Yu H, Teng L, Meng Q, Li Y, Sun X, Lu J, et al. Development of liposomal ginsenoside Rg3:

formulation optimization and evaluation of its anticancer effects. Int J Pharm. 2013; 450:250-258.
26. Stensrud G, Sande SA, Kristensen S, Smistad G. Formulation and characterisation of primaquine loaded liposomes prepared by a pH gradient using experimental design. Int J Pharm. 2000; 198:213–228.
27. Londhe VY, Sharma S. Formulation, characterization, optimization and in-vivo evaluation of methazolamide liposomal in-situ gel for treating glaucoma. J Drug Deliv. Sci. Technol. 2022; 67:102951.
28. Sun X, Zhang Z. Optimizing the novel formulation of liposome-polycation-DNA complexes (LPD) by central composite design. Arch. Pharm. Res. 2004; 27:797–805.
29. Suman B, Das TK. Liposome-based drug delivery systems: from laboratory research to industrial production—instruments and challenges. Chem Engineering. 2025;9(3):56.
30. Yao X, Bunt C, Cornish J, Quek SY, Wen J. Preparation, optimization and characterization of bovine lactoferrin-loaded liposomes and solid lipid particles modified by hydrophilic polymers using factorial design. Chem Biol Drug Des. 2014; 83:560–575.
31. Liu Z, Ma X, Deng B, Huang Y, Bo R, Gao Z, et al. Development of liposomal Ganoderma lucidum polysaccharide: formulation optimization and evaluation of its immunological activity. Carbohydr Polym. 2015; 117:510–517.
32. Tefas LR, Sylvester B, Tomuta I, Sesarman A, Licarete E, Banciu M, et al. Development of antiproliferative long-circulating liposomes co-encapsulating doxorubicin and curcumin, through the use of a quality-by-design approach. Drug Des. Devel. Ther. 2017; 11:1605–1621.
33. Tefas LR, Muntean D-M, Vlase L, Porfire AS, Achim M, Tomuță I. Quercetin-loaded liposomes: formulation optimization through a D-optimal experimental design. Farmacia. 2015; 63:126–133.
34. Riccardi D, Baldino L, Reverchon E. Liposomes, transfersomes and niosomes: production methods and their applications in the vaccinal field. J Transl Med. 2024; 22:339.
35. Dejeu IL, Vicaș LG, Marian E, Ganea M, Frenț OD, Maghiar PB, et al. Innovative approaches to enhancing the biomedical properties of liposomes. Pharmaceutics. 2024; 16:1525.
36. Khan MS, Gupta G, Alsayari A, Wahab S, Sahebkar A, Kesharwani P. Advancements in liposomal formulations: a comprehensive exploration of industrial production techniques. Int J Pharm. 2024; 124212.
37. Qian J, Guo Y, Xu Y, Wang X, Chen J, Wu X. Combination of micelles and liposomes as a promising drug delivery system: a review. Drug Deliv Transl Res. 2023;13:2767–2789.
38. Pande S. Liposomes for drug delivery: review of vesicular composition, factors affecting drug release and drug loading in liposomes. Artif. Cells Nanomed. Biotechnol. 2023; 51:428–440.
39. Sengar A. Liposomal drug delivery systems: an intro as a primer for advanced. Environment. 2025; 1:2.
40. Khafoor AA, Karim AS, Sajadi SM. Recent progress in synthesis of nano based liposomal drug delivery systems: a glance to their medicinal applications. Results Surf. Interfaces. 2023; 11:100124.
41. Abdelbari MA, Mosallam S. Liposome's incorporating cyclodextrins as a promising drug delivery system to augment the bioavailability of poorly soluble drugs. J. Liposome Res. 2025; 1–9.
42. Pardhi E, Yadav R, Chaurasiya A, Madan J, Guru SK, Singh SB, et al. Multifunctional targetable liposomal drug delivery system in the management of leukemia: potential, opportunities, and emerging strategies. Life Sci. 2023; 325:121771.
43. Kumbham S, Ajjarapu S, Ghosh B, Biswas S. Current trends in the development of liposomes for chemotherapeutic drug delivery. J. Drug Deliv. Sci. Technol. 2023; 87:104854.
44. Meng Y, Niu X, Li G. Liposome nanoparticles as a novel drug delivery system for therapeutic and diagnostic applications. Curr. Drug Deliv. 2023; 20:41–56.
45. Akram N, Afzaal M, Saeed F, Shah YA, Faisal Z, Asghar A, et al. Liposomes: A promising delivery system for active ingredients in food and nutrition. Int J Food Prop. 2023; 26:2476-2492.
46. Yusuf A, Almotairy ARZ, Henidi H, Alshehri OY, Aldughaim MS. Nanoparticles as drug delivery systems: a review of the implication of nanoparticles' physicochemical properties on responses in biological systems. Polymers (Basel). 2023; 15:1596.
47. Eltahir AKAE, Ahad HA, Haranath C, Meharajunnisa B, Dheeraj S, Sai BN. Novel phytosomes as drug delivery systems and its past decade trials. 2023.
48. Ahad HA, Haranath C, Vikas SS, Varam NJ, Ksheerasagare T, Gorantla SPR. A review on enzyme activated drug delivery system. Res J Pharm Technol. 2021; 14:516-522.
49. Visht S, Awasthi R, Rai R, Srivastav P. Development of dehydration-rehydration liposomal system using film hydration technique followed by sonication. Cur Drug Del. 2014; 11(6):763-770.
50. Haranath C, Vamsi KS, Qarmout YA, Ahad HA, Chandana S, Anchan RB, et al. Impact of Vroman's effect on pharmacodynamics and pharmacokinetics on nanoparticulate drug delivery systems. J. Young Pharm. 2022; 14: xx.
51. Gowda SR, Ahad HA, Kumar ES, Sreedhara A, Venkatesh R. A deep dive into microspheres—a comprehensive review for researchers uncovering triumphs, innovations and future directions. Asian J Res Pharm Sci. 2024; 14.
52. Yu B, Lee RJ, Lee LJ. Microfluidic methods for the production of liposomes. Methods in Enzymology. 2009;465:129-141.
53. William B, Noemie P, Brigitte E, Geraldine P. Supercritical fluid methods: An alternative to conventional methods to prepare liposomes. Chem Eng J. 2020;383:123106.

54. Khan A, Alsahli MA, Aljasir MA, Maswadeh H, Mobark MA, Azam F, et al. Safety, stability, and therapeutic efficacy of long-circulating TQ-incorporated liposomes: implication in the treatment of lung cancer. Pharmaceutics. 2022; 14:153.
55. Has C, Sunthar P. A comprehensive review on recent preparation techniques of liposomes. J. Liposome Res. 2020; 30:336-365.
56. Khan AA, Allemailem KS, Almatroodi SA, Almatroudi A, Rahmani AH. Recent strategies towards the surface modification of liposomes: an innovative approach for different clinical applications. 3 Biotech. 2020; 10:163.
57. Duong TT, Yen TTH, Nguyen LT, Nguyen T-D, Pham HT, Raal A, et al. Berberine-loaded liposomes for oral delivery: preparation, physicochemical characterization and in-vivo evaluation in an endogenous hyperlipidemic animal model. Int J Pharm. 2022; 616:121525.
58. Jyothi VGS, Bulusu R, Rao BVK, Pranothi M, Banda S, Bolla PK, et al. Stability characterization for pharmaceutical liposome product development with focus on regulatory considerations: an update. Int J Pharm. 2022; 624:122022.
59. Begum MY, Osmani RAM, Alqahtani A, Ghazwani M, Hani U, Ather H, et al. Development of stealth liposomal formulation of celecoxib: in vitro and in vivo evaluation. PLoS One. 2022; 17:e0264518.
60. Kim E-M, Jeong H-J. Liposomes: biomedical applications. Chonnam Med J. 2021; 57:27.
61. Szoka FC. Liposomal drug delivery: current status and future prospects. In: Membr Fusion. 2019; 845-890.
62. Liu P, Chen G, Zhang J. A review of liposomes as a drug delivery system: current status of approved products, regulatory environments, and future perspectives. Molecules. 2022; 27:1372.
63. Gonzalez Gomez A, Hosseinidoust Z. Liposomes for antibiotic encapsulation and delivery. ACS Infect. Dis. 2020; 6:896-908.
64. Crommelin DJ, van Hoogevest P, Storm G. The role of liposomes in clinical nanomedicine development. What now? Now what?. J Control Release. 2020; 318:256-263.

RESEARCH PAPER

# Synergistic effect of Zinc Phthalocyanine (ZnPC)@MIL-101 framework and laser radiation on mcf-7 breast cancer cells: an experimental combination study

*Mahin Velayati[1, 2], Zahra Sabouri[2, 3], Ramin Rezaee[1], Mohammad Hasan Soheilifar[4], Hoda Keshmiri Neghab[4], Samaneh Hashemi Ghoochani[3], Alireza Hashemzadeh[3], Majid Darroudi[5]**

[1] Applied Biomedical Research Center, Mashhad University of Medical Sciences, Mashhad, Iran
[2] Student Research Committee, Mashhad University of Medical Sciences, Mashhad, Iran
[3] Department of Medical Biotechnology and Nanotechnology, Faculty of Medicine, Mashhad University of Medical Sciences, Mashhad, Iran
[4] Department of Medical Laser, Medical Laser Research Center, Yara Institute, ACECR, Tehran, Iran
[5] Nuclear Medicine Research Center, Mashhad University of Medical Sciences, Mashhad, Iran

## ABSTRACT

***Objective(s):*** Zinc phthalocyanine (ZnPC), a potent photosensitizer for photodynamic therapy (PDT), often suffers from poor solubility and aggregation, limiting its efficacy. Metal-organic frameworks (MOFs) like MIL-101 can serve as nanocarriers to overcome these issues. This experimental study investigates the synthesis, characterization, and synergistic anticancer efficacy of ZnPC incorporated within the MIL-101 framework (ZnPC@MIL-101) against MCF-7 breast cancer cells. ZnPC was chosen for its strong red-light absorption and high reactive oxygen species (ROS) generation, while MIL-101 offers a stable, porous platform to enhance ZnPC delivery and photoactivity.

***Materials and Methods:*** ZnPC@MIL-101 (Cr) was synthesized via a double-solvent method. Characterization involved PXRD, BET analysis, FESEM, DLS, EDX spectroscopy, and UV-Vis spectroscopy. The loading capacity was determined, and singlet oxygen generation was quantified. Anticancer efficacy and PDT synergy with 660 nm laser radiation were evaluated on MCF-7 cells using MTT assays. Statistical analysis was performed using ANOVA.

***Result:*** Successful synthesis of crystalline ZnPC@MIL-101 was confirmed. The loading capacity of ZnPC was found to be 8.5%. BET analysis showed reduced surface area (1709.4 $m^2/g$) and pore size (1.71 nm) post-ZnPC loading, indicating effective incorporation. FESEM/DLS showed particle sizes around 368/439.7 nm, respectively. EDX confirmed uniform Zn distribution. The UV-Vis spectrum of ZnPC@MIL-101 displayed the characteristic Q-band of ZnPC, and the nanocomposite exhibited significant singlet oxygen generation upon laser irradiation. ZnPC@MIL-101 exhibited moderate dark toxicity ($IC_{50}$: 25 µg/mL), which was significantly enhanced upon laser irradiation ($IC_{50}$: 10 µg/mL, $p < 0.01$).

***Conclusion:*** ZnPC@MIL-101 combined with laser radiation demonstrated a significant synergistic reduction in MCF-7 cell viability. This highlights its potential as an effective PDT agent, offering a promising strategy to enhance ZnPC-based cancer treatment.

***Keywords:*** *Metal-Organic frameworks; Photosensitizing agents; Drug delivery; Nanocarrier; Cytotoxicity.*

**How to cite this article**
*Velayati M, Sabouri Z, Rezaee R, Soheilifar MH, Keshmiri Neghab H, Hashemi Ghoochani S, Hashemzadeh A, Darroudi M. Synergistic effect of zinc phthalocyanine (ZnPC)@MIL-101 framework and laser radiation on mcf-7 breast cancer cells: an experimental combination study. Nanomed J. 2026; 13(2): 296-309. DOI: 10.22038/NMJ.2026.89968.2274*

## INTRODUCTION

Photodynamic therapy (PDT) is a minimally invasive treatment that requires administering a photosensitizing agent and subsequently activating it with specific wavelength light, usually in an oxygen-rich environment [1]. Upon light irradiation, the PS generates reactive oxygen species (ROS), primarily singlet oxygen, which induce oxidative damage to cellular components, leading to cell death in targeted tissues like cancer cells [2]. Breast cancer is one of the most commonly diagnosed cancers and a leading cause of cancer-

* *Corresponding author:* Majid Darroudi, Assistant Professor, Nuclear Medicine Research Center, Mashhad University of Medical Sciences, Mashhad, Iran. E-Mail address: darroudim@mums.ac.ir.
Note. This manuscript was submitted on July 27, 2025; approved on November 26, 2025.

related mortality in women globally, necessitating the development of more effective and less toxic treatment strategies [3-6].

The unique characteristics of metal-organic frameworks (MOFs), like tunable porosity, high surface area, and biocompatibility, have made them a subject of great interest for various biomedical applications, including their use as carriers in photodynamic therapy [7, 8]. Integrating therapeutic molecules into MOFs can enhance their delivery, stability, and efficacy, making them a promising platform for cancer treatment [9, 10]. Among the numerous MOFs, MIL-101, a chromium-based MOF, has emerged as a prominent candidate for such applications because of its exceptionally large surface area, robust and stable porous structure, which makes it an ideal carrier for therapeutic agents [11, 12].

Zinc phthalocyanine (ZnPC) is a well-established second-generation photosensitizer frequently employed in PDT [13-15]. It exhibits strong absorption in the red region of the light spectrum (Q-band, typically 670-680 nm), which allows for deeper tissue penetration of activating light compared to PS absorbing at shorter wavelengths [16, 17]. Furthermore, ZnPC is known for its high ROS generation efficiency and relatively low dark toxicity [18]. However, the clinical application of free ZnPC is often hindered by its poor aqueous solubility and strong tendency to aggregate in biological environments; aggregation can quench its photoactivity and significantly reduce its therapeutic efficacy [19, 20].

To overcome these limitations, various nanocarrier systems have been developed for ZnPC. Encapsulating ZnPC within MOFs such as MIL-101 (forming ZnPC@MIL-101) is a strategy to improve its dispersibility, prevent aggregation, and maintain its monomeric, photoactive state [21-23]. The large pore volume and high surface area of MIL-101 are expected to facilitate efficient loading and stabilization of ZnPC molecules [21]. Moreover, the robust framework of MIL-101 can protect the encapsulated ZnPC from premature degradation and can enhance its accumulation at the tumor site, often through passive targeting via the Enhanced Permeability and Retention (EPR) effect common to nanosized drug delivery systems [24, 25]**.** Such integration is anticipated not only to improve the bioavailability of ZnPC but also to enhance its overall photodynamic activity [26-28]. Indeed, studies have demonstrated that MOF-based delivery systems can enhance the photodynamic activity of various photosensitizers, including porphyrins and phthalocyanines, by improving their solubility, cellular uptake, and ROS generation capabilities [23, 29-31]**.** For example, a study by Ghoochani *et al*. (10) explored Zn(II) porphyrin encapsulated in MIL-101 for the PDT of breast cancer cells, underscoring the potential of MIL-101 as a nanocarrier in this context [32]**.**

The novelty of the present study lies in the synthesis, detailed physicochemical and photophysical characterization, and in vitro evaluation of the synergistic anticancer efficacy of ZnPC specifically incorporated within the MIL-101(Cr) framework when combined with laser radiation against MCF-7 human breast cancer cells. While MOFs have been explored as drug carriers, this work provides a focused investigation into the ZnPC@MIL-101 (Cr) system, quantifying its drug loading, singlet oxygen generation, and demonstrating a statistically significant, dose-dependent synergistic phototoxic effect in a relevant breast cancer model. MCF-7 cells were chosen as a well-established and commonly used human breast adenocarcinoma cell line, representing estrogen receptor-positive breast cancer, to evaluate the potential of ZnPC@MIL-101 in a relevant cancer model [23, 25, 33-35]. This study aims to elucidate the potential of this specific nanocomposite system to improve ZnPC-mediated PDT outcomes.

## MATERIALS AND METHODS

### *Equipment and reagents*

All chemicals were sourced from Sigma and Merck Co.

### *Characterization methods*

The synthesized materials were characterized using various analytical techniques. A Fourier Transform Infrared Spectrometer (FTIR; Shimadzu-8400, Japan) was used to identify functional groups. Powder X-ray Diffraction (PXRD; Philips, Netherlands) was employed to determine the crystalline structure and phase purity of the samples. The crystallite size (D) was estimated from the PXRD data using the Scherrer equation: $D = K\lambda / (\beta \cos\theta)$, where K is the shape factor (0.9), λ is the X-ray wavelength (0.154 nm), β is the full width at half maximum (FWHM) of the diffraction peak in radians, and θ is the Bragg angle**.** The surface area and pore characteristics were analyzed using BET analysis (BELSORP Mini II, Microtrac MRB, Japan) via N2 adsorption-desorption isotherms. The morphology and particle size of the materials were observed using a FESEM (Hitachi S-4800, Japan), which was also equipped for EDX spectroscopy to determine elemental composition and distribution.

DLS (Malvern Zetasizer Nano ZS, UK) was used to measure the hydrodynamic size (Z-Average, reported as an intensity-weighted mean) and polydispersity index (PI) of the particles in suspension. UV-Visible (Shimadzu UV-2600 spectrophotometer) absorption spectra were recorded to confirm the incorporation of ZnPC.

***Preparation of MIL-101***

The synthesis of MIL-101 was initiated by combining $Cr(NO_3)_3{\cdot}9H_2O$ (4.0 g, 10.0 mmol), terephthalic acid ($C_8H_6O_4$) (1.66 g, 10.0 mmol), and deionized water (40 mL) in an autoclave. This mixture was then subjected to hydrothermal conditions by heating it to 218 ˚C for 18 h, allowing the formation of the MIL-101 framework. After the reaction, the resulting precipitates were carefully separated from the mixture [36]. These precipitates were then immersed in N, N-dimethylformamide ($C_3H_7NO$) (40 mL) and maintained at 70 °C for 8 h to facilitate the removal of any unreacted organic linkers and impurities. Subsequently, the product was washed multiple times with water, acetone ($C_3H_6O$), and methanol to ensure purity. In the end, the purified product was dried at 25 °C, resulting in the formation of MIL-101.

***Preparation of ZnPc@MIL-101(Cr)***

Synthesis of ZnPc@MIL-101(Cr) was initiated by incorporating $Zn^{2+}$ ions into the pores of MIL-101(Cr) using a double-solvent process [37]. This method involves distinct roles for each solvent: dry n-hexane serves as a non-polar medium to ensure good dispersion of the activated MIL-101(Cr) and facilitate the initial even distribution and adsorption of $ZnCl_2$ onto the framework surfaces and into the pore entrances, while ethanol is subsequently used as a polar solvent for efficiently dissolving and mixing the Zn@MIL-101(Cr) complex with phthalonitrile before the cyclization reaction in DES. Initially, activated MIL-101 (Cr, 200 mg) was added to dry n-hexane (40 mL) and stirred for 30 min. This step ensures that the MIL-101(Cr) particles are well-dispersed in the solvent, facilitating the subsequent loading of $Zn^{2+}$ ions. Subsequently, a solution of $ZnCl_2$ (0.123 mL, 1 M) was added dropwise under stirring. The dropwise addition allows for the gradual incorporation of $Zn^{2+}$ ions in the MIL-101, preventing agglomeration and ensuring uniform distribution. The mixture was continuously stirred for 3 h to allow sufficient time for the $Zn^{2+}$ ions to penetrate the pores of MIL-101 (Cr). After this period, the powder was filtered and dried at 130 °C for 12 h to remove residual solvents and stabilize the Zn@MIL-101(Cr) complex. For the synthesis of ZnPc@MIL-101(Cr), 200 mg of the dried Zn@MIL-101(Cr) was combined with 2 mL of ethanol and briefly sonicated to ensure thorough mixing [37]. Phthalonitrile (0.492 mmol) was then added to it and stirred for 60 min to facilitate the formation of the phthalocyanine complex. Following this, ethanol was removed to concentrate the reaction mixture, and 2 mL of DES (Deep Eutectic Solvent) was added to the remaining solid. The mixture was then placed at 150 °C/30 min, forming ZnPc@MIL-101(Cr), as indicated by the deep blue color of the as-prepared sample. This heating step promotes the cyclization of phthalonitrile to form the phthalocyanine ring structure, which coordinates with the $Zn^{2+}$ ions within the MIL-101(Cr) framework. The synthesized nanovehicle was subsequently dried and activated at 150 °C overnight to remove any remaining solvents and enhance the stability and activity of ZnPc@MIL-101(Cr) before cancer treatment.

***Cell culture and preparation***

In the initial stage of cell culture, MCF-7 human breast adenocarcinoma cells were obtained from the Pasteur Institute (Tehran, Iran). The cells were cultured in Dulbecco's Modified Eagle Medium (DMEM) supplemented with 10% Fetal Bovine Serum (FBS), penicillin (100 IU/mL), and streptomycin (100 µg/mL). Cultivation was carried out in a humidified incubator at 37 °C with an atmosphere of 5% $CO_2$. For subculturing and experiments, cells were detached using a 0.025% trypsin-0.02% EDTA solution and washed with phosphate-buffered saline (PBS).

***Determination of encapsulation efficiency and loading capacity***

The amount of ZnPC loaded into MIL-101 was determined by UV-Vis spectroscopy. A known amount of ZnPC@MIL-101 was dissolved in dimethylformamide (DMF) to release the encapsulated ZnPC. The concentration of ZnPC was then measured by recording the absorbance at its characteristic Q-band peak (λmax ≈ 670 nm) and comparing it to a standard calibration curve of free ZnPC in DMF. The loading capacity (LC) was calculated using the following formula:

LC (%) = (Weight of loaded ZnPC / Weight of ZnPC@MIL-101) × 100%

***Singlet oxygen generation assay***

The generation of singlet oxygen ($^1O_2$) by ZnPC@MIL-101 upon irradiation was detected chemically using 1,3-diphenylisobenzofuran (DPBF) as a probe. DPBF reacts with $^1O_2$, leading to a

decrease in its absorbance at 415 nm. In a typical experiment, a solution of ZnPC@MIL-101 and DPBF in DMF was irradiated with a 660 nm laser (2 J/cm²). The absorbance of DPBF at 415 nm was monitored at regular intervals using a UV-Vis spectrophotometer. A solution containing only DPBF was used as a negative control.

***Cell proliferation assay***

The assessment of cell proliferation was conducted utilizing the MTT assay, which measures cellular metabolic activity as an indicator of viability. MCF-7 cells were plated into 96-well plates at a density of approximately $8 \times 10^4$ cells/well and allowed to adhere for 24 h. Following this period, cells were treated with the test compounds as described for the photodynamic treatment evaluation. After the respective incubation and/or irradiation procedures, 10 µL of MTT solution (5 mg/mL) was added to each well, and the plates were incubated for an additional 4 h. Afterward, 100 µL of Dimethyl Sulfoxide was added to each well to dissolve the formazan crystals formed by metabolically active cells. The absorbance was measured at 570 nm with a reference wavelength of 630 nm using an ELISA plate reader. Cell survival rates were expressed as a percentage of the untreated control. Each experiment was performed in triplicate. $IC_{50}$ values (the concentration of compound required to inhibit cell growth by 50%) were calculated from the dose-response curves.

***Photodynamic treatment evaluation***

For photodynamic treatment evaluation, two main experimental conditions were established: (1) incubation with compounds in darkness (Dark group) and (2) incubation followed by laser exposure (Treatment group). MCF-7 breast cancer cells were incubated with varying concentrations (0-100 µg/mL) of MIL-101 or ZnPC@MIL-101 for 24 h in darkness. For the Treatment group, after the 24 h incubation and replacement of the medium with fresh medium, cells were exposed to a 660 nm diode laser (continuous wave) at an energy density of 2 J/cm². The laser power output was adjusted to deliver this energy density over the calculated exposure time. The impact on cell viability was also specifically assessed using the determined $IC_{50}$ concentrations of ZnPC@MIL-101: 25 µg/mL for the dark condition and 10 µg/mL for the laser-irradiated condition. The cellular uptake of nanoparticles was qualitatively inferred from the observed phototoxicity. The 24-hour incubation period was selected based on common protocols, allowing sufficient time for particle-cell interaction and internalization in PDT studies [38].

***Statistical analysis***

Quantitative results from cell proliferation assays are displayed as the mean ± standard deviation (SD), derived from a minimum of three separate experiments. To assess statistical significance across groups, a one-way ANOVA was employed, complemented by Tukey's post-hoc test for multiple comparisons, with a p-value below 0.05 denoting statistical significance. The $IC_{50}$ values were calculated by applying a sigmoidal curve model to the dose-response data within GraphPad Prism software.

**RESULTS**

***PXRD pattern***

The PXRD patterns depicted in Fig. 1 provide valuable insights into the crystal structure of ZnPC@MIL-101. The black line represents the simulated PXRD pattern for MIL-101. Notably, this pattern exhibits several sharp peaks, indicative of a well-defined crystalline structure. The diffraction angle (2θ) values range from 5 to 80°. The green line corresponds to the experimental PXRD pattern of ZnPC@MIL-101. Remarkably, this pattern closely aligns with the simulated MIL-101 pattern, with minor variations. This alignment suggests that ZnPC@MIL-101 retains the crystalline structure of MIL-101. The agreement between the experimental and simulated patterns supports the successful synthesis of ZnPC@MIL-101.

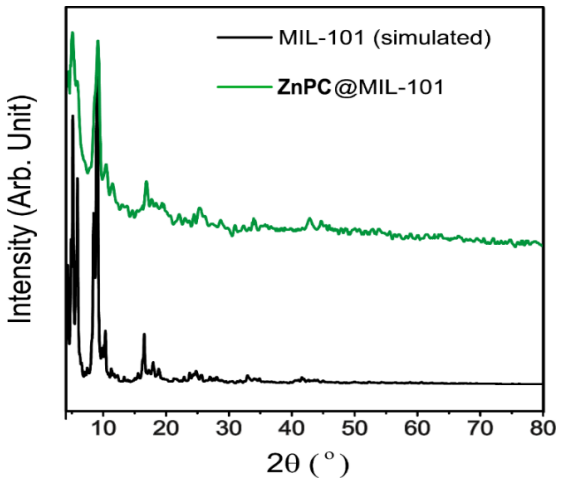


Fig. 1. PXRD pattern of ZnPC@MIL-101 vs. simulated pattern.

Furthermore, the close match between the two patterns implies phase purity, indicating that

ZnPC@MIL-101 predominantly consists of the desired crystalline phase. The major peaks are indexed with their Miller indices ((111), (220), (311), (400), (511), (531), (822), and (753)), confirming the crystalline structure of the MIL-101. The crystallite size of ZnPC@MIL-101 was determined using the Scherrer equation. The calculated crystallite size is 47.91 nm, providing valuable information about the material's nanostructure. In summary, the PXRD data confirm the successful synthesis of ZnPC@MIL-101, its phase purity, and its structural compatibility with MIL-101.

***Surface area and pore characteristics***

The BET analysis provides critical insights into the materials' surface area and pore structure. In our study, we investigated two materials: MIL-101 and ZnPC@MIL-101 (Fig. 2).

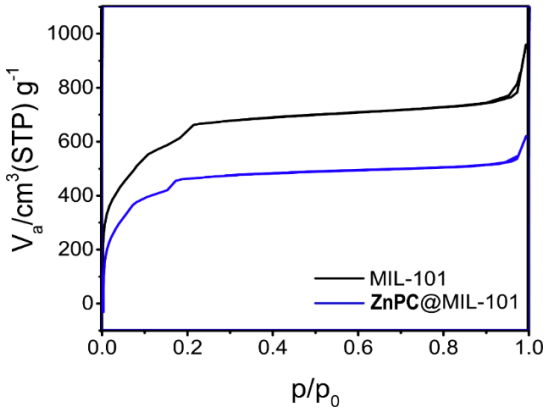


Fig. 2. BET analysis of MIL-101 and ZnPC@MIL-101.

The specific surface area, determined through N2 adsorption-desorption isotherms, revealed that MIL-101 exhibited a surface area of 2282.9 m²/g. At the same time, ZnPC@MIL-101 had a decreased surface area of 1709.4 m²/g. Notably, after loading with ZnPC, the BET surface area decreased by 573.5 m²/g. This reduction suggests that the ZnPC molecules were effectively immobilized within the pores of MIL-101, leading to a structural integration. Beyond surface area, pore size is a crucial parameter. Our results indicated a significant decrease in pore size from 2.52 nm for MIL-101 to 1.71 nm for ZnPC@MIL-101 upon ZnPC loading. This reduction in pore diameter further supports the hypothesis that ZnPC molecules penetrated the pores and became an integral part of the material's structure. Additionally, the total pore volume decreased from 1.44 cm³/g for MIL-101 to 0.94 cm³/g for ZnPC@MIL-101, representing a 35% reduction. These findings underscore the successful functionalization of ZnPC@MIL-101 and confirm the impregnation method's efficacy in introducing ZnPC into the porous framework.

***Morphology and particle size***

The FESEM images provide valuable insights into the structural characteristics of these materials (Fig. 3). The distinct morphologies impact surface area, porosity, and reactivity. In MIL-101, we observe a heterogeneous arrangement of octahedral and polyhedral crystals. These crystals exhibit well-defined edges and smooth faces, suggesting a high-quality structure. Zooming in, individual octahedral crystals with sharp vertices become apparent, contributing to the overall surface area. The minimal surface defects enhance the material's integrity. In contrast, ZnPC@MIL-101 displays polyhedral structures, albeit less well-defined than MIL-101. The surfaces appear rougher, likely due to the incorporation of ZnPC molecules. This roughness could enhance adsorption properties or catalytic activity. Closer examination reveals surface texture differences, indicating successful integration of ZnPC into the MIL-101 framework. The FESEM images (Fig. 3c, d) suggest a generally uniform contribution of MIL-101 as the structural base with ZnPC influencing the surface texture rather than forming distinct, separate agglomerates. This is further supported by EDX elemental mapping (Fig. 6a, b), which shows a diffuse, widespread distribution of zinc, indicating that ZnPC is incorporated throughout the MIL-101 matrix rather than existing as large, separate clusters. This homogenous incorporation is beneficial for consistent photodynamic activity throughout the nanoparticle. Similar morphological analyses confirming MOF integrity after photosensitizer loading have been documented for ZIF-8 frameworks used in PDT [39].

The particle size distribution obtained from FESEM analysis of MIL-101 shows a peak frequency within the range of approximately 200–400 nm (mean size 395.50 nm) (Fig. 4). This suggests that MIL-101 primarily consists of particles falling within this size range. Similarly, the particle size distribution for ZnPC@MIL-101 exhibits a peak frequency in the same 200–400 nm range. However, compared to MIL-101, ZnPC@MIL-101 has a narrower distribution, with a mean particle size of 368.07 nm. The observed decrease in mean particle size for ZnPC@MIL-101 suggests that the encapsulation or combination process involved in creating ZnPC@MIL-101 may influence the final particle dimensions compared to MIL-101 alone.

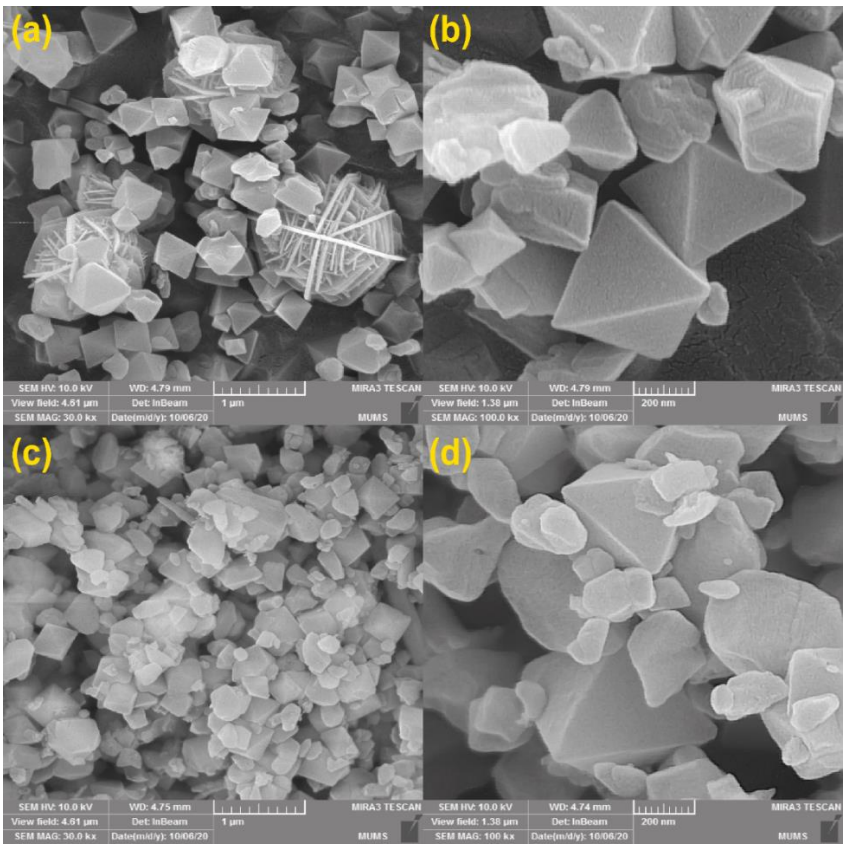


Fig. 3. FESEM of MIL-101 (a, b) and ZnPC@MIL-101 (c, d). Image (a) shows larger octahedral crystals of MIL-101, while (b) is a magnified view showing well-defined crystal faces. Image (c) depicts the polyhedral structure of ZnPC@MIL-101 with a rougher surface, and (d) offers a closer look at this altered morphology due to ZnPC incorporation.

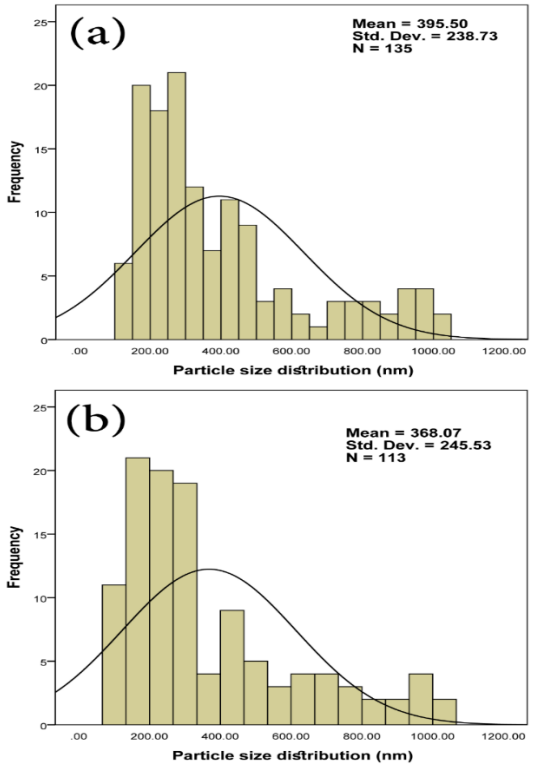


Fig. 4. Particle size distribution histograms obtained from FESEM images of MIL-101 (a) and ZnPC@MIL-101 (b).

Understanding the difference between hydrodynamic and solid phase sizes is crucial for interpreting Dynamic Light Scattering (DLS) data. The hydrodynamic size provides insight into how the particles will behave in a fluid environment, which is essential for applications where the particles are used in solution. On the other hand, the solid phase size gives information about the intrinsic properties of the particles themselves. ZnPC@Mil-101, where ZnPC is integrated with the MIL-101, has shown a pronounced peak in the DLS measurement (intensity-weighted distribution), signifying that most particles cluster around a specific diameter. The Z-Average (mean diameter) is precisely 439.7 nm (Fig. 5). Additionally, the Polydispersity Index (PI) stands at 0.491, indicating a relatively narrow size distribution within the sample. The hydrodynamic size is typically more prominent than the solid phase size due to the solvent layer and interactions in the fluid medium. The EDX analysis confirms the presence of carbon, nitrogen, oxygen, and zinc in ZnPC@MIL-101 (Fig. 6). Interestingly, the 3D distribution of zinc shows scattered bright specks throughout the material. Rather than forming large clusters, zinc is uniformly distributed in small quantities. This uniform elemental distribution, evident from EDX, complements the FESEM observations by suggesting homogenous incorporation of ZnPC throughout the MIL-101 framework rather than surface deposition or isolated clustering, which is beneficial for predictable drug loading and release characteristics. The BET and EDX data strongly suggest successful incorporation. Future work should quantify this encapsulation efficiency for a more complete assessment.

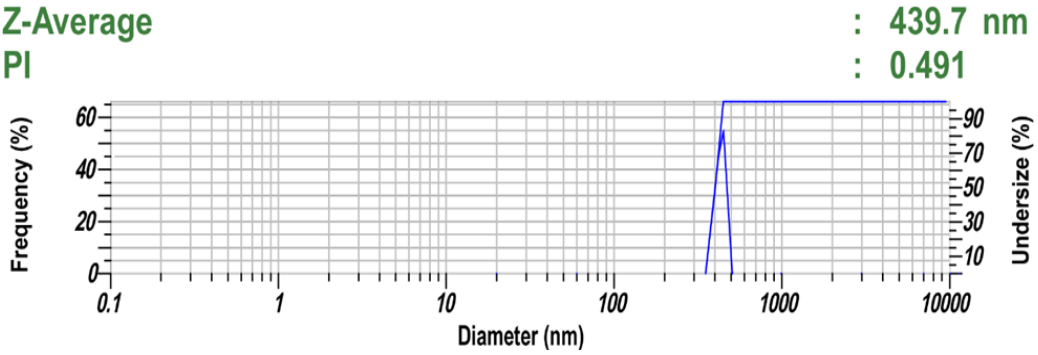


Fig. 5. DLS of ZnPC@MIL-101.

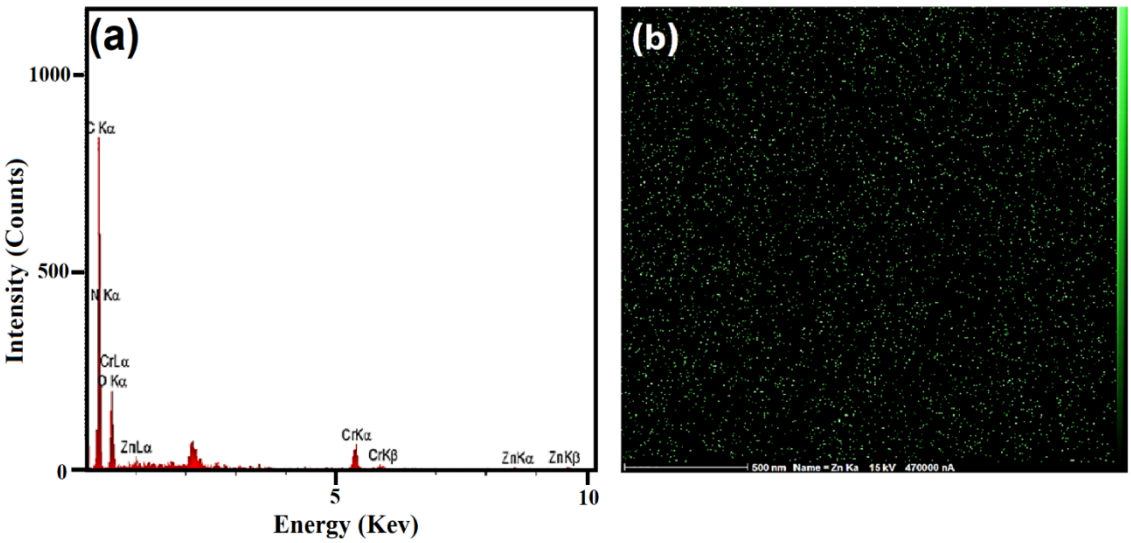


Fig. 6. The EDX analysis (a) spectrum of ZnPC@MIL-101 confirming elemental composition, and (b) elemental mapping showing the 3D distribution of Zinc in the sample.

***Photophysical properties and ROS generation***

The UV-Vis absorption spectra of Free ZnPC in DMF exhibit a sharp and intense Q-band absorption peak at approximately 670 nm, which is characteristic of its monomeric form. The spectrum of ZnPC@MIL-101 dispersed in DMF also shows this characteristic Q-band, confirming that ZnPC was successfully incorporated into the MIL-101 framework and retains its essential photophysical properties. The slight broadening of the peak in the nanocomposite suggests some interaction with the MOF structure, but critically, the absence of significant new peaks indicates that aggregation of ZnPC has been effectively prevented.

The ability of ZnPC@MIL-101 to generate singlet oxygen, the primary cytotoxic agent in PDT, was evaluated using DPBF as a chemical trap. The absorbance of DPBF at 415 nm decreased rapidly over time when mixed with ZnPC@MIL-101 and exposed to 660 nm laser light. In contrast, the control group containing only DPBF showed a negligible decrease in absorbance under the same irradiation conditions. This result clearly demonstrates that ZnPC@MIL-101 is highly effective at generating singlet oxygen upon light activation, a prerequisite for a successful PDT agent.

***Encapsulation efficiency and loading capacity***

The encapsulation of ZnPC within the MIL-101 framework was quantified using UV-Vis spectroscopy. Based on the standard calibration curve for ZnPC, the loading capacity was calculated to be 8.5%. This indicates a successful loading of the photosensitizer into the MOF nanocarrier, which is consistent with the changes observed in the BET analysis.

***Cellular studies***

The viability of MCF-7 cells after treatment with MIL-101 alone, both in dark conditions and with laser irradiation, is presented in Fig. 7. In the dark, MIL-101 exhibited a dose-dependent reduction in cell viability, with approximately 50% viability observed at 100 µg/mL. Laser irradiation (660 nm, 2 J/cm²) alone (0 µg/mL MIL-101, red bar) showed minimal effect on cell viability, which remained near 100%. When MIL-101 was combined with laser radiation, a further decrease in cell viability was observed at higher concentrations compared to MIL-101 in the dark, although this enhancement was not substantial across all concentrations.

Fig. 8 shows the effect of ZnPC@MIL-101 on MCF-7 cell viability. In dark conditions (striped bars), ZnPC@MIL-101 caused a dose-dependent decrease in cell viability, with an $IC_{50}$ value determined to be 25 µg/mL. Upon laser irradiation (red bars), the cytotoxic effect of ZnPC@MIL-101 was significantly enhanced, resulting in a lower $IC_{50}$ value of 10 µg/mL. This more than two-fold decrease in $IC_{50}$ was statistically significant ($p < 0.01$). This indicates a synergistic effect between the ZnPC@MIL-101 nanocomposite and laser activation, leading to a more pronounced reduction in cancer cell viability compared to the nanocomposite alone or MIL-101 with laser irradiation.

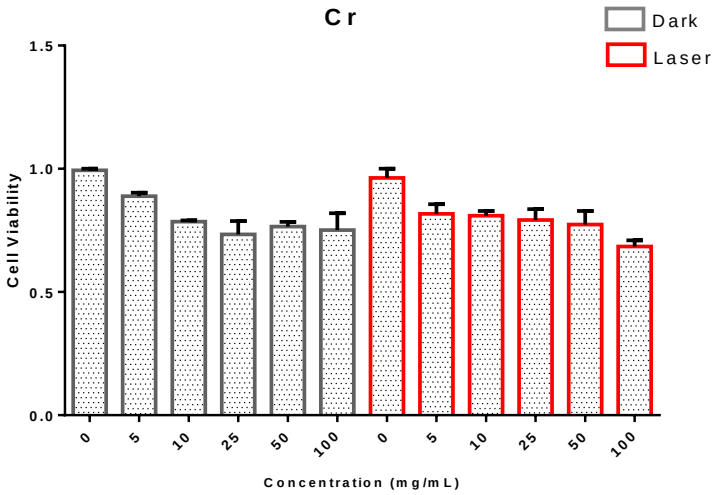


Fig. 7. The effect of different concentrations of MIL-101 on breast cancer MCF-7 cells after 24 h of incubation in the dark and then low-power laser radiation with a wavelength of 660 nm and an energy density of 2 J/cm². Data are presented as mean ± SD (n=3). $p < 0.01$ compared to the corresponding dark group.

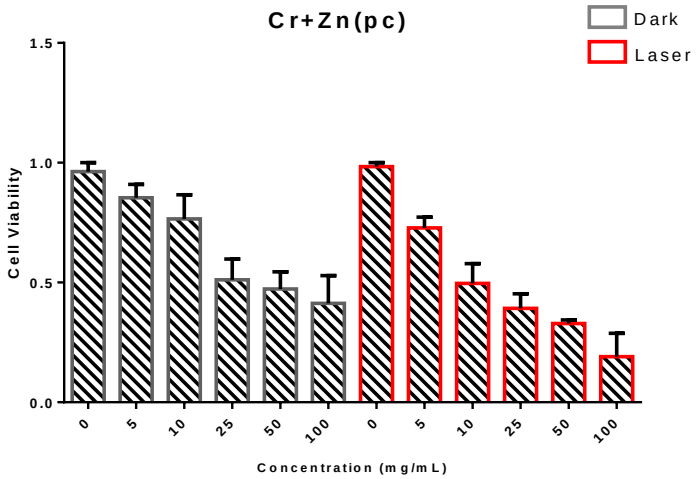


Fig. 8. The effect of different concentrations of ZnPC@MIL-101 combination on breast cancer MCF-7 cells after 24 h of incubation in the dark and then low-power laser irradiation with a wavelength of 660 nm and an energy density of 2 J/cm$^2$. Data are presented as mean ± SD (n=3). $p < 0.01$ compared to the corresponding dark group.

**DISCUSSION**

The successful development of a nanocarrier-based PDT agent relies on a thorough characterization of its physicochemical properties to ensure it can effectively deliver the photosensitizer and elicit a phototoxic response. In this study, we employed a suite of analytical techniques to validate the synthesis and properties of ZnPC@MIL-101. PXRD (Fig. 1) was essential to confirm that the crystalline structure of the MIL-101 framework was preserved after the incorporation of ZnPC, which is crucial for maintaining the stability and porous nature of the carrier. The BET analysis (Fig. 2) provided quantitative evidence of ZnPC loading by showing a significant reduction in surface area and pore volume, confirming that the photosensitizer molecules occupy the internal voids of the MOF. FESEM and DLS (Figs. 3-5) were used to determine the morphology and size distribution of the nanoparticles, which are critical parameters for their biological interactions and potential for passive tumor targeting via the EPR effect. Finally, EDX analysis (Fig. 6) confirmed the elemental composition and, importantly, the uniform distribution of zinc throughout the nanoparticles, suggesting a homogeneous loading of ZnPC rather than simple surface adsorption. Together, these characterizations provide a comprehensive picture of the ZnPC@MIL-101 nanocomposite and form the basis for interpreting its biological activity.

The primary goal of this research was to investigate the potential of a ZnPC@MIL-101 nanocomposite as an effective agent for the photodynamic therapy of MCF-7 breast cancer cells. ZnPC is a well-regarded photosensitizer due to its strong absorption in the 600-700 nm range (its Q-band) [40, 41], which aligns well with the 660 nm laser used in this study and allows for reasonable tissue penetration for PDT applications [42-46]. The photodynamic action of ZnPC is primarily mediated through the generation of singlet oxygen and other ROS upon light activation, leading to oxidative damage of cellular components and subsequent cell death, often via apoptosis or necrosis [18, 47]. While ZnPC can interact with cellular macromolecules like DNA [48] and proteins such as albumin (which influences its in vivo transport) [35, 49, 50]. Its therapeutic effect in PDT stems mainly from this ROS-mediated damage rather than specific molecular target binding in the manner of classical enzyme inhibitors or DNA intercalators.

A significant challenge with free ZnPC is its hydrophobicity and tendency to aggregate in aqueous physiological environments, which quenches its photoactivity [20, 51]. Nanocarriers like MOFs are employed to address these issues by improving solubility, preventing aggregation, and facilitating delivery [52-54]. MIL-101, with its high surface area and robust porous structure, is a suitable candidate [55]. Our synthesis of ZnPC@MIL-101, confirmed by PXRD retaining the MIL-101 crystallinity (Fig. 1), and the observed decrease in BET surface area and pore volume (Fig. 2), strongly suggests successful incorporation of ZnPC within the MOF framework. This encapsulation is crucial for maintaining ZnPC in a

monomeric, photoactive state, which is essential for efficient singlet oxygen generation [22, 23]. The FESEM and EDX analyses (Fig. 3, 6) further supported the formation of the nanocomposite with a fairly uniform distribution of Zn, indicating homogenous ZnPC loading rather than mere surface adsorption. This consistent distribution is vital for predictable photodynamic performance. Such loading has been shown in other MOF-PS systems to enhance PDT efficacy [39].

The cellular studies demonstrated a clear synergistic effect when ZnPC@MIL-101 was combined with laser irradiation (Fig. 8). The $IC_{50}$ value for ZnPC@MIL-101 decreased from 25 µg/mL in the dark to 10 µg/mL upon laser activation. This enhanced phototoxicity is attributed to the efficient ROS generation by the MOF-encapsulated ZnPC. In contrast, while MIL-101 itself showed some dark cytotoxicity at higher concentrations (Fig. 7, $IC_{50}$ > 100 µg/mL in dark), its combination with laser did not yield a comparable photodynamic enhancement, underscoring the critical role of ZnPC as the photosensitizer. It is noteworthy that MIL-101 in the dark at 100 µg/mL reduced cell viability to ~50%, whereas laser irradiation alone had a negligible effect. This inherent cytotoxicity of the MOF material at high concentrations must be considered when evaluating the net photodynamic effect. Such baseline toxicity of carrier materials is a known factor in nanomedicine. Comparing our findings with the literature, Ghoochani *et al*. [32] reported $IC_{50}$ values of 14.3 µg/mL (light) and 81.6 µg/mL (dark) for Zn[TPP]@MIL-101 on MCF-7 cells. Our ZnPC@MIL-101 showed a dark $IC_{50}$ of 25 µg/mL and a light $IC_{50}$ of 10 µg/mL. The differences can be attributed to the type of photosensitizer (ZnPC vs. Zn [TPP]), loading efficiencies (our study found an 8.5% loading capacity), and potentially minor variations in experimental conditions. However, both studies highlight the utility of MIL-101 in enhancing the photodynamic effect of entrapped photosensitizers. Other studies employing ZnPC in different nanoformulations for MCF-7 cells have also reported significant PDT efficacy [34, 56-60], generally involving apoptotic cell death pathways triggered by caspase activation and mitochondrial dysfunction [57, 61, 62]. While the specific signaling pathways were not delineated here, such mechanisms are likely operative in the cell death observed with ZnPC@MIL-101-PDT. The results indicate that ZnPC@MIL-101 is a promising system for PDT. The MIL-101 framework likely improves ZnPC's dispersibility and prevents aggregation, thereby enhancing ROS generation upon irradiation. The observed synergistic effect confirms that the photodynamic action is the dominant mechanism for the enhanced cytotoxicity under laser light.

***Potential Applications and Future Directions***

The strengths of this study include the successful synthesis and thorough characterization of a ZnPC@MIL-101 nanocomposite and the demonstration of its synergistic photodynamic effect on MCF-7 breast cancer cells in vitro. The use of the well-established MIL-101 framework offers a stable and porous platform for ZnPC delivery, enhancing its photophysical properties by reducing aggregation, as confirmed by UV-Vis spectroscopy and singlet oxygen detection. The successful synthesis and characterization of ZnPC@MIL-101 and its demonstrated anticancer efficacy open up several potential applications and avenues for future research. The composite material's structural stability, high surface area, and effective photodynamic activity make it fit for biomedical applications comprising drug delivery and imaging. Further studies could explore optimizing ZnPC loading, quantifying encapsulation efficiency, and tuning the release kinetics. Assessment of ROS and singlet oxygen generation dosimetry, as well as photobleaching rates under therapeutic irradiation, would be essential for refining PDT protocols [16, 63]. Investigation into the cellular uptake mechanisms and quantification would also provide valuable insights. Additionally, the uniform distribution of ZnPC within the MIL-101 framework suggests that the composite could be used in other therapeutic contexts, such as antimicrobial treatments or environmental applications where photocatalytic activity is desired. Modifying the MIL-101 framework to incorporate different photosensitizers or functional molecules could further expand the material's versatility and range of applications. Furthermore, molecular modeling or simulation approaches, such as Density Functional Theory (DFT), as reported for other Zn-phthalocyanine systems [64], could be employed in future studies to theoretically investigate the electronic properties of ZnPC@MIL-101 and to better understand the interactions between the photosensitizer and the MOF framework, potentially guiding the design of even more effective PDT agents.

However, the study has several limitations. While we have now included foundational photophysical data, a more comprehensive photophysical characterization, including quantitative ROS/singlet oxygen dosimetry (crucial for understanding PDT efficiency) and

photobleaching rate determination (important for assessing sustained activity), was not performed. Cellular uptake was inferred from phototoxicity rather than directly quantified (e.g., by ICP-MS for zinc content or fluorescence microscopy of ZnPC). Additionally, the study was limited to a single breast cancer cell line (MCF-7) and did not explore the effects on normal, non-cancerous cells (to assess selectivity and potential for minimal side effects) or employ more complex in vitro models (e.g., 3D spheroids) or in vivo studies. These latter investigations are necessary to evaluate systemic toxicity, biodistribution, and true therapeutic potential in a more physiologically relevant context. These aspects were not explored in the current work primarily due to budgetary constraints and limitations in the available experimental setup.

## CONCLUSION

In conclusion, this study successfully synthesized and characterized ZnPC@MIL-101, demonstrating its potential as an effective agent for photodynamic therapy against MCF-7 breast cancer cells. The structural and photophysical characterization confirmed the successful integration of ZnPC into the MIL-101 framework, with consequent impacts on the material's surface area, pore size, and morphology, suggestive of efficient photosensitizer loading. The cellular studies highlighted the statistically significant synergistic effect of ZnPC@MIL-101 and laser radiation in reducing the viability of MCF-7 cells, showcasing the composite's potential for targeted cancer treatment via PDT. These findings pave the way for further exploration of ZnPC@MIL-101 in various biomedical applications, highlighting the material's versatility and promising therapeutic potential, provided the acknowledged limitations are addressed in future research.

## FUNDING

This research received no specific grant from any funding agency in the public, commercial, or not-for-profit sectors.

## ETHICAL APPROVAL

For this type of study, ethical approval was not required.

## CONFLICTS OF INTEREST

The authors have declared no conflict of interest.

## CONSENT TO PARTICIPATE

Not applicable.

## CONSENT FOR PUBLICATION

Not applicable.

## AVAILABILITY OF DATA AND MATERIAL

Not applicable.

## AUTHOR CONTRIBUTIONS

**M. V:** Data curation, Formal analysis, Investigation, Methodology, Software, and Writing an original draft. **Z.S:** Data curation, Formal analysis, Investigation, Methodology, Software, and Writing-Review & Editing. **R.R:** Data curation, Formal analysis, Investigation, Software, and Writing-Review & Editing. **M.S.:** Data curation and Formal analysis. **H.N:** Data curation and Formal analysis. **S.H.G:** Data curation, Formal analysis, and Writing-Review & Editing. **A.H:** Data curation, Formal analysis, and Writing-Review & Editing. **M.D:** Supervision, Project administration, and Writing-Review & Editing.

## REFERENCES

1. Correia JH, Rodrigues JA, Pimenta S, Dong T, Yang Z. Photodynamic Therapy Review: Principles, Photosensitizers, Applications, and Future Directions. Pharmaceutics. 2021;13(9):1332.
2. Dougherty TJ, Gomer CJ, Henderson BW, Jori G, Kessel D, Korbelik M, et al. Photodynamic therapy. J Natl Cancer Inst. 1998;90(12):889-905.
3. Tunç T, Karakuş G, Sümer Z. Investigation of Cytotoxic and Antimicrobial Effects of Polyanhydride-Based Poly[(maleic anhydride)-co-(vinyl Acetate)] Conjugates Combined with Methotrexate and Gemcitabine in Breast Cancer Treatment. ACS Omega. 2025;10(12):12152-12162.
4. Khan SY, Bah T, Layeequr Rahman R. The Role of Molecular Profiling in De-Escalation of Toxic Therapy in Breast Cancer. Int J Mol Sci. 2025;26(3):1332.
5. Fakudze N, Abrahamse H, George B. Nanoparticles improved pheophorbide-a mediated photodynamic therapy for cancer. Lasers Med Sci. 2025;40(1): 1-8.
6. Erdemir GY, Kuruçay A, Ates B, Altundas A. Development of 1,2,3-Triazolopyridazinone Derivatives as Potential Caspase 3 and Apoptosis Inducers: Design, Synthesis and Anticancer Activity Studies. J Biochem Mol Toxicol. 2025;39(3):e70216.
7. Khosrojerdi S, Gholami L, Khazaei M, Hashemzadeh A, Darroudi M, Oskuee RK. Synthesis and evaluation of gene delivery vectors based on PEI-modified metal-organic framework (MOF) nanoparticles. Iran J Basic Med Sci. 2024;27(2):203.
8. Hashemzadeh A, Drummen GP, Avan A, Darroudi M, Khazaei M, Khajavian R, et al. When metal–organic framework–mediated smart drug delivery meets gastrointestinal cancers. J Mater Chem B 2021;9(19):3967-3982.
9. Xue Z, Zhu M, Dong Y, Feng T, Chen Z, Feng Y, et al. An integrated targeting drug delivery system based

on the hybridization of graphdiyne and MOFs for visualized cancer therapy. Nanoscale. 2019;11(24):11709-11718.
10. Li B, Ashrafizadeh M, Jiao T. Biomedical application of metal-organic frameworks (MOFs) in cancer therapy: Stimuli-responsive and biomimetic nanocomposites in targeted delivery, phototherapy and diagnosis. Int J Biol Macromol. 2024; 260:129391.
11. Shaabani A, Sepahvand H, Amini MM, Hashemzadeh A, Boroujeni MB, Badali E. Tandem oxidative isocyanide-based cycloaddition reactions in the presence of MIL-101 (Cr) as a reusable solid catalyst. Tetrahedron. 2018;74(15):1832-1837.
12. Boroujeni MB, Hashemzadeh A, Faroughi M-T, Shaabani A, Amini MM. Magnetic MIL-101-SO 3 H: a highly efficient bifunctional nanocatalyst for the synthesis of 1, 3, 5-triarylbenzenes and 2, 4, 6-triaryl pyridines. RSC advances. 2016;6(102):100195-100202.
13. Kocaağa N, Türkkol A, Bilgin MD, Erdoğmuş A. The synthesis of novel water-soluble zinc (II) phthalocyanine based photosensitizers and exploring of photodynamic therapy activities on the PC3 cancer cell line. Photochem Photobiol Sci. 2023;22(9):2037-2053.
14. Halkiotis KN, Uzunoglu NK, Loukas S, Pantelias GE, Trafalis D, Yova D, editors. Influence of drug and light dose in determining PDT efficacy in human pancreatic cancer cells, treated with zinc tetrasulfonated phthalocyanines (ZnTSPc). Proc SPIE-Int Soc Opt Eng. 1997;3191:243-252.
15. Feuser PE, Cordeiro AP, de Bem Silveira G, Borges Corrêa MEA, Lock Silveira PC, Sayer C, et al. Co-encapsulation of sodium diethyldithiocarbamate (DETC) and zinc phthalocyanine (ZnPc) in liposomes promotes increases phototoxic activity against (MDA-MB 231) human breast cancer cells. Colloids Surf B. 2021;197:111434.
16. Wysocki M, Ziental D, Biyiklioglu Z, Jozkowiak M, Baş H, Dlugaszewska J, et al. Non-peripheral octasubstituted zinc(II) phthalocyanines bearing pyridinepropoxy substituents – Antibacterial, anticancer photodynamic and sonodynamic activity. J Inorg Biochem. 2025;262:112751.
17. Demirbaş Ü, Pişkin M, Durmuş M, Kantekin H. Metal or metal-free phthalocyanines containing morpholine substituents: synthesis, spectroscopic and photophysicochemical properties. J Coord Chem. 2022;75(9-10):1243-1255.
18. Roguin LP, Chiarante N, García Vior MC, Marino J. Zinc(II) phthalocyanines as photosensitizers for antitumor photodynamic therapy. Int J Biochem Cell Biol. 2019;114:105575.
19. Nash GT, Luo T, Lan G, Ni K, Kaufmann M, Lin W. Nanoscale Metal-Organic Layer Isolates Phthalocyanines for Efficient Mitochondria-Targeted Photodynamic Therapy. J Am Chem Soc. 2021;143(5):2194-2199.
20. Yang Z, Li P, Chen Y, Dong E, Feng Z, He Z, et al. Preparation of zinc phthalocyanine-loaded amphiphilic phosphonium chitosan nanomicelles for enhancement of photodynamic therapy efficacy. Colloids Surf B. 2021;202:111693.
21. Kong J, Cai M, Zhu R, Zhang Y, Du Y, Jing X, et al. The utilization of metal-organic frameworks in tumor-targeted drug delivery systems. J Sci: Adv Mater Devices. 2024;9(3):100770.
22. Luo T, Nash GT, Xu Z, Jiang X, Liu J, Lin W. Nanoscale Metal-Organic Framework Confines Zinc-Phthalocyanine Photosensitizers for Enhanced Photodynamic Therapy. J Am Chem Soc. 2021;143(34):13519-13524.
23. Liu J, Kang DW, Fan Y, Nash GT, Jiang X, Weichselbaum RR, et al. Nanoscale Covalent Organic Framework with Staggered Stacking of Phthalocyanines for Mitochondria-Targeted Photodynamic Therapy. J Am Chem Soc. 2024;146(1):849-857.
24. Mhettar P, Kale N, Pantwalawalkar J, Nangare S, Jadhav N. Metal-organic frameworks: Drug delivery applications and future prospects. Admet dmpk. 2024;12(1):27-62.
25. Li D, Cai S, Wang P, Cheng H, Cheng B, Zhang Y, et al. Innovative Design Strategies Advance Biomedical Applications of Phthalocyanines. Adv Healthc Mater. 2023;12(22):2300263.
26. Ye Y, Zhao Y, Sun Y, Cao J. Recent Progress of Metal-Organic Framework-Based Photodynamic Therapy for Cancer Treatment. Int J Nanomedicine. 2022;17:2367-2395.
27. Zhao W, Wang L, Zhang M, Liu Z, Wu C, Pan X, et al. Photodynamic therapy for cancer: mechanisms, photosensitizers, nanocarriers, and clinical studies. MedComm. 2024;5(7):e603.
28. Li M, Zhang Z, Yu Y, Yuan H, Nezamzadeh-Ejhieh A, Liu J, et al. Recent advances in Zn-MOFs and their derivatives for cancer therapeutic applications. Mater Adv. 2023;4(21):5050-5093.
29. Zhong YT, Cen Y, Xu L, Li SY, Cheng H. Recent Progress in Carrier-Free Nanomedicine for Tumor Phototherapy. Adv Healthc Mater. 2023;12(4):2202307.
30. Sun J, Zhang X, Zhang D, Chen YP, Wang F, Li L, et al. Building Block Symmetry Relegation Induces Mesopore and Abundant Open-Metal Sites in Metal-Organic Frameworks for Cancer Therapy. CCS Chem. 2022;4(3):996-1006.
31. Kalhori F, Yazdyani H, Khademorezaeian F, Hamzkanloo N, Mokaberi P, Hosseini S, et al. Enzyme activity inhibition properties of new cellulose nanocrystals from Citrus medica L. pericarp: A perspective of cholesterol lowering. Luminescence. 2022;37(11):1836-1845.
32. Ghoochani SH, Hosseini HA, Sabouri Z, Soheilifar MH, Neghab HK, Hashemzadeh A, et al. Zn(II) porphyrin–encapsulated MIL-101 for photodynamic therapy of breast cancer cells. Lasers Med Sci. 2023;38(1):151.
33. Chota A, Abrahamse H, George BP. Green synthesis and characterization of AgNPs, liposomal loaded AgNPs, and ZnPcS4 photosensitizer for enhanced photodynamic therapy effects in MCF-7 breast

cancer cells. Photodiagn Photodyn Ther. 2024;48:104252.
34. Chota A, Abrahamse H, George BP. Chemotoxic and phototoxic effects of liposomal co-delivery of green synthesized silver nanoparticles and ZnPcS4 for enhanced photodynamic therapy in MCF-7 breast cancer cells: An in vitro study. Biomed Pharmacother. 2025;185:117986.
35. Larroque C, Pelegrin A, Van Lier JE. Serum albumin as a vehicle for zinc phthalocyanine: Photodynamic activities in solid tumour models. BR J CANCER. 1996;74(12):1886-1890.
36. Hashemzadeh A, Amini MM, Tayebee R, Sadeghian A, Durndell LJ, Isaacs MA, et al. A magnetically-separable $H_3PW_{12}O_{40}$@ $Fe_3O_4$/EN-MIL-101 catalyst for the one-pot solventless synthesis of 2H-indazolo [2, 1-b] phthalazine-triones. Mol Catal. 2017;440:96-106.
37. Yeganeh AD, Amini MM, Safari N. In situ synthesis and encapsulation of copper phthalocyanine into MIL-101 (Cr) and MIL-100 (Fe) pores and investigation of their catalytic performance in the epoxidation of styrene. J Porphyrins Phthalocyanines. 2019;23(10):1118-1131.
38. Manoto SL, Houreld N, Hodgkinson N, Abrahamse H. Modes of Cell Death Induced by Photodynamic Therapy Using Zinc Phthalocyanine in Lung Cancer Cells Grown as a Monolayer and Three-Dimensional Multicellular Spheroids. Molecules. 2017;22(5):791.
39. Xu D, You Y, Zeng F, Wang Y, Liang C, Feng H, et al. Disassembly of Hydrophobic Photosensitizer by Biodegradable Zeolitic Imidazolate Framework-8 for Photodynamic Cancer Therapy. ACS Appl Mater Interfaces. 2018;10(18):15517-15523.
40. Ben-Hur E, Chan WS. Phthalocyanines in Photobiology and Their Medical Applications. The Porphyrin Handbook: Multporphyrins, Multiphthalocyanines and Arrays. 2012;19:1-35.
41. Ramya E, Momen N, Desai N. Preparation of Multiwall Carbon Nanotubes with Zinc Phthalocyanine Hybrid Materials and Their Nonlinear Optical (NLO) Properties. J Nanosci Nanotechnol. 2018;18:4764-4770.
42. Pişkin M. The novel 2,6-dimethoxyphenoxy substituted phthalocyanine dyes having high singlet oxygen quantum yields. Polyhedron. 2016;104:17-24.
43. Guo S, Gu D, Yang Y, Tian J, Chen X. Near-infrared photodynamic and photothermal co-therapy based on organic small molecular dyes. J Nanobiotechnol. 2023;21(1):348.
44. Tu J, Wang T, Shi W, Wu G, Tian X, Wang Y, et al. Multifunctional ZnPc-loaded mesoporous silica nanoparticles for enhancement of photodynamic therapy efficacy by endolysosomal escape. Biomaterials. 2012;33:7903-7914.
45. Borzęcka W, Domiński A, Kowalczuk M. Recent Progress in Phthalocyanine-Polymeric Nanoparticle Delivery Systems for Cancer Photodynamic Therapy. Nanomaterials. 2021;11(9):2426.
46. Zhou Z, Song J, Nie L, Chen X. Reactive oxygen species generating systems meeting challenges of photodynamic cancer therapy. Chem Soc Rev. 2016;45(23):6597-6626.
47. Roguin LP, Chiarante N, García Vior MC, Marino J. Zinc(II) phthalocyanines as photosensitizers for antitumor photodynamic therapy. Int J Biochem Cell Biol. 2019;114:105575.
48. Yan S, Guo H, Su J, Chen J, Song X, Huang M, et al. Effects of hydroxyl radicals produced by a zinc phthalocyanine photosensitizer on tumor DNA. Dyes Pigm. 2020;173:107894.
49. Çakir V, Çakir D, Pişkin M, Durmuş M, Biyiklioğlu Z. Water soluble peripheral and non-peripheral tetrasubstituted zinc phthalocyanines: Synthesis, photochemistry and bovine serum albumin binding behavior. J Lumin. 2014;154:274-284.
50. Li R, Zheng K, Hu P, Chen Z, Zhou S, Chen J, et al. A novel tumor targeting drug carrier for optical imaging and therapy. Theranostics. 2014;4(6):642-659.
51. Obata M, Ishihara E, Hirohara S. Effect of tertiary amino groups in the hydrophobic segment of an amphiphilic block copolymer on zinc phthalocyanine encapsulation and photodynamic activity. RSC Adv. 2022;12(28):18144-18153.
52. Zha Z, Miao Y, Huiling T, Herrera-Balandrano D, Yin H, Wang S. Heparosan-based self-assembled nanocarrier for zinc(II) phthalocyanine for use in photodynamic cancer therapy. Int J Biol Macromol. 2022;219:31-43
53. Tong L, Zhang S, Huang R, Yi H, Wang J-W. Extracellular vesicles as a novel photosensitive drug delivery system for enhanced photodynamic therapy. Front Bioeng Biotechnol. 2022;10:1032318.
54. Udrea AM, Smarandache A, Dinache A, Mares C, Nistorescu S, Avram S, et al. Photosensitizers-Loaded Nanocarriers for Enhancement of Photodynamic Therapy in Melanoma Treatment. Pharmaceutics. 2023;15(8):2124.
55. Shaabani A, Mohammadian R, Hashemzadeh A, Afshari R, Amini MM. Amine-functionalized MIL-101 (Cr) embedded with Co (ii) phthalocyanine as a durable catalyst for one-pot tandem oxidative A 3 coupling reactions of alcohols. New J Chem. 2018;42(6):4167-4174.
56. Mantareva V, Iliev I, Sulikovska I, Durmuş M, Angelov I. Cobalamin (Vitamin B12) in Anticancer Photodynamic Therapy with Zn(II) Phthalocyanines. Int J Mol Sci. 2023;24(5): 4400.
57. Ma C, Wang Y, Chen W, Hou T, Zhang H, Zhang H, et al. Caspase-1 Regulates the Apoptosis and Pyroptosis Induced by Phthalocyanine Zinc-Mediated Photodynamic Therapy in Breast Cancer MCF-7 Cells. Molecules. 2023;28(16): 5934.
58. Ahmetali E, Sen P, Süer NC, Nyokong T, Eren T, Şener MK. Photodynamic therapy activities of phthalocyanine-based macromolecular photosensitizers on MCF-7 breast cancer cells. J Macromol Sci Part A Pure Appl Chem. 2021;58(11):748-757.
59. Yan S, Dong L, Hu Z, Zhang Y, Xu W, Xing J, et al. A Photosensitizer-Loaded Polydopamine Nanomedicine Agent for Synergistic Photodynamic

and Photothermal Therapy. Molecules. 2023;28(15): 5874.
60. Oshiro-Junior JA, Sato MR, Boni FI, Santos KLM, de Oliveira KT, de Freitas LM, et al. Phthalocyanine-loaded nanostructured lipid carriers functionalized with folic acid for photodynamic therapy. Mater Sci Eng C. 2020;108:110462.
61. Mfouo-Tynga I, Houreld NN, Abrahamse H. Induced cell death pathway post photodynamic therapy using a metallophthalocyanine photosensitizer in breast cancer cells. Photomed Laser Surg. 2014;32(4):205-211.
62. Valli F, García Vior MC, Roguin LP, Marino J. Crosstalk between oxidative stress-induced apoptotic and autophagic signaling pathways in Zn(II) phthalocyanine photodynamic therapy of melanoma. Free Radic Biol Med. 2020;152:743-754.
63. Malek-Esfandiari Z, Rezvani-Noghani A, Sohrabi T, Mokaberi P, Amiri-Tehranizadeh Z, Chamani J. Molecular dynamics and multi-spectroscopic of the interaction behavior between bladder cancer cells and calf thymus DNA with rebeccamycin: apoptosis through the down regulation of PI3K/AKT signaling pathway. J Fluoresc. 2023;33(4):1537-1557.
64. Aydogdu S, Yasa Atmaca G, Erdoğmuş A, Hatipoglu A. Synthesis of a new Zn-phthalocyanine, photophysical, photochemical, and sono-photochemical properties and DFT studies. Polyhedron. 2024;256:116989.

RESEARCH PAPER

# L-Carnosine-coated nanoceria promotes proliferation of human embryonic lung fibroblasts via STAT3/BCL2 axis activation

***Elena V. Proskurnina[1,2*], Madina M. Sozarukova[1], Elizaveta S. Ershova[3], Natalia N. Veiko[3], Matvei A. Popkov[1], Edmund V. Kostyuk[1], Vladimir K. Ivanov[1], Svetlana V. Kostyuk[1,3]***

*[1]Kurnakov Institute of General and Inorganic Chemistry of the Russian Academy of Sciences, Moscow, Russia*
*[2] Faculty of Chemistry, Biology and Biotechnology, North Ossetian State University named after Kosta Levanovich Khetagurov, Vladikavkaz, Russia*
*[3] Institute of Longevity with a Clinic of Rehabilitation and Preventive Medicine, Russian Scientific Center of Surgery named after Academician B.V. Petrovsky, Moscow, Russia*

**ABSTRACT**

***Background:*** Nanoceria exhibits unique catalytic activity toward reactive oxygen species (ROS), mimicking the functions of natural enzymes—a property that underlies its biomedical applications, given the essential role of ROS in living organisms. Carnosine is a pH buffer with intrinsic antioxidant properties; it chelates metals and binds carbonyl compounds.

***Objective(s):*** Using human embryonic lung fibroblast model, this study investigates the impacts of carnosine-conjugated nanoscale $CeO_2$ on cell survival, cellular oxidative status, ROS-induced DNA oxidation, dual-strand DNA breaks, activation of DNA repair response, and gene and protein expression of NOX4, NRF2, STAT3, as well as proliferation and autophagy markers.

***Results:*** Carnosine-conjugated nanoceria proved to be non-cytotoxic at millimolar concentrations. Its effects on cytotoxicity, genotoxicity, DNA repair, mitochondrial membrane potential, autophagy, and NOX4 and NRF2 expression were similar to those of bare nanoceria. The principal differences were observed in the expression of STAT3, PCNA, and BCL2 proteins, where carnosine-coated nanoceria induced a pronounced activating impact after 24 h of exposure, thus promoting proliferation and increasing concentration of the PCNA proliferation marker.

***Conclusion:*** We hypothesize that carnosine-coated nanoceria directly activates the STAT3/BCL2 axis. These findings may facilitate the development of new molecular models for studying signaling pathways and advance in characterization of the nanoceria's biochemical roles in regulating ROS-driven cellular pathways. Moreover, carnosine-coated nanoceria could be considered a potential agent for enhancing the survival of cell cultures—such as hematopoietic cultures intended for transplantation—through activation of the STAT3/BCL2 axis.

***Keywords****: Ceric oxide; carnosine; cell proliferation; reactive oxygen species; fibroblasts*

**How to cite this article**

*Proskurnina E.V, Sozarukova M.M, Ershova E.S, Veiko N.N, Popkov M.A, Kostyuk E.V, Ivanov V.K, Kostyuk S.V. L-Carnosine-coated nanoceria promotes proliferation of human embryonic lung fibroblasts via STAT3/BCL2 axis activation. Nanomed J. 2026; 13(2): 310-326. DOI: 10.22038/NMJ.2026.90673.2292*

**ABBREVIATIONS**

***BRCA1:*** breast cancer type 1 susceptibility protein; ***DCF:*** 2′,7′-dichlorofluorescein; ***DLS:*** dynamic light scattering; ***FTIR-ATR:*** Fourier transform infrared spectroscopy with attenuated total reflectance; **γH2AX:** H2A histone family member X; ***H2DCFH-DA:*** 2′,7′-dichlorodihydrofluorescein diacetate; ***IL:*** interleukin; ***JAK:*** Janus kinase; ***LC3:*** 1A/1B-light chain 3; ***MAPK:*** mitogen-activated protein kinase; ***MTT:*** 3-(4,5-Dimethylthiazol-2-yl)-2,5-diphenyltetrazolium bromide; ***NF-κB:*** nuclear factor kappa-light-chain-enhancer of activated B cells; ***NOX4:*** NADPH oxidase 4; ***NRF2:*** nuclear factor erythroid 2-related factor 2; ***8-oxo-dG:*** 8-oxo-2′-deoxyguanosine; ***PBS:*** phosphate-buffered saline; ***PCNA:*** proliferating cell nuclear antigen; qRT-PCR, real-time quantitative reverse transcription polymerase chain reaction; ***ROS:*** reactive oxygen species; ***SOCS3:*** suppressor of cytokine signaling 3; ***STAT3:*** signal transducer and activator of transcription 3; ***TMRM:*** tetramethylrhodamine, methyl ester; ***XRD:*** X-ray diffraction; ***VEGF:*** vascular endothelial growth factor

* *Corresponding author:* Elena V. Proskurnina, Professor, Kurnakov Institute of General and Inorganic Chemistry of the Russian Academy of Sciences, Moscow, Russia. E-Mail address: *proskurnina@gmail.com.*

Note. This manuscript was submitted on August 22, 2025; approved on November 25, 2025.

## INTRODUCTION

Cerium dioxide nanoparticles (nanoceria) exhibit unique catalytic activity toward reactive oxygen species (ROS), mimicking natural enzymes—a property that underlies all biomedical applications of nanoceria, given the crucial role of ROS in living systems (1) (2). Depending on the surface coating and environmental conditions, nanoceria may exert either anti- or pro-oxidant effects. In cancer cells under low-pH conditions, nanoceria functions as an ROS generator, cytotoxic agent, and even radiosensitizer (3) (4). Additionally, nanoceria generates molecular oxygen within tumors, sensitizing malignant cells to light- and radio-based therapy, as well as to chemotherapeutic interventions (5). In normal cells, nanoceria has anti-inflammatory and antibacterial activity, supporting its use in tissue engineering (6). Both bare and functionalized nanoceria demonstrate strong potential to accelerate healing in acute and chronic wounds (7). Furthermore, nanoceria has been proposed as an antidiabetic agent (3) and a protective drug in retinal macular degeneration (8).

The application of nanoceria carries toxicological risks that depend on the route of exposure, dose, and chemical composition of the nanoparticles. Being a non-degradable compound, nanoceria persists in organs for a long time (at least for several months) with slow elimination rates. The acute toxicity of nanoceria is quite low, but accumulated nanoparticles can cause granuloma and fibrosis in the lungs and granuloma in the liver (9). Owing to its biostability, there is a risk of adverse effects from prolonged exposure to this nanomaterial; consequently, surface modification of ceria nanoparticles is generally required for biomedical applications.

Carnosine is an essential endogenous dipeptide predominantly found in skeletal muscle, the central nervous system, olfactory neurons, and the lens of the eye in various vertebrates, including humans (10). It functions as a pH buffer and possesses intrinsic antioxidant properties; it chelates metals such as iron and copper and binds to carbonyl compounds, which are advanced glycation and lipoperoxidation end products (11) (12) (13). Carnosine has been shown to improve muscle function in athletes (14), myocardial function (15), and vascular health (16). Additionally, it plays active roles in bone physiology and biochemistry (17), acts as a neuroprotector (18), and inhibits oxidative stress (19). Carnosine activates the NRF2 anti-inflammatory pathway (20) (21), which contributing to its beneficial effects (22) (23). Moreover, carnosine exhibits anti-aging properties (24), slowing the aging process of cultured human diploid fibroblasts by modulating protein metabolism (25) (26). Cells cultured in the presence of carnosine display a slower rate of telomere shortening and an extended lifespan (27).

Carnosine is also utilized to functionalize various nanomaterials. For example, carnosine functionalization significantly increases the solubility of carbon nanotubes, enhancing their biomedical applications (28). It enhances the antibacterial activity of graphene oxide (29). Magnetic nanoparticles coated with L-carnosine have been developed to amplify the chemotherapeutic efficacy of the dipeptide (30). Furthermore, $Fe_3O_4$ magnetic nanoparticles functionalized with L-carnosine and loaded with dexamethasone have emerged as an effective drug delivery platform in ischemic stroke (31). Hydrolyzed polyacrylonitrile nanofibers functionalized with L-carnosine and loaded with zinc oxide nanoparticles have been employed in the development of an anti-melanoma wound dressing (32).

Therefore, carnosine-coated nanoceria represents a promising hybrid compound that combines the advantageous biochemical properties of both carnosine and nanoceria. Understanding how surface modifications influence the performance and biocompatibility of nanoscale $CeO_2$ is essential to evaluate its advantages and risks associated with its biomedical applicability. However, studies on the impacts of carnosine-coated nanoceria on human gene expression are scarce or nonexistent. Human embryonic lung fibroblasts represent a robust and sensitive in vitro system for investigating the genetic effects of nanosubstances. Using human embryonic lung fibroblasts, this study investigates the impacts of carnosine-conjugated nano-$CeO_2$ on cell survival, cellular oxidative status, ROS-induced DNA oxidation, dual-strand DNA breaks, activation of DNA repair response, and gene and protein expression of NADPH-oxidase 4 (NOX4), nuclear factor erythroid 2-related factor 2 (NRF2), signal transducer and activator of transcription 3 (STAT3), as well as proliferation and autophagy markers.

## MATERIALS AND METHODS

### *Preparation of pristine and carnosine-conjugated $CeO_2$ nanoparticles*

An aqueous cerium dioxide ($CeO_2$) sol was prepared by thermal hydrolysis of $(NH_4)_2[Ce(NO_3)_6]$ (#215473, Sigma, St. Louis, MO, USA) (33). Briefly, a 100 g/L salt solution was incubated at 95 °C for 24 hours, resulting in the precipitation of cerium dioxide. The precipitate was subjected to three consecutive washes with isopropanol and redispersed in distilled water. Remaining

isopropanol was boiled off at 100°C under constant stirring for 1 h.

A solution of L-carnosine (β-alanyl-L-histidine, #305-84-0, Sigma, St. Louis, MO, USA) was prepared by dissolving carnosine in distilled water. Carnosine-conjugated nano-$CeO_2$ was synthesized by gradual addition the $CeO_2$ sol to the ligand solution under constant stirring. The molar ratio of components in the final $CeO_2$ sol was 1:1. The pH adjustment of the suspension to 7.4 was performed using aqueous $NH_3$.

***Materials characterization***

***Concentration Determination***

Quantification of the $CeO_2$ sol concentration was performed gravimetrically. Portions were transferred into pre-weighed crucibles, evaporated in a box furnace, and subsequently heated at 900 °C for 240 min until constant weight.

***X-Ray Powder Diffraction (XRD)***

Using a Bruker D8 Advance diffractometer (CuKα line), XRD characterization of the dried $CeO_2$ samples was performed across a 2θ angular range of 3 to 120°, at step sizes between 0.01° and 0.02°, with data acquisition lasting at least 0.3 seconds for each step.

***Particle Size Distribution and ζ-Potential***

Particle size range characterization and ζ-potential were measured on a Photocor Compact-Z analyzer (Photocor, Moscow, Russia) using a 636.65 nm laser at 20 °C. For each sample, the autocorrelation function was obtained by averaging 10 individual runs (20 s each). The hydrodynamic radius was calculated using the regularization algorithm implemented in DynalS software.

***UV–Visible Spectroscopy***

Using 10-mm quartz cuvettes, UV–Vis absorption was measured from 200 to 800 nm at 1 nm intervals on an SF-2000 spectrophotometer (OKB SPECTR LLC, St. Petersburg, Russia) employing a deuterium–halogen lamp.

***Fourier Transform Infrared Spectroscopy (FTIR)***

Binding of ligand molecules to the nanoparticle surface was assessed using FTIR spectroscopy. Spectra were acquired in the 400–4000 $cm^{-1}$ range at 2 $cm^{-1}$ resolution with an InfraLUM FT-08 spectrometer (Lyume'ks, St. Petersburg, Russia).

***Cultivation of cells***

The 4th-passage human embryonic lung fibroblasts were obtained from the Research Centre for Medical Genetics (Moscow, Russia) and maintained in Dulbecco's Modified Eagle's Medium (DMEM; PanEco, Moscow, Russia) containing 10% fetal bovine serum (PAA, Vienna, Austria), 50 U/mL penicillin, 50 μg/mL streptomycin, and 10 μg/mL gentamicin. Cells were suspended at a concentration of 17,000 cells/mL. The cells were maintained in culture at 37 °C for 24 hours before nanoparticle exposure. Uncoated nanoceria or carnosine-conjugated nanoceria were then added, next cells were incubated for 1, 3, 24, or 72 h. Negative controls used cell cultures without nanoparticles. Positive controls included 10% dimethyl sulfoxide (Sigma, St. Louis, MO, USA) for the MTT assay and interleukin-6 (10 ng/mL, Sigma, St. Louis, MO, USA) to evaluate the induction of the STAT3 signaling cascade.

***Viability of cells and evaluation of mitochondrial membrane potential***

Cell viability determination was performed via a 72-hour MTT assay with 3'-(4,5-dimethylthiazol-2-yl)-2,5-diphenyl tetrazolium bromide. Absorbance at 550 nm was measured using an EnSpire plate reader (PerkinElmer, Turku, Finland). Control cells were maintained nanoparticle-free.

Mitochondrial membrane potential was evaluated using tetramethylrhodamine methyl ester (TMRM; Thermo Fisher Scientific, Waltham, MA, USA) according to previously described protocols (34).

***Fluorescence microscopy***

Fluorescence micrographs were captured using an Axio Imager A2 microscope (Carl Zeiss, Oberkochen, Germany). Approximately $5 \times 10^5$ cells were plated in slide-bottom flasks. Cells were washed with PBS (phosphate-buffered saline) following medium removal, then incubated with 2',7'-dichlorodihydrofluorescein diacetate ($H_2$DCFDA; stock concentration 2 mg/mL in PBS, diluted 1:200) for 15 min, and washed again with PBS. No fewer than 100 fields, selected at random, were examined. Signal collection lasted from 6 to 10 seconds. Images were processed using the ZEN 3.10 software platform (Carl Zeiss, Oberkochen, Germany).

***Flow cytometric measurement***

***Cellular reactive oxygen species***

Cellular reactive oxygen species were quantified with flow cytometry. Cells were incubated with 10 μM $H_2$DCFH-DA in PBS (Molecular Probes/Invitrogen, Carlsbad, CA, USA) for 15 minutes in darkness, followed by PBS washing, resuspension in PBS, and flow cytometric analysis in the FITC channel on a CytoFLEX S flow cytometer (Beckman Coulter, Brea, CA, USA).

***Expression of proteins and markers***

Following washing with Versene solution (Thermo Fisher Scientific, Waltham, MA, USA), cells were incubated with 0.25% trypsin (PanEco, Moscow, Russia), washed with culture medium, resuspended in PBS with pH 7.4 (PanEco, Moscow, Russia), and fixed using paraformaldehyde (Sigma-Aldrich, St. Louis, MO, USA) at 37°C for 10 min. Cells were subjected to three washes with 0.5% BSA-PBS, permeabilized either by 0.1% Triton X-100 in PBS for 15 minutes at room temperature (20 °C) or by 90% methanol at 4 °C, and subsequently washed three additional times with 0.5% BSA-PBS. The cell samples were treated with 1 μg/mL conjugated primary antibodies for 2 hours at room temperature, followed by PBS washing and flow cytometric analysis.

Primary antibodies were as follows: DyLight488-γH2AX (pSer139) (nb100-78356G, NovusBio, Centennial, CO, USA), FITC-NRF2, (bs1074r-fitc, Bioss Antibodies Inc. Woburn, MA, USA), FITC-BRCA1 (Nb100-598F, NovusBio, Centennial, CO, USA), PE-8-oxo-dG (sc-393871 PE, Santa Cruz Biotechnology, Dallas, TX, USA), CY5.5-NOX4 (bs-1091r-cy5-5, Bioss Antibodies Inc. Woburn, MA, USA), A350-BCL2 (bs-15533r-a350, Bioss Antibodies Inc. Woburn, MA, USA), LC3 (NB100-2220 NovusBio, Centennial, CO, USA), and PCNA (ab2426, Abcam plc, Cambridge, UK).

Secondary antibody: anti-rabbit IgG-FITC (sc-2359, Santa Cruz Biotechnology, Dallas, TX, USA).

***Quantitative mRNA analysis***

Total RNA was isolated using the RNeasy Mini Kit (Qiagen, Hilden, Germany), treated with DNase I, and reverse-transcribed using the Reverse Transcriptase Kit (Sileks, Moscow, Russia). Quantitative reverse transcription PCR (qRT-PCR) with SYBR Green PCR Master Mix (Applied Biosystems, Foster City, CA, USA) was performed on a StepOnePlus system (Applied Biosystems), using *TBP* as the reference gene.

Primers were as follows (Sintol, Moscow, Russia): *BAX* (F: CCCGAGAGGTCTTTTTCCGAG, R: CCAGCCCATGATGGTTCTGAT); *BCL2* (F: TTTGGAAATCCGACCACTAA; R: AAAGAAATGCAAGTGAATGA); *NRF2* (NFE2L2) (F: TCCAGTCAGAAACCAGTGGAT, R: GAATGTCTGCGCCAAA AGCTG); *NOX4* (F: TTGGGGCTAGGATTGTGTCTA; R: GAGTGTTCGGCACATGGGTA); *STAT3* (F: GGGTGGAGAAGGACATCAGCGGTAA, R: GCCGACAATACTTTCCGAATGC); *Ki-67* (F: ACGCCTGGTTACTATCAAAAGG; R: CAGACCCATTTACTTGTGTTGGA); *NF-κB1* (F: CAGATGGCCCATACCTTCAAAT; R: CGGAAACGAAATCCTCTCTGTT); *BRCA1* (F: TGTGAGGCACCTGTGGTGA, R: CAGCTCCTGGCACTGGTAGAG); and *TBP* (reference gene) (F: GCCCGAAACGCCGAATAT, R: CCGTGGTTCGTGGCTCTCT).

***Statistics***

Results represent the mean ± standard deviation of three separate experiments. The non-parametric Mann–Whitney U test with Bonferroni correction was applied to assess statistical significance. Taking the Bonferroni correction into account, a *p*-value below 0.004 indicated statistical significance. The calculations were performed with StatPlus 2007 Pro v4.9.2 software (AnalystSoft Inc., Walnut, CA, USA).

**RESULTS**

***Synthesis and physicochemical characterization of nanoparticles***

Bare cerium dioxide samples were prepared via thermal hydrolysis of a solution containing $(NH_4)_2[Ce(NO_3)_6]$ (33). The resulting cerium dioxide sol had a concentration of 0.130 ± 0.004 mol/L (22 g/L).

Figure S1a (see Supplementary Information, Figure S1a) presents the X-ray diffraction (XRD) patterns for cerium dioxide sols dried at 50°C and for pure carnosine. XRD patterns confirmed that both bare and carnosine-modified $CeO_2$ sols consist of single-phase fluorite-structured cerium dioxide (PDF2 34-0394). Full-pattern analysis of XRD results indicated that the coherent scattering region dimensions of the $CeO_2$ powders ranged from 2.7 to 3.4 nm (Table 1). Thus, modification of the $CeO_2$ sol with carnosine did not affect the phase composition of the solid phase, as evidenced by the unchanged positions of the (111), (200), (220), and (311) reflections (see Supplementary Information, Figure S1a).

Table 1. Particle size and ζ-potential of bare and carnosine-coated $CeO_2$ nanoparticles

| Sample | Particle size, nm | ζ, mV |
|---|---|---|
| Bare $CeO_2$ | 2.7 ± 0.2 | 32.6 ± 0.5 |
| Carnosine-coated $CeO_2$ | 3.4 ± 0.1 | 5.4 ± 0.2 |

Figure S1b (see Supplementary Information, Figure S1b (after references section)) presents the size distribution of cerium dioxide particles in aqueous solutions measured by dynamic light scattering (DLS). The bare $CeO_2$ sol contained aggregates with sizes ranging from 10 to 30 nm. Functionalization of the cerium dioxide sol with carnosine resulted in larger aggregates, with size modes of approximately 65 nm and 335 nm.

For bare $CeO_2$ nanoparticles, the ζ-potential was +32.6 ± 0.5 mV (Table 1), indicating high electrostatic stability of the colloidal system. Coating $CeO_2$

nanoparticles with carnosine reduced the ζ-potential to approximately +5.4 mV (Table 1). Partial neutralization of the nanoparticle surface charge decreases electrostatic repulsion, allowing particles to approach one another more closely and promoting the formation of larger aggregates (see Supplementary Information, Figure S1b). This is further supported by the broader dispersion observed in the hydrodynamic diameter distribution.

To confirm the reproducibility of the synthesis and long-term stability of sol, we established that gradually adding a diluted $CeO_2$ sol to an equal volume of ligand solution is essential for obtaining a stable carnosine-coated cerium dioxide sol. This protocol proved highly reproducible across multiple batches ($n$ = 3). The sol retained its aggregate stability without visible precipitation for at least two months, as supported by zeta potential monitoring. The measured values were +23.7 ± 0.3 mV (day 1), +5.4 ± 0.2 mV (month 2), and +1.01 ± 0.03 mV (month 3). Despite this gradual decrease, which we attribute to the slow oxidation of the ligand molecules, the colloidal stability was maintained for this period.

**Spectral characterization**

Figure S1c (see Supplementary Information, Figure S1c) presents the UV–Vis absorption spectra of $CeO_2$ solutions and pure carnosine. Both bare and carnosine-coated $CeO_2$ sols display an absorption band in the 280–300 nm range, characteristic of nanoscale cerium dioxide, which is consistent with previous reports (35). Hence, coating $CeO_2$ nanoparticles with carnosine did not change the sol's optical absorption properties.

The infrared spectrum of pristine cerium oxide (see Supplementary Information, Figure S1d) includes a broad absorption band at 3550–3200 $cm^{-1}$, corresponding to antisymmetric and symmetric O–H stretching vibrations (36, 37). The band in the 1630–1600 $cm^{-1}$ range is assigned to H–O–H bending vibrations. Low-intensity bands at 1440 $cm^{-1}$ and 1280 $cm^{-1}$ correspond to with residual nitrate ions adsorbed on the $CeO_2$ surface (36, 37). The Ce–O bond stretching vibrations appear in the 480–430 $cm^{-1}$ region.

The FTIR spectrum of carnosine (see Supplementary Information, Figure S1d) shows a band at 3240 $cm^{-1}$ characteristic of $–NH_2$ stretching vibrations (38, 39), overlapping with a broad O–H stretching band. Asymmetric and symmetric stretching of carboxylate anions are observed at 1563 $cm^{-1}$ and 1406 $cm^{-1}$, respectively. A peak at 2855 $cm^{-1}$ is attributed to symmetric C–H stretching (38), and the band at 1643 $cm^{-1}$ is characteristic of absorbed water (38) (40). In the FTIR spectrum of carnosine-coated nanoceria (see Supplementary Information, Figure S1d), a new absorption band appears at 477 $cm^{-1}$, corresponding to Ce–O stretching vibrations, confirming the presence of $CeO_2$ in the composite. The composite spectrum also shows shifts in the carnosine carboxylate bands from 1563 to 1553 $cm^{-1}$ and from 1406 to 1384 $cm^{-1}$, indicating interaction between the ligand and the $CeO_2$ nanoparticle surface. Similar spectral shifts have been reported for carnosine-coated iron oxide nanoparticles (38).

***Cell viability and mitochondrial potential***

A standardized 72-h MTT assay (3-(4,5-dimethylthiazol-2-yl)-2,5-diphenyltetrazolium bromide) was used to evaluate cytotoxicity (Figure 1a), and the TMRM assay (tetramethylrhodamine methyl ester) was employed to assess mitochondrial membrane potential (Figure 1b). Carnosine-coated nanoceria exhibited cytotoxicity at concentrations above 0.53 mM.

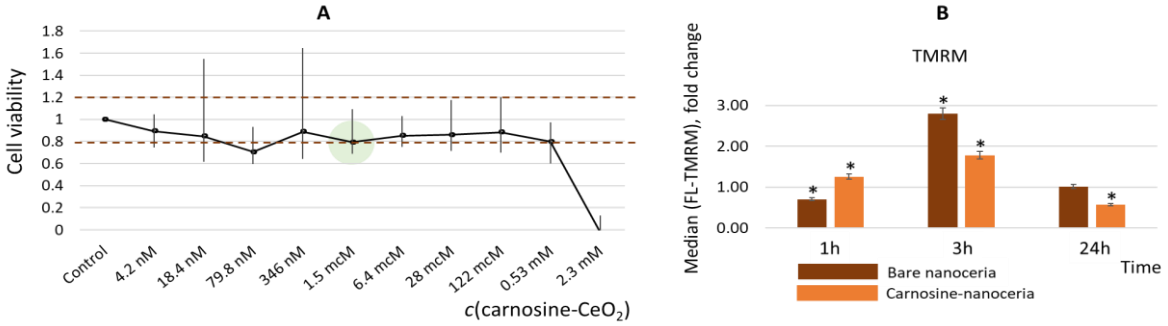


Fig. 1. (A) Cell viability of carnosine-coated nanoceria assessed using the 72-h MTT assay, where the brown dotted lines indicate the viability limits of 80%–120%; the green circle marks the 1.5 µmol/L concentration selected for further experiments; (**B**) mitochondrial membrane potential in cells exposed to bare and carnosine-coated nanoceria (1.5 µmol/L) compared with control values. Here, asterisks denote statistically significant differences in the Mann–Whitney U test with Bonferroni correction ($p$ = 0.004). Both in panels A and B, control cells were incubated without nanoparticles.

In selecting concentrations for studying gene and protein expression, we primarily relied on a proven safe concentration and existing literature data. In *in vitro* models, concentrations around 1 µmol/L are typically used, which ensure system homogeneity, absence of nanoparticle agglomeration, and cell safety (41) (42). In numerous preliminary experiments, we studied nanoceria concentrations ranging from 0.1 to 10 µmol/L and demonstrated a linear effect within this range. Thus, for subsequent experiments, a non-toxic concentration of 1.5 µmol/L—within the middle of the tested range—was selected (highlighted with a green circle in Figure 1a).

Regarding mitochondrial membrane potential, bare and carnosine-coated nanoceria produced similar effects at 3 h and 24 h; however, carnosine functionalization attenuated the impact. Bare nanoceria changed the fluorescence probe intensity by 0.70 times ($p$ = 0.0006) and 2.81 times ($p$ < 0.0001) after 1 and 3 hours of exposure, respectively. Carnosine-coated cerium increased the fluorescence probe intensity by 1.26 times ($p$ = 0.002) after 1 hour of exposure, by 1.78 times ($p$ = 0.001) after 3 hours of exposure, and by 0.57 times ($p$ = 0.0009) after 24 hours of exposure.

***Visualization and assessment of intracellular ROS quantity***

Since nanoceria exhibits intrinsic red fluorescence (43), we obtained fluorescence micrographs of cells incubated with 1.5 µmol/L nanoparticles for 3 h. The images indicate that carnosine-coated $CeO_2$ nanoparticles successfully enter the cells (Figure 2)

The internalization was studied by measuring the fluorescence of cells in the red channel of a flow cytometer (Figure 3). The data indicate that the nanoparticles are efficiently internalized into the cells.

Quantification of intracellular reactive oxygen species was performed by flow cytometry employing 2′,7′-dichlorodihydrofluorescein diacetate ($H_2$DCFH-DA). Pristine $CeO_2$ exhibited an antioxidant impact after 1 h and 3 h of incubation (fluorescence intensity decreased to 71.8% ($p$ = 0.0012) and 75.5% ($p$ = 0.0011) of control, respectively), whereas carnosine-coated nanoceria induced a 28.0% increase in ROS levels after 24 h ($p$ = 0.0007). (Figure 4)

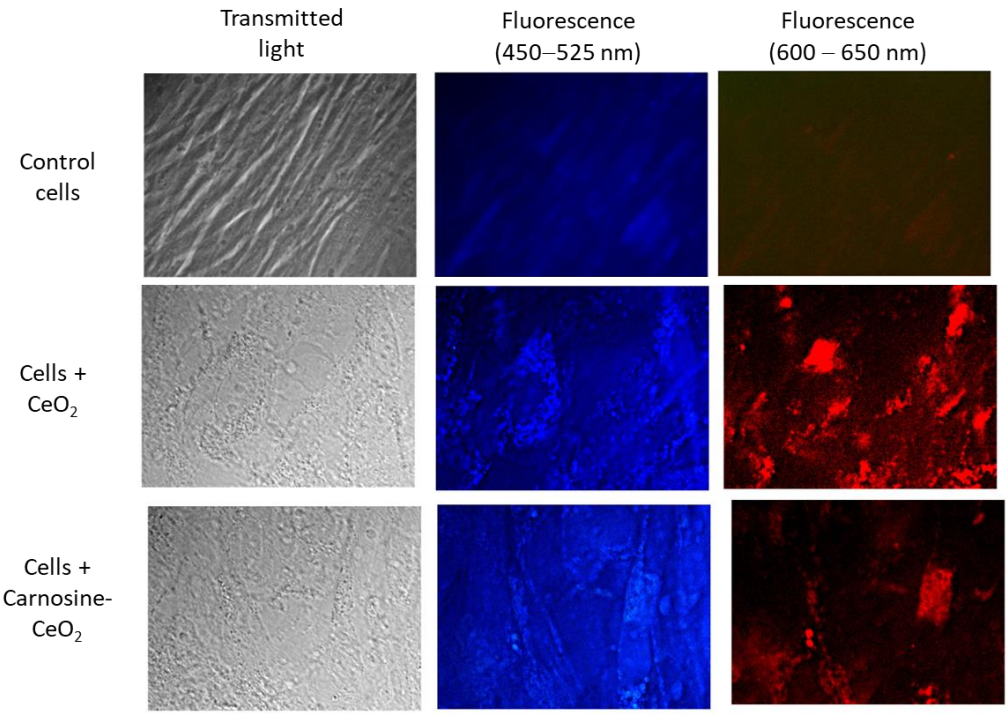


Fig. 2. Visualization of cells during nanoparticle internalization — transmitted-light images (left column) and fluorescence images obtained using a blue filter (middle column, passband 450–525 nm) and a red filter (right column, passband 600–650 nm). The top row shows images of human fetal lung fibroblasts incubated without nanoparticles (control cells); the middle row shows cells after 3 h of exposure to bare nanoceria (1.5 µmol/L); the bottom row shows cells after 3 h of exposure to carnosine-coated nanoceria (1.5 µmol/L); magnification, 100×.

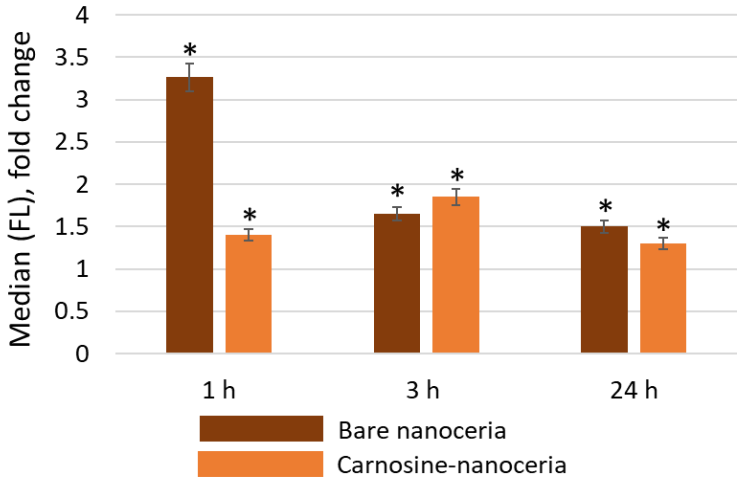


Fig. 3. Fluorescence of cells relative to the control (cells incubated without nanoparticles) after 1, 3, and 24 h of exposure to bare nanoceria and carnosine-coated nanoceria (1.5 μmol/L); asterisks denote statistically significant differences in the Mann–Whitney U test with Bonferroni correction ($p$ = 0.004).

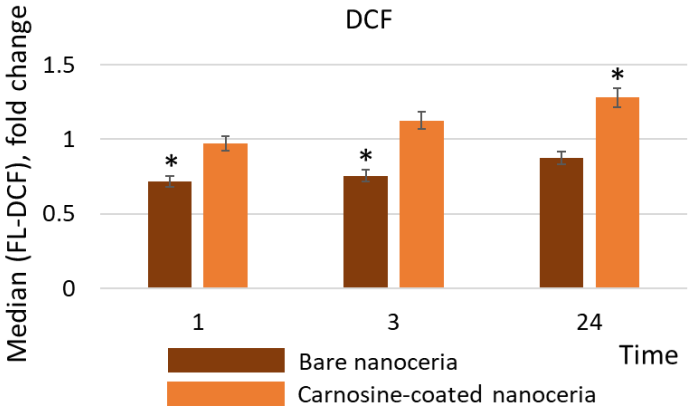


Fig. 4. Intracellular ROS levels relative to control, measured by flow cytometry with dichlorofluorescein (DCF). Cells were exposed to bare or carnosine-coated nanoceria (1.5 μmol/L) for 1, 3, or 24 h; asterisks denote statistically significant differences in the Mann–Whitney U test with Bonferroni correction ($p$ = 0.004). Control cells were incubated without nanoparticles.

**Genotoxicity**

To assess genotoxicity, quantification of 8-oxo-2′-deoxyguanosine (8-oxo-dG), a biomarker for oxidative DNA damage, and phosphorylated γH2AX, a marker for DNA double-strand breaks, was performed (Figure 5a,b). The DNA repair system function was analyzed through BRCA1 (breast cancer type 1 susceptibility protein) expression measurement (Figure 5c).

For oxidative DNA damage, differences were observed after 1 h of exposure: bare nanoceria reduced oxidative damage to 53.7% of control ($p$ = 0.001) (interquartile range [51.2%; 56.0%]), whereas carnosine-coated nanoceria increased it 1.29-fold ($p$ = 0.002) (Figure 5a). In contrast, for DNA double-strand breaks and BRCA1 protein expression, the response dynamics were similar, with carnosine functionalization exerting a mitigating effect (Figure 5b,c). After 24 hours, γH2AX expression increased 1.38-fold ($p$ = 0.002) in cells incubated with bare nanoceria and 1.34-fold ($p$ = 0.002) in cells incubated with carnosine-coated nanoceria. After 72 hours, γH2AX expression decreased to 23.9% of the control level for bare nanoceria ($p$ < 0.0001) and to 78.7% for carnosine-coated nanoceria ($p$ = 0.0038). The expression of the DNA repair marker — BRCA1 protein decreased to 56.5% after 1 hour of exposure ($p$ = 0.001) and to 68.3% after 72 hours ($p$ = 0.003) for bare nanoceria. For carnosine-coated nanoceria, BRCA1 expression did not differ significantly from the control.

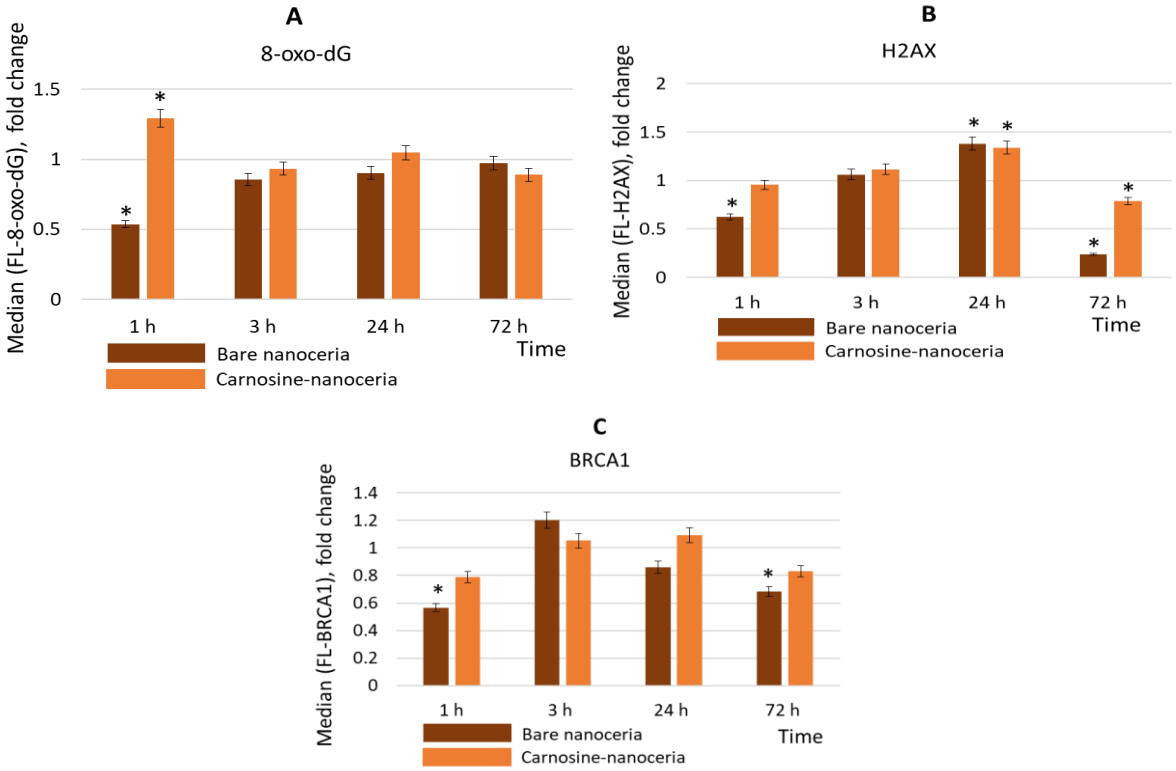


Fig. 5. (A) Concentrations of 8-oxo-2′-deoxyguanosine (8-oxo-dG) relative to control, (B) expression of phosphorylated γH2AX protein relative to control, and (C) expression of BRCA1 protein relative to control values. In all cases, the cells were exposed to bare or carnosine-coated nanoceria (1.5 μmol/L) for 1–72 h; asterisks denote statistically significant differences in the Mann–Whitney U test with Bonferroni correction ($p$ = 0.004); control cells were incubated without nanoparticles.

***ROS-mediated and inflammatory signaling pathways***

NOX4 (NADPH oxidase 4) is a major oxidant enzyme, whereas NRF2 (nuclear factor erythroid 2-related factor 2) is a key regulator of anti-inflammatory and antioxidant responses. For pristine nanoceria, NOX4 expression showed a slight increase after 3 hours of exposure (1.23-fold, $p$ = 0.004) and decreased to 64% of control levels after 72 hours ($p$ = 0.002) (Figure 6a). For carnosine-coated nanoceria, NOX4 expression decreased to 76.8% of control levels after 72 hours ($p$ = 0.003). Changes in NRF2 expression did not reach statistical significance at 1, 3, or 24 h (Figure 6b). Overall, the impacts of pristine and carnosine-conjugated nanoceria were qualitatively similar, although carnosine functionalization again resulted in a less pronounced cellular response.

For STAT3 (signal transducer and activator of transcription 3), bare nanoceria elicited the activating response after 1 h of incubation (1.27-fold increase in expression, $p$ = 0.002), followed by a decline to 26.9% of control levels by 72 hours ($p$ < 0.0001). In contrast, carnosine-coated nanoceria induced STAT3 activation predominantly after 24 hours of exposure, when expression increased 1.30-fold ($p$ = 0.001) (Figure 6c).

**Proliferation and autophagy**

LC3 (microtubule-associated protein 1 light chain 3) and BECLIN-1 are established autophagy biomarkers. Exposure to either bare or carnosine-coated nanoceria did not result in significant changes in their expression, except for a slight decrease in BECLIN-1 levels at 3 h (to 67.4% for bare nanoceria, $p$ = 0.003, to 70.0% for carnosine-coated nanoceria, $p$ = 0.003) and 72 h (to 70.0% for bare nanoceria, $p$ = 0.003) (Figure 7a,b).

For the proliferation marker PCNA (proliferating cell nuclear antigen), bare nanoceria induced an increase in PCNA expression after 1 hour of incubation by 1.26-fold ($p$ = 0.003), however, expression subsequently decreased to 63.9% ($p$ = 0.0001) and 23.9% ($p$ < 0.0001) of control levels at 24 and 72 hours, respectively. Carnosine-coated nanoceria caused a decrease in PCNA expression after 3 h of exposure to 74.0% of control levels ($p$ = 0.003) and after 72 h of exposure to 42.1% of control levels ($p$ < 0.0001). A sharp increase in PCNA expression was observed after 24 hours of exposure, reaching 2.36-fold ($p$ < 0.0000) (Figure 7c).

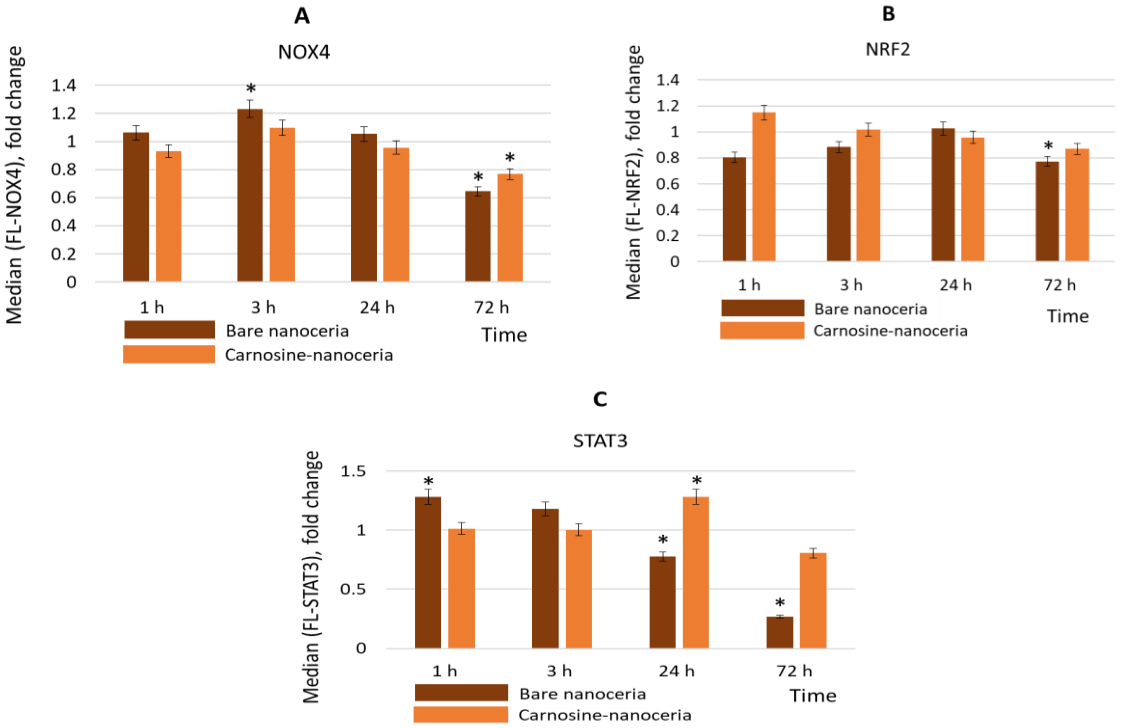


Fig. 6. (A) Expression of NOX4 protein relative to control, (B) expression of NRF2 protein relative to control, and (C) expression of STAT3 protein relative to control. In all cases, the cells were exposed to bare or carnosine coated nanoceria (1.5 μmol/L) for 1–72 h; asterisks denote statistically significant differences in the Mann–Whitney U test with Bonferroni correction ($p$ = 0.004); control cells were incubated without nanoparticles.

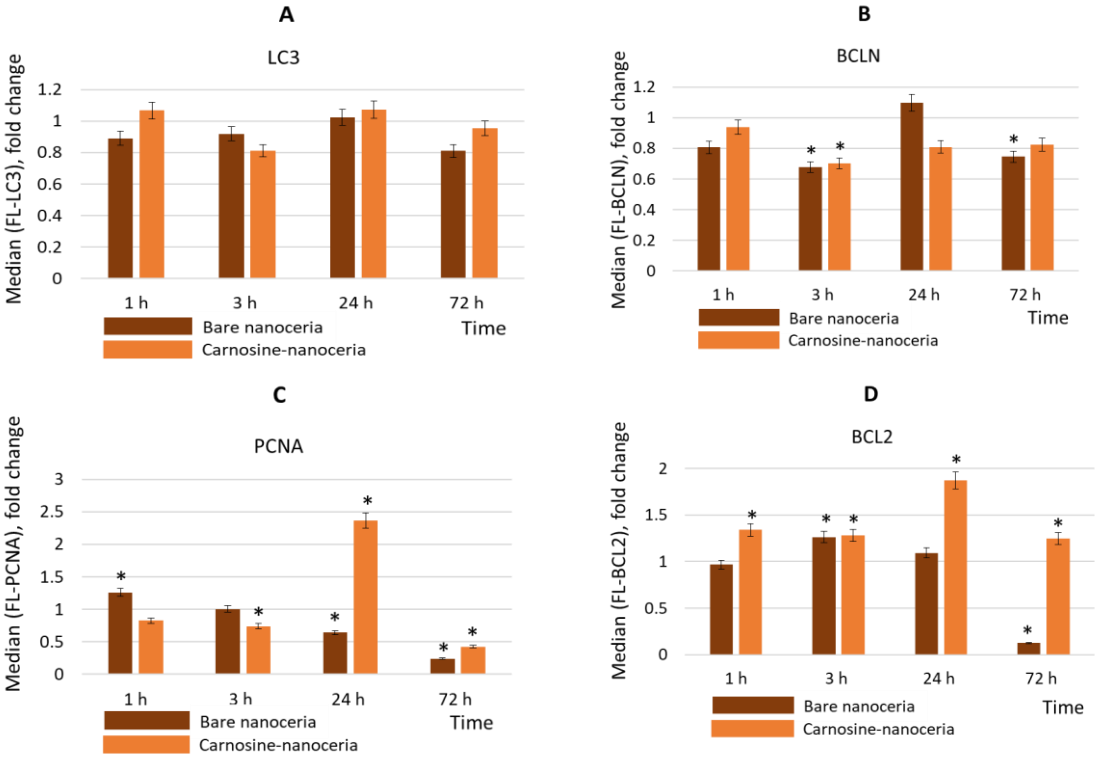


Fig. 7. (A) Expression of LC3 protein relative to control, (B) expression of BECLIN-1 protein relative to control, (C) expression of PCNA protein relative to control, and (D) expression of BCL-2 protein relative to control. In all cases, cells were exposed to bare or

carnosine-coated nanoceria (1.5 µmol/L) for 1–72 h; asterisks denote statistically significant differences in the Mann–Whitney U test with Bonferroni correction ($p$ = 0.004); control cells were incubated without nanoparticles.

An anti-apoptotic protein BCL-2 (B-cell lymphoma 2) was differentially affected. Bare nanoceria caused an increase in the expression of this protein by 1.26-fold after 3 hours of exposure ($p$ = 0.003), followed by a sharp decrease to 12.6% of control levels after 72 hours ($p$ < 0.0000). In contrast to bare nanoceria, carnosine-coated nanoceria significantly upregulated BCL-2 expression at at all exposure times (Figure 7d). The expression increase was 1.33-fold ($p$ = 0.002), 1.28-fold ($p$ = 0.003), 1.87-fold ($p$ = 0.0001), and 1.25-fold ($p$ = 0.003) after 1, 3, 27, and 72 hours of exposure, respectively.

**Gene expression**

We subsequently assessed the expression of selected genes to evaluate whether the observed changes occurred in protein levels were regulated at the transcriptional level. The primary targets included *STAT3*, *BAX*, *BCL2*, *Ki-67* (encoding the proliferation marker protein), *BRCA1*, as well as *NOX4*, *NF-κB*, and *NRF2*. Based on the pronounced activation of the STAT3/BCL2 axis at 1 h and 24 h, these two exposure times were selected for analysis (Figure 8).

The results confirmed activation of *STAT3*, *BCL2*, and *Ki-67* gene expression at 24 h, with minimal or no effect on the ROS-dependent genes *NOX4*, *NF-κB*, and *NRF2*, and no effect on the pro-apoptotic *BAX* or DNA repair *BRCA1* genes. After 24 h, *STAT3* mRNA expression increased 1.73-fold ($p$ < 0.0001), *BCL2* gene expression increased 1.96-fold ($p$ = 0.002), and *Ki-67* gene expression increased 2.21-fold. ($p$ < 0.0001) These findings support the hypothesis that carnosine-coated nanoceria activates the STAT3/BCL2 axis, most likely through a direct mechanism independent of ROS-mediated pathways.

To sum, carnosine functionalization modifies the cellular response to nanoceria, enhancing survival- and proliferation-associated signaling through the STAT3/BCL2 axis while maintaining low overall cytotoxicity, thus highlighting its potential as a targeted nanobiomaterial for biomedical applications.

**DISCUSSION**

The experimental data reveal that carnosine-coated nanoceria exhibits many similarities to bare nanoceria in terms of cytotoxicity, genotoxicity, DNA repair, mitochondrial potential, autophagy, as well as NOX4 and NRF2 protein expression. However, notable differences arise in the activation of STAT3, PCNA, and BCL2 proteins, where carnosine-coated nanoceria induces a pronounced activating effect after 24 hours of exposure. Additionally, carnosine-coated nanoceria. creates a more oxidative intracellular environment following 24 hours of exposure. It should be noted that excessive intracellular reactive oxygen species did not lead to oxidative DNA damage, and overall, the studied nanoparticles do not exhibit genotoxicity. The absence of oxidative DNA damage indicates sufficient antioxidant capacity within the cell, possibly enhanced by the antioxidant potential of carnosine.

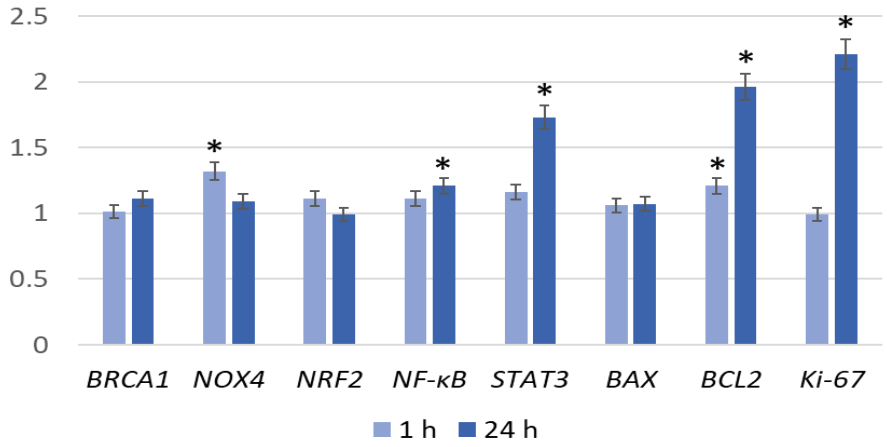


Fig. 8. Relative gene expression in cells exposed to carnosine-coated nanoceria (1.5 µmol/L) for 1 h and 24 h, compared with control values. '*' denotes statistically significant differences in the Mann–Whitney U test with Bonferroni correction ($p$ = 0.005). Control cells were incubated without nanoparticles.

STAT3 is a pivotal component of the JAK/STAT signaling cascade. Upon activation by phosphorylation, STAT3 translocates to the nucleus, where it regulates gene transcription. STAT3 is extensively studied as a prospective target for therapy in cancer due to its frequent overexpression across diverse tumor types, where it promotes cancer cell proliferation, survival, invasion, stemness, angiogenesis, and resistance to chemotherapy (44) (45). The JAK/STAT cascade, especially involving Janus kinases associated with cytokine receptors, plays an important role in mediating inflammatory signaling downstream of IL-6 and IL-10 cytokines in inflammation and cancer (46) (47). Beyond oncology, STAT3 inhibition is being explored as a potential treatment strategy for neurodegenerative diseases (48), cardiac fibrosis (49), and bone diseases (50), although effective clinical antagonists remain under development (51).

The JAK/STAT3 signaling pathway interacts closely with other major signaling cascades such as PI3K/AKT/mTOR and MAPK/ERK (52), and its activity is finely modulated by oxidative stress (53). Specifically, hydrogen peroxide can inhibit intracellular tyrosine phosphatases, which leads to enhanced STAT3 tyrosine phosphorylation (54). Interestingly, oxidative stress not only activates STAT3 but also maintains cytokine-induced STAT3 phosphorylation and its active state in the nucleus (55). Antioxidants like alantolactone and resveratrol have been shown to effectively reduce STAT3 activation by counteracting oxidative stress (56), (57). In our study, while intracellular hydrogen peroxide levels were elevated after exposure to carnosine-coated nanoceria, the lack of significant changes in NOX4 and NRF2 expression casts some doubt on oxidative stress being the sole cause of STAT3 activation. his suggests that the STAT3 activation observed may stem from a direct effect of the carnosine coating itself, possibly through mechanisms independent of classical ROS signaling. Nevertheless, the increased oxidative environment may still contribute to sustaining or supporting STAT3 activation alongside this direct activation. This nuanced interplay points to a complex regulatory network where carnosine-coated nanoceria modulates STAT3 activity both directly and indirectly, highlighting its potential for targeted modulation of cellular survival and proliferation pathways.

The close association between STAT3, BCL2, and PCNA expression in our study is well supported by extensive literature demonstrating their interconnected roles in regulating cell survival, proliferation, and apoptosis inhibition. Alas *et al*. showed that Bcl-2 expression is controlled by the STAT3 signaling pathway, which is modulated by endogenously secreted IL-10 (58). Primary B-cell lymphoma tissues demonstrated a strong linkage between STAT3 expression or phosphorylation and Bcl-2 levels (59). Phospholipase D regulates Bcl-2 expression through activation of the STAT3 signaling pathway (60). STAT3 inactivation reduced PCNA, CyclinD1, and Bcl2 expression in glioma cells (61). STAT3 inhibitor ethanol extract of *Spica Prunellae* resulted in an increase in the proapoptotic Bax/Bcl-2 ratio and a decrease in the expression of proproliferative Cyclin D1 and CDK4 ultimately leading to the activation of apoptosis and inhibition of cell proliferation in colorectal cancer (62). Activation of STAT3 in a mouse model of photocarcinogenesis led to increased transcription of the proliferative and antiapoptotic genes PCNA, Cyclin-D1, Bcl-2, and Bcl-xl (63). STAT 3 activation following polyamine depletion enhances transcription and expression of Bcl-2 and IAP anti-apoptotic proteins and consequently enhancing resistance to tumor necrosis factor-alpha-induced apoptosis (64). Phosphatidic acid increases Bcl-2 expression via STAT3 activation (65). The JAK2/STAT3 signaling cascade plays a critical role in the proliferation of damaged vessel wall cells, which is accompanied by an increase in PCNA (66). Thus, the close association of STAT3 and BCL2 allows their integration into the IL-10/STAT3/BCL2 axis (67) and TYK2/STAT3/Bcl2 (68), which are the basis of chemoresistance and inhibition of apoptosis. The synergistic change in the expression of STAT3, BCL2 and PCNA in our studies indicates that carnosine-coated nanoceria does indeed affect this signaling pathway.

There is some data on the anti-proliferative effect of carnosine in cancer, although the full mechanism is unclear. Rybakova *et al*. showed that carnosine selectively inhibited the proliferation of human glioblastoma cells compared to breast and oral cavity cancer cells (69). In cultured rat pheochromocytoma cells, carnosine led to a slowdown in cell proliferation (70). Carnosine inhibited the proliferation of human colon cancer HCT116 cells (71). Carnosine suppressed the proliferation of human colorectal cancer cells through reduction of beta-catenin/Tcf-4 signaling, induction of both autophagy and necroptosis, and inhibition of angiogenesis-related processes (72). Carnosine demonstrates significant suppression on the proliferation of human cervical carcinoma cells *via* effects on mitochondrial bioenergetics and glycolytic pathways and the cell cycle (73).

On the other hand, L-carnosine contributes significantly to apoptosis inhibition by activating the anti-apoptotic protein BCL2. Neuronal apoptosis induced by acute cerebral ischemia was suppressed by carnosine through activation of the STAT3/Bcl2 signaling cascade (74). Carnosine was effective in protecting rat liver from ethanol damage by maintaining glutathione levels and BCL2 expression (75), and in protecting the retina from ischemic damage also by increasing BCL2 expression (76). The neuroprotective effect of carnosine in a mouse model of aging is based on a decrease in malondialdehyde and ROS levels and an increase in BCL2 expression (77). Carnosine treatment significantly increased BCL2 levels in lipopolysaccharide-treated *Caenorhabditis elegans*, protecting them from apoptosis (78). Carnosine inhibited apoptosis in $H_2O_2$-damaged human kidney tubular epithelial cells (79). In a rat acute kidney injury model, carnosine decreased Bax expression and increased Bcl2 expression, inhibiting renal tissue damage and improving survival (80). In frozen and thawed cattle embryos, addition of carnosine to the preservation solution significantly reduced reactive oxygen species production, decreased apoptosis, and increased *Bcl2* mRNA expression (81). Thus, the increase in BCL2 and PCNA expression in our experiments is consistent with literature data indicating the anti-apoptotic and proliferative effect of carnosine.

Thus, we suppose that the activation of STAT3, BCL2 and PCNA is a single pathway and occurs precisely due to carnosine. According to our findings, carnosine-coated nanoceria is found to be an activator of the STAT3/BCL2 axis, which should be taken into account when developing applications. Although the activation of the STAT3/BCL2 axis often needs to be suppressed, since this pathway is associated with increased cancer cell survival, anti-apoptosis, angiogenesis, and chemoresistance (82) (83), in some cases the active STAT3/BCL2 pathway is necessary to inhibit apoptosis. Oritani *et al.* showed that STAT3/BCL2 activation inhibits IL-6-induced apoptosis of macrophages (84). Sepulveda *et al.* proved that IL-6-mediated STAT3 activation supports an anti-apoptotic beneficial effect in human cord blood CD34+ cells, primarily due to bcl-2 overexpression, which is useful for optimizing *ex vivo* cultures for clinical applications (85). Lee *et al.* demonstrated that Deficiency in Stat3 may predispose T cells to apoptosis by attenuating Bcl-2 and Bcl-xL (86). We propose that carnosine-coated nanoceria, as an activator of the STAT3/BCL2 pathway with negligible impact on the oxidative intracellular balance, may be considered a potential agent for promoting the survival of ex vivo cell cultures or organs. Thus, several biomedical scenarios can be proposed for the future practical application of the studied hybrid nanomaterial: a) optimizing *ex vivo* expansion and transplantation of hematopoietic stem cells, b) host defense and intestinal epithelial maintenance, where STAT3 activation regulates antimicrobial peptide expression and suppresses apoptosis, supporting barrier integrity and defense against intestinal infections, c) under conditions of stress or nutrient deficiency, STAT3 pathway activation will promote cell survival, which may be useful in tissue regeneration and wound healing after injuries. However, additional research is necessary to comprehensively understand the biological capabilities of this nanomaterial.

**LIMITATIONS**

In our study, we proposed the hypothesis of proliferation activation via the STAT3/BCL2 signaling pathway, based on measurements of reporter gene and signaling pathway protein expression under exposure to carnosine-coated nanoceria. However, to confirm this hypothesis, mechanistic experiments using inhibitors or specific siRNA/shRNA knockdown of key signaling components should be conducted.

**CONCLUSIONS**

Using an *in vitro* model of human embryonic lung fibroblasts, we investigated the impacts of carnosine-coated nanoceria on cell survival, cellular uptake, intracellular ROS balance, genotoxicity and DNA repair systems, markers of proliferation and autophagy, and expression of NOX4, NRF2, and STAT3 proteins and genes. Carnosine-conjugated nanoceria exhibits no cytotoxicity up to 0.53 mM. Within 3 h, both pristine and carnosine-conjugated $CeO_2$ nanoparticles were efficiently internalized by cells. Carnosine-coated nanoceria behaved similarly to bare nanoceria with respect to cytotoxicity, genotoxicity, DNA repair, effects on mitochondrial membrane potential and autophagy, and regulation of NOX4 and NRF2 proteins. The main differences were observed in the expression of STAT3, PCNA, and BCL2 proteins, where carnosine-coated nanoceria induced a pronounced activating effect after 24 h of exposure. In addition, carnosine-coated nanoceria generated an oxidative intracellular environment after 24 h. We hypothesize that carnosine-coated nanoceria directly activates the STAT3/BCL2 axis while

exerting minimal effect on intracellular oxidative metabolism. These findings may aid the development of new molecular models for studying signaling pathways and contribute to biochemical mechanisms of nanoceria as a regulator of cell metabolism. From a practical perspective, carnosine-coated nanoceria, as an activator of the STAT3/BCL2 pathway with negligible impact on intracellular oxidative balance, may be considered a potential agent for promoting the survival of *ex vivo* cell cultures or organs. However, additional research is necessary to comprehensively understand the biological capabilities of this nanomaterial.

**ACKNOWLEDGMENTS**

The authors thank Dr. Larisa Kameneva for assistance with cell culturing.

**CONFLICTS OF INTEREST**

The authors confirm that they have no conflicts of interest to disclose.

**FUNDING SOURCES**

The research was financially supported by the Russian Science Foundation, project No. 24-13-00370.

**ETHICAL CONSIDERATIONS AND CODE**

The study was conducted in accordance with the Declaration of Helsinki and approved by the Ethics Committee of the Research Centre for Medical Genetics (Approval #5, 3 July 2017).

**AUTHOR CONTRIBUTIONS**

The manuscript was written through contributions of all authors. All authors have given approval to the final version of the manuscript.

**ARTIFICIAL INTELLIGENCE (AI)**

The authors declare that generative artificial intelligence (AI) was not used in the preparation of this article.

**REFERENCES**

1. Wong LL, McGinnis JF. Nanoceria as bona fide catalytic antioxidants in medicine: what we know and what we want to know. Adv Exp Med Biol. 2014;801:821-828.
2. Saifi MA, Seal S, Godugu C. Nanoceria, the versatile nanoparticles: Promising biomedical applications. J Control Release. 2021;338:164-189.
3. Thakur N, Manna P, Das J. Synthesis and biomedical applications of nanoceria, a redox active nanoparticle. J Nanobiotechnology. 2019;17(1):84.
4. Alvandi M, Shaghaghi Z, Farzipour S, Marzhoseyni Z. Radioprotective Potency of Nanoceria. Curr Radiopharm. 2024;17(2):138-147.
5. Tang JLY, Moonshi SS, Ta HT. Nanoceria: an innovative strategy for cancer treatment. Cell Mol Life Sci. 2023;80(2):46.
6. Kargozar S, Baino F, Hoseini SJ, Hamzehlou S, Darroudi M, Verdi J, Hasanzadeh L, Kim HW, Mozafari M. Biomedical applications of nanoceria: new roles for an old player. Nanomedicine (Lond). 2018;13(23):3051-3069.
7. Sadidi H, Hooshmand S, Ahmadabadi A, Javad Hosseini S, Baino F, Vatanpour M, Kargozar S. Cerium Oxide Nanoparticles (Nanoceria): Hopes in Soft Tissue Engineering. Molecules. 2020;25(19).
8. Tisi A, Passacantando M, Ciancaglini M, Maccarone R. Nanoceria neuroprotective effects in the light-damaged retina: A focus on retinal function and microglia activation. Exp Eye Res. 2019;188:107797.
9. Yokel RA, Hussain S, Garantziotis S, Demokritou P, Castranova V, Cassee FR. The Yin: An adverse health perspective of nanoceria: uptake, distribution, accumulation, and mechanisms of its toxicity. Environ Sci Nano. 2014;1(5):406-428.
10. Budzen S, Rymaszewska J. The biological role of carnosine and its possible applications in medicine. Adv Clin Exp Med. 2013;22(5):739-744.
11. Boldyrev AA, Aldini G, Derave W. Physiology and pathophysiology of carnosine. Physiol Rev. 2013;93(4):1803-1845.
12. Cararo JH, Streck EL, Schuck PF, Ferreira Gda C. Carnosine and Related Peptides: Therapeutic Potential in Age-Related Disorders. Aging Dis. 2015;6(5):369-379.
13. Ghodsi R, Kheirouri S. Carnosine and advanced glycation end products: a systematic review. Amino Acids. 2018;50(9):1177-1186.
14. Sale C, Artioli GG, Gualano B, Saunders B, Hobson RM, Harris RC. Carnosine: from exercise performance to health. Amino Acids. 2013;44(6):1477-1491.
15. Creighton JV, de Souza Goncalves L, Artioli GG, Tan D, Elliott-Sale KJ, Turner MD, Doig CL, Sale C. Physiological Roles of Carnosine in Myocardial Function and Health. Adv Nutr. 2022;13(5):1914-1929.
16. Feehan J, Hariharan R, Buckenham T, Handley C, Bhatnagar A, Baba SP, de Courten B. Carnosine as a potential therapeutic for the management of peripheral vascular disease. Nutr Metab Cardiovasc Dis. 2022;32(10):2289-2296.
17. Yang H, Hou X, Xing L, Tian F. Carnosine and bone (Review). Mol Med Rep. 2023;27(1).
18. Berezhnoy DS, Stvolinsky SL, Lopachev AV, Devyatov AA, Lopacheva OM, Kulikova OI, Abaimov DA, Fedorova TN. Carnosine as an effective neuroprotector in brain pathology and potential neuromodulator in normal conditions. Amino Acids. 2019;51(1):139-150.
19. Babizhayev MA. The detox strategy in smoking comprising nutraceutical formulas of non-hydrolyzed

carnosine or carcinine used to protect human health. Hum Exp Toxicol. 2014;33(3):284-316.
20. Caruso G, Privitera A, Antunes BM, Lazzarino G, Lunte SM, Aldini G, Caraci F. The Therapeutic Potential of Carnosine as an Antidote against Drug-Induced Cardiotoxicity and Neurotoxicity: Focus on Nrf2 Pathway. Molecules. 2022;27(14).
21. Zhou JY, Lin HL, Qin YC, Li XG, Gao CQ, Yan HC, Wang XQ. l-Carnosine Protects Against Deoxynivalenol-Induced Oxidative Stress in Intestinal Stem Cells by Regulating the Keap1/Nrf2 Signaling Pathway. Mol Nutr Food Res. 2021;65(17):e2100406.
22. Prokopieva VD, Yarygina EG, Bokhan NA, Ivanova SA. Use of Carnosine for Oxidative Stress Reduction in Different Pathologies. Oxid Med Cell Longev. 2016;2016:2939087.
23. Artioli GG, Sale C, Jones RL. Carnosine in health and disease. Eur J Sport Sci. 2019;19(1):30-39.
24. Hipkiss AR, Baye E, de Courten B. Carnosine and the processes of ageing. Maturitas. 2016;93:28-33.
25. McFarland GA, Holliday R. Retardation of the senescence of cultured human diploid fibroblasts by carnosine. Exp Cell Res. 1994;212(2):167-175.
26. McFarland GA, Holliday R. Further evidence for the rejuvenating effects of the dipeptide L-carnosine on cultured human diploid fibroblasts. Exp Gerontol. 1999;34(1):35-45.
27. Shao L, Li QH, Tan Z. L-carnosine reduces telomere damage and shortening rate in cultured normal fibroblasts. Biochem Biophys Res Commun. 2004;324(2):931-936.
28. Ketabi S, Rahmani L. Carbon nanotube as a carrier in drug delivery system for carnosine dipeptide: A computer simulation study. Mater Sci Eng C Mater Biol Appl. 2017;73:173-181.
29. Gholibegloo E, Karbasi A, Pourhajibagher M, Chiniforush N, Ramazani A, Akbari T, Bahador A, Khoobi M. Carnosine-graphene oxide conjugates decorated with hydroxyapatite as promising nanocarrier for ICG loading with enhanced antibacterial effects in photodynamic therapy against Streptococcus mutans. J Photochem Photobiol B. 2018;181:14-22.
30. Farid RM, Gaafar PME, Hazzah HA, Helmy MW, Abdallah OY. Chemotherapeutic potential of L-carnosine from stimuli-responsive magnetic nanoparticles against breast cancer model. Nanomedicine (Lond). 2020;15(9):891-911.
31. Lu X, Zhang Y, Wang L, Li G, Gao J, Wang Y. Development of L-carnosine functionalized iron oxide nanoparticles loaded with dexamethasone for simultaneous therapeutic potential of blood brain barrier crossing and ischemic stroke treatment. Drug Deliv. 2021;28(1):380-389.
32. Homaeigohar S, Kordbacheh D, Banerjee S, Gu J, Zhang Y, Huang Z. Zinc Oxide Nanoparticle Loaded L-Carnosine Biofunctionalized Polyacrylonitrile Nanofibrous Wound Dressing for Post-Surgical Treatment of Melanoma. Polymers (Basel). 2025;17(2).
33. Shcherbakov AB, Teplonogova MA, Ivanova OS, Shekunova TO, Ivonin IV, Baranchikov AY, Ivanov VK. Facile method for fabrication of surfactant-free concentrated CeO2 sols. Materials Research Express. 2017;4(5):055008.
34. Creed S, McKenzie M. Measurement of Mitochondrial Membrane Potential with the Fluorescent Dye Tetramethylrhodamine Methyl Ester (TMRM). Methods Mol Biol. 2019;1928:69-76.
35. Huang Y-C, Wu S-H, Hsiao C-H, Lee A-T, Huang MH. Mild synthesis of size-tunable CeO2 octahedra for band gap variation. Chemistry of Materials. 2020;32(6):2631-2638.
36. Prabaharan DMDM, Sadaiyandi K, Mahendran M, Sagadevan S. Structural, optical, morphological and dielectric properties of cerium oxide nanoparticles. Materials Research. 2016;19(2):478-482.
37. Sozarukova M, Proskurnina E, Mikheev I, Polevoy L, Baranchikov A, Ivanov V. Anti-and Pro-Oxidant Properties of Cerium Oxide Nanoparticles Functionalized with Gallic Acid. Russian Journal of Inorganic Chemistry. 2023;68(8):1108-1116.
38. Durmus Z, Kavas H, Baykal A, Sozeri H, Alpsoy L, Çelik S, Toprak M. Synthesis and characterization of l-carnosine coated iron oxide nanoparticles. Journal of Alloys and Compounds. 2011;509(5):2555-2561.
39. Torreggiani A, Tamba M, Fini G. Binding of copper (II) to carnosine: Raman and IR spectroscopic study. Biopolymers: Original Research on Biomolecules. 2000;57(3):149-159.
40. Wagner CC, Baran EJ. Vibrational spectra of polaprezinc, a polymeric Zn (II) complex of carnosine. Journal of Raman Spectroscopy: An International Journal for Original Work in all Aspects of Raman Spectroscopy, Including Higher Order Processes, and also Brillouin and Rayleigh Scattering. 2008;39(4):474-477.
41. Singh S, Ly A, Das S, Sakthivel TS, Barkam S, Seal S. Cerium oxide nanoparticles at the nano-bio interface: size-dependent cellular uptake. Artificial Cells, Nanomedicine, and Biotechnology. 2018;46(sup3):956-963.
42. Bailey ZS, Nilson E, Bates JA, Oyalowo A, Hockey KS, Sajja V, Thorpe C, Rogers H, Dunn B, Frey AS, Billings MJ, Sholar CA, Hermundstad A, Kumar C, VandeVord PJ, Rzigalinski BA. Cerium Oxide Nanoparticles Improve Outcome after In Vitro and In Vivo Mild Traumatic Brain Injury. J Neurotrauma. 2020;37(12):1452-1462.
43. Proskurnina EV, Sozarukova MM, Ershova ES, Savinova EA, Kameneva LV, Veiko NN, Teplonogova MA, Saprykin VP, Ivanov VK, Kostyuk SV. Lipid Coating Modulates Effects of Nanoceria on Oxidative Metabolism in Human Embryonic Lung Fibroblasts: A Case of Cardiolipin. Biomolecules. 2025;15:53.
44. Shi D, Tao J, Man S, Zhang N, Ma L, Guo L, Huang L, Gao W. Structure, function, signaling pathways and clinical therapeutics: The translational potential of STAT3 as a target for cancer therapy. Biochim Biophys Acta Rev Cancer. 2024;1879(6):189207.

45. Hashemi M, Abbaszadeh S, Rashidi M, Amini N, Talebi Anaraki K, Motahhary M, Khalilipouya E, Harif Nashtifani A, Shafiei S, Ramezani Farani M, Nabavi N, Salimimoghadam S, Aref AR, Raesi R, Taheriazam A, Entezari M, Zha W. STAT3 as a newly emerging target in colorectal cancer therapy: Tumorigenesis, therapy response, and pharmacological/nanoplatform strategies. Environ Res. 2023;233:116458.
46. Huynh J, Etemadi N, Hollande F, Ernst M, Buchert M. The JAK/STAT3 axis: A comprehensive drug target for solid malignancies. Semin Cancer Biol. 2017;45:13-22.
47. Kitamura H, Ohno Y, Toyoshima Y, Ohtake J, Homma S, Kawamura H, Takahashi N, Taketomi A. Interleukin-6/STAT3 signaling as a promising target to improve the efficacy of cancer immunotherapy. Cancer Sci. 2017;108(10):1947-1952.
48. Panda SP, Kesharwani A, Datta S, Prasanth D, Panda SK, Guru A. JAK2/STAT3 as a new potential target to manage neurodegenerative diseases: An interactive review. Eur J Pharmacol. 2024;970:176490.
49. Jiang H, Yang J, Li T, Wang X, Fan Z, Ye Q, Du Y. JAK/STAT3 signaling in cardiac fibrosis: a promising therapeutic target. Front Pharmacol. 2024;15:1336102.
50. Li J, Yin Z, Huang B, Xu K, Su J. Stat3 Signaling Pathway: A Future Therapeutic Target for Bone-Related Diseases. Front Pharmacol. 2022;13:897539.
51. Shih PC. Revisiting the development of small molecular inhibitors that directly target the signal transducer and activator of transcription 3 (STAT3) domains. Life Sci. 2020;242:117241.
52. El-Habr EA, Levidou G, Trigka EA, Sakalidou J, Piperi C, Chatziandreou I, Spyropoulou A, Soldatos R, Tomara G, Petraki K, Samaras V, Zisakis A, Varsos V, Vrettakos G, Boviatsis E, Patsouris E, Saetta AA, Korkolopoulou P. Complex interactions between the components of the PI3K/AKT/mTOR pathway, and with components of MAPK, JAK/STAT and Notch-1 pathways, indicate their involvement in meningioma development. Virchows Arch. 2014;465(4):473-485.
53. Xu Z, Wu H, Zhang H, Bai J, Zhang Z. Interleukins 6/8 and cyclooxygenase-2 release and expressions are regulated by oxidative stress-JAK2/STAT3 signaling pathway in human bronchial epithelial cells exposed to particulate matter </=2.5 mum. J Appl Toxicol. 2020;40(9):1210-1218.
54. Carballo M, Conde M, El Bekay R, Martin-Nieto J, Camacho MJ, Monteseirin J, Conde J, Bedoya FJ, Sobrino F. Oxidative stress triggers STAT3 tyrosine phosphorylation and nuclear translocation in human lymphocytes. J Biol Chem. 1999;274(25):17580-17586.
55. Ng IH, Yeap YY, Ong LS, Jans DA, Bogoyevitch MA. Oxidative stress impairs multiple regulatory events to drive persistent cytokine-stimulated STAT3 phosphorylation. Biochim Biophys Acta. 2014;1843(3):483-494.
56. Maryam A, Mehmood T, Zhang H, Li Y, Khan M, Ma T. Alantolactone induces apoptosis, promotes STAT3 glutathionylation and enhances chemosensitivity of A549 lung adenocarcinoma cells to doxorubicin via oxidative stress. Sci Rep. 2017;7(1):6242.
57. Kohandel Z, Farkhondeh T, Aschner M, Pourbagher-Shahri AM, Samarghandian S. STAT3 pathway as a molecular target for resveratrol in breast cancer treatment. Cancer Cell Int. 2021;21(1):468.
58. Alas S, Bonavida B. Rituximab inactivates signal transducer and activation of transcription 3 (STAT3) activity in B-non-Hodgkin's lymphoma through inhibition of the interleukin 10 autocrine/paracrine loop and results in down-regulation of Bcl-2 and sensitization to cytotoxic drugs. Cancer Res. 2001;61(13):5137-5144.
59. Kang J, Chong SJ, Ooi VZ, Vali S, Kumar A, Kapoor S, Abbasi T, Hirpara JL, Loh T, Goh BC, Pervaiz S. Overexpression of Bcl-2 induces STAT-3 activation via an increase in mitochondrial superoxide. Oncotarget. 2015;6(33):34191-34205.
60. Choi HJ, Han JS. Overexpression of phospholipase D enhances Bcl-2 expression by activating STAT3 through independent activation of ERK and p38MAPK in HeLa cells. Biochim Biophys Acta. 2012;1823(6):1082-1091.
61. Tan Y, Huang N, Zhang X, Hu J, Cheng S, Pi L, Cheng Y. KIAA0247 suppresses the proliferation, angiogenesis and promote apoptosis of human glioma through inactivation of the AKT and Stat3 signaling pathway. Oncotarget. 2016;7(52):87100-87113.
62. Lin W, Zheng L, Zhuang Q, Zhao J, Cao Z, Zeng J, Lin S, Xu W, Peng J. Spica prunellae promotes cancer cell apoptosis, inhibits cell proliferation and tumor angiogenesis in a mouse model of colorectal cancer via suppression of stat3 pathway. BMC Complement Altern Med. 2013;13:144.
63. Agilan B, Rajendra Prasad N, Kanimozhi G, Karthikeyan R, Ganesan M, Mohana S, Velmurugan D, Ananthakrishnan D. Caffeic Acid Inhibits Chronic UVB-Induced Cellular Proliferation Through JAK-STAT3 Signaling in Mouse Skin. Photochem Photobiol. 2016;92(3):467-474.
64. Bhattacharya S, Ray RM, Johnson LR. STAT3-mediated transcription of Bcl-2, Mcl-1 and c-IAP2 prevents apoptosis in polyamine-depleted cells. Biochem J. 2005;392(Pt 2):335-344.
65. Choi HJ, Lee JH, Park SY, Cho JH, Han JS. STAT3 is involved in phosphatidic acid-induced Bcl-2 expression in HeLa cells. Exp Mol Med. 2009;41(2):94-101.
66. Zhao J, Zhang M, Li W, Su X, Zhu L, Hang C. Suppression of JAK2/STAT3 signaling reduces end-to-end arterial anastomosis induced cell proliferation in common carotid arteries of rats. PLoS One. 2013;8(3):e58730.
67. Wu D, Wang Z. Gastric Cancer Cell-Derived Kynurenines Hyperactive Regulatory T Cells to Promote Chemoresistance via the IL-10/STAT3/BCL2 Signaling Pathway. DNA Cell Biol. 2022;41(4):447-455.
68. Qin W, Peng C, Yang X, Jiang A, Zhong N, Liu Y, Zhang X, Hirbe AC, Ma M, Yue X. SS18-SSX drives TYK2 expression to activate STAT3/Bcl2 axis, facilitating

apoptosis evasion and advancing synovial sarcoma progression. Cell Biol Toxicol. 2024;41(1):8.
69. Rybakova YS, Kalen AL, Eckers JC, Fedorova TN, Goswami PC, Sarsour EH. [Increased manganese superoxide dismutase and cyclin B1 expression in carnosine-induced inhibition of glioblastoma cell proliferation]. Biomed Khim. 2015;61(4):510-518.
70. Rybakova YS, Boldyrev AA. Effect of carnosine and related compounds on proliferation of cultured rat pheochromocytoma PC-12 cells. Bull Exp Biol Med. 2012;154(1):136-140.
71. Iovine B, Iannella ML, Nocella F, Pricolo MR, Bevilacqua MA. Carnosine inhibits KRAS-mediated HCT116 proliferation by affecting ATP and ROS production. Cancer Lett. 2012;315(2):122-128.
72. Hsieh SL, Li JH, Dong CD, Chen CW, Wu CC. Carnosine suppresses human colorectal cancer cell proliferation by inducing necroptosis and autophagy and reducing angiogenesis. Oncol Lett. 2022;23(2):44.
73. Bao Y, Ding S, Cheng J, Liu Y, Wang B, Xu H, Shen Y, Lyu J. Carnosine Inhibits the Proliferation of Human Cervical Gland Carcinoma Cells Through Inhibiting Both Mitochondrial Bioenergetics and Glycolysis Pathways and Retarding Cell Cycle Progression. Integr Cancer Ther. 2018;17(1):80-91.
74. Wang JP, Yang ZT, Liu C, He YH, Zhao SS. L-carnosine inhibits neuronal cell apoptosis through signal transducer and activator of transcription 3 signaling pathway after acute focal cerebral ischemia. Brain Res. 2013;1507:125-133.
75. Baykara B, Micili SC, Tugyan K, Tekmen I, Bagriyanik H, Sonmez U, Sonmez A, Oktay G, Yener N, Ozbal S. The protective effects of carnosine in alcohol-induced hepatic injury in rats. Toxicol Ind Health. 2014;30(1):25-32.
76. Ji YS, Park JW, Heo H, Park JS, Park SW. The neuroprotective effect of carnosine (beta-alanyl-L-histidine) on retinal ganglion cell following ischemia-reperfusion injury. Curr Eye Res. 2014;39(6):634-641.
77. Dai Z, Lu XY, Zhu WL, Liu XQ, Li BY, Song L, Liu HF, Cai WW, Deng YX, Xu TT, Wang Q, Zhang SJ. Carnosine ameliorates age-related dementia via improving mitochondrial dysfunction in SAMP8 mice. Food Funct. 2020;11(3):2489-2497.
78. Ma J, Xu X, Wang R, Yan H, Yao H, Zhang H, Jiang S, Xu A. Lipopolysaccharide exposure induces oxidative damage in Caenorhabditis elegans: protective effects of carnosine. BMC Pharmacol Toxicol. 2020;21(1):85.
79. Cao Y, Xu J, Cui D, Liu L, Zhang S, Shen B, Wu Y, Zhang Q. Protective effect of carnosine on hydrogen peroxide-induced oxidative stress in human kidney tubular epithelial cells. Biochem Biophys Res Commun. 2021;534:576-582.
80. Wang H, Fang Z, Qiu G, Zhang C, Tang M, Zhou B. Bioprotective and Functional Effect of Carnosine on Sepsis Induced Renal Damage in Male Albino Rat Model through Targeting IL-1beta and TNF-alpha Production. Dokl Biochem Biophys. 2021;500(1):408-414.
81. Ishii T, Mori-Kobayashi K, Nakamura S, Ohkura S, Matsuyama S. Carnosine supplementation in cryopreservation solution improved frozen-thawed bovine embryo viability. J Reprod Dev. 2024;70(5):279-285.
82. Zhuang L, Lee CS, Scolyer RA, McCarthy SW, Zhang XD, Thompson JF, Hersey P. Mcl-1, Bcl-XL and Stat3 expression are associated with progression of melanoma whereas Bcl-2, AP-2 and MITF levels decrease during progression of melanoma. Mod Pathol. 2007;20(4):416-426.
83. Ma J, Song X, Xu X, Mou Y. Cancer-Associated Fibroblasts Promote the Chemo-resistance in Gastric Cancer through Secreting IL-11 Targeting JAK/STAT3/Bcl2 Pathway. Cancer Res Treat. 2019;51(1):194-210.
84. Oritani K, Tomiyama Y, Kincade PW, Aoyama K, Yokota T, Matsumura I, Kanakura Y, Nakajima K, Hirano T, Matsuzawa Y. Both Stat3-activation and Stat3-independent BCL2 downregulation are important for interleukin-6-induced apoptosis of 1A9-M cells. Blood. 1999;93(4):1346-1354.
85. Sepulveda P, Encabo A, Carbonell-Uberos F, Minana MD. BCL-2 expression is mainly regulated by JAK/STAT3 pathway in human CD34+ hematopoietic cells. Cell Death Differ. 2007;14(2):378-380.
86. Lee JK, Won C, Yi EH, Seok SH, Kim MH, Kim SJ, Chung MH, Lee HG, Ikuta K, Ye SK. Signal transducer and activator of transcription 3 (Stat3) contributes to T-cell homeostasis by regulating pro-survival Bcl-2 family genes. Immunology. 2013;140(3):288-300.

# SUPPLEMENTARY INFORMATION

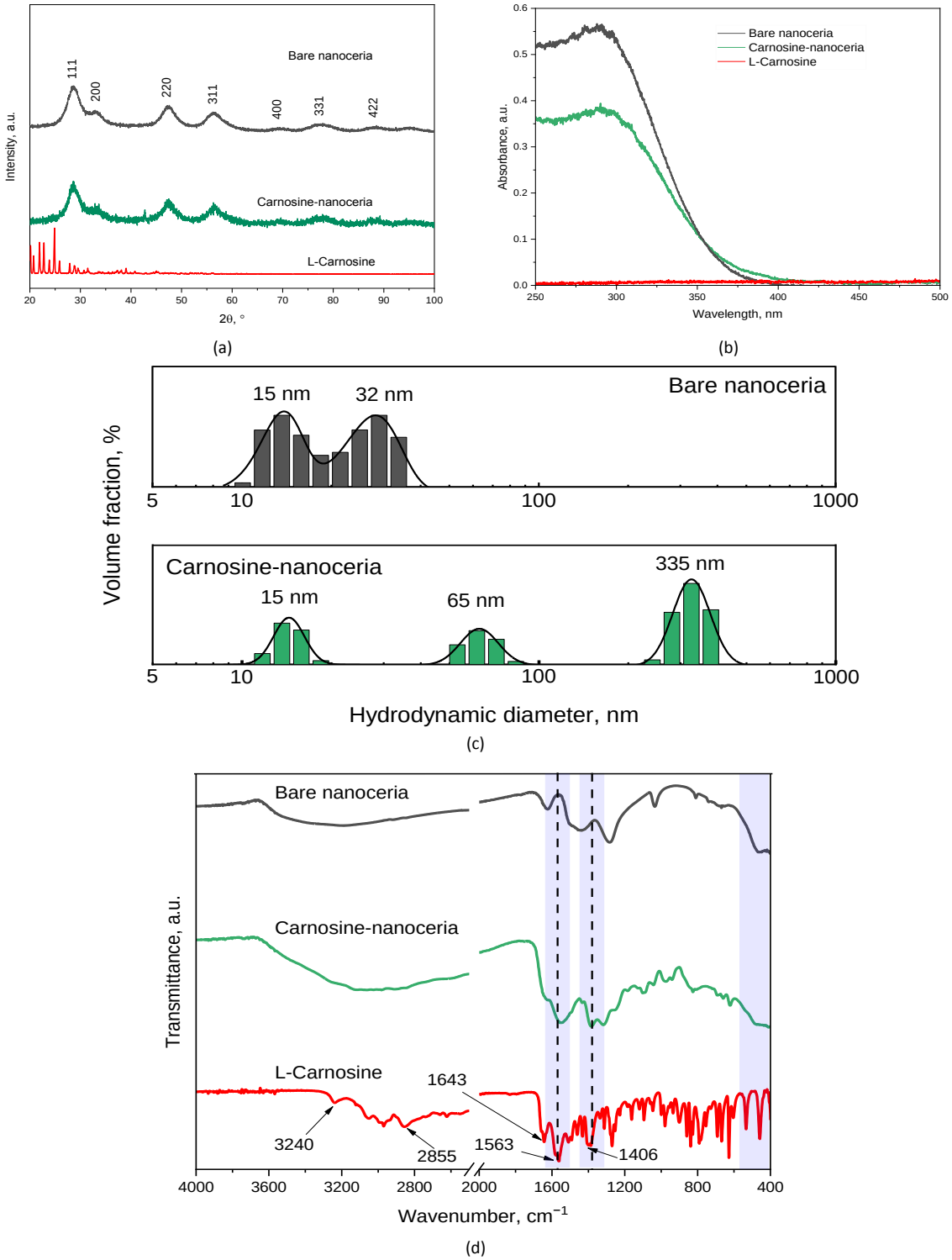


Fig. S1. (a) XRD patterns of the dried ceria sols and pure carnosine; (b) UV-Vis absorption spectra of the ceria sols and pure carnosine; (c) hydrodynamic diameter distributions of the ceria sols; (d) FTIR spectra of the nanoceria sols and pure carnosine.

RESEARCH PAPER

# Curcumin/Ag conjugated nanoparticles confer neuroprotection against hyoscine-induced acute psychosis: behavioral and biochemical evidence

***Setayesh Abdolkarimi[1#], Mahsa Salehirad[1#], A. Wallace Hayes[2], Majid Motaghinejad[3*], Malak Hekmati[4]***

*[1] Department of Pharmaceutical Chemistry, Faculty of Pharmaceutical Chemistry, Tehran Medical Sciences, Islamic Azad University, Tehran, Iran*
*[2] University of South Florida College of Public Health, Tampa, FL, USA and Institute for Integrative Toxicology, Michigan State University, East Lansing, MI, USA*
*[3] Pediatric Respiratory Disease Research Center, National Research Institute of Tuberculosis and Lung Disease, Shahid Beheshti University of Medical Sciences, Tehran, Iran*
*[4] Department of Organic Chemistry, Faculty of Pharmaceutical Chemistry, Tehran Medical Sciences, Islamic Azad University, Tehran, Iran*

***# Equal first authors***

**ABSTRACT**

***Obejctive(s):*** Psychosis is a prevalent psychiatric disorder. Chemicals that modulate the dopaminergic system have been the primary treatment, but these drugs have not always been effective, and some have deleterious side effects. During the last several years, a concerted effort has been made to advance the development of novel pharmaceuticals, utilizing approaches such as nanotechnology, natural compounds, and Eastern medicinal practices. Nanotechnology, including Ag-based nanoparticles, is an exciting option for optimizing drug performance, including reduced side effects and improved pharmacological and clinical profiles. The impact of curcumin-Ag conjugated nanoparticles (Cur/Ag NPs) was evaluated in a rodent model of psychosis.

***Materials and Methods:*** Cur/Ag NPs were synthesized and characterized by FTIR, FE-SEM, EDX, and UV-vis spectrophotometry. The effect of Cur-Ag NPs was determined for several psychosis-related behaviors (Yawning number, rearing number, and stereotype score) and blood levels of the inflammatory factors CRP, TNF-α, and IL-1β, and cortisol in an animal model of hyoscine-induced psychosis.

***Results:*** Cur/Ag NPs modulated the Yawning number, rearing number, and stereotypic score in hyoscine-induced acute psychosis and attenuated the blood levels of inflammatory parameters, including TNF-α, IL-1β, C-reactive protein, and cortisol. Cur/Ag NPs demonstrated greater efficacy compared to curcumin, altering these effects at lower concentrations.

***Conclusion:*** Cur/Ag NPs and Curcumin were effective in a mouse model of psychosis, exhibiting protective effects against hyoscine-induced acute psychosis, and may be potential candidates for further clinical investigation for treating psychosis-related behavior.

***Keywords:*** *Psychosis; Curcumin/Ag conjugated nanoparticles; Curcumin.*

**How to cite this article**

*Abdolkarimi S, Salehirad M, Hayes A.W, Motaghinejad M, Hekmati M. Curcumin/Ag conjugated nanoparticles confer neuroprotection against hyoscine-induced acute psychosis: behavioral and biochemical evidence. Nanomed J. 2026; 13(2): 327-343. DOI: 10.22038/NMJ.2026.86441.2178*

**ABBREVIATIONS**

**AD:** Alzheimer Disease, **Ag:** Silver, **BSA:** Bovine Serum Albumin, **C.longa:** *Curcuma longa*, **CRP:** C-Reactive Protein, **Cur:** Curcumin, **Cur-Ag NPs:** Curcumin-silver nanoparticles, **ddH2O:** Double-distilled water, **EDS:** Energy Dispersive X-ray Spectroscopy, **ELISA:** Enzyme-Linked Immunosorbent Assay, **FESEM:** Field emission scanning electron microscope, **FTIR:** Fourier transform infrared, **GPx:** Glutathione Peroxidase, **GR:** Glutathione Reductase, **HAL:** Haloperidol, **HYO:** Scopolamine, **IL-1β:** Interleukin-1 beta, **KOH:** Potassium Hydroxide, **MAP:** Mapping Analysis, **NPs:** nanoparticles, **PD:** Parkinson Disease, **RNS:** Reactive Nitrogen Species, **ROS:** Reactive Oxygen Species, **SOD:** Superoxide Dismutase, **TNF-α:** Tumor Necrosis Factor-alpha, **UV-Vis:** ultraviolet-visible spectroscopy, **XRD:** X-ray diffractometer.

## INTRODUCTION

Schizophrenia is a neurobehavioral and psychiatric disorder that involves a combination of genetics and brain chemistry [1, 2]. A proposed mechanism involves the excessive production of gamma-aminobutyric acid (GABA)- ergic neurons, which utilize GABA as their neurotransmitter. GABAergic neurons are found in

* *Corresponding author:* Majid Motaghinejad, Pediatric Respiratory Disease Research Center, National Research Institute of Tuberculosis and Lung Disease, Shahid Beheshti University of Medical Sciences, Tehran, Iran. Tel: +98 21 26109484, Fax: +98 21 26109680, Emails: Dr.motaghinejad6@gmail.com.

Note. This manuscript was submitted on March 01, 2025; approved on October 01, 2025.

the hippocampus, thalamus, basal ganglia, hypothalamus, and brainstem, significantly impacting dopamine secretion and dysfunction through the mesocortical-mesolimbic nucleus pathways [3, 4].

It has been suggested that increased dopamine levels or activity in the nucleus of the mesolimbic system is associated with the emergence of positive symptoms. At the same time, decreases are manifested as negative symptoms [5, 6]. Several models for the induction of psychosis, most of which are based on increasing dopamine and decreasing the cholinergic system, are available [7-10]. Scopolamine (hyoscine) can cause symptoms similar to acute psychosis in rodents [7-9, 11-13]. Other drugs, such as ketamine and apomorphine, induce chronic psychosis [12, 14-16]. Accordingly, and considering the pharmacological properties of hyoscine in inhibiting the cholinergic system and enhancing dopaminergic, and on substantial evidence of psychosis induction following its use in humans, as well as our pilot study and published literature [7-9, 17], we selected hyoscine as the psychosis-inducing agent for our study [7-9, 11-13].

The acute phase of schizophrenia involves altered inflammatory parameters that affect behavioral disorders [1, 2, 18, 19]. Chemicals that modulate the dopaminergic system have been the primary treatment, but these drugs have not always been effective, and some have deleterious side effects [5, 6, 20-22]. Therefore, during the last several years, research has focused on developing new drugs, including strategies employing nanotechnology, natural compounds, and Eastern medicines [23, 24].

Curcumin, the primary ingredient in turmeric, is a pharmacologically active, safe, accessible, and effective natural product [25, 26]. Curcumin demonstrates a variety of pharmacological effects, including free radical scavenging, anti-inflammatory activity, inhibition of cell proliferation, antimicrobial effects, pain relief, antimalarial activity, tumor suppression, induction of programmed cell death, and inhibition of new blood vessel formation [26-29].

Nanotechnology, including Ag-based nanoparticles [30-33], is an exciting option for optimizing drug performance, including reduced side effects and improved pharmacological and clinical profiles [30-33]. Curcumin nanoparticles as modulators of neurobehavioral and neurologic disorders such as anxiety, depression, PD, and AD have been investigated, but the involvement of curcumin nanoparticles in the management of schizophrenia and psychotic-like disorders has not been evaluated [34]. Effects exerted by curcumin-Ag conjugated nanoparticles on several inflammatory parameters were assessed in a rat model of acute psychosis.

## MATERIALS AND METHODS

### *Agents and Materials*

Curcumin, silver nitrate ($AgNO_3$), ethanol, and potassium hydroxide were obtained from Merck (New Jersey, USA). Reagents were of analytical grade and applied as supplied (DNA Co, Iran, Tehran).

### *Synthesis of curcumin-Ag conjugated nanoparticles*

An eco-friendly method capitalizing on curcumin's reductive and stabilizing properties was used for synthesizing the curcumin-Ag conjugated nanoparticles [35, 36]. Curcumin (5mg) was dissolved in 50 mL of double-distilled water at neutral pH and heated to 85–90°C, resulting in an orange-colored solution. Fifty mL of a silver nitrate solution (0.1 M) was gradually added to the orange-colored solution, yielding a yellow-colored solution. This mixture was refluxed at 85–90°C for one hour and cooled to 4°C. The solution was brought to a pH of about 8 using potassium hydroxide (0.1 M), during which the color transitioned from yellow to pale yellow and ultimately to dark orange, accompanied by the emergence of brown, flaky precipitates.

The silver ions ($Ag^+$) interacted with curcumin to form a stable silver-curcumin complex, stabilizing the ions and initiating the reduction process (Equation 1). The aldehyde group in curcumin (R-CHO), the reducing agent, was oxidized to carboxylic acid (R-COOH). At the same time, the reduction of silver ions in the complex formed metallic silver nanoparticles (Equation 2). This mechanism also promoted nucleation and stabilized the nanoparticles in a colloidal state.

(1) $Ag^+(aq) + Curcumin \rightarrow [Ag(Curcuma.longa)]^+$

(2) $[Ag(C.longa)]^+ + R–CHO \rightarrow [Ag(Curcuma.longa)]^+ + R–COOH$

### *Characterization studies of nanoparticles*

The Cur/Ag NPs were characterized using analytical techniques to confirm their structural, compositional, and morphological properties. UV-Vis spectroscopy monitored the optical properties and validated the successful formation of nanoparticles by identifying characteristic plasmon resonance peaks. The crystallographic structure was determined using XRD, providing insights into the crystalline and lattice arrangement of the nanoparticles.

The Cur/Ag NPs' elemental composition and distribution were analyzed using EDS and MAP, which determined elemental ratios and their spatial dispersion within the nanoparticles. FESEM was utilized to investigate the nanoparticles' surface morphology, size, and shape, offering high-resolution visualizations of the nanoscale architecture.

FTIR identified functional groups and confirmed the interaction between curcumin and silver ions. This analysis also provided information about the nanoparticles' stability and potential surface modifications. These techniques allowed an understanding of the physicochemical properties and structural integrity of the Cur/Ag NPs.

***Stability of curcumin-Ag conjugated nanoparticles***

The stability of the curcumin-Ag conjugated nanoparticles is influenced by the chemical interaction between functional groups of Cur and silver ions, forming a robust bond that enhances the nanoparticle integrity. These nanoparticles exhibited remarkable stability due largely to curcumin's antioxidant and reducing properties, which prevented oxidation and agglomeration of silver particles. FTIR and XRD analyses confirmed the nanoparticles' strong coordination and crystalline structure, indicating resistance to degradation over time. Additionally, their stability was further validated by energy dispersive spectroscopy, which revealed a uniform elemental distribution. These morphological observations were confirmed through electron microscopy.

***In-vivo study***

***Animals***

One hundred and forty-four male and 50 female BALB/c mice (30–35g) were purchased from Experimental Animal Center of IUMS and held for two weeks before initiating experimental procedures. Animals have free access to water and animal special pellet feed (Parsfeed Co, Tehran, Iran). The animal house was controlled with standard room temperature: 22 ± 2°C; relative humidity: 5-40%; and light/dark cycles (12-hour). Both series of animal protocols were confirmed and approved by the ethics committees of research at the Pharmacy and Pharmaceutical Branches Faculty at Islamic Azad Tehran Medical Sciences University [Protocol and Ethical Code Number: IR. IAU.PS.REC.1398.348] [37]. Signs of toxicity were evaluated in the animals 24 hours after treatment and continuously during weeks one and two.

***Experimental animal procedure***

***Pilot study evaluating the toxicity of the eco-friendly synthesized nanoparticles***

Mice (8/sex/group) were administered intraperitoneally 1000, 1250, 1500, 1750, or 2000 mg/kg Cur/Ag NPs and observed for behavioral changes and signs of toxicity throughout the initial 24 hours and daily for two weeks. Brain, liver, heart, testes, and lungs were prepared for histopathological evaluation. This evaluation showed normal cellular architecture without evidence of inflammation, degeneration, or necrosis; thus, this nanoparticle [38, 39].

***Effect of curcumin-Ag conjugated nanoparticles on behavioral and molecular changes in a rodent psychosis model*** (Fig. 1)

Male mice (8/group) were randomly divided into eight groups as follows:

- Group 1: received 0.2 mL of normal saline (control).
- Group 2: Hyoscine (HYO) (0.125 mg/kg).
- Group 3: HYO (0.125 mg/kg) and haloperidol (HAL) (5 mg/kg).
- Groups 4-6: HYO (0.125 mg/kg) and Cur/Ag NPs (20, 40 and 60 mg/kg).
- Group 7: HYO (0.125 mg/kg) and also Cur (40 mg/kg).
- Group 8: HYO (0.125 mg/kg) and Ag (40 mg/kg).

All treatments were given intraperitoneally (ip). The main experimental procedures, protocol and also associated timeline are schematically illustrated in Figure 1. Dose selection for HYO [10, 40-42], HAL [43-46], Cur [30, 47, 48], and Ag[49, 50] was based on the literature. Cur/Ag NPs doses were chosen based on previous results [51-53]. In groups 3–8, injections were administered at one-hour intervals. Psychosis-related behavior (Yawning number, rearing number, and stereotype score) was observed as early as one hour after drug administration in the experimental groups but not in control animals.

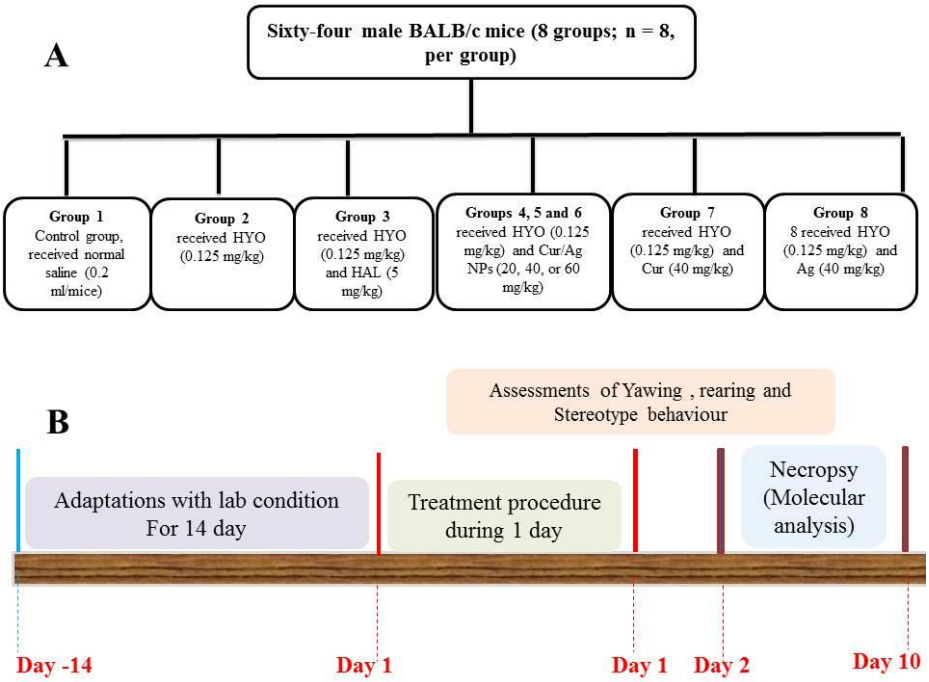


Fig. 1. (A) Schematic illustration of experimental grouping and (B) Timeline for experimental procedure and evaluation

***Investigation of rearing responses induced by novelty***

Central excitatory locomotor behavior was evaluated by a blinded observer using novelty-induced rearing behavior [54-56] in a transparent Plexiglas chamber (50 cm ×30 cm × 30 cm). The number of rearing was characterized by the number of standings on their hind limbs or standing with their forelimbs against the wall of the observation box or free in the air. Rearing behavior was measured over 10 minutes [54, 55]. The testing chamber was cleaned with 10% ethanol between testing runs to eliminate potential olfactory bias [54-56].

***Behavioral assessment of Yawning***

Yawning behavior, a standard behavior in rodents that closely mimics psychosis [56-58], is characterized by prolonged (more than 1 s) and a significant mouth opening, quickly succeeded by closure [56, 57]. This behavior was evaluated by a blinded observer observing the Yawning behavior of the mice in a transparent Plexiglas chamber (50 cm ×30 cm × 30 cm). Yawning was measured over 10 minutes, and the testing chamber was cleaned with 10% ethanol between testing runs to prevent possible olfactory interference [56-58].

***Assessment of stereotypic behavior***

Stereotypic behaviors are a series of standard psychosis-related behaviors that can be observed in rodents [59-61]. The signs of stereotypy sniffing and gnawing are scored as follows: absence of stereotypy was scored as 0, occasional sniffing was scored as 1, occasional sniffing with occasional gnawing was scored as 2, frequent gnawing was scored as 3, intense continuous gnawing was scored as 4, and marked gnawing activity along with staying in place was scored as 5 [59-61]. Scores are summed over 10 minutes for each animal. A blinded observer determined scores while the animals were in the transparent Plexiglas chamber (50 cm ×30 cm × 30 cm).

After the behavioral assessments, Animals were subjected to thiopental sodium-induced anesthesia (50 mg/kg) and then euthanized. Blood samples were collected directly from the heart to measure inflammatory factors such as TNF-alpha, CRP, IL-1beta, and cortisol levels. Samples were centrifuged and stored at -20 °C until analyzed.

***Assessment of blood cortisol level***

The cortisol concentration (µg/dL) was measured using electrochemical luminescence kits (DNA Co., Tehran, Iran) [62, 63]. Results are reported as µg/dL [62, 63].

***Measurements of total protein***

Total protein levels were quantified using the Bradford special assay kit (Bio-Rad, Providence, RI, USA). A standard protein curve was constructed with BSA using serially diluted BSA solutions in the range of 0.1–1.0 mg/mL. Zero, 0.5, 10, 15, 20, 25, 30, or 35 µL of serum was added to separate wells, and then the Bradford reagent was added. Using a Hiperion Microplate Reader (MPR4+, Rayto Company, China),

absorbance between 630 and 635 nm was recorded to evaluate protein content in each well [64-66].

***Assessment of TNF-α, IL-1β and CRP***

Commercial Enzyme-linked immunosorbent assay (ELISA) and antibody-based kits (Sino Biological Co., Eschborn, Germany) for TNF-α (SEK50349), IL-1β (50101-R001), and CRP ( KIT11250A) were used to determine serum levels of CRP, TNF-α, and IL-1β. Sheep anti-mouse TNF-α, IL-1β, and CRP polyclonal antibodies (Sino Biological CO, Eschborn, Germany) were washed three times with a wash buffer (0.5M NaCl, 2.5mM $Na_{H2}PO_4$, 7.5mM $Na_2HPO_4$, 0.1% Tween 20), pH, 7.2. In individual wells, ovalbumin solution [100µL of 1% (w/v)] (Sigma Chemical Co., Poole, Dorset, U.K.) was added and maintained at room tmeparture with 37° C for 1.5 hours. All wells were then washed three times with the provided buffer solution. One hundred µL of standard solution or sample was added to all wells and incubated at 45 °C for 24 hours. Then, all wells were washed (3 times with the buffer), and 100 µL of sheep-based TNF-α, IL-1β, or CRP antibody was added to the appropriate wells (Antibodies diluted as 1:1000 in wash buffer containing 1% sheep serum, Sigma Chemical Co., Poole and Dorset, U.K.). All wells were incubated at room temperature for 60 minutes and washed three times with the buffer solution. Next, 100µL of Avidin-HRP (Dako Ltd, U.K.), diluted 1:5000 in wash buffer, was added to each well, followed by incubation for 20 minutes. All wells were washed (3 times) with the wash buffer, and 100µL of TMB substrate (3,3',5,5'-Tetramethylbenzidine) solution (Dako Ltd., U.K.) was added to each well and incubated (16 min) at room temperature. In the final step, 100µL of 1M $H_2SO_4$ was added to all wells to stop the reaction. Optical density was read at 450 nm, and results for TNF-α, IL-1β, and CRP are given in pg/mL [67-70].

***Statistical analysis***

All statistical evaluations and analyses were performed with special software, GraphPad PRISM v.6 (2016) (GraphPad Company, San Diego, USA). The mean ± standard deviation (SD) was calculated for all parameters and all experiments, then analyzed by a one-way ANOVA (Analysis of Variance), *F*-test. Differences and comparisons between each group were evaluated using Bonferroni's post-hoc test. The continuous variables were confirmed to follow a normal distribution by Kolmogorov-Smirnov test, and Levene's or Bartlett's test was used for analysis of variance consistency among groups. Data met ANOVA assumptions of normality (Kolmogorov-Smirnov, P>0.05) and equal variances (Levene's test, P>0.05), justifying the use of parametric tests. P<0.05 was considered significant. For each experimental parameter, the number in parentheses indicates the F (7, 56) statistic, with the subsequent P value provided.

**RESULT**

***Cur/Ag NPs synthesis***

The successful/effective synthesis of the Cur/Ag NPs was confirmed.

***FT-IR spectroscopy characterization***

The FT-IR spectrum of the curcumin-silver nanoparticles, illustrated in Figure 2, offers insights into the nanoparticle's chemical functionality and surface modification. Although signals associated with carbon-carbon bonds are common in organic compounds, they generate overlapping bands that are generally weak and do not provide clear diagnostic information. A broad absorption band in the 2400–3450 $cm^{-1}$ range was observed, indicative of hydroxyl (–OH) stretching vibrations. This feature was attributed to oxidative processes introducing hydroxyl and carboxyl functional groups at the surface of the nanoparticle, which play a significant role in surface stabilization and functionalization.

A significant peak in the absorption spectrum at 1627 $cm^{-1}$ corresponded to the stretching vibration of carbonyl (C=O) groups, while the band at 1278 $cm^{-1}$ was assigned to C–O stretching vibrations, highlighting the presence of ester or phenolic functional groups, supporting the chemical interaction between curcumin and silver ions in forming and stabilizing the nanoparticle. The peaks at 1510 $cm^{-1}$ and 1514 $cm^{-1}$ were associated with the aromatic C=C stretching vibrations intrinsic to the curcumin structure. The peaks confirmed that curcumin retained its aromatic structure, which is essential for its biochemical activity.

The absorption bands at 3014 $cm^{-1}$ and 3049 $cm^{-1}$ represented $sp^2$-hybridized alkenyl (C–H) stretching vibrations, while the band at 2972 $cm^{-1}$ indicated the presence of $sp^3$-hybridized aliphatic (C–H) bonds. These characteristic functional groups and vibrational modes provided an extensive insight into the molecular interactions and surface chemistry of the curcumin-silver nanoparticles. The FTIR analysis indicated a shift to lower stretching frequency values, suggesting effective coordination between curcumin's functional groups and silver ions. This shift signified strong interaction and stabilization during the nanoparticle synthesis process. These results support the successful synthesis of curcumin-silver nanoparticles.

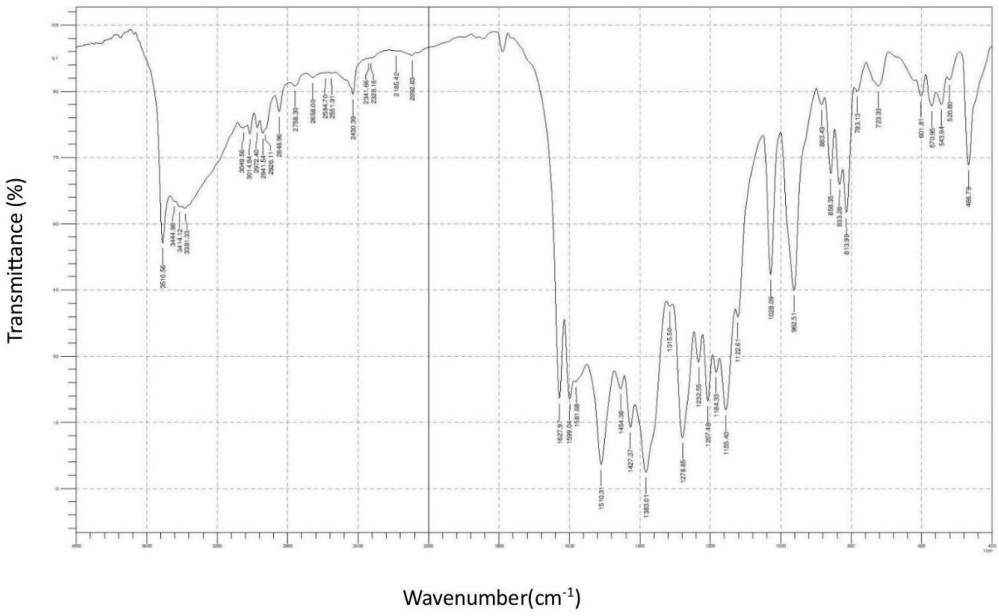


Fig. 2. FT-IR spectrum of Cur/Ag NPs

***Characterization by UV–Vis spectrophotometry***

The UV-Vis analysis identified a strong absorption peak at 428 nm (Figure 3), confirming the successful formation of silver nanoparticles. This peak affirmed the nanoscale size and interaction with curcumin. It also highlights the coordination between silver and curcumin's functional groups, demonstrating effective stabilization and synthesis of nanoparticles.

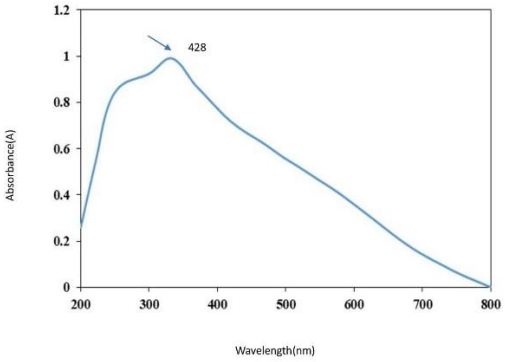


Fig. 3. UV-Vis analysis of Cur/Ag NPs

***Morphological insights from FESEM and EDX studies***

The FESEM (Figure 4) spectrum provided further evidence of successful nanoparticle formation. The results confirmed that curcumin effectively acted as a reducing agent, converting silver ions into silver nanoparticles. Additionally, the morphology of the nanoparticles and the identification of their constituent profile are illustrated in the following figures, offering additional validation of the structural characteristics of the curcumin-silver nanoparticles. The constituent elements of the curcumin–silver nanoparticles produced were characterized through EDS (Figure 5). EDS results validated the detection of silver (Ag), chlorine (Cl), carbon (C), nitrogen (N) and oxygen (O) as constituents of the nanoparticles. Figure 6 illustrates the elemental mapping, showcasing the presence of C, N, O, Cl, and Ag in the curcumin-silver nanoparticles. High-resolution FESEM images combined with EDS analysis further confirmed the successful incorporation of silver, revealing its even distribution throughout the curcumin matrix. This consistency highlighted the contribution of curcumin as an efficient reducing and stabilizing factor during the synthesis process. Figure 7 offers a spatial visualization of the elements, showing the successful incorporation of silver nanoparticles within the curcumin-silver framework and verifying the presence of silver while demonstrating its uniform distribution alongside carbon, nitrogen, oxygen, and chlorine.

***XRD analysis***

The diffraction pattern revealed the crystalline lattice structure of the silver metal nanoparticle. As shown in Figure 8, the diffraction peak at 23.8° was attributed to the presence of hexagonal graphite. The diffraction pattern exhibited strong signals at 38.1°, 44.3°, 64.4°, 77.4°, and 81.5°, consistent with silver's crystallographic planes, confirming the crystalline state of silver and the proper synthesis of curcumin–silver nanoparticle. The matching diffraction peaks with standard silver patterns further demonstrated the reliability of the synthesis process.

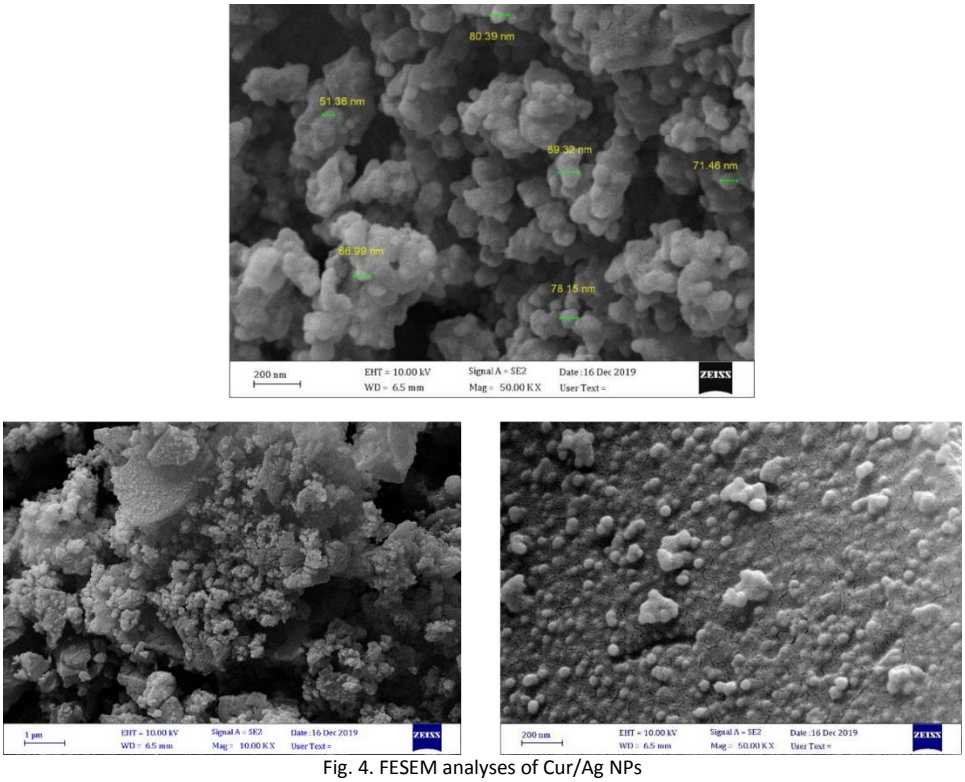


Fig. 4. FESEM analyses of Cur/Ag NPs

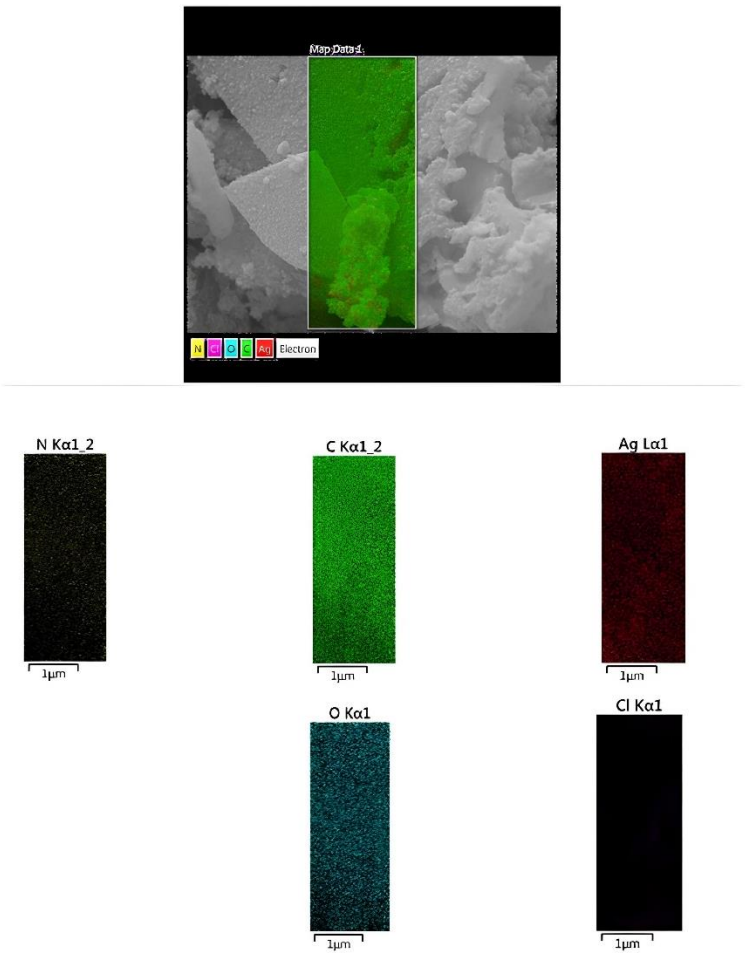


Fig. 5. EDS analyses of Cur/Ag NPs

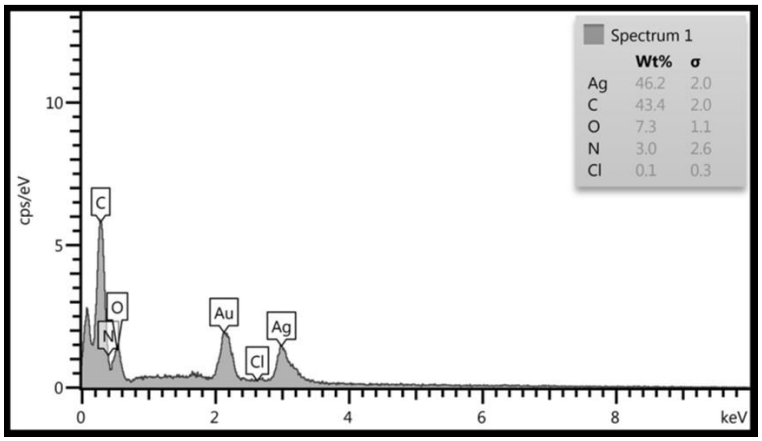


Fig. 6. Elemental mapping of Cur/Ag NPs

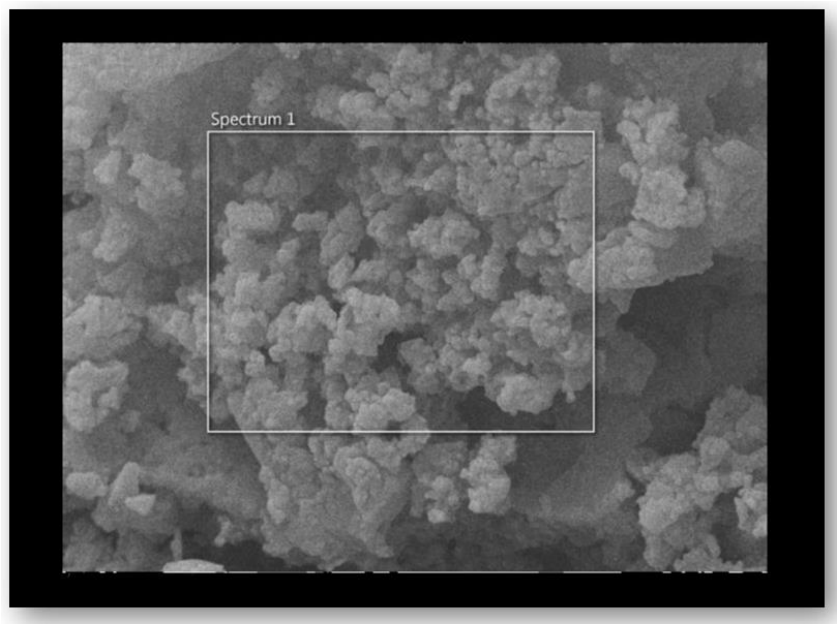


Fig. 7. FESEM combined with EDS of Cur/Ag NPs

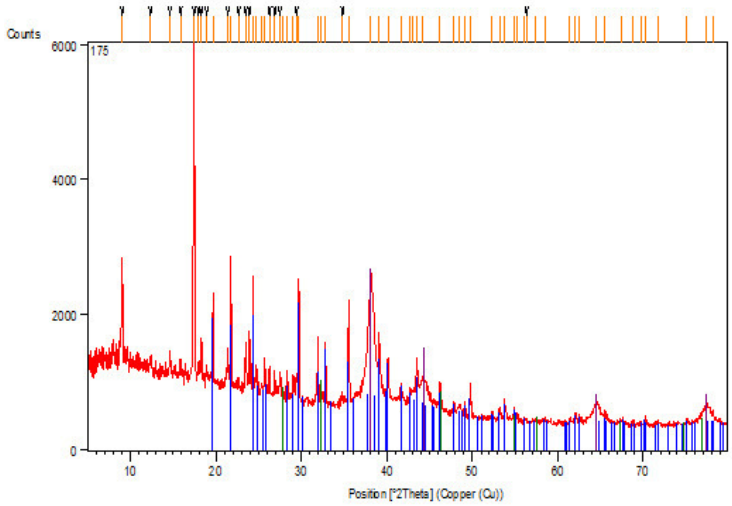


Fig. 8. XRD analyses of Cur/Ag NPs

***Cur/Ag NPs effects against psychosis related behavior***

***Cur/Ag NPs effects on HYO-prompted CHANGES in rearing behavior***

HYO (0.125 mg/kg) increased rearing number (6.600; P<0.05). HAL (5 mg/kg) reduced the rearing number in the HYO (0.125 mg/kg) treated mice (6.600; P<0.05) (Figure 9). Cur/Ag NPs with doses of 40 or 60 mg/kg reduced the rearing number in HYO-treated mice (6.600; P<0.05). Cur (40 mg/kg) and Ag (40 mg/kg) did not alter the rearing number in HYO-treated mice (Figure 9).

***Cur/Ag NPs effects on HYO-prompted changes in Yawning behavior***

HYO (0.125 mg/kg) increased the Yawning behavior (5.323; P<0.05) (Figure 10). HAL (5 mg/kg) reduced the Yawning behavior in HYO-treated mice (5.323; P<0.05) (Figure 10). Cur/Ag NPs with doses of 40 and 60 mg/kg also reduced Yawning behavior in the HYO-treated mice (5.323; P<0.05). Cur as 40 mg/kg and Ag, with a dose of 40 mg/kg did not change the Yawning behavior in HYO-treated mice (Figure 10).

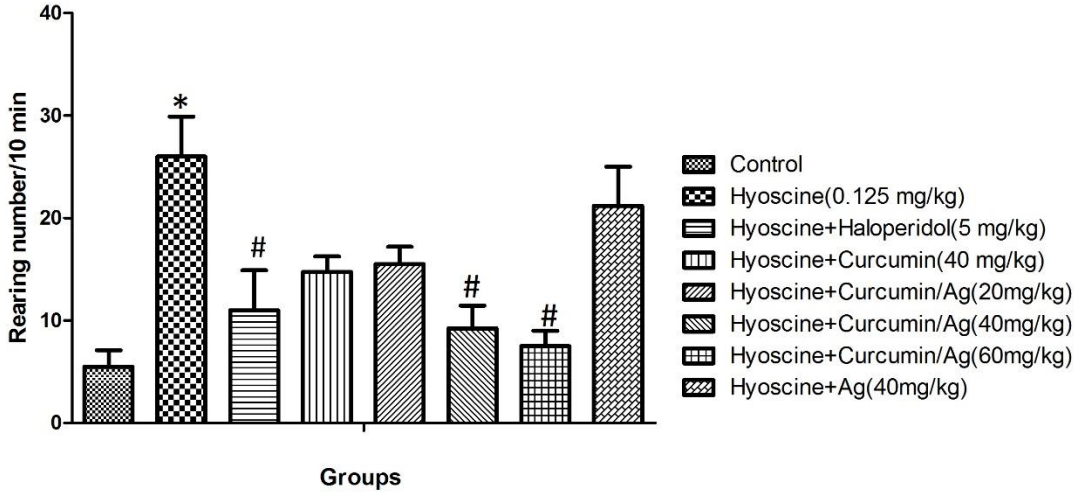


Fig. 9. Effects of Cur/Ag NPs on HYO-induced Alteration in Rearing Number.
Data are Mean ± SD (n=8). * P< 0.001 vs. control. # P< 0.001 vs. HYO (5 mg/kg).
HYO: Hyoscine, Cur: Curcumin, Cur/Ag N.P.s: Curcumin-silver nanoparticles, HAL: Haloperidol.

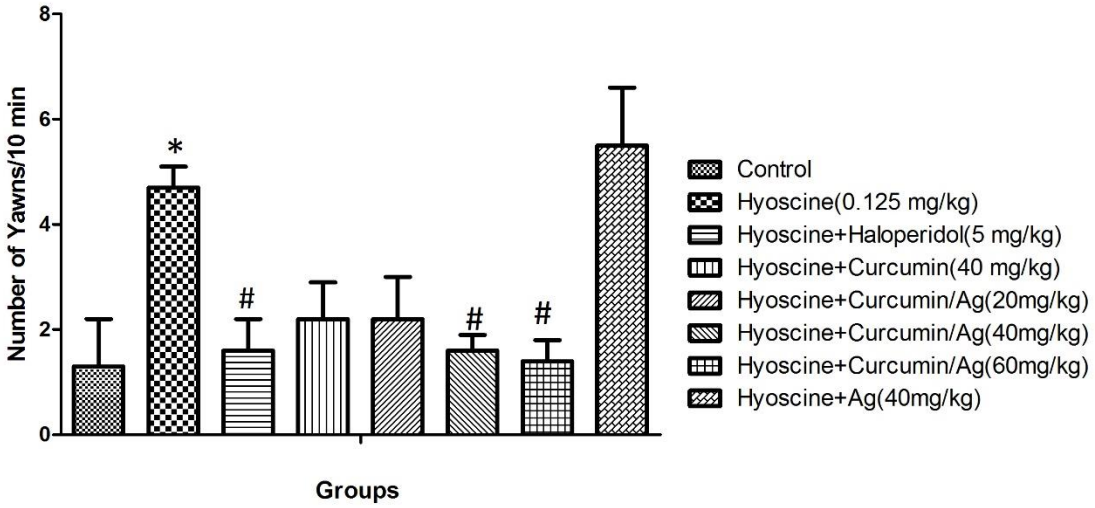


Fig. 10. Effects of Cur/Ag NPs on HYO-induced Alteration in Yawning Number.
Data are Mean ± SD (n=8). * P< 0.001 vs. control. # P< 0.001 vs. HYO (5 mg/kg).
HYO: Hyoscine, Cur: Curcumin, Cur/Ag N.P.s: Curcumin-silver nanoparticles, HAL: Haloperidol.

***Cur/Ag NPs effects on HYO- HYO-prompted changes in stereotype behavior***

HYO (0.125 mg/kg) increased stereotype behavior scores (4.553; P<0.05) (Figure 11). HAL (5 mg/kg) reduced the stereotype behavior scores in HYO (0.125 mg/kg) treated mice (4.553; P<0.05) (Figure 11). Cur as 40 mg/kg and Cur/Ag NPs with doses of 40 and 60 mg/kg reduced stereotype behavior scores in HYO (0.125 mg/kg) treated mice (4.553; P<0.05) (Figure 11). Ag (40 m/kg) did not change these scores in HYO (0.125 mg/kg) treated mice (Figure 11).

***Cur/Ag NPs effects against psychosis related inflammatory biomarkers***

***Cur/Ag NPs effect on HYO-induced changes in blood cortisol level***

HYO (0.125 mg/kg) increased blood cortisol levels (4.393; P<0.05) (Figure 12). HAL (5 mg/kg) reduced these levels in HYO (0.125 mg/kg) treated mice (4.393; P<0.05) (Figure 12). Cur as 40 mg/kg and Cur/Ag NPs with doses of 40 and 60 mg/kg reduced blood cortisol levels in HYO (0.125 mg/kg) treated mice (4.393; P<0.05) (Figure 12). Ag (40 m/kg) did not affect the blood cortisol levels in HYO (0.125 mg/kg) treated mice (Figure 12).

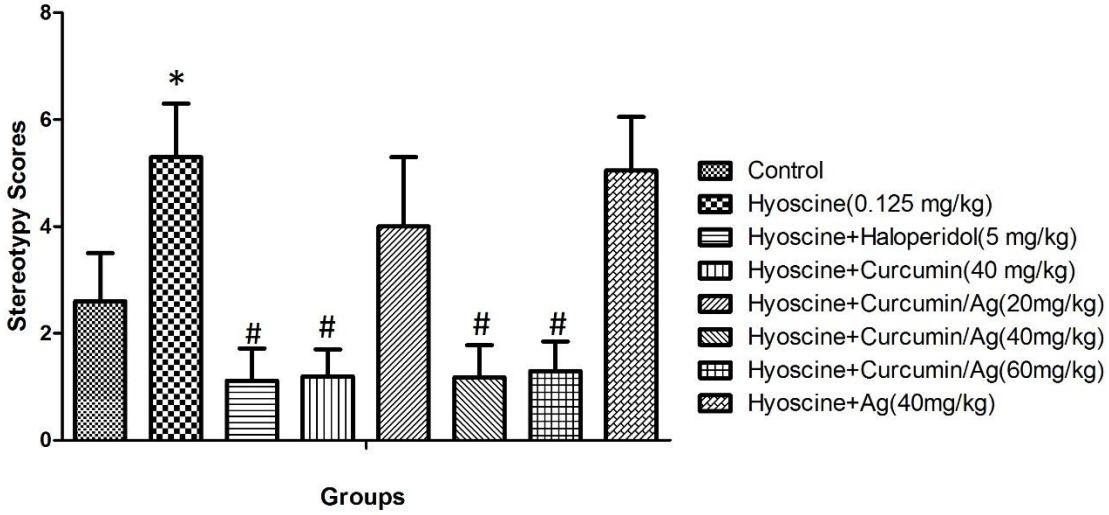


Fig. 11. Effects of Cur/Ag NPs on HYO-induced Alteration in Stereotype Score.
Data are Mean ± SD (n=8). * P< 0.001 vs. control. # P< 0.001 vs. HYO (5 mg/kg).
HYO: Hyoscine, Cur: Curcumin, Cur/Ag N.P.s: Curcumin-silver nanoparticles, HAL: Haloperidol.

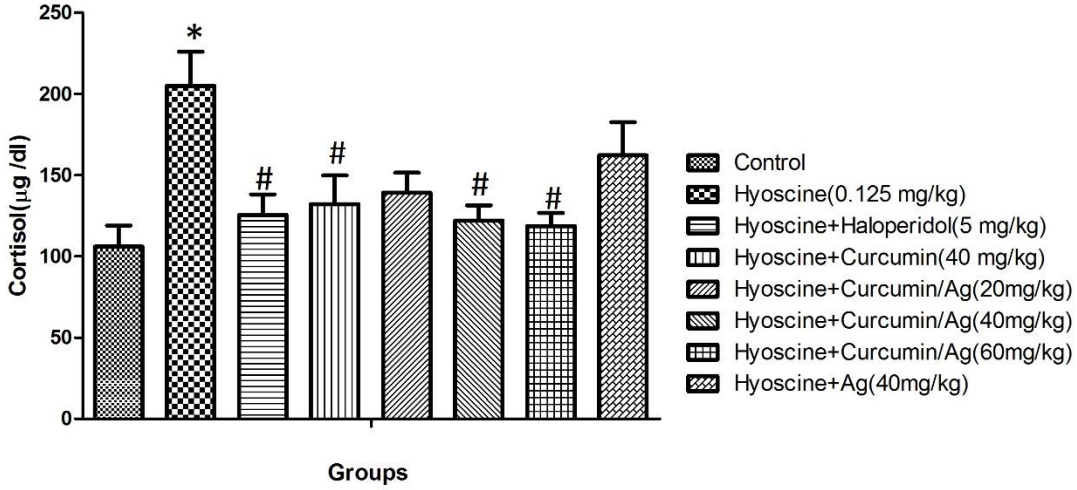


Fig. 12. Effects of Cur/Ag NPs on HYO-induced Alteration in Cortisol Level.
Data are Mean ± SD (n=8). * P< 0.001 vs. control. # P< 0.001 vs. HYO (5 mg/kg).
HYO: Hyoscine, Cur: Curcumin, Cur/Ag N.P.s: Curcumin-silver nanoparticles, HAL: Haloperidol.

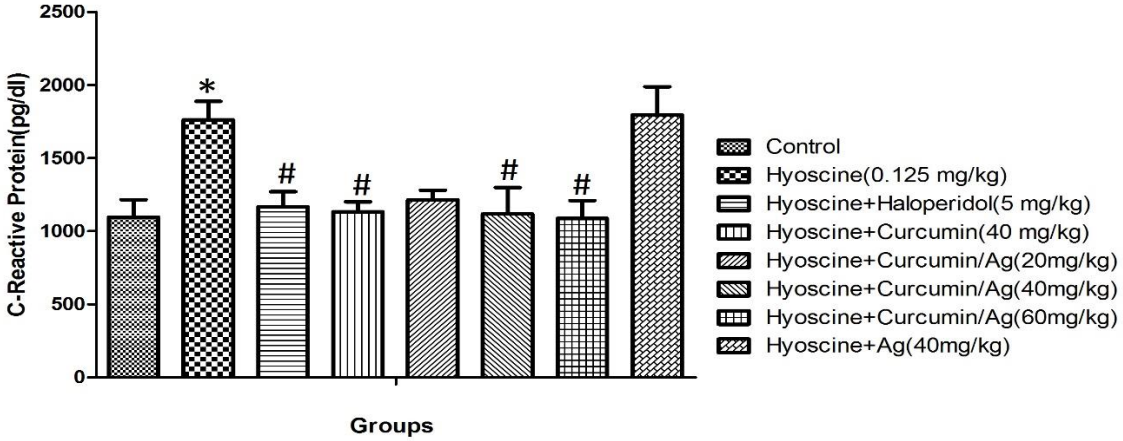


Fig. 13. Effects of Cur/Ag NPs on HYO-induced Alteration in C-reactive Protein Level.
Data are expressed as Mean ± SD (n=8). * P< 0.001 vs. control. # P< 0.001 vs. HYO (5mg/kg).
HYO: Hyoscine, Cur: Curcumin, Cur/Ag N.P.s: Curcumin-silver nanoparticles, HAL: Haloperidol.

***Cur/Ag NPs effect on HYO-induced changes in blood CRP level***

HYO (0.125 mg/kg) increased blood CRP levels (5.375; P<0.05) (Figure 13). HAL (5 mg/kg) reduced the blood CRP levels in HYO (0.125 mg/kg) treated mice (5.375; P<0.05) (Figure 13). Cur with doses of 40 mg/kg and Cur/Ag NPs with doses of 40 and 60 mg/kg reduced blood CRP levels in HYO (0.125 mg/kg) treated mice (5.375; P<0.05) (Figure 13). Ag (40 m/kg) did not change the blood CRP levels in HYO (0.125 mg/kg) treated mice (Figure 13).

***Cur/Ag NPs effect on HYO-induced changes in blood TNF-α, IL-1β level***

HYO (0.125 mg/kg) increased blood TNF-α (5.332; P<0.05) and IL-1β (6.466; P<0.05) levels (Figure 14 A and B). The analysis revealed stable levels of TNF-α in the blood (5.332) or IL-1β (6.466) in HYO (0.125 mg/kg) treated mice (Figure 14 A and B) given HAL (5 mg/kg). Cur with a dose of 40 mg/kg and Cur/Ag NPs as 40 and 60 mg/kg reduced blood TNF-α (5.332; P<0.05) and IL-1β (6.466; P<0.05) levels in HYO (0.125 mg/kg) treated mice (5.375; P<0.05) (Figure 14 A and B). Ag (40 m/kg) did not change the blood TNF-α (5.332) and IL-1β (6.466) levels in HYO (0.125 mg/kg) treated mice (Figure 14 A and B).

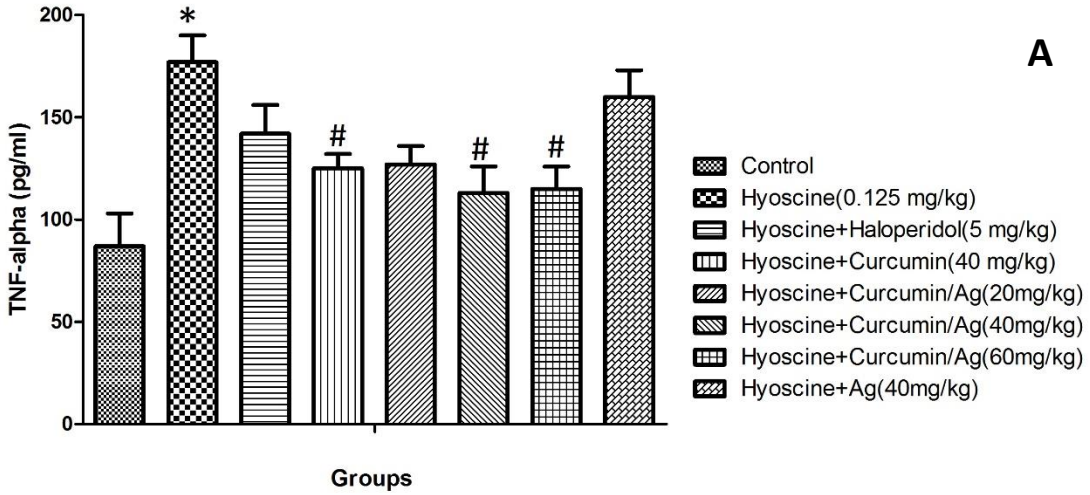

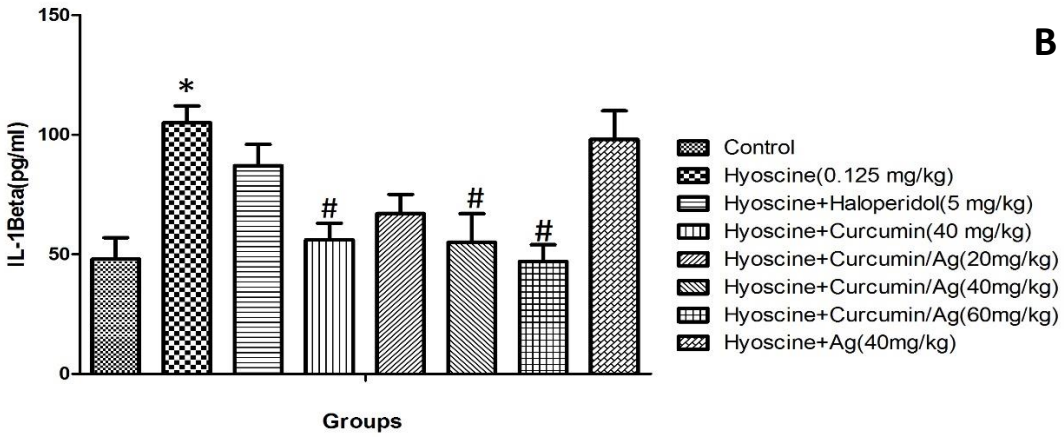


Fig.-14. Effects of Cur/Ag NPs on HYO induced alteration in TNF-α (A) and IL-1β (B) level.
Data are expressed as Mean ± SD (n=8). * P< 0.001 vs. control. # P< 0.001 vs. HYO (5mg/kg).
HYO: Hyoscine, Cur: Curcumin, Cur/Ag N.P.s: Curcumin-silver nanoparticles, HAL: Haloperidol.

**DISCUSSION**

As a chronic psychiatric illness, schizophrenia profoundly impacts cognitive functions, affective states, and social conduct. Managing schizophrenia requires ongoing treatment [1, 2]. Disorders of dopamine and secretion function in the nucleus of mesocortical-mesolimbic are primary mechanisms of psychosis [3, 4]. Most antipsychotic drugs, such as haloperidol (HAL), act by altering the amount and strength of dopamine and serotonin and/or their associated receptors [71, 72]. Several models, based on increasing dopamine levels and decreasing acetylcholine and glutamate, are available for the induction of psychosis in rodents [7-9, 11-13]. Hyoscine and ketamine are examples of drugs that induce acute psychosis in experimental animals. Hyoscine was used in our study to induce behavioral effects associated with acute psychosis [7-9, 11-13].

Neuroinflammation and increased systemic inflammatory status have critical roles in psychosis-related behavioral disorders [73-76]. Because of the increased inflammatory response in such disorders, new therapeutic strategies should consider targeting these molecular events [77, 78]. Thus, modulating or reducing neuroinflammation and systemic inflammation may be valuable targets for new drug development [79, 80]. Such anti-inflammatory drugs are likely to be more specific, hopefully, with fewer side effects than traditional antipsychotic drugs [79-81].

Curcumin, the active ingredient in turmeric [82, 83], has antioxidant, anti-inflammatory, and anti-cell death properties [82-85]. Curcumin as a modulator in the management of behavioral disorders, such as mood, cognitive, and motor disorders, has been suggested [85]. Curcumin, however, as an effective drug in psychotic disorders, has been less studied [25, 86]. Furthermore, its role in the management of schizophrenia and psychotic-like disorders has not been sufficiently evaluated [25, 86]. Accordingly, the role of curcumin and curcumin nanoparticles in the management of some neurobehavioral and neurologic disorders, such as anxiety, depression, PD, AD, and other similar disorders, was investigated. In our study, curcumin positively altered behavioral parameters by modulating several inflammatory pathways. Thus, it could represent a potential therapeutic option for psychosis, particularly when delivered in a nanoparticle-based formulation [25, 82, 83, 86].

Nanotechnology has significantly contributed to drug development [87, 88] by increasing drug specificity and improving pharmacodynamic efficacy, pharmacokinetic properties, and the overall pharmacologic profile [88]. Nanotechnology has also reduced adverse side effects [87, 88].

The green synthesis of our nanoparticle avoided toxic chemicals, highlighting curcumin's potential for sustainable and biocompatible production of nanoparticles. By leveraging curcumin's chemistry, this process demonstrated its applicability in nanotechnology and sustainable material science, emphasizing the importance of eco-conscious strategies in nanoparticle synthesis and showcasing curcumin as a significant contributor to green chemistry initiatives. Selected tissues from mice exposed to doses of the synthesized Cur/Ag nanoparticles as high as 2000 mg/kg daily for two weeks revealed no notable changes or tissue damage. They further displayed normal cellular architecture without evidence of inflammation, degeneration, or necrosis. These findings confirmed the non-toxic nature of Cur/Ag NPs, supporting its safety profile.

The effects of Cur/Ag NPs on several inflammatory and behavioral parameters were evaluated in the hyoscine-induced rodent model of acute psychosis. Cur/Ag NPs protected against hyoscine-induced acute psychosis in a mouse model. Cur/Ag NPs modulated the Yawning number, rearing number, and stereotypic score in the hyoscine-induced acute psychosis. Cur/Ag NPs also inhibited the blood levels of the inflammatory factors TNF-α, IL-1β, C-reactive protein, and cortisol.

HYO administration caused an increase in rearing numbers [89]. In contrast, HAL, a dopamine D2 receptor antagonist, reduced the rearing number in HYO-treated mice, which confirmed its antipsychotic role [90]. Cur/Ag NPs with doses of 40 and 60 mg/kg reduced the rearing number in HYO (0.125 mg/kg) treated mice. However, neither Cur nor Ag alone altered the rearing numbers. The nanocomposite of Cur/Ag NPs enhanced the curcumin effects and exerted an anti-psychosis role, supporting previous studies [30, 31].

Yawning behavior was increased by YOH but inhibited by HAL. The effects of YOH and HAL on Yawning behavior were consistent with previous results and confirmed the psychotic role of YOH [89] and the antipsychotic role of HAL [90]. Cur/Ag NPs with doses of 40 and 60 mg/kg reduced the Yawning behavior in HYO-treated mice. Cur as 40 mg/kg and Ag (40 mg/kg) did not change the Yawning behavior.

HYO increased the stereotype behavior scores, while HAL reduced the stereotype behavior scores in HYO-treated mice. Cur and Cur/Ag NPs reduced stereotype behavior scores in HYO-treated mice. However, our curcumin-metal nanocomposite particles enhanced the antipsychotic effects of this herbal compound (curcumin). As shown in Figures 9, 10, and 11, 40 mg/kg of curcumin and 40 mg/kg of Cur/Ag NPs positively affected rearing numbers, Yawning behavior, and stereotype behavior scores. The Cur/Ag NPs altered these parameters, however, to a greater degree than curcumin alone.

HYO increased blood cortisol and CRP levels and enhanced the blood level of TNF-α and IL-1β, and HAL reduced these inflammatory parameters. In contrast, curcumin alone and Cur/Ag NPs (40 and 60 mg/kg) decreased TNF-α, IL-1β, and attenuated CRP and blood cortisol levels in HYO-treated mice. Ag (40 m/kg) did not change cortisol, TNF-α, IL-1β, or CRP blood levels. The Cur/Ag NPs exerted their protective effects against these inflammatory parameters at lower doses (Figures 12, 13, and 14). Although some of these changes were not statistically significant, these changes, nonetheless, support the potential beneficial effects of nanoparticles [87, 88].

Earlier research has suggested that inflammatory processes are strongly involved in the development of psychosis [73-76] and that inflammation can predispose degenerative damage and subsequent behavioral disorders such as psychosis [73-76, 91]. Cytokines may be valid biomarkers of psychosis in patients with this disease [91, 92]. The development of new anti-inflammatory drugs should be designed with mechanisms that inhibit inflammatory pathways in mind [79]. Both curcumin and Cur/Ag NPs may have a place in the management of psychosis by reducing oxidative stress and free radical activity, while increasing antioxidants such as superoxide dismutase, glutathion peroxidase, and glutathione reductase, and enhancing glutathione, and reducing the levels of reactive nitrogen species and reactive oxygen species [93-96].

Curcumin nanoparticle compounds with greater potency and potentially fewer side effects can play an effective anti-inflammatory role [30, 31]. In addition to the role of oxidative stress and inflammation, cell death-related pathways such as apoptosis and autophagy play a critical role in the mechanism and pathophysiology of psychosis [96-99]. Some of the effects of curcumin and Cur/Ag NPs may be explained by their potential anti-cell death properties [95-99]. Although we did not evaluate oxidative stress and cell death-related pathways, future studies should consider these pathways. In addition, since curcumin modulates neurotransmitters such as acetylcholine, dopamine, serotonin and glutamate [96-99], both curcumin and Cur-Ag NPs may have a potential role in managing acute psychosis [100-105].

## CONCLUSION

Although we did not evaluate cell death-related pathways in the present study, both curcumin and curcumin-silver nanoparticles (Cur/Ag NPs) showed antioxidant properties potentially beneficial for psychosis management, possibly through modulation of neurotransmitter systems like dopamine and serotonin (98-101). Cur/Ag NPs demonstrated efficacy at lower doses than curcumin alone in reducing psychosis-like behaviors and inflammation in the hyoscine-induced rodent model of acute psychosis, with no observed toxicity at tested doses, suggesting their promise as safe therapeutic candidates (102-107). In addition to the role of oxidative stress and inflammation, cell death-related pathways such as apoptosis and autophagy play an essential role in the pathophysiology of acute psychosis [96-99].

Additional research, works and studies are required to clarify mechanisms, chronic safety, and clinical effectiveness (95-101).

**ACKNOWLEDGMENT**

We are grateful for the support of the Islamic Azad University, Tehran Medical Branch. The nanocomposite synthesis was conducted in the laboratories of Dr. Malak Hekmati, and the data were part of Mrs. Setayesh Abdolkarimi's master's thesis.

**FUNDING**

No other financial support.

**CONFLICT OF INTEREST**

None to declare.

**REFERENCES**

1. Bishop JR, Zhang L, Lizano P. Inflammation subtypes and translating inflammation-related genetic findings in schizophrenia and related psychoses: a perspective on pathways for treatment stratification and novel therapies. Harv Rev Psychiatry. 2022;30(1):59-70.
2. Williams JA, Burgess S, Suckling J, Lalousis PA, Batool F, Griffiths SL, et al. Inflammation and brain structure in schizophrenia and other neuropsychiatric disorders: a Mendelian randomization study. JAMA Psychiatry. 2022;79(5):498-507.
3. Arciniegas DB. Psychosis. Continuum (Minneap Minn). 2015;21(3):715-736.
4. Bebbington P. Unravelling psychosis: psychosocial epidemiology, mechanism, and meaning. Shanghai Arch Psychiatry. 2015;27(2):70.
5. De Oliveira IR, Juruena M. Treatment of psychosis: 30 years of progress. J Clin Pharm Ther. 2006;31(6):523-534.
6. Demjaha A, Lappin J, Stahl D, Patel M, MacCabe J, Howes O, et al. Antipsychotic treatment resistance in first-episode psychosis: prevalence, subtypes and predictors. Psychol Med. 2017;47(11):1981-1989.
7. Barak S, Weiner I. Towards an animal model of an antipsychotic drug-resistant cognitive impairment in schizophrenia: scopolamine induces abnormally persistent latent inhibition, which can be reversed by cognitive enhancers but not by antipsychotic drugs. Int J Neuropsychopharmacol. 2009;12(2):227-241.
8. Blokland A. Cholinergic models of memory impairment in animals and man: scopolamine vs. biperiden. Behav Pharmacol. 2022;33(4):231-237.
9. Barak S, Weiner I. Scopolamine induces disruption of latent inhibition which is prevented by antipsychotic drugs and an acetylcholinesterase inhibitor. Neuropsychopharmacology. 2007;32(5):989-999.
10. Ham S, Kim TK, Chung S, Im HI. Drug abuse and psychosis: new insights into drug-induced psychosis. Exp Neurobiol. 2017;26(1):11-20.
11. Forrest AD, Coto CA, Siegel SJ. Animal models of psychosis: current state and future directions. Curr Behav Neurosci Rep. 2014;1(2):100-116.
12. Piontkewitz Y, Arad M, Weiner I. Tracing the development of psychosis and its prevention: what can be learned from animal models. Neuropharmacology. 2012;62(3):1273-1289.
13. Winship IR, Dursun SM, Baker GB, Balista PA, Kandratavicius L, Maia-de-Oliveira JP, et al. An overview of animal models related to schizophrenia. Can J Psychiatry. 2019;64(1):5-17.
14. Jones CA, Watson D, Fone K. Animal models of schizophrenia. Br J Pharmacol. 2011;164(4):1162-1194.
15. Geyer MA, Moghaddam B. Animal models relevant to schizophrenia disorders. Neuropsychopharmacology. 2002;50:690-701.
16. Yadav M, Parle M, Jindal DK, Sharma N. Potential effect of spermidine on GABA, dopamine, acetylcholinesterase, oxidative stress and proinflammatory cytokines to diminish ketamine-induced psychotic symptoms in rats. Biomed Pharmacother. 2018;98:207-213.
17. Emorinken A, Akpasubi BO, Izirein HO, Oyerinde A. Acute-onset psychosis induced by a therapeutic dose of parenteral hyoscine butylbromide: a case report. Indian J Case Reports. 2023;9(3):65-67.
18. Mongan D, Ramesar M, Focking M, Cannon M, Cotter D. Role of inflammation in the pathogenesis of schizophrenia: a review of the evidence, proposed mechanisms and implications for treatment. Early Interv Psychiatry. 2020;14(4):385-397.
19. Bergink V, Gibney SM, Drexhage HA. Autoimmunity, inflammation, and psychosis: a search for peripheral markers. Biol Psychiatry. 2014;75(4):324-331.
20. Al-Diwani AA, Pollak TA, Irani SR, Lennox BR. Psychosis: an autoimmune disease? Immunology. 2017;152(3):388-401.
21. Mondelli V, Ciufolini S, Belvederi Murri M, Bonaccorso S, Di Forti M, Giordano A, et al. Cortisol and inflammatory biomarkers predict poor treatment response in first episode psychosis. Schizophr Bull. 2015;41(5):1162-1170.
22. Fusar-Poli P, Davies C, Solmi M, Brondino N, De Micheli A, Kotlicka-Antczak M, et al. Preventive treatments for psychosis: umbrella review (just the evidence). Front Psychiatry. 2019;10:764.
23. Hoenders HR, Bartels-Velthuis AA, Vollbehr NK, Bruggeman R, Knegtering H, de Jong JT. Natural medicines for psychotic disorders: a systematic review. J Nerv Ment Dis. 2018;206(2):81-101.
24. Otimenyin SO, Ior LD. Medicinal plants used in the management of psychosis. In: Complementary Therapies. IntechOpen; 2021.
25. Miodownik C, Lerner V, Kudkaeva N, Lerner PP, Pashinian A, Bersudsky Y, et al. Curcumin as add-on to antipsychotic treatment in patients with chronic schizophrenia: a randomized, double-blind, placebo-controlled study. Clin Neuropharmacol. 2019;42(4):117-122.
26. Kucukgoncu S, Guloksuz S, Tek C. Effects of curcumin on cognitive functioning and inflammatory state in schizophrenia: A double-blind, placebo-controlled pilot trial. J Clin Psychopharmacol. 2019;39(2):182-184.

27. Sudakaran SV, Venugopal JR, Vijayakumar GP, Abisegapriyan S, Grace AN, Ramakrishna S. Sequel of MgO nanoparticles in PLACL nanofibers for anticancer therapy in synergy with curcumin/β-cyclodextrin. Mater Sci Eng C. 2017;71:620-628.
28. Motaghinejad M, Bangash MY, Hosseini P, Karimian SM, Motaghinejad O. Attenuation of morphine withdrawal syndrome by various dosages of curcumin in comparison with clonidine in mouse: possible mechanism. Iran J Med Sci. 2015;40(2):125.
29. Ahmadinasab H, Motaghinejad M, Nosratabad BA, Bozorgniahosseini S, Rostami P, Jafarabadi GS, et al. Hepatoprotection effect of curcumin against methylphenidate-induced hepatotoxicity: histological and biochemical evidences. Int J Prev Med. 2022;13(1):65.
30. Mobinhosseini F, Salehirad M, Wallace Hayes A, Motaghinejad M, Hekmati M, Safari S, et al. Curcumin-ZnO conjugated nanoparticles confer neuroprotection against ketamine-induced neurotoxicity. J Biochem Mol Toxicol. 2024;38(1):e23611.
31. Adibipour F, Salehirad M, Hayes AW, Hekmati M, Motaghinejad M. Preventive effect of ZnO-metformin nanocomposite against carbon tetrachloride-induced hepatotoxicity. Nanomed Res J. 2024;9(2):155-163.
32. Kheiri R, Koohi MK, Sadeghi-Hashjin G, Nouri H, Khezli N, Hassan MA, et al. Comparison of the effects of iron oxide, as a new form of iron supplement, and ferrous sulfate on the blood levels of iron and total iron-binding globulin in the rabbit. Iran J Med Sci. 2017;42(1):79.
33. Rai M, Pandit R, Gaikwad S, Yadav A, Gade A. Potential applications of curcumin and curcumin nanoparticles: from traditional therapeutics to modern nanomedicine. Nanotechnol Rev. 2015;4(2):161-172.
34. Moniruzzaman M, Min T. Curcumin, curcumin nanoparticles and curcumin nanospheres: a review on their pharmacodynamics based on monogastric farm animal, poultry and fish nutrition. Pharmaceutics. 2020;12(5):447.
35. Runjun S, Kumar DM, Lakshi S, Anand R, Ratul S. Conjugation of curcumin with Ag nanoparticle for improving its bioavailability and study of the bioimaging response. Nanosyst Phys Chem Math. 2021;12(4):528-535.
36. El Khoury E, Abiad M, Kassaify ZG, Patra D. Green synthesis of curcumin-conjugated nanosilver for applications in nucleic acid sensing and antibacterial activity. Colloids Surf B Biointerfaces. 2015;127:274-280.
37. Percie du Sert N, Hurst V, Ahluwalia A, Alam S, Avey MT, Baker M, et al. The ARRIVE guidelines 2.0: updated guidelines for reporting animal research. J Cereb Blood Flow Metab. 2020;40(9):1769-1777.
38. Sadeghi R, Razzaghdoust A, Bakhshandeh M, Nasirinezhad F, Mofid B. Nanocurcumin as a radioprotective agent against radiation-induced mortality in mice. Nanomed J. 2019;6(1)
39. Jantawong C, Priprem A, Intuyod K, Pairojkul C, Pinlaor P, Waraasawapati S, et al. Curcumin-loaded nanocomplexes: acute and chronic toxicity studies in mice and hamsters. Toxicol Rep. 2021;8:1346-1357.
40. Abbas MM. The effect of hyoscine on serum serotonin and acetylcholine levels and their impacts on neurobehavior in mice. Egypt J Vet Sci. 2024;1:1-6.
41. Hosseinzadeh H, Ramezani M, Akhtar Y, Ziaei T. Effects Boswellia carterii gum resin fractions on intact memory and hyoscine-induced learning impairments in rats performing the morris water maze task. Med Plants. 2010;9(34):95-101.
42. Furuie H, Yamada K, Ichitani Y. MK-801-induced and scopolamine-induced hyperactivity in rats neonatally treated chronically with MK-801. Behavioural Pharmacology. 2013;24(8):678-683.
43. Arruda MdOV, Soares PM, Honório JER, Lima RCdS, Chaves EMC, Lobato RDFG, et al. Activities of the antipsychotic drugs haloperidol and risperidone on behavioural effects induced by ketamine in mice. Sci Pharm. 2008;76(4):673-688.
44. Tada M, Shirakawa K, Matsuoka N, Mutoh S. Combined treatment of quetiapine with haloperidol in animal models of antipsychotic effect and extrapyramidal side effects: comparison with risperidone and chlorpromazine. Psychopharmacology (Berl). 2004;176(1):94-100.
45. Motaghinejad M, Motevalian M, Shabab B. Possible involvements of glutamate and adrenergic receptors on acute toxicity of methylphenidate in isolated hippocampus and cerebral cortex of adult rats. Fundamental & Clinical Pharmacology. 2017;31(2):208-225.
46. Motaghinejad O, Motaghinejad M, Motevalian M, Rahimi-Sharbaf F, Beiranvand T. The effect of maternal forced exercise on offspring pain perception, motor activity and anxiety disorder: the role of 5-HT2 and D2 receptors and CREB gene expression. J Exerc Rehabil. 2017;13(5):514-521
47. Salehirad M, Hayes AW, Motaghinejad M, Gholami M. Protective effects of curcumin/magnesium oxide nanoparticles on ketamine-induced neurotoxicity in the mouse hippocampus. Res Pharm Sci. 2025;20(3):416-433.
48. Mach CM, Mathew L, Mosley SA, Kurzrock R, Smith JA. Determination of minimum effective dose and optimal dosing schedule for liposomal curcumin in a xenograft human pancreatic cancer model. Anticancer Res. 2009;29(6):1895-1899.
49. Tiwari DK, Jin T, Behari J. Dose-dependent in-vivo toxicity assessment of silver nanoparticle in Wistar rats. Toxicol Mech Methods. 2011;21(1):13-24.
50. Perkasa DP, Arozal W, Kusmardi K, Syaifudin M, Purwanti T, Laksmana RI, et al. Toxicity and biodistribution of alginate-stabilized AgNPs upon 14-days repeated dose oral administration in mice. Appl Pharm Sci. 2024;14(6):135-146.
51. Mohammadi E, Amini SM, Mostafavi SH, Amini SM. An overview of antimicrobial efficacy of curcumin-silver nanoparticles. Nanomed Res J. 2021;6(2):105-111.

52. Loo C-Y, Rohanizadeh R, Young PM, Traini D, Cavaliere R, Whitchurch CB, et al. Combination of silver nanoparticles and curcumin nanoparticles for enhanced anti-biofilm activities. J Agric Food Chem. 2016;64(12):2513-2522.
53. Monisha K, Shilpa SA, Anandan B, Hikku G. Ethanolic curcumin/silver nanoparticles suspension as antibacterial coating mixture for gutta-percha and cotton fabric. Eng Res Express. 2023;5(2):025054.
54. Stedenfeld KA, Clinton SM, Kerman IA, Akil H, Watson SJ, Sved AF. Novelty-seeking behavior predicts vulnerability in a rodent model of depression. Physiol Behav. 2011;103(2):210-216.
55. Ghafarimoghadam M, Mashayekh R, Gholami M, Fereydani P, Shelley-Tremblay J, Kandezi N, et al. A review of behavioral methods for the evaluation of cognitive performance in animal models: current techniques and links to human cognition. Physiol Behav. 2022;244:113652.
56. Yadav M, Kumar A. Behavioural and Non-behavioural Experimental Models of Psychosis: Current State and Future Aspects. Animal Models for Neurological Disorders. 2021:65-77.
57. Li S-M, Collins GT, Paul NM, Grundt P, Newman AH, Xu M, et al. Yawning and locomotor behavior induced by dopamine receptor agonists in mice and rats. Behav Pharmacol. 2010;21(3):171-181.
58. Daquin G, Micallef J, Blin O. Yawning. Sleep Med Rev. 2001;5(4):299-312.
59. Kostrzewa RM, Kostrzewa JP, Kostrzewa RA, Kostrzewa FP, Brus R, Nowak P. Stereotypic progressions in psychotic behavior. Neurotox Res. 2011;19:243-252.
60. Dahlen A, Zarei M, Melgoza A, Wagle M, Guo S. THC-induced behavioral stereotypy in zebrafish as a model of psychosis-like behavior. Sci Rep. 2021;11(1):15693.
61. Martin RS, Secchi RL, Sung E, Lemaire M, Bonhaus DW, Hedley LR, et al. Effects of cannabinoid receptor ligands on psychosis-relevant behavior models in the rat. Psychopharmacology (Berl). 2003;165:128-135.
62. Gong S, Miao Y-L, Jiao G-Z, Sun M-J, Li H, Lin J, et al. Dynamics and correlation of serum cortisol and corticosterone under different physiological or stressful conditions in mice. PLoS One. 2015;10(2):e0117503.
63. Sentari M, Harahap U, Sapiie TWA, Ritarwan K. Blood cortisol level and blood serotonin level in depression mice with basil leaf essential oil treatment. Open Access Maced J Med Sci. 2019;7(16):2652.
64. Bose U, Broadbent JA, Juhász A, Karnaneedi S, Johnston EB, Stockwell S, et al. Protein extraction protocols for optimal proteome measurement and arginine kinase quantitation from cricket Acheta domesticus for food safety assessment. Food Chem. 2021;348:129110.
65. Fernández-Vizarra E, Fernández-Silva P, Enríquez JA. Isolation of mitochondria from mammalian tissues and cultured cells. In: Cell Biology. Elsevier; 2006; 69-77.
66. Kruger NJ. The Bradford method for protein quantitation. In: The Protein Protocols Handbook. 2009:17-24.
67. Kirby DM, Thorburn DR, Turnbull DM, Taylor RW. Biochemical assays of respiratory chain complex activity. Methods Cell Biol. 2007;80:93-119.
68. Bénit P, Goncalves S, Dassa EP, Brière J-J, Martin G, Rustin P. Three spectrophotometric assays for the measurement of the five respiratory chain complexes in minuscule biological samples. Clin Chim Acta. 2006;374(1-2):81-86.
69. Hnasko R. ELISA. Springer; 2015
70. Crowther JR. The ELISA guidebook. Springer Science & Business Media; 2008.
71. Willner K, Vasan S, Patel P, Abdijadid S. Atypical antipsychotic agents. StatPearls [Internet]. StatPearls Publishing; 2024.
72. Meltzer HY, Gadaleta E. Contrasting typical and atypical antipsychotic drugs. Focus. 2021;19(1):3-13.
73. Misiak B, Bartoli F, Carrà G, Stańczykiewicz B, Gładka A, Frydecka D, et al. Immune-inflammatory markers and psychosis risk: A systematic review and meta-analysis. Psychoneuroendocrinology. 2021;127:105200.
74. Dunleavy C, Elsworthy RJ, Upthegrove R, Wood SJ, Aldred S. Inflammation in first-episode psychosis: the contribution of inflammatory biomarkers to the emergence of negative symptoms, a systematic review and meta-analysis. Acta Psychiatr Scand. 2022;146(1):6-20.
75. Kose M, Pariante CM, Dazzan P, Mondelli V. The role of peripheral inflammation in clinical outcome and brain imaging abnormalities in psychosis: a systematic review. Front Psychiatry. 2021;12:612471.
76. Ullah I, Awan HA, Aamir A, Diwan MN, de Filippis R, Awan S, et al. Role and perspectives of inflammation and C-reactive protein (CRP) in psychosis: an economic and widespread tool for assessing the disease. Int J Mol Sci. 2021;22(23):13032.
77. Zajkowska Z, Mondelli V. First-episode psychosis: an inflammatory state? Neuroimmunomodulation. 2014;21(2-3):102-108.
78. Fraguas D, Díaz-Caneja CM, Ayora M, Hernández-Álvarez F, Rodríguez-Quiroga A, Recio S, et al. Oxidative stress and inflammation in first-episode psychosis: a systematic review and meta-analysis. Schizophr Bull. 2019;45(4):742-751.
79. Jeppesen R, Christensen RH, Pedersen EM, Nordentoft M, Hjorthøj C, Köhler-Forsberg O, et al. Efficacy and safety of anti-inflammatory agents in treatment of psychotic disorders–A comprehensive systematic review and meta-analysis. Brain Behav Immun. 2020;90:364-380.
80. Çakici N, Van Beveren N, Judge-Hundal G, Koola M, Sommer I. An update on the efficacy of anti-inflammatory agents for patients with schizophrenia: a meta-analysis. Psychol Med. 2019;49(14):2307-2319.
81. Hong J, Bang M. Anti-inflammatory strategies for schizophrenia: a review of evidence for therapeutic applications and drug repurposing. Clin Psychopharmacol Neurosci. 2020;18(1):10.

82. Karthikeyan A, Senthil N, Min T. Nanocurcumin: A promising candidate for therapeutic applications. Front Pharmacol. 2020;11:487.
83. Hassanizadeh S, Shojaei M, Bagherniya M, Orekhov AN, Sahebkar A. Effect of nano-curcumin on various diseases: a comprehensive review of clinical trials. Biofactors. 2023;49(3):512-533.
84. Peng Y, Ao M, Dong B, Jiang Y, Yu L, Chen Z, et al. Anti-inflammatory effects of curcumin in inflammatory diseases: status, limitations and countermeasures. Drug Des Devel Ther. 2021;15:4503-4525.
85. Hussain Z, Thu HE, Amjad MW, Hussain F, Ahmed TA, Khan S. Exploring recent developments to improve antioxidant, anti-inflammatory and antimicrobial efficacy of curcumin: A review of new trends and future perspectives. Mater Sci Eng C Mater Biol Appl. 2017;77:1316-1326.
86. Rabiee R, Hosseini Hooshiar S, Ghaderi A, Jafarnejad S. Schizophrenia, curcumin and minimizing side effects of antipsychotic drugs: possible mechanisms. Neurochem Res. 2023;48(3):713-724.
87. Teleanu DM, Chircov C, Grumezescu AM, Volceanov A, Teleanu RI. Blood-brain delivery methods using nanotechnology. Pharmaceutics. 2018;10(4):269.
88. Naqvi S, Panghal A, Flora S. Nanotechnology: a promising approach for delivery of neuroprotective drugs. Front Neurosci. 2020;14:494.
89. Bulut NS, Arpacıoğlu ZB. Acute onset psychosis with complex neurobehavioural symptomatology following the intramuscular injection of hyoscine butylbromide: a case report with an overview of the literature. Eur J Hosp Pharm. 2022;29(5):294-297.
90. Dold M, Samara MT, Li C, Tardy M, Leucht S. Haloperidol versus first-generation antipsychotics for the treatment of schizophrenia and other psychotic disorders. Cochrane Database Syst Rev. 2015;1:CD009831
91. Perry BI, Upthegrove R, Thompson A, Marwaha S, Zammit S, Singh SP, et al. Dysglycaemia, inflammation and psychosis: findings from the UK ALSPAC birth cohort. Schizophr Bull. 2019;45(2):330-338.
92. Park S, Miller BJ. Meta-analysis of cytokine and C-reactive protein levels in high-risk psychosis. Schizophr Res. 2020;226:5-12.
93. Silva-Buzanello RA, Souza MF, Oliveira DA, Bona E, Leimann FV, Cardozo Filho L, et al. Preparation of curcumin-loaded nanoparticles and determination of the antioxidant potential of curcumin after encapsulation. Polimeros. 2016;26:207-214.
94. Scuto MC, Mancuso C, Tomasello B, Ontario ML, Cavallaro A, Frasca F, et al. Curcumin, hormesis and the nervous system. Nutrients. 2019;11(10):2417.
95. Jin W, Botchway BO, Liu X. Curcumin can activate the Nrf2/HO-1 signaling pathway and scavenge free radicals in spinal cord injury treatment. Neurorehabil Neural Repair. 2021;35(7):576-584.
96. Mittal A, Nagpal M, Vashistha VK, Arora R, Issar U. Recent advances in the antioxidant activity of metal-curcumin complexes: a combined computational and experimental review. Free Radic Res. 2024;58(1):11-26.
97. Yang C, Han M, Li R, Zhou L, Zhang Y, Duan L, et al. Curcumin nanoparticles inhibiting ferroptosis for the enhanced treatment of intracerebral hemorrhage. Int J Nanomedicine. 2021;16:8049-8065.
98. Prasad S, DuBourdieu D, Srivastava A, Kumar P, Lall R. Metal–curcumin complexes in therapeutics: an approach to enhance pharmacological effects of curcumin. Int J Mol Sci. 2021;22(13):7094.
99. Yan H, Wang L, Mu Y. Biosynthesis of Ag/Cu nanocomposite mediated by Curcuma longa: evaluation of its antibacterial properties against oral pathogens. Open Chem. 2024;22(1):20240059.
100. Khadrawy YA, Hosny EN, Magdy M, Mohammed HS. Antidepressant effects of curcumin-coated iron oxide nanoparticles in a rat model of depression. Eur J Pharmacol. 2021;908:174384.
101. Yavarpour-Bali H, Ghasemi-Kasman M, Pirzadeh M. Curcumin-loaded nanoparticles: A novel therapeutic strategy in treatment of central nervous system disorders. Int J Nanomedicine. 2019:4449-4460.
102. He X, Zhu Y, Wang M, Jing G, Zhu R, Wang S. Antidepressant effects of curcumin and HU-211 coencapsulated solid lipid nanoparticles against corticosterone-induced cellular and animal models of major depression. Int J Nanomedicine. 2016:4975-4990.
103. Sandhir R, Yadav A, Mehrotra A, Sunkaria A, Singh A, Sharma S. Curcumin nanoparticles attenuate neurochemical and neurobehavioral deficits in experimental model of Huntington's disease. Neuromolecular Med. 2014;16(1):106-118.
104. Fahmy HM, Aboalasaad FA, Mohamed AS, Elhusseiny FA, Khadrawy YA, Elmekawy A. Evaluation of the therapeutic effect of curcumin-conjugated zinc oxide nanoparticles on reserpine-induced depression in Wistar rats. Biol Trace Elem Res. 2024;202(6):2630-2644.
105. Naserzadeh P, Hafez AA, Abdorahim M, Abdollahifar MA, Shabani R, Peirovi H, et al. Curcumin loading potentiates the neuroprotective efficacy of Fe3O4 magnetic nanoparticles in cerebellum cells of schizophrenic rats. Biomed Pharmacother. 2018;108:1244-1252.

RESEARCH PAPER

# Monte Carlo simulation of Au@MNP nanoparticles for MRI-guided proton therapy: tailoring core-shell architecture for dose enhancement

***Maryam Bordbar[1], Mohammadreza Parishan[1*], Rasool Safari[1], Zahra Rakeb[1]***

*[1]Department of Nuclear Engineering, School of Mechanical Engineering, Shiraz University, Shiraz, Iran*

## ABSTRACT

***Objective(s):*** Integrating magnetic resonance imaging (MRI) with proton therapy holds significant promise for enhancing treatment efficacy. Magnetic nanoparticles (MNPs), such as gadolinium and superparamagnetic iron oxide nanoparticles (SPIONs), are well-known for improving tissue contrast in MRI. In this study, we investigate the potential of core–shell nanoparticles (Au@MNPs) as agents that can enhance the delivery of therapeutic doses to targeted tissues. Specifically, we examine how variations in core diameter and shell thickness, using either gadolinium oxide ($Gd_2O_3$) or SPION shells, influence dose enhancement.

***Materials and Methods:*** A simulated proton beam with a weighted energy spectrum—representing both primary and secondary protons within the Spread-Out Bragg Peak (SOBP) region—was used to irradiate the nanoparticles. The energy deposited within the nanoparticles, as well as the phase space of surrounding secondary particles, was evaluated. Key parameters, including energy efficiency, total energy release, and the number of secondary electrons, were analyzed to compare the performance of various nanoparticle designs.

***Results:*** Our findings indicate that incorporating a gold core is advantageous for thin magnetic layers (<15 nm), as it enhances the dose around the nanoparticle while maintaining a size compatible with MRI applications (<20 nm). In contrast, for thicker magnetic layers (greater than 20 nm), a larger gold core diameter is required to achieve effective dose enhancement.

***Conclusion:*** These results suggest that embedding a gold core with a diameter of less than 15 nm within MRI-compatible nanoparticles is a promising strategy for enhancing dose delivery in proton therapy. Further studies are warranted to investigate the impact of core–shell nanoparticles on magnetic properties, which are critical for their theranostic potential.

***Keywords****: Theranostic nanomedicine, Radiosensitizing agents, Proton therapy, Magnetic Resonance imaging, Metal nanoparticles, Monte Carlo method.*

**How to cite this article**

Bordbar M, Parishan M, Safari R, Rakeb Z. Monte Carlo simulation of Au@MNP nanoparticles for MRI-guided proton therapy: tailoring core-shell architecture for dose enhancement. Nanomed J. 2026; 13(2): 344-355. *DOI: 10.22038/NMJ.2025.81909.2039*

## INTRODUCTION

MRI-guided proton therapy represents a significant advancement in cancer treatment by synergistically combining the characteristic Bragg peak profile of proton beams with the real-time imaging capabilities of magnetic resonance imaging (MRI) [1,2]. This integration enables highly conformal dose delivery to tumor targets while minimizing exposure to surrounding healthy tissues, thereby supporting a more personalized and potentially curative treatment approach [3]. Nanoparticles—particularly superparamagnetic iron oxide nanoparticles (SPIONs) and gadolinium (Gd)-based nanoparticles—exhibit high biocompatibility and tunable surface properties [4]. These characteristics, along with their intrinsic magnetic properties, make them promising candidates not only as T1 and T2 MRI contrast agents but also for magnetic hyperthermia and various other medical applications [5–8].

The fight against cancer has also highlighted a critical role for metallic nanoparticles (NPs) in radiation therapy [9,10]. By incorporating NPs into radiotherapeutic protocols, researchers aim to enhance treatment efficacy against cancer cells while minimizing—or at least maintaining—the risk of complications in healthy tissues [11]. A wide

* *Corresponding author:* Mohammadreza Parishan, Ph.D. Department of Nuclear Engineering, School of Mechanical Engineering, Shiraz University, Shiraz, Iran. Tel: +98 71 36473474, Emails: *m.r.parishan@shirazu.ac.ir*.

Note. This manuscript was submitted on August 13, 2024; approved on July 01, 2025.

range of elements, from titanium (atomic number 22) to bismuth (atomic number 83), is currently being investigated as potential dose-enhancing agents in conventional photon-based radiotherapy and ion therapy [12,13]. Although both SPIONs and gadolinium-based magnetic nanoparticles (MNPs) have been studied for their dose-enhancing potential [14–17], gold nanoparticles (AuNPs) have attracted significantly greater research interest due to their advantageous combination of high atomic number, high density, and excellent biocompatibility [18–21]. Proton irradiation of NPs can result in localized dose enhancement through the generation of low-energy secondary electrons. It is hypothesized that a substantial fraction of these excess electrons, observed in the secondary electron spectra emitted from the NPs, originates from Auger electron emission processes [22,23].

SPIONs and gadolinium-based nanoparticles can be simultaneously utilized for both imaging and dose enhancement. Incorporating gold into these nanoparticles further amplifies their dose-enhancing capabilities. The integration of magnetic nanoparticles with gold can take various structural forms, one of which is the Au@MNP configuration, where gold serves as the core and the magnetic material forms the outer shell [24]. This theranostic nanoparticle structure has been investigated for a wide range of medical applications [25,26]. One advantage of this hybrid design is that it largely preserves the magnetic properties of the nanoparticle, thereby maintaining its efficacy as an MRI contrast agent [27]. Additionally, secondary electrons generated in the gold core experience less attenuation as they traverse the magnetic shell, and electrons produced within the shell can also directly contribute to dose enhancement.

A limited number of studies have investigated the radiosensitizing properties of core–shell nanoparticles, particularly in the context of radiation therapy. To the best of our knowledge, only two studies have specifically examined core–shell structures for this purpose. Slama et al. explored the potential of 8 nm $Fe_3O_4$@Au core–shell nanoparticles to enhance radiation-induced effects on redox status, pro-inflammatory markers, and cell death in A549 human lung cancer cells [28]. In their study, megavoltage (MV) X-rays were applied at a dose rate of 600 cGy/min, and the results demonstrated that $Fe_3O_4$@Au nanoparticles significantly increased the radiosensitivity of cancer cells. In another study, Xu et al. employed Monte Carlo simulations to evaluate the physical dose enhancement of $Fe_3O_4$@Au core–shell nanoparticles (comprising a 60 nm $Fe_3O_4$ core and a 20 nm Au shell) under irradiation with a 50 keV photon beam [29]. Both studies confirmed the potential of $Fe_3O_4$@Au nanoparticles as effective radiosensitizers. However, these investigations were limited to X-ray irradiation, and date, no research has addressed the radiosensitization effects of core–shell nanoparticles in the context of proton therapy. This gap underscores the novelty of our current study, which aims to explore the potential of core–shell nanoparticles for dose enhancement in proton therapy.

Several methods have been successfully developed for the synthesis of Au@MNP core–shell nanostructures. For example, Orlando et al. synthesized gold–maghemite (Au@γ-$Fe_2O_3$) core–shell nanoparticles by nucleating an iron oxide shell onto pre-synthesized gold seeds, resulting in particles approximately 16 nm in diameter with a 4.7 nm outer shell [30]. Similarly, Lin and Doong fabricated Au@$Fe_3O_4$ yolk–shell nanocatalysts via thermal decomposition of iron pentacarbonyl, yielding nanoparticles with diameters ranging from 8 to 15 nm and shell thicknesses of 2.0–2.4 nm [31]. Another approach, reported by Shevchenko et al., involved the random nucleation of iron onto pre-formed gold nanoparticles through thermal decomposition, producing Au@SPIONs with core diameters of 4. 5 nm and shell thicknesses of 2.5–3.3 nm [32].

Furthermore, Liu et al. prepared bifunctional Au@$Fe_3O_4$ hybrid core–shell nanoparticles by first synthesizing Au nanoparticles via thermal reduction, followed by the thermal decomposition of $Fe(acac)_3$ on the gold surface [33]. The resulting particles exhibited an average diameter of 11 nm, comprising an 8 nm gold core. Umut et al. synthesized Au@$Fe_3O_4$ hybrid nanoparticles as potential MRI contrast agents using wet chemical methods, producing particles with gold cores ranging from 5 to 8 nm and an average overall diameter of 15.9 nm [34]. Additionally, Oliveira-Filho et al. synthesized Au@$Fe_3O_4$ core–shell nanoparticles via thermal decomposition, yielding nanocomposites with a 10.5 nm gold core and a 1.85 nm thick shell [35]. Felix et al. also investigated Au@$Fe_3O_4$ core–shell nanoparticles fabricated through thermal decomposition, resulting in particles with a 6.9 nm gold core and a 3.5 nm $Fe_3O_4$ shell [36].

Collectively, these studies highlight the versatility of core–shell nanoparticle synthesis methods and demonstrate the potential for precise control over core and shell dimensions to meet the specific requirements of various biomedical applications.

The impact of core size and magnetic shell thickness on the dose enhancement efficacy of Au@MNP nanoparticles during proton radiotherapy was investigated using Monte Carlo simulations. This study examines the interplay between the increased probability of proton interactions and the self-absorption of secondary electrons within the nanoparticle structure. While enlarging the core and shell can improve the likelihood of proton collisions, it may also intensify intra-nanoparticle absorption of therapeutic secondary electrons. Moreover, given the limited tissue uptake of nanoparticles, their mass concentration must be carefully optimized to achieve the desired effect. Therefore, achieving a balance among core size, shell thickness, and total nanoparticle mass is essential for maximizing dose deposition. In this work, we evaluate the dosimetric performance of Au@MNP nanoparticles with varying geometrical configurations under proton irradiation using Monte Carlo methods. Due to the inherent complexities involved, the magnetic properties of these nanoparticles will be addressed in future studies focused on synthesis and characterization.

The subsequent sections outline the methodology used to simulate a proton beam with a weighted energy spectrum that reflects interactions with nanoparticles at various depths within the tumor. This approach accounts for spatial variations in nanoparticle distribution within the tumor microenvironment. Nanoparticles with varying core sizes and shell thicknesses are irradiated using this beam model, enabling the extraction of key physical and dosimetric parameters. The investigation further examines how nanoparticle mass and energy efficiency impact the formation of secondary particles and the resulting yield of distinct chemical species. We anticipate that these findings will offer valuable guidance in optimizing the design of Au@MNP hybrid theranostic nanoparticles, ultimately supporting effective dose enhancement strategies in proton therapy.

## MATERIALS AND METHODS

In pencil beam scanning (PBS) proton therapy, where nanoparticles are uniformly distributed within the tumor volume, individual nanoparticles are exposed to proton beams with varying energy spectra. This variation arises from the stepwise modulation of proton beam energy used to sequentially target different depth layers within the treatment volume. Such spectral heterogeneity necessitates evaluating nanoparticle responses across the full range of incident energies to ensure optimal therapeutic efficacy. An ideal nanoparticle design would either exhibit consistent radiosensitizing performance at the average energy and intensity of the proton beam or be optimized to respond effectively to the weighted energy spectrum characteristic of PBS irradiation

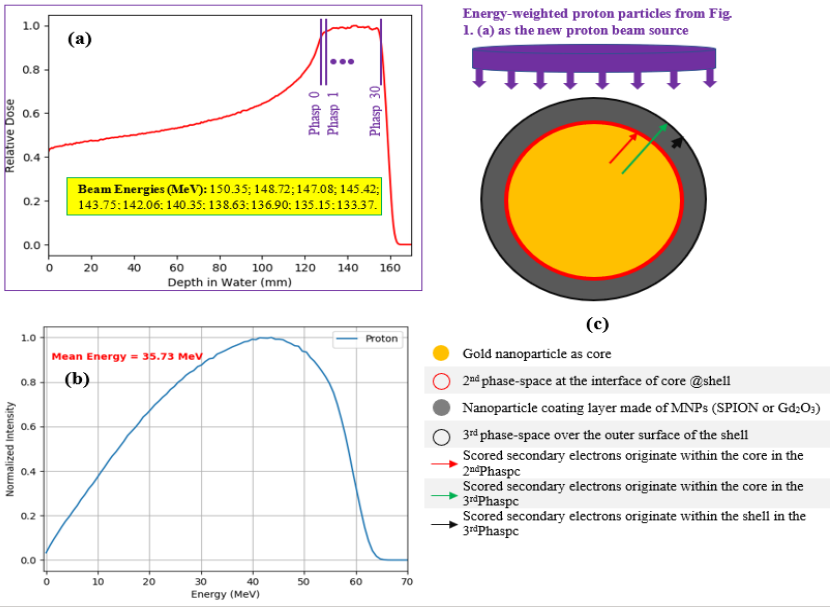


Fig. 1. Simulation geometry and nanoparticle irradiation process. (a): Depth dose profile of proton beams in a water phantom. Thirty-one phase-spaces within the SOBP were recorded at 1.0 mm intervals. (b): Energy spectrum of the proton particles recorded in the 31 phase-spaces in SOBP. (c) A disc-shaped proton source irradiates the nanoparticle. The descriptions of the different part of the nanoparticle are shown at the bottom of the Fig. 1(c).

Monte Carlo simulations were conducted using the TOPAS and TOPAS-nBio toolkits [37–39]. A total of 31 phase spaces, each separated by 1 mm, were extracted from a water phantom irradiated with proton beams (Figure 1a). The proton beam energy and the resulting spread-out Bragg peak (SOBP) are illustrated in Figure 1a. All primary and secondary protons within these phase spaces were incorporated to construct a new proton beam with a weighted energy spectrum, as shown in Figure 1b. Subsequently, a disk-shaped proton source with a diameter equivalent to the nanoparticle size was defined and assigned the weighted energy spectrum (Figure 1b) to simulate nanoparticle irradiation. Protons from this source were emitted in parallel and directed toward the nanoparticle (Figure 1c). For each simulation, approximately 50 million incident protons were used as primary histories.

The nanoparticles investigated in this study consist of a gold core coated with a magnetic component—either superparamagnetic iron oxide (SPION) or gadolinium oxide ($Gd_2O_3$) nanoparticles—as illustrated in Figure 1c. A comprehensive set of simulations was performed using gold cores with eleven distinct diameters: 3, 5, 7, 9, 12, 15, 20, 30, 40, 50, and 70 nm. The thickness of the magnetic shell was varied across ten values: 0, 5, 7, 10, 15, 20, 25, 30, 40, and 50 nm. Simulations were conducted using the Livermore low-energy physics model, configured with a 10-eV threshold for secondary particle production and a maximum step size of 1 nm. To accurately capture the complete de-excitation cascade, Auger electron emission, fluorescence, and proton-induced X-ray emission (PIXE) were all included. Additionally, the energy cutoff was bypassed during cascading processes to ensure precise modeling of secondary electron emissions.

Following this simulation step, data were collected from three distinct phase spaces: (1) the core–shell interface, capturing secondary particles generated in the core and exiting into the magnetic shell; (2) the outer nanoparticle surface, recording secondary particles originating from both the core and the shell, separated into two distinct datasets. In addition, the total energy deposited by both primary and secondary particles within the entire nanoparticle (core + magnetic shell) was quantified. For subsequent analysis, only electrons were considered, as they are the most abundant and influential contributors to local dose distribution around the nanoparticle.

The collected data were used to generate several visualizations, including the energy spectrum of secondary electrons, their total number, and average energy, analyzed separately for the core and the entire nanoparticle. To evaluate the effect of core size and magnetic shell thickness on dose enhancement efficacy around the nanoparticle, we calculated the ratio of energy emitted from the nanoparticle surface to the total energy transferred to the nanoparticle volume (including both deposited and emitted energy). This ratio, referred to as energy efficiency, serves as a key metric for assessing the nanoparticle's effectiveness in enhancing local dose deposition. For comparison, the energy efficiency of individual SPIONs, $Gd_2O_3$, gold, and hypothetical water nanoparticles—each with identical mass—was also analyzed. Furthermore, in light of the limited mass concentrations achievable in tumors, the specific energy released per unit nanoparticle mass (mass-normalized energy release) was evaluated.

The complete chemical stage of the simulation was performed for each nanoparticle. The source of secondary particles at the nanoparticle surface was defined using a phase space containing all secondary electrons emitted from the entire nanoparticle volume. Five types of nanoparticles with comparable mass were investigated: gold, SPION, $Gd_2O_3$, Au@MNP (gold core with magnetic nanoparticle shell), and a hypothetical water nanoparticle surrounded by a 1 mm diameter water sphere. The simulations utilized the TsEmDNAPhysics and TsEmDNAChemistry modules, which account for both physical and chemical interactions. For thermalized solvated electrons, the well-established Ritchie model was used. The diffusion and interaction of chemical species were simulated using the independent reaction times (IRT) method, chosen for its high computational efficiency, which is particularly beneficial for modeling low linear energy transfer (LET) particles, such as electrons. The yields of various chemical species were tracked over time steps ranging from 1 picosecond to 1 microsecond. However, for clarity and brevity, only the results corresponding to two representative species are presented.

**RESULTS**

Figure 1a illustrates the dose profile and the spread-out Bragg peak (SOBP) generated by proton beams of specific energies within a tumor phantom measuring 3 cm in diameter.

Figure 1b presents the corresponding weighted energy spectrum, derived from 31 phase spaces sampled along the SOBP region. This spectrum has an average energy of 35.73 MeV and displays

negative skewness. The observed skew toward higher energies is attributed to the greater abundance of high-energy protons in phase spaces corresponding to shallower tumor layers—an effect inherent to active pencil beam scanning techniques.

Figure 2 presents the energy spectra of secondary electrons emitted from various nanoparticles with different core diameters and shell thicknesses. All spectra are normalized to the number of primary protons in the beam. Figures 2a and 2b specifically focus on electrons originating from the gold core and reaching the nanoparticle surface. Both spectra exhibit a distinct peak at approximately 1 keV. As shown in Figure 2b, the number of core-originated electrons decreases with increasing shell thickness (either SPION or $Gd_2O_3$). In contrast, Figure 2a shows that increasing the gold core diameter—while keeping shell thickness constant—leads to a higher number of emitted electrons. In terms of attenuation, the SPION shell exhibits lower attenuation for sub-1 keV electrons compared to the $Gd_2O_3$ shell. However, this trend reverses at energies above 1 keV, where the $Gd_2O_3$ shell becomes more transparent to core-emitted electrons.

Figures 2c and 2d depict the energy spectra of secondary electrons emitted from the entire nanoparticle, including both core and shell contributions. At energies below 1 keV, characteristic peaks corresponding to Auger electrons from specific atomic shells of SPION and $Gd_2O_3$ are evident. Notably, the SPION-coated nanoparticles exhibit a higher intensity of emitted electrons in this low-energy range (below 1 keV). However, this trend reverses at energies above 1 keV, where $Gd_2O_3$-coated nanoparticles demonstrate greater electron emission.

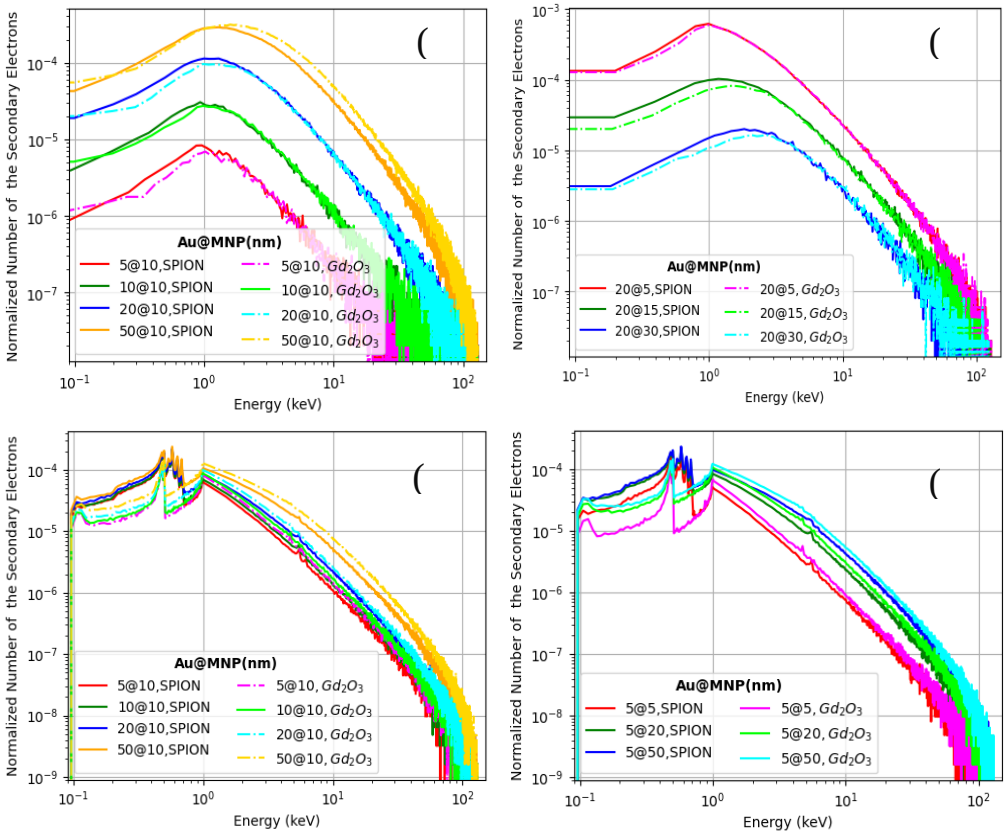


Fig. 2. Energy spectra of secondary electrons reaching the nanoparticle surface following proton irradiation. Variations in core diameter and shell thickness are investigated. The number of energy bins differs between panels (a) and (b) compared to (c) and (d) due to differing analysis requirements. (a) Electrons originating from the nanoparticle core: core diameter is fixed, while MNP shell thickness varies. (b) Electrons originating from the core: core diameter varies, while MNP layer thickness is constant. (c) Electrons originating from the entire NP (core + layer): core diameter is fixed, while MNP layer thickness varies. (d) Electrons originating from the entire nanoparticle: core diameter varies, while MNP layer thickness is constant.

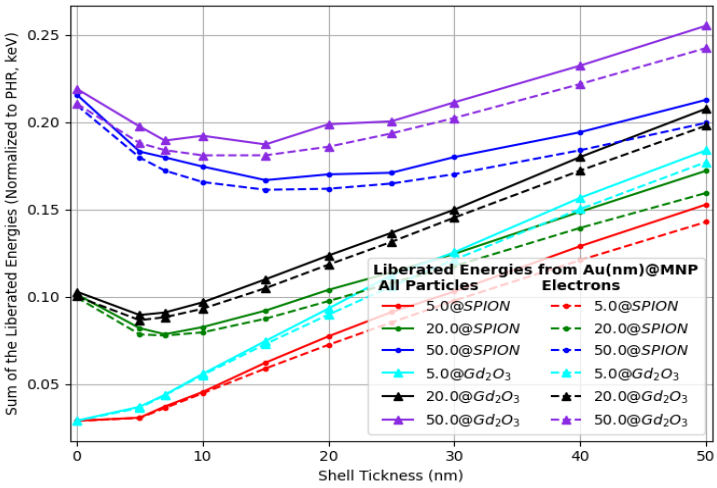


Fig. 3. Total energy released from the outer surface of Au@SPION (circular marker) and Au@$Gd_2O_3$ (triangular marker) nanoparticles of three different sizes (indicated by legend) following proton irradiation. Continuous lines represent the sum of all secondary particles and photons, while dashed lines depict the contribution solely from secondary electrons.

Figure 3 illustrates the normalized total energy emitted from the nanoparticle surface per incident proton (keV/proton). Two data series are presented: one representing the combined energy emitted by all particles and photons, and the other showing energy emission by secondary electrons only. The figure demonstrates that secondary electrons are the primary contributors to the outward energy flux from the nanoparticle. For a fixed core size, increasing the shell thickness results in a growing divergence between the total emitted energy and the energy attributable solely to secondary electrons. Nevertheless, both curves follow a broadly similar trend. As a result, the remainder of this study will focus exclusively on analyzing secondary electron emission.

Figure 4a illustrates the dependence of emitted electron yield on magnetic shell thickness for various core diameters. For cores smaller than 12 nm, the number of emitted electrons increases with increasing shell thickness. This trend is attributed to two primary factors: (1) the enhanced probability of interactions between the primary proton beam and the nanoparticle due to increased overall interaction volume, and (2) reduced self-absorption of electrons within smaller cores. For cores larger than 12 nm, a different behavior is observed: the number of emitted electrons initially decreases with increasing shell thickness before rising again. The increased likelihood of electron self-absorption within larger cores explains this. In such cases, many of the electrons generated within the core lose energy before reaching the core–shell interface. As a result, even a thin shell may absorb a substantial portion of these low-energy electrons, reducing the overall emitted yield. However, as shell thickness increases further, more electrons generated in the core are fully absorbed within the nanoparticle. Consequently, the emitted electron yield becomes increasingly dominated by electrons produced within the shell. This, combined with rising self-absorption within the thicker shell, leads to a convergence of the emission curves across different core sizes, as observed in Figure 4a.

Figure 4b quantifies the contribution of core-generated electrons to the total emitted yield as a function of shell thickness for various core diameters. The data reveal a rapid decline in this contribution with increasing shell thickness. Notably, the rate of decrease is steeper for smaller cores. For example, a 12 nm gold core shows a sharp drop in its contribution to the total yield, decreasing to approximately 10% when the shell thickness reaches 10 nm. This effect is even more pronounced for a 3 nm core, where the contribution falls to less than 1% at the same shell thickness.

Given the limited tissue uptake of nanoparticles, their mass must be taken into account when evaluating surface-emitted energy. Figure 4c shows the total energy emitted per unit mass of each nanoparticle, normalized by both the number of incident primary protons and the individual nanoparticle mass. The results indicate that, for a fixed core diameter, thinner magnetic shells yield more favorable energy output per unit mass. Furthermore, for a given shell thickness, nanoparticles with smaller cores exhibit higher energy release per unit mass.

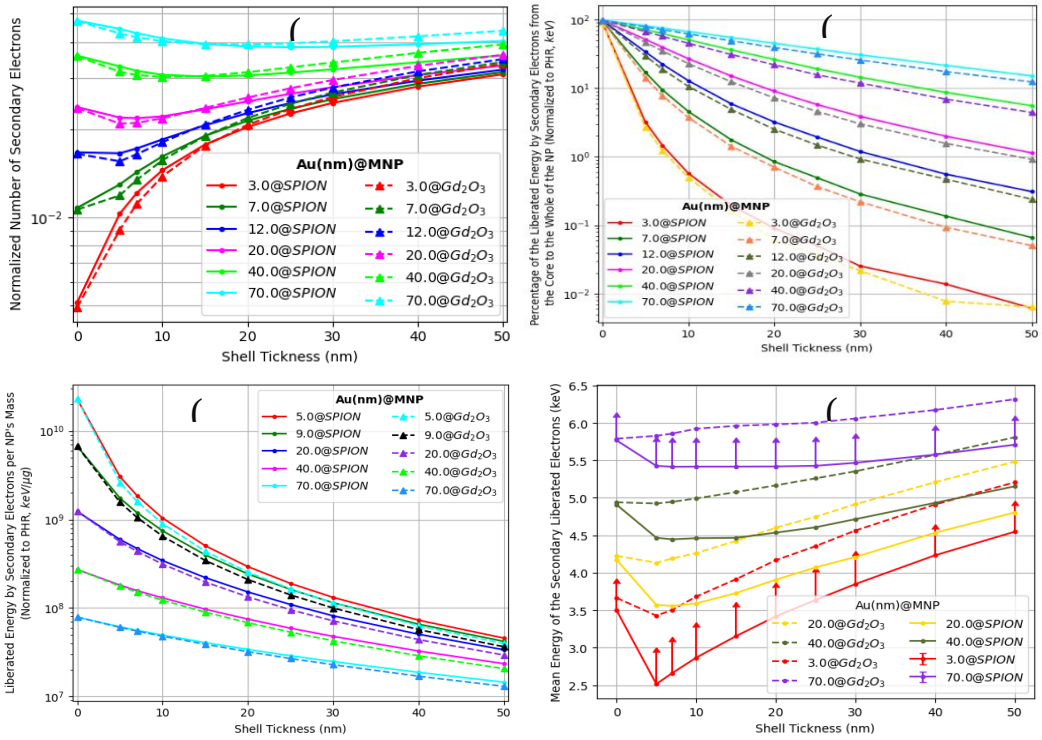


Fig. 4. (a) Number of electrons released from the outer surface of Au@SPION and Au@$Gd_2O_3$. (b) Percentage contribution of released energy by core electrons to the total energy of all electrons released from the outer surface of the nanoparticle. (c) Normalized released energy by the total secondary electrons to the NP's mass. (d) Mean energy distribution of secondary electrons is depicted. Error bars represent the standard deviation (SD) normalized to the $(5 \times mean\ energy)$ (indicated by circles). Only the positive side of the bars is shown for clarity. For the first three sub*Fig.*s, the parameters are divided to the number of primary protons in the run.

Figure 4d presents the average energy of electrons emitted from the nanoparticle surface. The error bars indicate the relative standard deviation (i.e., the ratio of standard deviation to mean energy) for each data point. For clarity, only one-fifth of the positive error value is displayed. The average electron energy shows a clear dependence on core size. For a fixed shell thickness, the diameter increases with the core diameter. This trend can be attributed to the preferential self-absorption of low-energy electrons within the nanoparticle, which results in a higher mean energy among the electrons that escape. Conversely, for a fixed core size, the average electron energy initially decreases and then increases with increasing shell thickness. This non-monotonic trend is more pronounced for smaller core sizes. The initial decrease is likely due to the increased contribution of Auger electrons generated within the shell, particularly those with energies below 1 keV.

These lower-energy electrons can readily reach the nanoparticle surface, resulting in a decrease in the average energy of the emitted electrons. As the shell thickness increases further, only Auger electrons generated near the outer surface can escape. Simultaneously, higher-energy electrons originating from deeper regions of the shell contribute more significantly, leading to an overall increase in the average energy. This behavior is also reflected in the spectra shown in Figure 1. The observed decrease–increase trend in average energy is more pronounced in nanoparticles containing SPIONs compared to those with $Gd_2O_3$ shells. This difference can be attributed to the higher abundance of low-energy Auger electrons (below 1 keV) produced in SPIONs. Additionally, for a given core size and shell thickness, $Gd_2O_3$-coated nanoparticles consistently exhibit higher average emitted electron energies than their SPION-coated counterparts.

Another important metric for evaluating nanoparticle performance is the energy transfer efficiency, defined as the ratio of the energy emitted by the nanoparticle to the total energy absorbed by it. In this study, total absorbed energy includes both the energy deposited within the nanoparticle volume and the energy emitted from its surface. In other words, it represents the total energy lost by incident protons during their interactions with the nanoparticle. Figure 5a presents the energy transfer efficiency as a function of core diameter for various magnetic shell thicknesses.

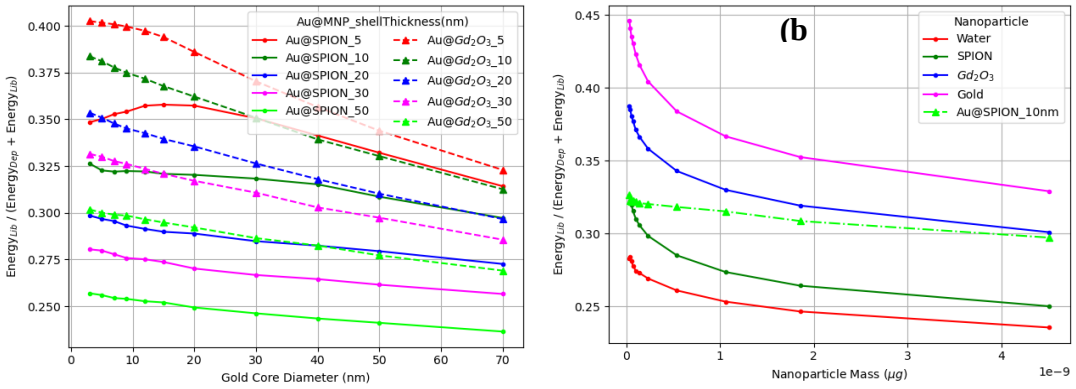


Fig. 5. (a) Energy efficiency, defined as the ratio of deposited energy within the nanoparticle to the total energy released or deposited, is presented for Au@MNP nanoparticles with varying core diameters and MNP shell thicknesses. (b) Energy efficiency defined for single gold nanoparticles, SPION, $Gd_2O_3$, and a hypothetical water nanoparticle with a mass equivalent to the Au@SPION_10nm configuration. The curve of Au@SPION_10nm nanoparticle are considered for comparison with the curves in Fig.5 (a).

Across all studied nanoparticles, the energy transfer efficiency remains below 40%. However, nanoparticles with $Gd_2O_3$ shells consistently exhibit higher efficiency compared to those coated with SPIONs. In $Gd_2O_3$-based nanoparticles, efficiency decreases with increasing gold core diameter, as well as with increasing shell thickness for a fixed core size. A similar trend is observed in SPION-based nanoparticles. However, for SPION shells with a thickness of 5 nm, an initial increase in efficiency is followed by a subsequent decrease as the core diameter increases. This non-monotonic behavior is also expected for SPION shell thicknesses below 5 nm.

Figure 5b compares the energy transfer efficiency of individual nanoparticles—gold (Au), SPION, $Gd_2O_3$, and hypothetical water—with the trends observed in Figure 5a. In this comparison, an Au@SPION nanoparticle with a 10 nm shell thickness serves as the baseline. By varying the core size of this reference nanoparticle, other single-material nanoparticles with equivalent mass were defined and subjected to proton irradiation. The diagram illustrates energy transfer efficiency as a function of nanoparticle mass. As shown in the figure, nanoparticles composed of elements with higher atomic numbers and physical densities exhibit improved energy transfer efficiency at a fixed mass. Accordingly, the Au@SPION nanoparticle demonstrates higher efficiency than a pure SPION nanoparticle, but remains less efficient than a pure gold nanoparticle. A similar trend is anticipated for Au@$Gd_2O_3$ structures. Notably, all nanoparticles in Figure 5b show higher efficiency than the hypothetical water nanoparticle, reinforcing the concept of localized dose enhancement through high-Z nanoparticles embedded within tissue.

Figure 6 presents the time-dependent G-values for hydroxyl radicals (•OH) and hydrogen peroxide ($H_2O_2$) species generated as secondary products from nanoparticle (NP) interactions within a surrounding water medium. The data show that nanoparticles with identical mass produce relatively similar G-values over time, regardless of composition. However, the G-values measured in the vicinity of the hypothetical water nanoparticle are significantly higher than those associated with other nanoparticle types.

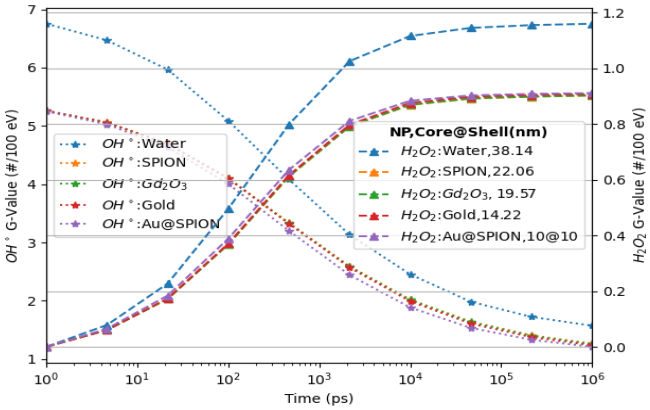


Fig. 6. Comparison of the G-value of two chemical Species for gold, $Gd_2O_3$, SPION, Au@SPION:10 nm@10 nm, and hypothetical water nanoparticles.

**DISCUSSION**

This study investigates the design of core–shell nanoparticles (Au@MNP) for dose enhancement in proton therapy, with a dual focus on maximizing energy deposition and preserving the magnetic properties necessary for effective MRI contrast. Monte Carlo simulations were conducted using a weighted energy spectrum that represents the proton beam, including both primary and secondary particles. This spectrum captures variations in beam characteristics experienced by nanoparticles located at different depths within the tumor. Specifically, nanoparticles situated deeper within the tumor are exposed to a proton beam with a distinct energy distribution and particle fluence compared to those closer to the surface. To account for this depth-dependent variation, the weighted spectrum was constructed using phase space data extracted from multiple positions along the tumor depth. Although a 3 cm-diameter tumor located at a 14 cm depth within a water phantom was modeled in this study, it is acknowledged that the energy distribution within the spread-out Bragg peak (SOBP) remains relatively consistent across different depths in water or tissue-equivalent phantoms. For simplicity, this investigation focuses primarily on interactions between the proton beam and the nanoparticles. However, it is recognized that other secondary particles—particularly neutrons and photons generated during therapy—may also contribute to dose enhancement through interactions with nanoparticles in the tumor microenvironment. In particular, neutron interactions with gadolinium-based contrast agents have been shown to further augment local dose deposition [40–42].

An alternative modeling approach could involve simulating nanoparticle interactions exclusively with the specific proton beam encountered at their respective locations within the tumor during each spot scan. This method would effectively place the nanoparticle within the Bragg peak region of individual beamlets, where protons reach their lowest kinetic energy. At these energies, high-Z elements such as gold exhibit near-maximum electronic stopping power, increasing the likelihood of electron interactions and potentially enhancing local dose deposition [43]. However, several additional factors must be taken into consideration. First, the energy of secondary electrons generated during proton–nanoparticle interactions is critical. These electrons must possess sufficient energy to traverse not only the magnetic coating layer but also any biocompatible surface layer surrounding the nanoparticle, to reach the surrounding tissue. Since higher-energy protons produce secondary electrons with greater kinetic energy, they offer improved penetration potential. Second, the number of protons per beamlet decreases progressively with increasing depth in tissue [44]. As a result, nanoparticles located proximal to the beam entrance are exposed to a greater number of protons than those situated near the distal edge or Bragg peak. Finally, even at relatively high nanoparticle concentrations, the probability of a single proton directly interacting with a specific nanoparticle during a single spot scan remains low, due to the small size of individual nanoparticles and the large number of protons delivered per spot area. Therefore, to achieve optimal dose enhancement, it is essential to consider not only the proton energy at the Bragg peak but also the total number of protons delivered across the entire tumor volume, as well as the spatial distribution of nanoparticles during the full course of spot scanning.

The number of electrons generated within hybrid nanoparticles is governed by the interplay between electron production and attenuation processes occurring in both the core and shell regions. When employing gold as the core material and either gadolinium oxide or SPION as the shell, the high density of gold leads to an increased probability of electron production compared to the surrounding shell materials. However, this advantage is offset by the higher likelihood of electron attenuation within gold itself. As a result, for nanoparticles with thin shells, a gold core can be beneficial for enhancing electron yield and, consequently, dose deposition. In contrast, for nanoparticles with thicker shells, the presence of a gold core contributes little to dose enhancement. Instead, it increases the overall nanoparticle mass, a crucial consideration given the clinical limitations on nanoparticle loading. The optimal shell thickness, which is often determined by imaging functionality (e.g., MRI contrast), thus becomes a critical design parameter for balancing radiation dose enhancement with imaging performance and mass constraints.

SPION nanoparticles used for MRI contrast typically range in size from a few nanometers up to approximately 20 nm [45,46]. As shown in Figure 4b, the contribution of core-generated electrons to the total energy emitted from the nanoparticle surface declines sharply with increasing magnetic shell thickness. To ensure nanoparticle sizes remain below the 20 nm threshold for optimal biocompatibility, various combinations of core diameter and shell thickness can be considered. For

example, with a 7 nm gold core and a shell thickness of up to 10 nm, the core electron contribution drops from 100% to approximately 5%. Alternatively, increasing the core diameter to 12 nm while limiting the shell to 8 nm reduces the contribution from 100% to around 20%. These results suggest that incorporating a gold core is beneficial primarily for very small or ultrasmall magnetic nanoparticles. However, in such cases, the potential effect of the gold core on the magnetic properties of the surrounding shell must be carefully evaluated to preserve MRI functionality.

Uncertainties related to chemical reactions at the nanoparticle–water interface, as well as within non-water-based nanoparticles, likely contribute to the observed discrepancies in radiolytic product yields between simulations with water-only and nanoparticle-containing systems. This highlights the need for further investigation. In pure water simulations, the homogeneous environment allows for more straightforward calculation of species production both within the hypothetical water nanoparticle and at its interface. In contrast, for simulations involving other nanoparticles dispersed in aqueous media, the model does not track chemical processes occurring inside the nanoparticles or at their interfaces [47]. This limitation introduces uncertainty into the calculated G-values (radiolytic product yields). Although the simulation accounts for some energy deposition from primary and secondary protons, as well as secondary electrons, within the nanoparticles, this deposited energy is only considered for the hypothetical water nanoparticle and not for others. As a result, the G-values for non-water nanoparticles may be underestimated in comparison. It is essential to acknowledge that the actual G-values for both water and other nanoparticles may differ from the simulated values due to these modeling limitations.

A key limitation of this study is the exclusion of a biocompatible layer over the magnetic shell. While the primary objective was not to quantify absolute dose enhancement, the investigation focused on assessing the influence of core and shell dimensions on secondary electron emission characteristics. Biocompatible coatings—such as polyethylene glycol (PEG)—are known to attenuate both the energy and quantity of electrons reaching surrounding tissues, potentially reducing the dose enhancement effect of nanoparticles [48]. Given the observed similarities in the extracted electron spectra across various nanoparticles, a comparable reduction in secondary electron energy and yield may be expected following the application of a biocompatible layer. However, the specific impact of such a layer is likely to vary depending on its composition, thickness, and density [49]. Further studies are necessary to quantitatively assess the extent of reduction in electron yield and total emitted energy caused by the presence of a biocompatible coating.

Biocompatible coatings are crucial for mitigating the toxicity of superparamagnetic iron oxide and gadolinium oxide nanoparticles when used as MRI contrast agents. Although this study does not quantify the magnetic properties or assess the impact of biocompatible coatings, it is recognized that such layers can significantly alter the energy and yield of emitted secondary electrons, thereby influencing the overall dose enhancement effect. Therefore, while the primary focus of this work is on the relationship between core and shell dimensions and secondary electron emission, the inclusion of biocompatible layers is strongly recommended in future studies, particularly those involving biological systems or in vivo applications.

## CONCLUSION

This study investigated the influence of core diameter and magnetic shell thickness on secondary electron emission from Au@MNP nanoparticles containing either $Gd_2O_3$ or SPION shells. The nanoparticles were irradiated by primary and secondary protons within the Spread-Out Bragg Peak (SOBP) region of a simulated proton beam. Our results indicate that the contribution of core electrons to dose enhancement is inversely proportional to the thickness of the magnetic shell. For small and ultrasmall nanoparticles—typically used as MRI contrast agents—incorporating a gold core can enhance dose delivery while maintaining an overall size compatible with MRI applications (i.e., below 20 nm). In contrast, for thicker magnetic shells, gold cores exceeding 20 nm in diameter may be more effective for dose enhancement; however, such particles may exceed the size limits for MRI and could instead be explored for alternative applications such as magnetic hyperthermia. Overall, our findings suggest that embedding a gold core with a diameter less than 15 nm within MRI-compatible nanoparticles represents a promising approach for enhancing proton therapy dose delivery. Further studies are warranted to assess the impact of these core–shell nanoparticles on magnetic properties, a critical consideration for their theranostic potential.

## AUTHOR CONTRIBUTIONS

Maryam Bordbar: Conceptualization, Modeling, Methodology, Writing – Original Draft, Validation, Review & editing. Mohammadreza Parishan: Project Administration, Conceptualization, Modeling, Validation, review. Rasool Safari: Investigation, Writing, review. Zahra rakeb: Methodology, Investigation, review.

## ACKNOWLEDGMENTS

This research did not receive any specific grant from funding agencies in the public, commercial, or not-for-profit sectors.

## CONFLICT OF INTEREST

The authors declare that they have no conflicts of interest.

## REFERENCES

1. Hoffmann A, Oborn B, Moteabbed M, Yan S, Bortfeld T, Knopf A, et al. MR-guided proton therapy: a review and a preview. Radiat Oncol. 2020;15(1):1–13.
2. Gantz S, Karsch L, Pawelke J, Peter J, Schellhammer S, Smeets J, et al. Direct visualization of proton beam irradiation effects in liquids by MRI. Proc Natl Acad Sci U S A. 2023;120(23):e2301160120.
3. Paganelli C, Oborn B, Hoffmann A, Riboldi M. Magnetic resonance imaging in particle therapy. Imaging Part Ther. 2024;7(1):7–21.
4. Smith L, Kuncic Z, Byrne HL, Waddington D. Nanoparticles for MRI-guided radiation therapy: a review. Cancer Nanotechnol. 2022;13(1):1–28.
5. Rahman M. Magnetic resonance imaging and iron-oxide nanoparticles in the era of personalized medicine. Nanotheranostics. 2023;7(4):424–442.
6. Szwed M, Marczak A. Application of nanoparticles for magnetic hyperthermia for cancer treatment—the current state of knowledge. Cancers. 2024;16(6):1156–1172.
7. Papi A, Irajirad R, Yousefvand M, Montazerabadi A, Mohammadi Z. Synthesis and evaluation of SPION@CMD@Ser-LTVSPWY peptide as a targeted probe for detection of HER2+ cancer cells in MRI. Nanomed J. 2021;8(4):279–289.
8. Salehian E, Safa R, Saffari M, Ashrafi S, Farhoudi R, Ebrahimi SES, et al. Synthesis and evaluation of Gd3+-Trp-PLGA as novel nanosized MR tumor imaging candidate. Nanomed J. 2021;8(2):117–123.
9. Peukert D, Kempson I, Douglass M, Bezak E. Metallic nanoparticle radiosensitisation of ion radiotherapy: a review. Phys Med. 2018;52:121–128.
10. Moradi F, Rezaee Ebrahim Saraee K, Abdul Sani SF, Bradley DA. Metallic nanoparticle radiosensitization: the role of Monte Carlo simulations towards progress. Radiat Phys Chem. 2021;180:109294.
11. Tremi I, Spyratou E, Souli M, Efstathopoulos EP, Makropoulou M, Georgakilas AG, et al. Requirements for designing an effective metallic nanoparticle (NP)-boosted radiation therapy (RT). Cancers. 2021;13(13):3185–3201.
12. Schuemann J, Bagley AF, Berbeco R, Bromma K, Butterworth KT, Byrne HL, et al. Roadmap for metal nanoparticles in radiation therapy: current status, translational challenges, and future directions. Phys Med Biol. 2020;65(21):21RM02.
13. Ahmadi Ganjeh Z, Mosleh-Shirazi MA. Macroscopic and microscopic investigation of maximum effectiveness of proton-boron capture therapy using Monte Carlo simulation. Radiat Phys Chem. 2024;214:111289.
14. Díaz-Galindo CA, Garnica-Garza HM. Radiation source personalization for nanoparticle-enhanced radiotherapy using dynamic contrast-enhanced MRI in the treatment planning process. Radiat Phys Chem. 2024;217:111518.
15. Brero F, Calzolari P, Albino M, Antoccia A, Arosio P, Berardinelli F, et al. Proton therapy, magnetic nanoparticles and hyperthermia as combined treatment for pancreatic BxPC3 tumor cells. Nanomaterials. 2023;13(5):791–805.
16. Parishan M, Faghihi R, Kadoya N, Jingu K. The effects of a transverse magnetic field on the dose enhancement of nanoparticles in a proton beam: a Monte Carlo simulation. Phys Med Biol. 2020;65(8):085002.
17. Rafiepour P, Sina S, Mortazavi SMJ, Zabihi A. The effects of magnetic field along with nanoparticles on DNA damage induced by a carbon beam: a Monte Carlo study. 2021 IEEE Nucl Sci Symp Med Imaging Conf Rec NSS/MIC. 2021;1–4.
18. Martinov MP, Fletcher EM, Thomson RM. Multiscale Monte Carlo simulations of gold nanoparticle dose-enhanced radiotherapy II. Cellular dose enhancement within macroscopic tumor models. Med Phys. 2023;50(9):5842–5852.
19. Nath P, Charchi N, Shvydka D, Ray A. Quantitative analysis of reactive oxygen species produced by core-shell gold nanoparticles during radiation therapy. Proc SPIE. 2024;PC12859:PC128590K.
20. Rasouli FS, Masoudi SF. Monte Carlo investigation of the effect of gold nanoparticles' distribution on cellular dose enhancement. Radiat Phys Chem. 2019;158:6–12.
21. Yaftian M, Saeedzadeh E, Khosravi H, Mohammadi E. Evaluation of the effect of gold and iron oxide nanoparticles dispersed on the bolus in radiation therapy by using Monte Carlo simulation. Nanomed J. 2023;10(2):153–162.
22. Wälzlein C, Scifoni E, Krämer M, Durante M. Simulations of dose enhancement for heavy atom nanoparticles irradiated by protons. Phys Med Biol. 2014;59(6):1441–1450.
23. Rudek B, McNamara A, Ramos-Méndez J, Byrne H, Kuncic Z, Schuemann J. Radio-enhancement by gold nanoparticles and their impact on water radiolysis for x-ray, proton and carbon-ion beams. Phys Med Biol. 2019;64(17):175005.
24. León Félix L, Coaquira JAH, Martínez MAR, Goya GF, Mantilla J, Sousa MH, et al. Structural and magnetic

properties of core-shell Au/Fe3O4 nanoparticles. Sci Rep. 2017;7(1):1–8.
25. Liu H, Wu J, Min JH, Kim YK. One-pot synthesis and characterization of bifunctional Au-Fe3O4 hybrid core-shell nanoparticles. J Alloys Compd. 2012;537:60–64.
26. Oliveira-Filho GB, Atoche-Medrano JJ, Aragón FFH, Mantilla Ochoa JC, Pacheco-Salazar DG, da Silva SW, et al. Core-shell Au/Fe3O4 nanocomposite synthesized by thermal decomposition method: structural, optical, and magnetic properties. Appl Surf Sci. 2021;563:150290.
27. Umut E, Pineider F, Arosio P, Sangregorio C, Corti M, Tabak F, et al. Magnetic, optical and relaxometric properties of organically coated gold-magnetite (Au-Fe3O4) hybrid nanoparticles for potential use in biomedical applications. J Magn Magn Mater. 2012;324(15):2373–2379.
28. Slama Y, Arcambal A, Septembre-Malaterre A, Morel AL, Pesnel S, Gasque P. Evaluation of core-shell Fe3O4@Au nanoparticles as radioenhancer in A549 cell lung cancer model. Heliyon. 2024;10(8):e29297.
29. Xu X, Wu J, Dai Z, Hu R, Xie Y, Wang L. Monte Carlo simulation of physical dose enhancement in core-shell magnetic gold nanoparticles with TOPAS. Front Oncol. 2022;12:1–12.
30. Orlando T, Capozzi A, Umut E, Bordonali L, Mariani M, Galinetto P, et al. Spin dynamics in hybrid iron oxide-gold nanostructures. J Phys Chem C. 2015;119(2):1224–1233.
31. Lin FH, Doong RA. Catalytic nanoreactors of Au@Fe3O4 yolk-shell nanostructures with various Au sizes for efficient nitroarene reduction. J Phys Chem C. 2017;121(14):7844–7853.
32. Shevchenko EV, Bodnarchuk MI, Kovalenko MV, Talapin DV, Smith RK, Aloni S, et al. Gold/iron oxide core/hollow-shell nanoparticles. Adv Mater. 2008;20(22):4323–4329.
33. Liu H, Wu J, Min JH, Kim YK. One-pot synthesis and characterization of bifunctional Au-Fe3O4 hybrid core-shell nanoparticles. J Alloys Compd. 2012;537:60–64.
34. Umut E, Pineider F, Arosio P, Sangregorio C, Corti M, Tabak F, et al. Magnetic, optical and relaxometric properties of organically coated gold-magnetite (Au-Fe3O4) hybrid nanoparticles for potential use in biomedical applications. J Magn Magn Mater. 2012;324(15):2373–2379.
35. Oliveira-Filho GB, Atoche-Medrano JJ, Aragón FFH, Mantilla Ochoa JC, Pacheco-Salazar DG, da Silva SW, et al. Core-shell Au/Fe3O4 nanocomposite synthesized by thermal decomposition method: structural, optical, and magnetic properties. Appl Surf Sci. 2021;563:150290.
36. León Félix L, Coaquira JAH, Martínez MAR, Goya GF, Mantilla J, Sousa MH, et al. Structural and magnetic properties of core-shell Au/Fe3O4 nanoparticles. Sci Rep. 2017;7(1):1–8.
37. Perl J, Shin J, Schümann J, Faddegon B, Paganetti H. TOPAS: an innovative proton Monte Carlo platform for research and clinical applications. Med Phys. 2012;39(11):6818–6837.
38. Faddegon B, Ramos-Méndez J, Schuemann J, McNamara A, Shin J, Perl J, et al. The TOPAS tool for particle simulation, a Monte Carlo simulation tool for physics, biology and clinical research. Phys Med. 2020;72:114–121.
39. Schuemann J, McNamara AL, Ramos-Méndez J, Perl J, Held KD, Paganetti H, et al. TOPAS-nBio: an extension to the TOPAS simulation toolkit for cellular and sub-cellular radiobiology. Radiat Res. 2018;191(2):125–138.
40. Van Delinder KW, Khan R, Gräfe JL. Radiobiological impact of gadolinium neutron capture from proton therapy and alternative neutron sources using TOPAS-nBio. Med Phys. 2021;48(7):4004–4016.
41. Seo SJ, Han SM, Cho JH, Hyodo K, Zaboronok A, You H, et al. Enhanced production of reactive oxygen species by gadolinium oxide nanoparticles under core-inner-shell excitation by proton or monochromatic X-ray irradiation: implication of the contribution from the interatomic de-excitation-mediated nanoradiator effect to dose enhancement. Radiat Environ Biophys. 2015;54(4):423–431.
42. Banoqitah E, Djouider F. Dose distribution and dose enhancement by using gadolinium nanoparticles implant in brain tumor in stereotactic brachytherapy. Radiat Phys Chem. 2016;127:68–71.
43. De Vera P, Abril I, Garcia-Molina R. Energy spectra of protons and generated secondary electrons around the Bragg peak in materials of interest in proton therapy. Radiat Res. 2018;190(3):282–297.
44. Newhauser WD, Zhang R. The physics of proton therapy. Phys Med Biol. 2015;60(8):R155–R209.
45. Avasthi A, Caro C, Pozo-Torres E, Pernia Leal M, García-Martín ML, Puente-Santiago AR, et al. Magnetic nanoparticles as MRI contrast agents. Top Curr Chem. 2021;378(3):1–43.
46. Wei H, Bruns OT, Kaul MG, Hansen EC, Barch M, Wiśniowska A, et al. Exceedingly small iron oxide nanoparticles as positive MRI contrast agents. Proc Natl Acad Sci U S A. 2017;114(9):2325–2330.
47. Johny J, van Halteren CER, Cakir FC, Zwiehoff S, Behrends C, Bäumer C, et al. Surface chemistry and specific surface area rule the efficiency of gold nanoparticle sensitizers in proton therapy. Chemistry. 2023;29(50):e202301260.
48. Peukert D, Kempson I, Douglass M, Bezak E. Gold nanoparticle enhanced proton therapy: a Monte Carlo simulation of the effects of proton energy, nanoparticle size, coating material, and coating thickness on dose and radiolysis yield. Med Phys. 2020;47(2):651–661.
49. Mansouri E, Mesbahi A, Hamishehkar H, Montazersaheb S, Hosseini V, Rajabpour S. The effect of nanoparticle coating on biological, chemical and biophysical parameters influencing radiosensitization in nanoparticle-aided radiation therapy. BMC Chem. 2023;17(1):1–14.

RESEARCH PAPER

# Comparative evaluation of cytotoxicity and inflammatory responses induced by free and eugenol-loaded titanium dioxide nanoparticles following intraperitoneal injection in mouse

***Farazdaq Nazar Al-Naffakh[1], Somayeh Reiisi[1*], Norolhoda Khalighi[2], Elham Moghtadaei Khorasgani[3]***

*[1] Department of Genetics, Faculty of Basic Sciences, Shahrekord University, Shahrekord, Iran*
*[2] Department of Pathobiology, Faculty of Veterinary Medicine, Shahrekord University, Shahrekord, Iran*
*[3] Department of Pathobiology, Shahrekord Branch, Islamic Azad University, Shahrekord, Iran*

**ABSTRACT**

***Objective(s)****:* Titanium dioxide nanoparticles ($TiO_2$ NPs), which are widely used in food and consumer products, have been associated with oxidative stress and inflammatory toxicity. Eugenol, a naturally occurring phenolic compound with well-established anti-inflammatory and antioxidant properties, may exert protective effects when delivered through nanocarriers.

***Materials and Methods****:* $TiO_2$ nanoparticles were synthesized via a co-precipitation method and subsequently functionalized with eugenol ($TiO_2$@eugenol). FTIR, XRD, DLS, zeta potential analysis, FE-SEM, and TEM were used to characterize the nanoparticles. Thirty-six BALB/cJ mice were randomly assigned to six groups (n = 6 per group). They received intraperitoneal injections of free eugenol, $TiO_2$ nanoparticles, or $TiO_2$@eugenol at low (50 mg/kg) or high (200 mg/kg) doses for 14 days. Following the treatment period, serum concentrations of IL-1β, IL-6, and TNF-α were measured using ELISA; hepatic caspase-3/7 activity was assessed; and histological examinations of the liver, kidney, and spleen were performed. Gene expression of antioxidant markers (SOD3, GR, GPx) in liver tissue was evaluated by qRT-PCR.

***Results****:* $TiO_2$ NPs significantly increased pro-inflammatory cytokines and hepatic caspase-3/7 activity. They also induced necrosis and inflammatory alterations in the liver, kidney, and spleen. In contrast, $TiO_2$@eugenol markedly suppressed cytokine release and apoptotic activity while preserving tissue architecture. qRT-PCR analysis showed that $TiO_2$ NPs downregulated antioxidant-related genes, whereas $TiO_2$@eugenol significantly upregulated their expression, indicating improved redox homeostasis.

***Conclusion****:* Eugenol functionalization improved the biocompatibility profile of $TiO_2$ NPs and provided substantial protection against $TiO_2$-induced toxicity by attenuating inflammation, apoptosis, and oxidative stress while restoring antioxidant defenses. These findings highlight the therapeutic potential of eugenol-loaded $TiO_2$ nanoparticles and support further investigation in extended exposure models and disease-specific applications.

***Keywords:*** *Titanium dioxide; NPs; Eugenol; Inflammation; Cytotoxicity*.

**How to cite this article**

*Al-Naffakh FN, Reiisi S, Khalighi N, Moghtadaei Khorasgani E. Comparative evaluation of cytotoxicity and inflammatory responses induced by free and eugenol-loaded titanium dioxide nps following intraperitoneal injection in mouse. Nanomed J. 2026; 13(2): 356-370. DOI: 10.22038/NMJ.2025.90454.2286*

## INTRODUCTION

The advent of nanotechnology has revolutionized multiple scientific disciplines by enabling the design, modification, and application of materials at the nanoscale. At this dimension, materials exhibit unique physicochemical properties that differ substantially from those of their bulk counterparts, including enhanced reactivity, improved solubility, and altered biological interactions [1, 2]. Among the wide range of engineered nanomaterials, titanium dioxide nanoparticles ($TiO_2$ NPs) have attracted considerable attention due to their biocompatibility, stability, photocatalytic activity,

* *Corresponding author:* Somayeh Reiisi; PhD, Department of Genetics, Faculty of Basic Sciences, Shahrekord University, Shahrekord, Iran. Email address: s.reiisi@yahoo.com; s.reiisi@sku.ac.ir.

Note. This manuscript was submitted on August 14, 2025; approved on November 26, 2025.

and cost-effectiveness. These nanoparticles are widely incorporated into cosmetics, sunscreens, paints, and food additives owing to their UV-blocking and whitening capabilities [3-5]. Furthermore, their emerging biomedical applications—such as antimicrobial therapies and targeted drug delivery—have intensified research into their interactions with biological systems. Despite these advantages, growing evidence indicates that $TiO_2$ NPs may elicit unintended cytotoxic and immunotoxic responses, particularly following systemic exposure [6, 7].

Nanoparticles such as $TiO_2$ can interact with biological fluids and tissues, forming a protein-rich coating known as the bio-corona. This layer, composed of proteins, lipids, and other biomolecules, defines the nanoparticle's biological identity and influences its cellular uptake, biodistribution, and immunogenicity [8, 9]. Upon internalization—particularly by immune cells such as macrophages and dendritic cells—$TiO_2$ NPs may initiate inflammatory signaling through mechanisms involving oxidative stress, inflammasome activation, and cytokine release [10, 11]. Prolonged exposure or accumulation of these particles may consequently result in chronic inflammation, tissue injury, or, in some cases, tumorigenesis [12, 13]. A major pathway through which nanoparticles exert toxicity is the excessive generation of reactive oxygen species (ROS). This occurs when the surface of $TiO_2$ NPs catalyzes redox reactions under UV or visible light exposure. ROS overproduction can induce oxidative damage to proteins, lipids, and nucleic acids, ultimately impairing cellular function and initiating apoptosis or necrosis [14, 15]. The anatase crystalline form of $TiO_2$ is particularly noted for its heightened photocatalytic activity and ROS-generating capacity, making it more bio-reactive—and potentially more toxic—than the rutile form [16, 17]. In light of these toxicological concerns, naturally derived compounds with antioxidant and anti-inflammatory properties have been explored as potential modifiers to mitigate NP-induced damage. One such compound is eugenol, a phenolic phytochemical predominantly found in clove, cinnamon, tulsi, and other aromatic plants. It exhibits a broad spectrum of biological activities, including antimicrobial, antioxidant, anti-inflammatory, and anticancer effects [18-20]. These properties position eugenol as a promising candidate for functionalizing or loading onto nanoparticles to enhance their therapeutic utility while diminishing toxicity. Recent research suggests that eugenol can attenuate inflammatory responses by reducing cytokine production, scavenging ROS, and stabilizing cellular membranes [20, 21]. When incorporated into nanoparticles, eugenol not only enhances biocompatibility but may also modulate immune function by lowering macrophage activation and neutrophil recruitment. Thus, eugenol-loaded $TiO_2$ NPs represent an innovative approach that integrates the structural advantages of nanomaterials with the biological potency of phytochemicals. Furthermore, the immune response to $TiO_2$ NPs is highly dependent on the nanoparticle's size, morphology, surface charge, and surface functionalization. These characteristics determine how the immune system recognizes and interacts with the particle, influencing processes such as opsonization, phagocytosis, and cytokine production [10, 22]. In the absence of surface modification, $TiO_2$ NPs are often perceived as foreign entities, triggering innate immune responses via toll-like receptors (TLRs) and inflammasome pathways, such as NLRP3. These interactions promote the release of pro-inflammatory cytokines, including IL-1β and IL-18, and recruit immune cells to the site of exposure [23, 24]. The adaptive immune system may also be activated, particularly if nanoparticles act as haptens by binding to proteins and forming complexes that can trigger antibody production or T-cell activation. Such immune recognition can be advantageous—for example, in vaccine adjuvant design—or detrimental, leading to hypersensitivity or autoimmune reactions [25-27]. Therefore, regulating the immune-modulatory properties of nanoparticles is essential to ensuring their safe and effective use in biomedical and industrial applications.

Despite the promising potential of $TiO_2$ NPs and the protective properties of eugenol, comprehensive in vivo studies evaluating their combined effects on cytotoxicity and inflammation remain limited. The route of administration plays a critical role in shaping the biodistribution and toxicological profile of nanoparticles; however, many existing studies rely primarily on in vitro assays or assess only a single biological endpoint. Although various investigations have characterized phytochemical–nanoparticle conjugates or explored $TiO_2$-induced toxicity in vitro, relatively few have provided an integrated, in vivo, head-to-head comparison of a free phytochemical versus the same compound delivered through an inorganic nanocarrier. Additionally, much of the previous work has been restricted either to physicochemical characterization or to isolated biological assessments. In this study, we combine (i) a reproducible eugenol functionalization of $TiO_2$ supported by comprehensive physicochemical

characterization (TEM, XRD, FTIR, DLS/zeta potential), (ii) in vitro release profiling with kinetic analysis under physiologically relevant pH conditions, and (iii) a 14-day in vivo comparison of free eugenol and $TiO_2$-loaded eugenol in liver, kidney, and spleen using histopathology, systemic cytokine profiling, apoptosis assays, and gene expression analysis of the Nrf2/HO-1 antioxidant axis. By integrating physicochemical, pharmacological, and mechanistic endpoints, our work provides a more translationally relevant evaluation of the potential advantages and safety profile of eugenol delivery via $TiO_2$ nanoparticles. This research aims to investigate the comparative effects of free $TiO_2$ NPs and eugenol-loaded $TiO_2$ NPs on cytotoxicity and inflammatory responses following intraperitoneal administration in a murine model. By elucidating how eugenol modulates the biological behavior of $TiO_2$ NPs, this study contributes to the development of safer nanoparticle designs for biomedical and industrial applications. Furthermore, it adds to the growing body of evidence supporting the incorporation of plant-derived compounds in nanomedicine to balance therapeutic efficacy with improved biocompatibility.

## MATERIALS AND METHODS

### *$TiO_2$ NPs synthesis and characterization*

Titanium dioxide nanoparticles ($TiO_2$ NPs) were synthesized via a co-precipitation method using analytical-grade reagents without further purification. Titanium tetrachloride ($TiCl_4$) and sodium hydroxide (NaOH) were mixed at a 1:1 molar ratio under ambient conditions. The resulting white precipitate was collected by centrifugation, thoroughly washed with distilled water, and filtered through cellulose nitrate membranes. The purified product was then dried at room temperature for 24 hours and subsequently sintered at 100 °C for an additional 24 hours. Characterization of $TiO_2$ NPs was performed using Fourier-transform infrared spectroscopy (FTIR), X-ray diffraction (XRD), dynamic light scattering (DLS), zeta potential analysis, field-emission scanning electron microscopy (FE-SEM), and transmission electron microscopy (TEM).

### *Eugenol loading onto $TiO_2$ NPs*

For drug loading, following the eugenol calibration assay, 100 mg of synthesized $TiO_2$ NPs was incubated with 50 mg of eugenol under continuous magnetic stirring at ambient temperature in the dark for 24 hours. After centrifugation (10,000 rpm for 10 min), the supernatant was collected to determine the loading efficiency. The precipitate, which contained the eugenol-loaded $TiO_2$ NPs, was stored at −20 °C for subsequent analyses. The amount of free eugenol in the supernatant was quantified using UV–Vis spectrophotometry at 280 nm after appropriate dilution. A standard calibration curve was constructed, and the drug-loading efficiency was calculated using the equation below and further confirmed by FTIR and zeta potential analysis.

$$\textbf{Efficacy of loaded drug\%} = \frac{\textbf{Initial drug Concentration} - \textbf{Concentration of unloaded drug}}{\textit{Initial drug concentration}} \times \mathbf{100}$$

### *Evaluation of drug release in vitro*

The release of eugenol was evaluated in PBS solutions at pH 7.2 and pH 4 using the dialysis bag diffusion method. Eugenol-loaded $TiO_2$ NPs (40 mg) were suspended in 500 µL of PBS and sealed within dialysis membranes. Each dialysis bag was immersed in 20 mL of the corresponding PBS solution and shaken at 100 rpm. At predetermined time intervals (0.5, 1, 2, 4, 6, 8, 10, 12, 24, and 48 h), a 1-mL aliquot of the release medium was withdrawn and replaced with an equal volume of fresh PBS. The amount of eugenol released was quantified using UV–Vis spectroscopy at 280 nm, and the cumulative release (%) was calculated accordingly.

### *In vivo animal model*

Thirty-six adult male BALB/cJ mice were selected for the study. All animals were similar in age (6–8 weeks) and body weight (18–20 g) to ensure consistency across experimental subjects. The mice were obtained from the Royan Institute for Biotechnology animal facility in Isfahan, Iran. They were provided with a standard rodent diet and had unrestricted access to water. To mimic natural conditions, the animals were housed at 25 ± 2 °C with a 12-hour light/dark cycle, and the relative humidity was maintained at 55 ± 5%. Before the experiment, the mice were allowed a one-week acclimatization period. All experimental procedures followed international guidelines for the care and use of laboratory animals and were approved by the Institutional Animal Ethics Committee of Shahrekord University (Code: IR.SKU.REC.1403.039). The mice were randomly assigned to six experimental groups (n = 6 per group) and received daily treatments at 9:00 a.m. for 14 consecutive days. The Control group consisted of healthy mice that received an intraperitoneal (i.p.) injection of 100 µL deionized distilled water, which served as the vehicle for both $TiO_2$ NPs and Eugenol-loaded $TiO_2$ NPs ($TiO_2$@Eugenol). The Eugenol group received an i.p.

injection of eugenol at 20 mg/kg body weight, dissolved in 1 mL of deionized distilled water; this dosage was selected based on previous studies in mice [28-31]. The Low-dose $TiO_2$ NPs group received 50 mg/kg body weight of $TiO_2$ NPs administered i.p. in 1 mL deionized distilled water, while the High-dose $TiO_2$ NPs group received 200 mg/kg body weight of $TiO_2$ NPs prepared in the same vehicle. The Low-dose $TiO_2$@Eugenol group received 50 mg/kg body weight of eugenol-loaded $TiO_2$ NPs, and the High-dose $TiO_2$@Eugenol group was administered 200 mg/kg body weight of the same formulation.

***Tissue and serum collection***

After the 14-day treatment period, all animals were fasted overnight. The following morning, they were necropsied under mild anesthesia to minimize pain and stress. Blood samples were collected via cardiac puncture and immediately processed by centrifugation. The samples were centrifuged at 1500 g for 10 minutes at 4 °C to obtain serum, which was then promptly stored at −80 °C for subsequent immunological analyses. The liver, kidney, and spleen were carefully excised from each animal. Tissue samples were collected for detailed microscopic evaluation and cytotoxicity assessments. The liver and spleen were mechanically homogenized with a tissue homogenizer, and the homogenates were centrifuged to separate cellular components by density. The resulting supernatants were stored at −80 °C, a temperature appropriate for maintaining biomolecular integrity for future analyses.

***ELISA analyze***

The enzyme-linked immunosorbent assay (ELISA) was performed to determine serum levels of the inflammatory cytokines IL-6, IL-1β, and TNF-α. Undiluted serum samples and standard solutions were added to the microplate wells and incubated with gentle shaking for two hours at room temperature. After incubation, the wells were washed five times with the washing buffer. A conjugated detection antibody was then added, followed by a one-hour incubation, and the wells were rewashed. Subsequently, the HRP–avidin reagent was added and incubated for 30 minutes. After a final wash, the substrate solution was added, and the reaction was allowed to proceed for 10 minutes before the stop solution was applied. Absorbance was measured at 450 nm using a microplate reader, and cytokine concentrations were quantified using a calibration curve generated from standard solutions.

***Assessment of Caspase-3/7 activity***

A colorimetric Caspase-3/7 Assay Kit based on the hydrolysis of the Ac-DEVD-pNA substrate—which releases p-nitroaniline (pNA) detectable at 405 nm—was used to measure caspase-3 and caspase-7 activities. Briefly, approximately 40 mg of tissue was lysed in Caspase Lysis Buffer using sonication or homogenization, and the lysates were centrifuged at 12,000 rpm for 15 minutes at 4 °C. The resulting supernatants were immediately stored at −80 °C until further analysis. A calibration curve was generated using a series of pNA standards (0–50 µM). For the assay, 50 µL of each sample, standard, or positive control was added in duplicate to a 96-well microplate. A working solution containing Caspase Buffer, DTT, and the DEVD-pNA substrate (55.5 µL per well) was then added, and the plate was incubated at 37 °C for 1.5–2 hours. Absorbance was measured at 405 nm using a microplate reader. Caspase activity was calculated based on the standard curve and expressed as nmol/min/mL (mU/mL).

***qRT-PCR analysis***

Total RNA was extracted from liver tissue using TRIzol reagent, and cDNA was synthesized using an M-MLV Reverse Transcription Kit with random hexamers and oligo(dT) primers. The resulting cDNA was stored at −20 °C until further analysis. For quantitative real-time PCR (qPCR), gene-specific primers were designed for the housekeeping gene and for oxidative stress–related genes (SOD3, GPx, and GR). Primer sequences are presented in Table 1. Each 10 µL qPCR reaction consisted of 5 µL Takara SYBR Green Master Mix, 0.6 µL of 10 µM forward and reverse primers, 1.2 µL cDNA, and 3 µL RNase-free water. The thermal cycling protocol included an initial denaturation at 95 °C for 5 minutes, followed by 40 cycles of denaturation at 95 °C for 10 seconds, annealing at 58 °C for 15 seconds, and extension at 72 °C for 10 seconds. A melt-curve analysis was performed from 64 °C to 95 °C to verify amplicon specificity. Relative gene expression levels were calculated using the ΔΔCt method, with ACTB serving as the internal reference gene.

Table1. Mouse qPCR forward and reverse primer sequences

| Gene name | Sequence | Product size |
|---|---|---|
| F-mACTB | 5′- GGACTCCTATGTGGGTGACG-3′ | 119 bp |
| R-mACTB | 5′- AGGTGTGGTGCCAGATCTTC-3′ | |
| F-mGpx | 5′-AATACCTTGAACTGAATGCAC-3′ | 111 bp |
| R-mGpx | 5′-GAGTTCTCGCCTGGCTCCTG-3′ | |
| F-mSOD3 | 5′- TTGACCCGGTTGAGAAGATAG-3′ | 121 bp |
| R-mSOD3 | 5′- ATCTCGGCAGCATCCACCTC-3′ | |
| F-mGR | 5′- GGCAGCTCCATCTCAGTCCG -3- | 126 bp |
| R-mGR | 5′- CTTTCAGGGCACTTGGTACTC-3′ | |

***Statistical analysis***

All experiments were performed in triplicate. Statistical analyses were conducted using Student's t-test and one-way ANOVA, followed by appropriate post hoc tests. Differences were considered statistically significant at $p < 0.05$.

**RESULTS**

***Description of $TiO_2$ NPs***

The synthesis of titanium dioxide ($TiO_2$) nanoparticles was performed using a precipitation method. The FTIR spectrum (Figure 1A) showed a broad absorption band between 450 and 800 $cm^{-1}$, corresponding to the stretching vibrations of Ti–O and Ti–O–Ti bonds. A peak at 1120 $cm^{-1}$ was attributed to the stretching modes of C–O, C–N, and $CH_3$ groups, while the peak at 1380 $cm^{-1}$ was explicitly associated with $CH_3$ stretching. The band observed at 1628 $cm^{-1}$ indicated the presence of hydroxyl groups on the nanoparticle surface. XRD analysis (Figure 1B) confirmed the crystalline nature and polymorphism of the $TiO_2$ NPs. The diffraction pattern displayed characteristic reflections corresponding to the (101), (004), (200), (211), (204), (220), (215), and (312) planes, consistent with the presence of anatase and rutile phases, both commonly observed in $TiO_2$ nanoparticle structures. DLS measurements revealed an average hydrodynamic diameter of 73.8 nm with a polydispersity index (PDI) of 0.38 (Figure 1C), indicating a relatively narrow size distribution suitable for predictable biological and physicochemical behavior. The zeta potential of −44 mV (Figure 1D) demonstrated strong colloidal stability and uniform dispersion in aqueous media. FE-SEM imaging (Figure 1E) showed that the $TiO_2$ NPs were predominantly spherical, with uniform morphology and distribution at a magnification scale of 500 nm. TEM analysis (Figure 1F) further confirmed the spherical architecture of the nanoparticles, revealing a slightly roughened surface at the 100 nm scale.

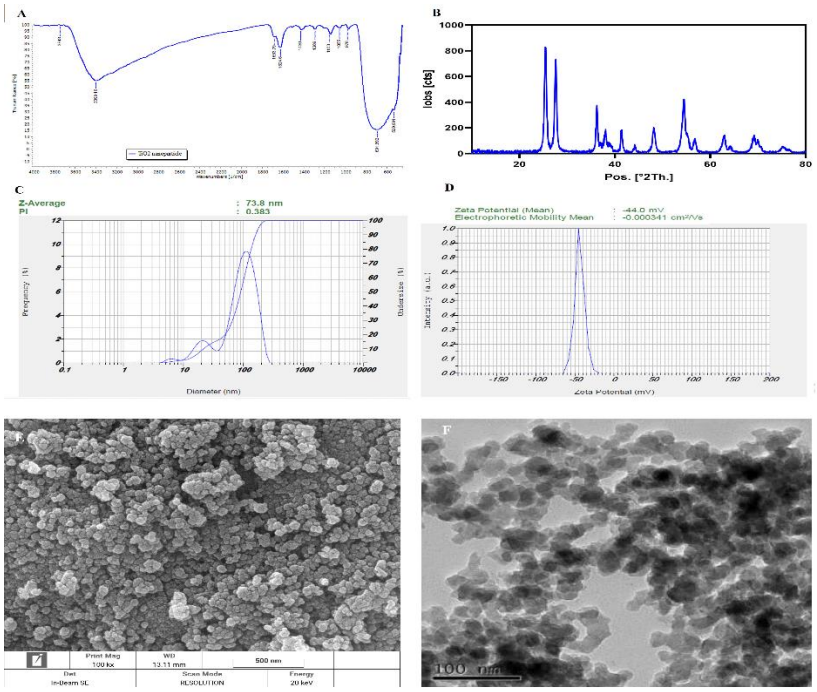


Fig. 1. $TiO_2$ NPs characterization. A) FTIR spectra of $TiO_2$ NPs, B) XRD pattern of $TiO_2$ NPs, C) Size and PDI of $TiO_2$ NPs determined to be 73.8 nm and 0.383, respectively, through DLS, D) Zeta potential of $TiO_2$ NPs obtained using the Zetasizer and found to be -44 mV. E) FE-SEM images of $TiO_2$ NPs to identify the surface morphology. The scale bars used here is 500 nm. F) TEM image of $TiO_2$ NPs. The scale bar used here is 100 nm.

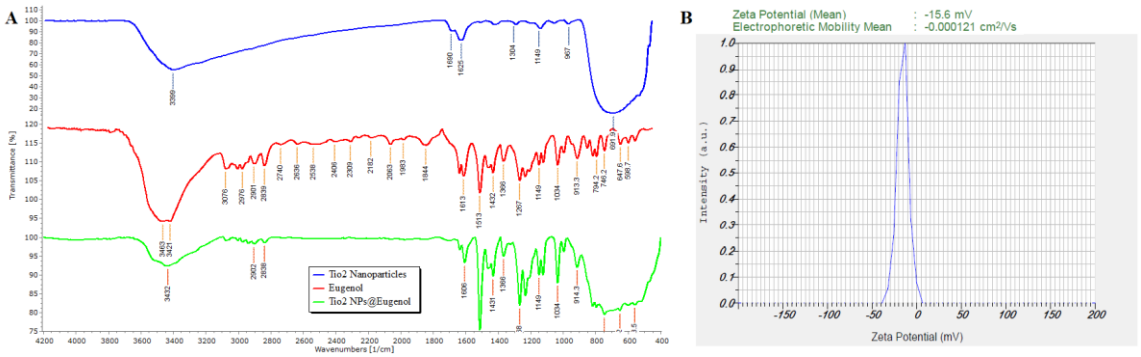


Fig. 2. $TiO_2$@Eugenol characterization indicating the successful loading of eugenol into $TiO_2$ NPs. A) FTIR spectra of $TiO_2$ NPs, eugenol, and $TiO_2$@Eugenol B) Zeta potential of $TiO_2$@Eugenol obtained using the Zeta sizer and found to be -15.6 mV.

***Loading efficiency of eugenol***

The eugenol loading efficiency was 99.4%. To verify the successful loading of eugenol onto the nanoparticles, FTIR and zeta potential analyses were conducted. The results of these assessments are shown in Figures 2A and 2B, respectively. Zeta potential measurements revealed a marked reduction in the negative surface charge of the nanoparticles—from −44 mV to −15 mV—confirming the presence of eugenol on the nanoparticle surface. Consistently, the FTIR spectrum of the loaded nanoparticles displayed overlapping characteristic peaks of both pure $TiO_2$ NPs and pure eugenol, indicating effective incorporation of eugenol. The absence of additional peaks suggests that no new chemical bonds or compounds were formed during loading.

***Eugenol release results***

As shown in Figure 3, a clear difference was observed between the release profiles of eugenol at pH 5.5 and pH 7.4 (the latter mimicking physiological conditions). In both media, the cumulative release increased over time, indicating sustained release over the 48 hours. The release rate was consistently higher under neutral conditions compared to acidic conditions, confirming the pH-responsive behavior of the $TiO_2$ nanoparticles. After approximately 8 hours, the release rate increased in both environments, with a more pronounced difference emerging between neutral and acidic media. At pH 7.4, eugenol release continued to rise gradually, reaching approximately 68% at 24 hours, followed by a plateau phase. In contrast, at pH 5.5, release occurred more slowly, reaching about 52% at 24 hours before stabilizing. Kinetic modeling of the release data indicated that the Higuchi model provided the best fit ($R^2$ = 0.97), suggesting a diffusion-controlled release mechanism.

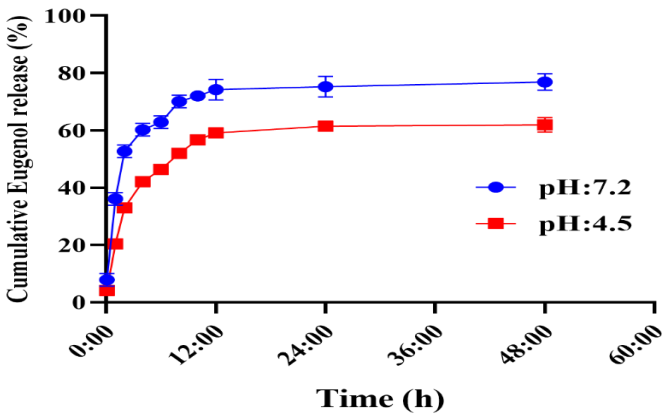


Fig. 3. Eugenol release profile over 48 hours at pH 4.5 (red curve) and pH 7.2 (blue curve).

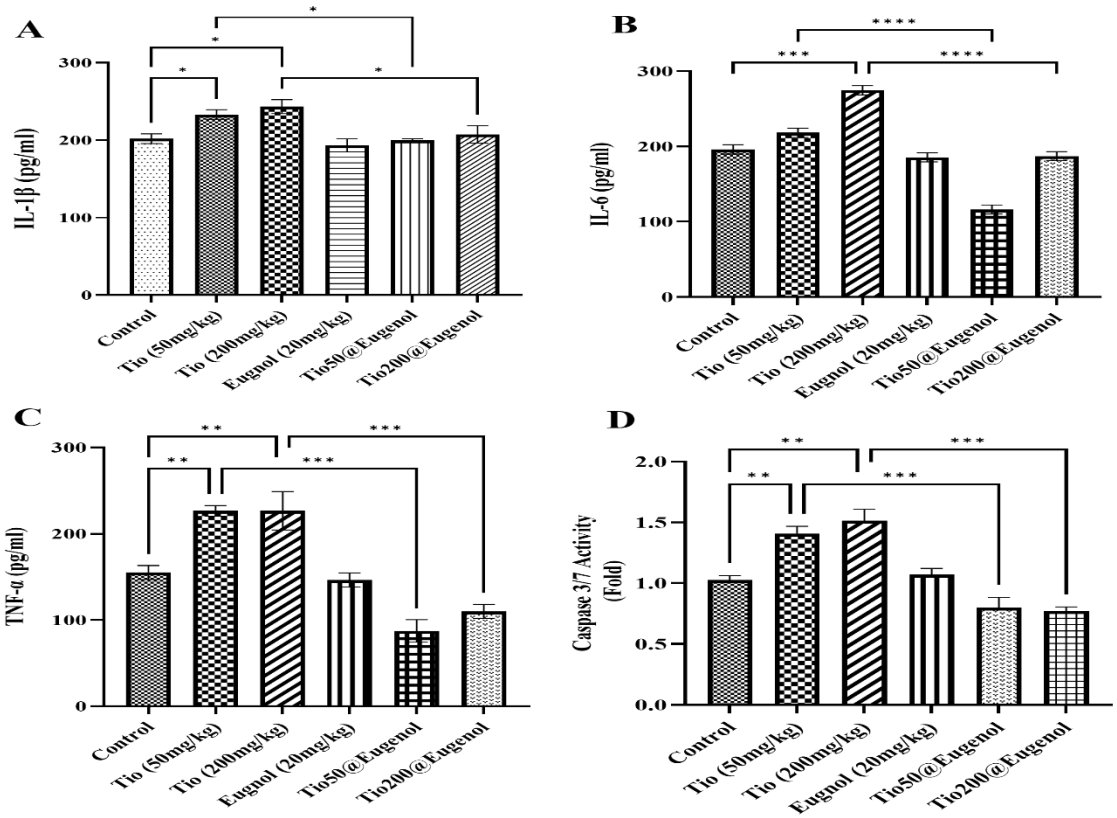


Fig. 4. ELISA assay results. Levels of (A) IL-1β, (B) IL-6, and (C) TNF-α D) Caspase 3/7 assay results, under individual and co-treatment with TiO2 NP, Eugenol and TiO2@Eugenol. *P < 0.05, ** P < 0.01, and *** P < 0.001, and **** indicate P < 0.0001

***Assessment of inflammatory factors in serum***

To quantify the inflammatory interleukins TNF-α, IL-1β, and IL-6 in serum samples from treated mice, an ELISA assay was performed (Figure 4). Analysis of IL-1β levels showed a significant dose-dependent increase in mice treated with $TiO_2$ NPs. In contrast, mice receiving eugenol-loaded NPs exhibited a marked reduction in IL-1β levels. This decrease was comparable between the two eugenol-loaded NP treatment groups (50 and 200 mg/kg).

Another inflammatory interleukin assessed in this study was IL-6. In mice treated with a high dose of $TiO_2$ NPs (200 mg/kg), IL-6 levels increased markedly, approximately 1.2-fold ($P < 0.001$). In contrast, treatment with $TiO_2$@eugenol reduced IL-6 levels, with the 50 mg/kg dose producing a greater decrease than the 200 mg/kg dose. Mice receiving eugenol alone also exhibited lower IL-6 levels, further supporting its anti-inflammatory effect.

In addition to assessing inflammatory interleukins, TNF-α levels were also evaluated. The analysis revealed a significant elevation in serum TNF-α in mice treated with both the low and high doses of $TiO_2$ NPs ($P < 0.001$). In contrast, mice receiving $TiO_2$@eugenol showed a marked reduction in TNF-α levels at both concentrations. Notably, compared with the nanoparticle-treated groups, the $TiO_2$@eugenol-treated mice exhibited nearly a twofold decrease in TNF-α levels. A similar reduction was also observed in mice treated with eugenol alone, further confirming its anti-inflammatory activity.

***Evaluation of Caspase-3/7 activity***

Another parameter evaluated in this study was caspase activity in liver extract samples from mice treated with either $TiO_2$ NPs alone or eugenol-loaded NPs. The results showed that caspase-3/7 activity increased by approximately 1.5-fold and 1.8-fold in mice treated with 50 and 200 mg/kg of $TiO_2$ NPs, respectively. In contrast, treatment with $TiO_2$@eugenol at 50 mg/kg resulted in a substantial reduction in caspase activity compared with $TiO_2$ NPs alone ($P < 0.0001$). A decrease in caspase activity was also observed in mice treated with $TiO_2$@eugenol at 200 mg/kg, although this reduction did not reach statistical significance. Overall, eugenol-loaded NPs demonstrated a pronounced inhibitory effect on caspase-3/7 activity.

***Histological analysis of liver, kidney, and spleen***

To evaluate the effects of the nanoparticles on inflammation and tissue damage, liver, spleen, and

kidney specimens were collected from treated mice. The samples were stained with hematoxylin and eosin (Figures 5, 6, and 7), and the extent of tissue alterations was examined. Histopathological analysis revealed that treatment with $TiO_2$ NPs at doses of 50 and 200 mg/kg led to a marked increase in necrosis and inflammation in hepatic tissue, the red and white pulp regions of the spleen, and renal tissue. In contrast, mice treated with eugenol-loaded NPs exhibited considerably reduced inflammation and necrosis. Liver sections from these groups displayed tissue morphology comparable to that of normal controls, and spleen samples also demonstrated significantly lower levels of structural damage and inflammatory infiltration.

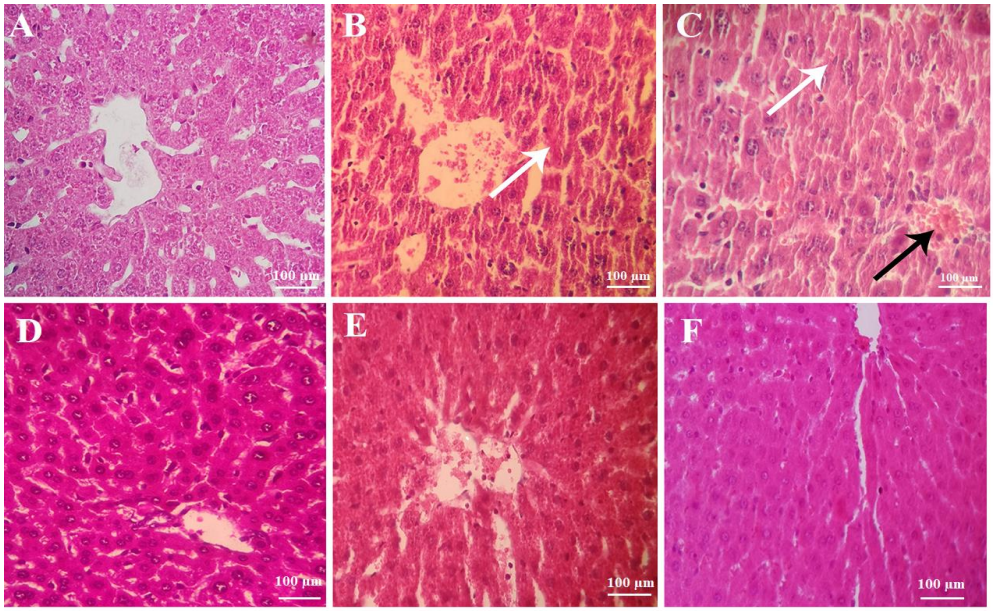


Fig. 5. Pathological Analysis of Liver Tissue: (A) Liver sample from the control group. (B) Liver sample from the group treated with 50 mg/kg of NPs, showing hepatocyte necrosis (indicated by the white arrow). (C) Liver sample treated with 200 mg/kg of NPs, displaying hepatocyte necrosis (white arrow) and central vein congestion (black arrow). (D) Liver sample from the eugenol treated group, where cells appear in normal condition. (E) Liver sample treated with eugenol-loaded NPs at 50 µg, with cells in a normal state. (F) Liver sample treated with eugenol-loaded NPs at 200 mg/kg, showing no hemorrhage or necrosis in the liver tissue.

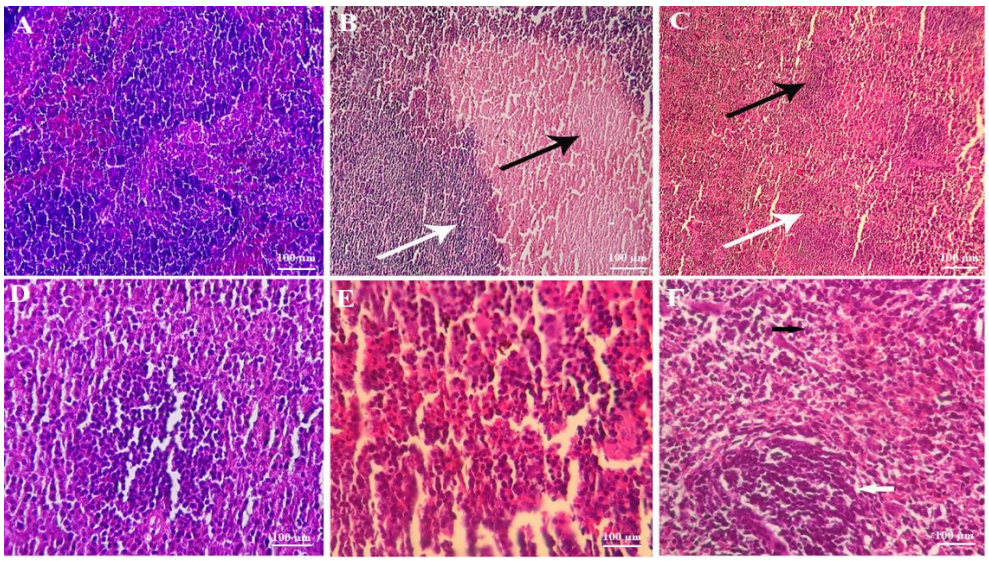


Fig. 6. Pathological Analysis of Spleen Tissue: (A) Spleen sample from the control group. (B) Spleen sample from the group treated with 50 µg of NPs, showing pulp necrosis (black arrow) and inflammation (white arrow). (C) Spleen sample treated with 200 µg of NPs, displaying necrosis in both red and white pulp (black and white arrows). (D) Spleen sample from the eugenol-treated group, where cells appear in normal condition. (E) Spleen sample treated with eugenol-loaded NPs at 50 µg, showing reduced necrosis compared to NPs alone. (F) Spleen sample treated with eugenol-loaded NPs at 200 µg, with decreased necrosis and clearly distinguishable red and white pulp.

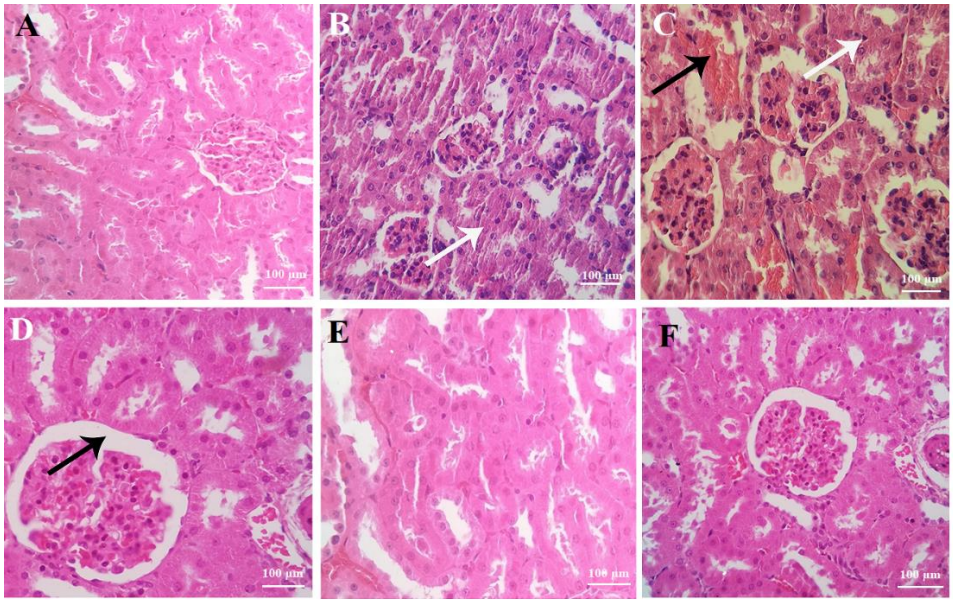


Fig. 7. Pathological Analysis of Kidney Tissue: (A) Kidney sample from the control group. (B) Kidney sample from the group treated with 50 µg of NPs, showing degeneration of renal tubular cells (white arrow). (C) Kidney sample treated with 200 µg of NPs, displaying degeneration of kidney cells (white arrow) and hemorrhage (black arrow). (D) Kidney sample from the eugenol treated group, where cells appear in normal condition, with an enlargement of Bowman's space. (E) Kidney sample treated with eugenol-loaded NPs at 50 µg, where cells are in a normal state. (F) Kidney sample treated with eugenol loaded NPs at 200 µg, showing normal kidney tissue, renal tubules, and glomeruli.

***Real-time quantitative data analysis***

As illustrated in Figure 8, treatment with bare $TiO_2$ NPs at concentrations of 50 µg and 200 µg induced an apparent reduction in the expression of transcripts encoding antioxidant enzymes, including SOD3, GR, and GPx. The extent of gene suppression was dose-dependent, with significantly greater inhibition observed at the higher concentration ($P < 0.01$), indicating potential pro-oxidant effects of bare NPs at elevated doses. In contrast, administration of eugenol alone or eugenol-loaded NPs resulted in a pronounced upregulation of these antioxidant-related genes. Specifically, liver tissues exposed to eugenol-loaded NPs exhibited a 1.7-fold increase in SOD3 expression, along with 1.5-fold and 1.2-fold increases in GR and GPx, respectively, compared with untreated controls and bare NP-treated groups. Notably, no statistically significant differences were observed between the 50 µg and 200 µg doses of eugenol-loaded NPs, suggesting a saturation effect or a potential upper limit in transcriptional activation within this dosage range. Collectively, these findings highlight eugenol's protective role against NP-induced oxidative stress and underscore its potential to modulate redox homeostasis at the molecular level through eugenol-functionalized nanocarriers.

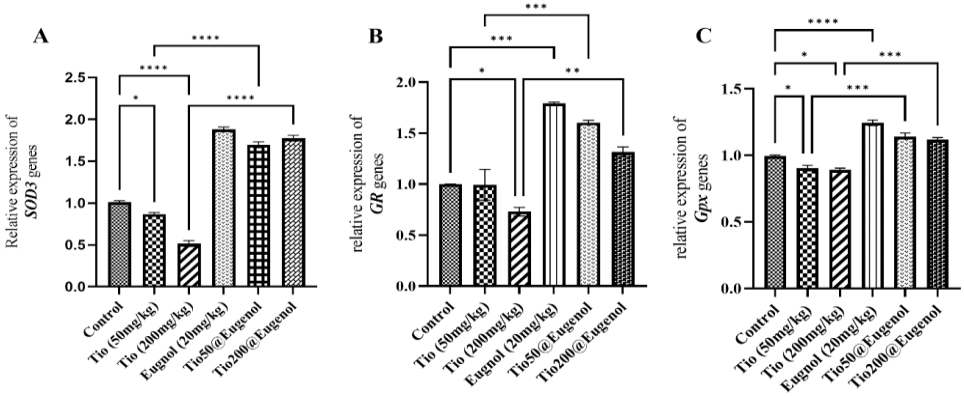


Fig. 8. Gene expression changes of SOD3, GR, and GPx under treatments with titanium dioxide NPs alone, eugenol alone, and eugenol-loaded NPs. Statistical significance of expression differences is shown in comparison to the control group and between loaded and single treatments: *p<0.01, **: p<0.001, ***: p<0.0001, ****: P<0.00001.

## DISCUSSION

With the expanding use of $TiO_2$ nanoparticles ($TiO_2$ NPs) in industrial and consumer products, human exposure has become increasingly unavoidable, leading to their accumulation in various organs. Such accumulation has been linked to oxidative damage, apoptosis, genotoxicity, and chromosomal instability [32, 33]. In the present study, we investigated the inflammatory, oxidative, and histopathological effects of $TiO_2$ NPs in their bare form and when functionalized with eugenol.

$TiO_2$ NP exposure is well documented to induce the production of inflammatory cytokines, primarily by activating immune cell responses and key inflammatory signaling pathways. $TiO_2$ NPs disrupt the inhibitory function of IκB, thereby facilitating NF-κB translocation into the nucleus and promoting the transcriptional upregulation of major inflammatory cytokines. This mechanism has been reported across multiple organs, including the lungs and brain, underscoring the systemic nature of $TiO_2$ NP–induced inflammation [34, 35]. In addition to NF-κB activation, $TiO_2$ NPs enhance the expression of Toll-like receptors (TLRs), particularly TLR2 and TLR4, on the surface of immune cells. These receptors are critical components of the innate immune system, recognizing pathogen-associated molecular patterns and amplifying downstream inflammatory signaling. Their upregulation further intensifies NF-κB activation, thereby contributing to the increased cytokine production observed following nanoparticle exposure [36].

The immune response to $TiO_2$ NPs also triggers the recruitment of inflammatory cells, primarily neutrophils and macrophages. These cells infiltrate affected tissues and secrete additional cytokines, creating a self-sustaining inflammatory loop that intensifies tissue damage [37]. Histopathological evaluations in multiple studies have confirmed such immune cell infiltration in organs exposed to $TiO_2$ NPs. Furthermore, $TiO_2$ NPs induce tissue-specific inflammation in organs such as the lungs, heart, and brain, resulting in observable structural damage. The extent and pattern of inflammation vary across organs, suggesting differential susceptibility and distinct response mechanisms [37-40]. Another essential aspect of $TiO_2$ NP-induced immunotoxicity is the disruption of the Th1/Th2 cytokine balance. Exposure to these nanoparticles tends to shift the immune response toward a Th1-dominant profile, accompanied by elevated transcriptional activation of inflammatory cytokines such as IL-1β and TNF-α. This imbalance may further potentiate chronic inflammation and contribute to long-term immune dysregulation [37].

In contrast, eugenol-loaded NPs significantly attenuated this inflammatory response, even at higher concentrations. The anti-inflammatory effects of eugenol, particularly when delivered via nanoparticles, arise from a combination of molecular and cellular mechanisms that synergistically modulate inflammatory signaling. A central aspect of eugenol's activity is the downregulation of key pro-inflammatory mediators. It markedly suppresses cytokine production and, subsequently, reduces the synthesis of critical inflammatory factors, such as nitric oxide (NO) and prostaglandins, thereby dampening the inflammatory cascade [41-43]. In addition to its immunomodulatory properties, eugenol possesses potent antioxidant activity. By effectively neutralizing reactive oxygen species (ROS), including superoxide and hydroxyl radicals, it mitigates oxidative stress—a well-established trigger of inflammatory signaling pathways. This reduction in ROS levels stabilizes cellular redox balance, thereby limiting ROS-mediated injury and inflammation [44]. At the intracellular level, eugenol interferes with major inflammatory signaling pathways, most notably the NF-κB and MAPK cascades, including ERK1/2 and p38. Inhibition of these pathways results in decreased expression of inflammation-related genes and reduced recruitment of immune cells to sites of tissue injury [45]. Furthermore, eugenol modulates immune cell behavior by reducing leukocyte adhesion and migration into inflamed tissues. It also suppresses macrophage activation and the subsequent release of inflammatory mediators, all without exerting cytotoxic effects on immune cells. This targeted immunoregulation helps limit tissue damage while preserving normal immune function [44].

Another noteworthy finding was that low-dose eugenol exerted a stronger inhibitory effect on IL-6 levels and caspase-3/7 activity than the higher dose. This outcome may reflect a hormetic response, wherein low concentrations of phenolic compounds activate protective antioxidant and anti-inflammatory pathways. In contrast, higher concentrations may paradoxically induce mild oxidative stress and diminish overall efficacy. Similar biphasic dose-dependent effects of eugenol have been reported in previous studies [46, 47].

Apoptosis analysis by caspase-3/7 activity revealed a notable increase in hepatic caspase activation following $TiO_2$ exposure, reaching up to 1.8-fold at 200 mg/kg, consistent with the observed cytotoxic and inflammatory responses. In contrast,

caspase activity was significantly reduced in mice treated with eugenol-loaded NPs, particularly at the 50 mg/kg dose, supporting eugenol's protective role. Previous studies have demonstrated the accumulation of $TiO_2$ NPs in rat tissues following intraperitoneal administration, with toxicity mediated mainly by reactive oxygen species (ROS) [48, 49]. Treatment with eugenol-loaded NPs has been shown to substantially reduce caspase activation in hepatic cells by mitigating oxidative stress, suppressing inflammatory signaling, and preserving cellular membrane integrity. These interconnected mechanisms collectively protect hepatocytes against apoptosis during liver injury. A central protective mechanism is eugenol's antioxidant activity, which efficiently scavenges free radicals and reduces lipid peroxidation (LPO) in hepatic tissue. By reducing oxidative stress, eugenol helps prevent mitochondrial dysfunction—a key trigger of the intrinsic apoptotic pathway that leads to caspase activation, particularly caspase-3 [50]. In this study, free eugenol provided only modest protection against $TiO_2$-induced oxidative stress and inflammation. This limited therapeutic effect aligns with the known pharmacokinetic limitations of eugenol, including its low solubility, chemical instability, and rapid systemic clearance [51]. In contrast, $TiO_2$@eugenol NPs exhibited markedly stronger protective effects, evidenced by reduced levels of TNF-α, IL-1β, and IL-6; decreased caspase-3 and caspase-7 activity; and restored expression of antioxidant genes. These enhanced outcomes can be attributed to the nanoparticle-based delivery system, which improves eugenol stability, prolongs its bioavailability, and enables controlled release at the target site [52, 53]. Collectively, these findings underscore the therapeutic advantage of nanoparticle functionalization in maximizing the protective potential of phytochemicals such as eugenol.

A limitation of this study is the absence of biodistribution analysis, which prevents confirmation of the precise organ-specific accumulation of $TiO_2$ and $TiO_2$@eugenol nanoparticles. Such investigations are essential for more accurately correlating histological and molecular alterations with actual tissue exposure. Another limitation is the potential toxicity associated with high-dose eugenol. Although eugenol has demonstrated potent antioxidant and anti-inflammatory activities, several studies have reported that, at elevated doses, it may exert hepatotoxic and pro-oxidant effects [54, 55]. Therefore, caution is warranted when extrapolating the protective effects observed here to higher or chronic dosing regimens. Future work should include biodistribution studies, pharmacokinetic profiling, and long-term toxicity evaluations to more comprehensively assess safety. Another limitation is that caspase-3/7 activity was evaluated only in liver tissue. This decision was based on the well-established tendency of $TiO_2$ nanoparticles to preferentially accumulate in the liver following systemic exposure [56, 57], as well as the focus of our gene expression analysis on hepatic antioxidant pathways. However, apoptosis in other organs, such as the kidney and spleen, may also contribute to systemic toxicity. Future studies should therefore incorporate multi-organ apoptosis assessments to provide a more complete evaluation of both protective and adverse effects.

Moreover, eugenol treatment restores the activity of endogenous antioxidant defenses, including SOD and GPx, as well as reduced glutathione (GSH) levels. This restoration of redox balance contributes to cellular stability and inhibits oxidative signals that drive apoptotic cascades [58]. In addition to its antioxidant effects, eugenol exerts significant anti-inflammatory activity by suppressing the production of inflammatory mediators that are known to be elevated during hepatic inflammation and injury. Because these cytokines play a critical role in promoting apoptotic signaling—particularly through extrinsic pathways—their downregulation leads to reduced caspase activation and diminished hepatocyte death [59]. Eugenol also plays an essential role in membrane stabilization, preserving the structural integrity of hepatocyte membranes and limiting cellular leakage and damage. This membrane-protective action reduces stimuli that trigger apoptotic signaling and further contributes to hepatoprotection [60]. Notably, both in vitro and in vivo studies have demonstrated that eugenol directly modulates apoptotic pathways by reducing caspase-3 expression and activity, a key executioner enzyme in the apoptotic process. The use of nanoparticles as a delivery system enhances these protective effects by improving eugenol's bioavailability and cellular uptake, thereby amplifying its therapeutic potential [59, 61].

Histological examination of the liver, spleen, and kidney further confirmed the systemic toxicity of $TiO_2$ NPs. Pronounced necrosis, hemorrhage, and inflammatory cell infiltration were evident in all three organs. Consistent with these findings, Liu et al. (2009) also reported substantial $TiO_2$ NP accumulation in the liver of mice [62]. In contrast, mice treated with eugenol-functionalized NPs exhibited markedly attenuated pathological alterations. Hepatic architecture, renal tubular structures, and splenic tissue displayed near-normal

morphology, underscoring the enhanced biocompatibility and therapeutic potential of eugenol-loaded NPs. $TiO_2$ NPs induce toxicity primarily through oxidative stress, generating ROS that drive lipid peroxidation, glutathione depletion, reduced antioxidant enzyme activity, DNA damage, and inflammation in vital organs such as the liver, kidney, and spleen. These molecular effects are accompanied by elevated biochemical markers (e.g., ALT, ALP) and histological indicators of tissue injury. Functionalization of $TiO_2$ NPs with eugenol substantially mitigated these toxic manifestations. Eugenol reduced lipid peroxidation, restored antioxidant defenses (e.g., GSH, SOD, GPx), decreased DNA damage, and normalized liver and kidney function markers. Furthermore, it improved mitochondrial integrity and reduced blood cell cytotoxicity [63]. At the molecular level, real-time PCR analysis revealed significant downregulation of key antioxidant genes (SOD3, GR, GPx) in animals treated with $TiO_2$ NPs, particularly at higher doses, supporting oxidative stress as a major mechanism of $TiO_2$-induced toxicity. In contrast, treatment with eugenol-loaded NPs resulted in robust upregulation of these antioxidant markers, with SOD3 expression increasing by 1.7-fold, GR by 1.5-fold, and GPx by 1.2-fold. One of the principal molecular mechanisms underlying eugenol's antioxidant and cytoprotective effects is its activation of the Nrf2/HO-1 antioxidant pathway [51]. This pathway plays a pivotal role in maintaining redox homeostasis by enhancing the expression of endogenous antioxidant enzymes and suppressing oxidative injury [64]. Under physiological conditions, nuclear factor erythroid 2 2-related factor 2 (Nrf2) is sequestered in the cytoplasm by its repressor, Kelch-like ECH-associated protein 1 (KEAP1), which targets it for ubiquitination and proteasomal degradation. Upon oxidative stress or eugenol exposure, structural modifications in KEAP1 prevent Nrf2 degradation, thereby stabilizing Nrf2 and promoting its nuclear translocation [64-66]. Among the downstream targets of Nrf2, heme oxygenase-1 (HO-1) serves as a critical effector. Activation of the Nrf2/HO-1 axis by eugenol reduces intracellular ROS levels, enhances antioxidant enzyme activity, and provides substantial protection against oxidative stress-induced apoptosis. These protective effects have been documented across various cell types, including pancreatic β-cells, hepatocytes, and immune cells, in which eugenol-mediated Nrf2 activation mitigates oxidative injury and promotes cell survival [66, 67]. Notably, experimental inhibition of Nrf2 abolishes eugenol's protective actions, further emphasizing the centrality of this pathway in mediating its antioxidant and cytoprotective effects [68].

## CONCLUSION

Overall, this study's findings demonstrate that bare $TiO_2$ NPs induce pronounced inflammatory and oxidative effects, particularly at higher concentrations. However, incorporation of eugenol into these nanoparticles not only mitigates these adverse outcomes but also enhances their therapeutic profile by reducing inflammation, apoptosis, and oxidative stress. Additionally, nanoparticle-based delivery markedly improves the pharmacokinetic properties of eugenol, including its solubility, stability, and cellular uptake. This enhanced delivery facilitates greater tissue penetration and increases local eugenol concentrations, thereby augmenting its anti-inflammatory and antioxidant efficacy, as reported in various experimental models. These results highlight the value of functionalizing nanoparticles with bioactive compounds, such as eugenol, to enhance biocompatibility and therapeutic efficacy. Further investigations—particularly those employing chronic exposure models and translational or clinical settings—are warranted to validate these findings and refine dosing strategies for future biomedical applications.

Future studies should extend these findings beyond short-term exposure by incorporating chronic or repeated-dose models to better characterize the long-term safety and efficacy of $TiO_2$@eugenol NPs. Comprehensive pharmacokinetic and biodistribution analyses will also be essential for determining systemic availability, organ-specific accumulation, and clearance mechanisms. Additionally, evaluating these nanoparticles in disease-specific contexts—such as metabolic liver disease, fibrosis, or cancer—where oxidative stress and inflammation play central pathological roles may further clarify their therapeutic potential and translational relevance.

## AUTHOR CONTRIBUTIONS

F. Al-Naffakh performed most of the experiments as part of his master's degree in Cellular and Molecular Biology. S. Reiisi coordinated the study, designed the experiments, performed data analysis, and revised the manuscript. N. Khalighi performed the NPs study and participated in intellectual discussions of the data. E. Moghtadaei Khorasgani performed pathological analysis.

## AVAILABILITY OF DATA AND MATERIALS

The authors declare that all generated and analyzed data are included in the manuscript.

## CONFLICT OF INTEREST

We certify that there is no conflict of interest with any financial organization.

**ETHICS APPROVAL**

This study is approved in accordance with international guidelines and ethical research principles (code: IR.SKU.REC.1403.039).

**CONSENT FOR PUBLICATION**

This article does not contain any person's data in any form.

**FUNDING**

No funding

**ACKNOWLEDGMENTS**

Grammarly and ChatGPT were used to improve the spelling, grammar, and overall English of the manuscript. These tools were not employed in the research design, data analysis, or the formulation of conclusions, or in any parts generally considered core requirements for authorship.

**REFERENCES**

1. McNeil SE. Nanotechnology for the biologist. J Leukoc Biol. 2005;78(3):585-594.
2. Nath D, Banerjee P. Green nanotechnology–a new hope for medical biology. Environ Toxicol Pharmacol. 2013;36(3):997-1014.
3. Chandoliya R, Sharma S, Sharma V, Joshi R, Sivanesan I. Titanium Dioxide Nanoparticle: A Comprehensive Review on Synthesis, Applications and Toxicity. Plants. 2024;13(21):2964.
4. Irshad MA, Nawaz R, Ur Rehman MZ, Adrees M, Rizwan M, Ali S, et al. Synthesis, characterization and advanced sustainable applications of titanium dioxide nanoparticles: A review. Ecotoxicol Environ Saf. 2021;212:111978.
5. Racovita AD. Titanium dioxide: structure, impact, and toxicity. Int J Environ Res Public Health. 2022;19(9):5681.
6. Kendall M, Holgate S. Health impact and toxicological effects of nanomaterials in the lung. Respirology. 2012;17(5):743-758.
7. Gao Y, Zhai H, She X, Si H. Quantitative structure-activity relationships; studying the toxicity of metal nanoparticles. Curr Top Med Chem. 2020;20(27):2506-2517.
8. del Pilar Chantada-Vázquez M, López AC, Bravo SB, Vázquez-Estévez S, Acea-Nebril B, Núñez C. Proteomic analysis of the bio-corona formed on the surface of (Au, Ag, Pt)-nanoparticles in human serum. Colloids Surf B Biointerfaces. 2019;177:141-148.
9. Lima T, Bernfur K, Vilanova M, Cedervall T. Understanding the lipid and protein corona formation on different sized polymeric nanoparticles. Sci Rep. 2020;10(1):1129.
10. Lee DS, Shin YK. Innate Immunity to Nanomaterials. Radionanomedicine. 2018:389-407.
11. Perciani CT, Liu LY, Wood L, MacParland SA. Enhancing immunity with nanomedicine: employing nanoparticles to harness the immune system. ACS Nano. 2020;15(1):7-20.
12. Tetley TD. Health effects of nanomaterials. Biochem Soc Trans. 2007;35(Pt 3):527-531.
13. Wu T, Tang M. Review of the effects of manufactured nanoparticles on mammalian target organs. J Appl Toxicol. 2018;38(1):25-40.
14. Park E-J, Park K. Oxidative stress and pro-inflammatory responses induced by silica nanoparticles in vivo and in vitro. Toxicol lett. 2009;184(1):18-25.
15. Tee JK, Ong CN, Bay BH, Ho HK, Leong DT. Oxidative stress by inorganic nanoparticles. Wiley Interdiscip Rev Nanomed Nanobiotechnol. 2016;8(3):414-438.
16. Domingues L, Carriello GM, Pegoraro GM, Mambrini GP. Synthesis of TiO2 nanoparticles by the solvothermal method and application in the catalysis of esterification reactions. An Acad Bras Cienc. 2024;96(suppl 3):e20240096.
17. Santos-Aguilar P, Bernal-Ramírez J, Vázquez-Garza E, Vélez-Escamilla LY, Lozano O, García-Rivas GJ, et al. Synthesis and Characterization of Rutile TiO(2) Nanoparticles for the Toxicological Effect on the H9c2 Cell Line from Rats. ACS Omega. 2023;8(21):19024-19036.
18. Barboza JN, da Silva Maia Bezerra Filho C, Silva RO, Medeiros JVR, de Sousa DP. An Overview on the Anti-inflammatory Potential and Antioxidant Profile of Eugenol. Oxid Med Cell Longev. 2018;2018:39-57.
19. Chaieb K, Hajlaoui H, Zmantar T, Kahla-Nakbi AB, Rouabhia M, Mahdouani K, et al. The chemical composition and biological activity of clove essential oil, Eugenia caryophyllata (Syzigium aromaticum L. Myrtaceae): a short review. Phytother Res. 2007;21(6):501-506.
20. Zari AT, Zari TA, Hakeem KR. Anticancer Properties of Eugenol: A Review. Molecules. 2021;26(23).
21. Nisar MF, Khadim M, Rafiq M, Chen J, Yang Y, Wan CC. Pharmacological Properties and Health Benefits of Eugenol: A Comprehensive Review. Oxid Med Cell Longev. 2021;2021:2497354.
22. Farrera C, Fadeel B. It takes two to tango: Understanding the interactions between engineered nanomaterials and the immune system. Eur J Pharm Biopharm. 2015;95(Pt A):3-12.
23. Boraschi D, Canesi L, Drobne D, Kemmerling B, Pinsino A, Prochazkova P. Interaction between nanomaterials and the innate immune system across evolution. Biol Rev. 2023;98(3):747-774.
24. Tsugita M, Morimoto N, Nakayama M. SiO 2 and TiO 2 nanoparticles synergistically trigger macrophage inflammatory responses. Part Fibre Toxicol. 2017;14:1-9.
25. Farrera C, Fadeel B. It takes two to tango: Understanding the interactions between engineered nanomaterials and the immune system. European Journal of Pharmaceutics and Biopharmaceutics. 2015;95:3-12.
26. Ghosh S, Bhattacherjee R, Banerjee D. Nanoparticles and adaptive immunity. Hum Immunol. 2022;25.
27. Ko C-N, Zang S, Zhou Y, Zhong Z, Yang C. Nanocarriers for effective delivery: Modulation of innate immunity for the management of infections and the associated complications. J Nanobiotechnology. 2022;20(1):380.

28. Basante-Romo M, Gutiérrez-M JO, Camargo-Amado R. Non-toxic doses of modified titanium dioxide nanoparticles (m-TiO2NPs) in albino CFW mice. Heliyon. 2021;7(3).
29. Kazimirova A, Baranokova M, Staruchova M, Drlickova M, Volkovova K, Dusinska M. Titanium dioxide nanoparticles tested for genotoxicity with the comet and micronucleus assays in vitro, ex vivo and in vivo. Mutat Res Genet Toxicol Environ Mutagen. 2019;843:57-65.
30. Alypoor S, Abdolmaleki A, Mamoudi F, Haghighat K, Soluki M. Evaluation of the Neuroprotective Effect of Eugenol on the Improvement of Sciatic Nerve Injury in Rats. Iran j toxicol. 2023;17(3):53-59.
31. Zhao Y-x, Wang D, Bais S, Wang H-x. Modulation of pro-inflammatory mediators by Eugenol in AlCl3 induced dementia in rats. 2019.
32. Baranowska-Wójcik E, Szwajgier D, Oleszczuk P, Winiarska-Mieczan A. Effects of titanium dioxide nanoparticles exposure on human health—a review. Biol Trace Elem Res. 2020;193(1):118-129.
33. Gilbert JD, Neubauer K, Byard RW. Macroscopic identification of visceral titanium pigment in an intravenous drug user. J Forensic Sci. 2021;66(5):2024-2028.
34. Ze Y, Sheng L, Zhao X, Hong J, Ze X, Yu X, et al. TiO2 nanoparticles induced hippocampal neuroinflammation in mice. PloS One. 2014;9(3):e92230.
35. Liu D, Zhou JL, Hong F, Zhang YQ. Lung inflammation caused by long-term exposure to titanium dioxide in mice involving in NF-κB signaling pathway. J Biomed Mater Res Part A. 2017;105(3):720-727.
36. Lehotska Mikusova M, Busova M, Tulinska J, Masanova V, Liskova A, Uhnakova I, et al. Titanium Dioxide Nanoparticles Modulate Systemic Immune Response and Increase Levels of Reduced Glutathione in Mice after Seven-Week Inhalation. Nanomaterials (Basel). 2023;13(4).
37. Hong F, Wang L, Yu X, Zhou Y, Hong J, Sheng L. Toxicological effect of TiO2 nanoparticle-induced myocarditis in mice. Nanoscale Res Lett. 2015;10(1):326.
38. Liu D, Zhou JL, Hong F, Zhang YQ. Lung inflammation caused by long-term exposure to titanium dioxide in mice involving in NF-κB signaling pathway. J Biomed Mater Res A. 2017;105(3):720-727.
39. Jeong J-S, Jegal H, Ko J-W, Kim J-W, Kim J-H, Chung E-H, et al. Titanium Dioxide Nanoparticle Exposure Provokes Greater Lung Inflammation in Females Than Males in the Context of Obesity. Int J Nanomed. 2025:5321-5336.
40. Lim J-O, Lee S-J, Kim W-I, Pak S-W, Moon C, Shin I-S, et al. Titanium dioxide nanoparticles exacerbate allergic airway inflammation via TXNIP upregulation in a mouse model of asthma. Int J Mol Sci. 2021;22(18):9924.
41. Barboza JN, da Silva Maia Bezerra Filho C, Silva RO, Medeiros JVR, de Sousa DP. An overview on the anti-inflammatory potential and antioxidant profile of eugenol. Oxid Med Cell Longev. 2018;2018(1):39-57.
42. Nisar M, Khadim M, Rafiq M, Chen J, Yang Y, Wan C. Pharmacological Properties and Health Benefits of Eugenol: A Comprehensive Review. Oxid Med Cell Longev. 2021: 2497354. 2021.
43. Kumar A, Siddiqi NJ, Alrashood ST, Khan HA, Dubey A, Sharma B. Protective effect of eugenol on hepatic inflammation and oxidative stress induced by cadmium in male rats. Biomed Pharm. 2021;139:111588.
44. Keshari R, Tharmatt A, Pillai MM, Chitkara D, Tayalia P, Banerjee R, et al. Eugenol-Loaded lipid Nanoparticles-Derived hydrogels ameliorate Psoriasis-like skin lesions by Lowering oxidative stress and modulating inflammation. ACS Pharmacol Transl Sci. 2024;7(11):3592-3606.
45. Leem H-H, Kim E-O, Seo M-J, Choi S-W. Antioxidant and anti-inflammatory activities of eugenol and its derivatives from clove (Eugenia caryophyllata Thunb.). J Korea Soc Food Sci Nutr. 2011;40(10):1361-1370.
46. Nagababu E, Rifkind JM, Boindala S, Nakka L. Assessment of antioxidant activity of eugenol in vitro and in vivo. Methods Mol Biol. 2010;610:165-180.
47. Pires Costa E, Maciel dos Santos M, de Paula RA, da Silva DA, Lopes RP, Teixeira RR, et al. Antioxidant and Anti-inflammatory Activity of Eugenol, Bis-eugenol, and Clove Essential Oil: An In Vitro Study. ACS omega. 2025;10(28):31033-31045.
48. Cui XueYan CX, Yin Jun YJ, Lin Ying LY, Li Na LN, Wang MeiZhen WM, Shen DongSheng SD. Towards a definition of harmless nanoparticles from an environmental and safety perspective. 2016.
49. Valentini X, Rugira P, Frau A, Tagliatti V, Conotte R, Laurent S, et al. Hepatic and renal toxicity induced by TiO2 nanoparticles in rats: a morphological and metabonomic study. J Toxicol. 2019;2019(1):5767012.
50. Zaky MY, Morsy HM, Abdel-Moneim A, Zoheir KM, Bragoli A, Abdel-Maksoud MA, et al. Anticancer potential of eugenol in hepatocellular carcinoma through modulation of oxidative stress, inflammation, apoptosis, and proliferation mechanisms. Discov Oncol. 2025;16(1):1080.
51. Ma L, Liu J, Lin Q, Gu Y, Yu W. Eugenol protects cells against oxidative stress via Nrf2. Exp Ther Med. 2021;21(2):107.
52. Pramod K, Ansari SH, Ali J. Eugenol: a natural compound with versatile pharmacological actions. Nat Prod Commun. 2010;5(12):1934578X1000501236.
53. Chowdhury S, Nath D, Chanda Das SR, Kar K, Chakraborty P, Kapoor DU, et al. Nanotechnology based herbal drug delivery system: Current insights and future prospects. Curr Nanomed. 2024.
54. Mohammadi Nejad S, Özgüneş H, Başaran N. Pharmacological and Toxicological Properties of Eugenol. Turk J Pharm Sci. 2017;14(2):201-206.
55. Carvalho RPR, Ribeiro FCD, Lima TI, Ervilha LOG, de Oliveira EL, Faustino AO, et al. High doses of eugenol cause structural and functional damage to the rat liver. Life Sci. 2022;304:120696.

56. Chen J, Dong X, Zhao J, Tang G. In vivo acute toxicity of titanium dioxide nanoparticles to mice after intraperitioneal injection. J Appl Toxicol. 2009;29(4):330-337.
57. Liu H, Ma L, Zhao J, Liu J, Yan J, Ruan J, et al. Biochemical toxicity of nano-anatase TiO2 particles in mice. Biol Trace Elem Res. 2009;129(1):170-180.
58. Yousef HN, Ibraheim SS, Ramadan RA, Aboelwafa HR. The ameliorative role of eugenol against silver nanoparticles-induced hepatotoxicity in male Wistar rats. Oxid Med Cell Longev. 2022;2022(1):3820848.
59. Majeed H, Antoniou J, Fang Z. Apoptotic effects of eugenol-loaded nanoemulsions in human colon and liver cancer cell lines. Asian Pac J Cancer Prev. 2014;15(21):9159-9164.
60. Binu P, Nellikunnath Priya M, Abhilash S, Vineetha RC, Nair H. Protective effects of eugenol against hepatotoxicity induced by arsenic trioxide: An antileukemic drug. Iran J med sci. 2018;43(3):305.
61. TR DP, Haykal MN. Eugenol nanoparticle encapsulated chitosan enhances cell cycle arrest in hela human cervical cancer cells. Sys Rev Pharm. 2021;12(2).
62. Cui Y, Liu H, Ze Y, Zengli Z, Hu Y, Cheng Z, et al. Gene expression in liver injury caused by long-term exposure to titanium dioxide nanoparticles in mice. Toxicol Sci. 2012;128(1):171-185.
63. Wani MR, Maheshwari N, Shadab G. Eugenol attenuates TiO2 nanoparticles-induced oxidative damage, biochemical toxicity and DNA damage in Wistar rats: an in vivo study. nviron Sci Pollut Res Int. 2021;28(18):22664-22678.
64. Jiang Y, He P, Sheng K, Peng Y, Wu H, Qian S, et al. The protective roles of eugenol on type 1 diabetes mellitus through NRF2-mediated oxidative stress pathway. Elife. 2025;13:RP96600.
65. Su H, Wang Z, Zhou L, Liu D, Zhang N. Regulation of the Nrf2/HO-1 axis by mesenchymal stem cells-derived extracellular vesicles: implications for disease treatment. Front Cell Dev Biol. 2024;12:1397954.
66. Yuan L, Wang Y, Li N, Yang X, Sun X, Tian He, et al. Mechanism of action and therapeutic implications of Nrf2/HO-1 in inflammatory bowel disease. Antioxidants. 2024;13(8):1012.
67. Luo Y, Lu S, Dong X, Xu L, Sun G, Sun X. Dihydromyricetin protects human umbilical vein endothelial cells from injury through ERK and Akt mediated Nrf2/HO-1 signaling pathway. Apoptosis. 2017;22(8):1013-1024.
68. Alonso-Piñeiro JA, Gonzalez-Rovira A, Sánchez-Gomar I, Moreno JA, Durán-Ruiz MC. Nrf2 and heme oxygenase-1 involvement in atherosclerosis related oxidative stress. Antioxidants. 2021;10(9):1463.